THE UNIVERSITY OF CHICAGO

HOW GALAXIES FORM STARS: THE CONNECTION BETWEEN LOCAL AND GLOBAL STAR FORMATION IN GALAXIES

A DISSERTATION SUBMITTED TO
THE FACULTY OF THE DIVISION OF THE PHYSICAL SCIENCES
IN CANDIDACY FOR THE DEGREE OF
DOCTOR OF PHILOSOPHY

DEPARTMENT OF ASTRONOMY AND ASTROPHYSICS

BY
VADIM SEMENOV

CHICAGO, ILLINOIS
AUGUST 2019

To my parents and wife for their unconditional support

TABLE OF CONTENTS

LIST OF FIGURES

LIST OF TABLES

ACKNOWLEDGMENTS

It is my great pleasure to thank all the people who accompanied me throughout my PhD and made the completion of this dissertation possible.

First and most importantly, I would like to express my deepest gratitude to my advisor, Andrey Kravtsov, for his exceptional guidance throughout my graduate studies. I cannot thank Andrey enough for his wisdom, patience, and for helping me with advice about not only science-related but also personal matters. Andrey's commitment and highest standards of doing research, teaching classes, and mentoring students will always be an inspiring example for me in my future career.

I am also greatly indebted to Nick Gnedin, whom I rightfully consider my second advisor. I am thankful to Nick for countless conversations about science, programming, and life in general. It was always great to drop by his office to discuss ideas and ask questions, and I will miss this opportunity in the future.

I am grateful to Damiano Caprioli and Rich Kron, for dedicating their time to serving on my thesis committee. Their comments, questions, and suggestions were very useful for writing this dissertation. I am also thankful to Damiano for numerous meetings and discussions of various intriguing aspects of cosmic ray physics that motivated me to start exploring this immensely rich field.

Finally, I would like to thank all the faculty, postdocs, students, and staff of the Department of Astronomy and Astrophysics at the University of Chicago who made my time in Chicago so awesome. Thanks to you all, the department became a home to me, and my years there flew by incredibly quickly.

The simulations and analyses presented in this dissertation have been carried out using the Midway cluster at the University of Chicago Research Computing Center, which I acknowledge for support. Presented work was greatly aided by the following free software packages: `yt` (Turk et al., 2011), `NumPy` (van der Walt et al., 2011), `SciPy` (Jones et al.,

2001-2016), `Matplotlib` (Hunter, 2007), and `GitHub`[1]. I have also extensively used the Astrophysics Data Service[2] and `arXiv`[3] preprint repository during this project and writing of the papers and this dissertation.

1. https://github.com

2. https://ui.adsabs.harvard.edu

3. https://arxiv.org

ABSTRACT

The fact that observed star-forming galaxies convert their gas into stars inefficiently posits a long-standing theoretical puzzle. Available gas in galaxies is depleted on a timescale of several Gyrs which is orders of magnitude longer than any timescale of the processes driving gas evolution in galaxies. Many galaxy simulations can reproduce observed long depletion times but the physical mechanism controlling their values is not well understood. In addition, some of the simulations show a rather counter-intuitive behavior: global depletion times appear to be almost insensitive to the assumptions about local star formation in individual star-forming regions, a phenomenon described as "self-regulation." Yet another part of the puzzle is the observed tight and near-linear correlation between star formation rates and the amount of molecular gas on kiloparsec and larger scales. A linear correlation implies that the depletion time of molecular gas is almost independent of molecular gas density on >kiloparsec scales, while a strong dependence is expected if, e.g., star formation is controlled by molecular gas self-gravity. We present an intuitive physical model that explains the origin of long gas depletion times in galaxies and the near-linear correlation between star formation rates and molecular gas. Our model is based on mass conservation of gas as the gas cycles between dense star-forming and diffuse states in the interstellar medium. We use simulations of an isolated $L_\star$ galaxy to illustrate our model and to explore the connection between global depletion times and the timescales of processes driving gas evolution on small scales. In particular, we show that our model can explain the physics of self-regulation of star formation in galaxies with efficient stellar feedback. We also show that a linear correlation between star formation rate and molecular gas emerges when feedback efficiently regulates and stirs the evolution of dense, molecular gas. Our model also provides insights into the likely origin of this relation in real galaxies on different scales.

This dissertation is based on the work published in Semenov et al. (2016, 2017, 2018, 2019).

CHAPTER 1

INTRODUCTION

Understanding how galaxies build up their stellar component is a key to understanding galaxy evolution. Formation of stars in galaxies is a complex multiscale process, as stars are formed from gravitationally bound gaseous cores on subparsec scales, while the formation of such cores is aided by bulk gas motions of the interstellar medium (ISM) on hundreds of parsec scales. Gas motions on all relevant scales are in turn affected by star formation, as young stars feed mass, energy, and momentum back to the gas, destroying dense star-forming regions, stirring the ISM turbulence, and shaping the gas distribution on large scales via energetic outflows.

Despite this complexity, the star formation rate (SFR) per unit gas mass on kiloparsec and larger scales appears to be surprisingly universal: the gas depletion time, $\tau = M_{\rm g}/\dot{M}_\star$, has a characteristic value and exhibits a relatively small scatter (see, e.g., Kennicutt & Evans, 2012, for a review). This universality is manifested in a correlation between the surface densities of gas and SFR known as the Kennicutt–Schmidt relation (KSR; Schmidt, 1959; Kennicutt, 1989, 1998, see also Sanduleak 1969, Madore et al. 1974). The KSR becomes especially tight and close to linear when only molecular gas is included in the estimate of the gas mass (Wong & Blitz, 2002; Bigiel et al., 2008, 2011; Leroy et al., 2008, 2013; Bolatto et al., 2017; Utomo et al., 2017; Colombo et al., 2018; de los Reyes & Kennicutt, 2019).

Although the KSR for both total and molecular gas was studied extensively in galaxy simulations (e.g., Kravtsov, 2003; Li et al., 2005; Saitoh et al., 2008; Schaye & Dalla Vecchia, 2008; Feldmann et al., 2011; Gnedin & Kravtsov, 2011; Rahimi & Kawata, 2012; Agertz et al., 2013; Gnedin et al., 2014; Agertz & Kravtsov, 2015; Khoperskov & Vasiliev, 2017; Capelo et al., 2018; Lupi et al., 2018; Orr et al., 2018) and in analytical frameworks (e.g., Wyse & Silk, 1989; Silk, 1997; Tan, 2000; Elmegreen, 2002; Krumholz & McKee, 2005; Li et al., 2005; Krumholz & Thompson, 2007; Krumholz et al., 2009b; Silk & Norman, 2009; Ostriker

et al., 2010; Ostriker & Shetty, 2011; Renaud et al., 2012; Faucher-Giguère et al., 2013; Federrath, 2013; Elmegreen, 2015; Salim et al., 2015), several rather fundamental questions remain widely debated. For instance, there is still no consensus about the physical origin of the KSR normalization, i.e. global depletion times in galaxies. Recent simulations used to explore this issue find a rather counter-intuitive behavior: global depletion times appear to be almost insensitive to the assumptions about local star formation in individual star-forming regions—a phenomenon described as "self-regulation" (e.g., Dobbs et al., 2011a; Agertz et al., 2013; Hopkins et al., 2013a, 2017a; Agertz & Kravtsov, 2015; Benincasa et al., 2016; Orr et al., 2018). The physics behind this phenomenon and, more generally, the connection between the KSR and the processes driving gas evolution on scales of star-forming regions was not rigorously explained in such studies. Finally, the shape of the KSR is also puzzling. In particular, it is not clear why in normal star-forming (non-starburst) galaxies, SFR correlates almost linearly with the amount of molecular gas on kiloparsec and larger scales. Answering these and related questions will be the focus of this dissertation.

1.1 Surprisingly long gas depletion times in galaxies

The first question we will address concerns the origin of the KSR normalization and global depletion times in galaxies. One of the widely recognized basic facts about observed galaxies is that they convert gas into stars inefficiently. Global depletion times of gas in galaxies are surprisingly long, given the expected time scales of processes driving star formation.

As an example, the SFR of the Milky Way (MW) is $\dot{M}_\star \sim 1$–$2\ \mathrm{M}_\odot\ \mathrm{yr}^{-1}$ (e.g., Licquia & Newman, 2015), while its gas mass is $M_\mathrm{g} \sim 10^{10}\ \mathrm{M}_\odot$ (e.g., Kalberla & Kerp, 2009), and thus the global gas depletion time of the MW is $\tau \equiv M_\mathrm{g}/\dot{M}_\star \sim 5$–$10$ Gyr. The depletion times of a population of normal star-forming galaxies are comparable and span a range of ~ 2–10 Gyr (Kennicutt, 1989, 1998; Bigiel et al., 2008). The denser molecular phase of the ISM is depleted on a similarly long time scale of $\tau_{\mathrm{H}_2} \equiv M_{\mathrm{H}_2}/\dot{M}_\star \sim 1$–$3$ Gyrs (Kennicutt,

1989, 1998; Wong & Blitz, 2002; Bigiel et al., 2008; Leroy et al., 2008, 2013; Bolatto et al., 2017).

Compared to the time scales of any dynamical processes that are potentially relevant for star formation, the observed gas depletion times are very long indeed. For example, the orbital period of gas at the solar radius is $t_{\rm orb} \sim 200$ Myr, and the MW is thus depleting its gas on the timescale of ~ 25–50 such periods. On average, galaxies deplete their gas on a timescale of ~ 10–20 orbital periods (Kennicutt, 1998; Wong & Blitz, 2002; Leroy et al., 2008; Daddi et al., 2010; Colombo et al., 2018).

The orbital period, $t_{\rm orb}$, is probably the longest of the relevant dynamical timescales one can think of. For example, the turbulent crossing time is usually $t_{\rm cross} = h/\sigma \sim 10$–$30$ Myr, where $\sigma \gtrsim 10\,{\rm km\,s^{-1}}$ is the velocity dispersion of gas in galactic disks and $h \sim 100$–300 pc is the disk scale height in the inner regions of galaxies. The free-fall time at the mean or midplane density, ρ_0, of galaxies spans a similar range: $t_{\rm ff,0} \equiv \sqrt{3\pi/32G\rho_0} \sim 10$–$50$ Myr. The timescale of molecular cloud collisions is $\lesssim 20$ Myr (e.g., Tan, 2000). A given gas mass encounters a spiral arm on a timescale of $t_{\rm arm} \sim 2\pi/(m[\Omega(R) - \Omega_{\rm p}])$, where $\Omega(R) = V_{\rm rot}/R$ is the angular frequency of gas rotation, $\Omega_{\rm p}$ is the pattern speed of spiral arms, and m is the number of spiral arms. This timescale is $t_{\rm arm} \sim 50$–200 Myr, if we assume $\Omega_{\rm p} \sim 20\,{\rm km\,s^{-1}\,kpc^{-1}}$ (e.g., Bissantz et al., 2003), $m \sim 2$–4 (e.g., Davis et al., 2015) and $V_{\rm rot} \sim 220\,{\rm km\,s^{-1}}$ typically derived for MW-like galaxies. Numerical simulations of gaseous galactic disks show that star-forming molecular clouds may form on even shorter timescales of a few tens of Myrs (Dobbs et al., 2012, 2015).

In addition to being slow on global galactic scales, star formation is inefficient even in dense molecular star-forming regions, which convert only $\lesssim 1$–10% of gas into stars per local free-fall time (Zuckerman & Evans, 1974; Zuckerman & Palmer, 1974; Krumholz & Tan, 2007; Krumholz et al., 2012a; Evans et al., 2014; Lee et al., 2016; Heyer et al., 2016). Such low efficiency arises because only ~ 0.1–10% of the dense gas is self-gravitating and

collapsing into stars (Froebrich & Rowles, 2010).

However, the inefficiency of star-forming regions alone cannot explain long global depletion times. The *local* depletion time in observed star-forming regions is $t_\star \sim 40$–500 Myr (e.g., Evans et al., 2009, 2014; Lada et al., 2010, 2012; Heiderman et al., 2010; Gutermuth et al., 2011; Schruba et al., 2017). Thus, although the scatter is significant, typical values of $t_\star$ are considerably smaller than the *global* depletion time of molecular gas, $\tau_{\rm H_2} \sim 1$–3 Gyr.

The large scatter in depletion times measured on small scales and the difference between local and global depletion time values indicate that only a fraction of molecular gas is actively forming stars at any given moment. Indeed, the global depletion time can be expressed as

$$\tau \equiv \frac{M_{\rm g}}{\dot{M}_\star} = \frac{\tau_\star}{f_{\rm sf}}, \tag{1.1}$$

where $M_{\rm g}$ is the total gas mass of the galaxy; $\tau_\star \equiv M_{\rm sf}/\dot{M}_\star = \langle 1/t_\star \rangle_{\rm sf}^{-1}$ is the mass-weighted average over the depletion time distribution in star-forming regions, $t_\star$; and $f_{\rm sf} \equiv M_{\rm sf}/M_{\rm g}$ is the gas mass fraction in actively star-forming regions. A similar expression can be written for the global depletion time of molecular gas, $\tau_{\rm H_2}$, via a corresponding star-forming fraction $f_{\rm sf,H_2} \equiv M_{\rm sf}/M_{\rm H_2}$:

$$\tau_{\rm H_2} \equiv \frac{M_{\rm H_2}}{\dot{M}_\star} = \frac{\tau_\star}{f_{\rm sf,H_2}}. \tag{1.2}$$

Thus, the depletion time measured on larger scales is longer than that in star-forming regions because, as the scale increases, more of non-star-forming gas is incorporated in the gas mass estimate. Likewise, when depletion time is estimated on larger scales, the scatter in τ and $\tau_{\rm H_2}$ decreases as we average over the distribution of local $t_\star$. Such a dependence of scatter on scale is indeed observed (Schruba et al., 2010, 2017), although some of the obtained variation may be due to observational effects (Feldmann et al., 2011; Kruijssen & Longmore, 2014).

Over the last three decades, a number of useful global star formation frameworks and

models have been developed to consider the physical origin of the KSR normalization and long depletion timescale. One class of such models associates long depletion times with the fraction of gas in dense, self-gravitating regions of cold, supersonic molecular clouds with the log-normal gas density PDF (Elmegreen, 2002; Krumholz & McKee, 2005; Krumholz et al., 2012a). Such models, however, assume that all of the molecular gas is in "virialized" star-forming molecular clouds and that the star formation efficiency in these clouds sets the global depletion time. This assumption, which has also been frequently adopted in galaxy simulations (e.g., Robertson & Kravtsov, 2008; Gnedin et al., 2009; Christensen et al., 2012; Kuhlen et al., 2012), is at odds with a growing number of observations indicating that the depletion time of *star-forming* molecular gas is in general considerably shorter than the global depletion time of *all* molecular gas, $\tau_{\rm H_2}$, estimated on kiloparsec and larger scales. Moreover, models and simulations of star formation in supersonic turbulent clouds show that the local efficiency of star formation is primarily a strong function of the virial parameter of the region, not just its density, temperature, and molecular fraction (e.g., Krumholz & McKee, 2005; Padoan et al., 2012, 2017), while the virial parameter can span a wide range of values (Dobbs et al., 2011b; Semenov et al., 2016, see also Appendix A.4).

Some models derive the KSR and its normalization by assuming that stellar feedback regulates ISM turbulence so as to maintain vertical and/or Toomre (1964) equilibrium within gaseous disks (Ostriker & Shetty, 2011; Faucher-Giguère et al., 2013; Hayward & Hopkins, 2017). However, it is not clear a priori why equilibrium can generically be expected in galaxies as a whole or in kiloparsec-scale patches and why the star formation rate does not instead reach values at which gas is driven out in a wind. Moreover, it is still debated whether the turbulence within galactic disks is mainly driven by stellar feedback or by gravitational instabilities (e.g., Krumholz & Burkhart, 2016).

Saitoh et al. (2008) argued that SFR is controlled by the rate at which gas is supplied from the general ISM to the star-forming state, which makes it insensitive to the local efficiency

of star formation. However, these authors measured the timescale at which gas is supplied to the star-forming state to be ~ 100 Myr and did not explain how this timescale relates to the much longer observed depletion times of total gas, $\tau \sim 2$–10 Gyrs.

In this work, we aim to clarify the origin of the observed long gas depletion timescale in galaxies, taking into account both the inefficiency of star formation in star-forming clouds and the fact that not all of the molecular gas is actively forming stars.

1.2 Insights from galaxy formation simulations

Major insights into the origin of depletion times and the KSR can be gained using numerical simulations of galaxy formation. Simulations enable us to vary systematically the parameters of star formation and stellar feedback operating on small scales and explore their effect on global star formation in galaxies.

Modeling of local star formation and feedback processes in galaxy simulations is admittedly rather crude. With some variations and few exceptions, star formation prescriptions usually follow ideas introduced for the first generation of simulations (Cen & Ostriker, 1992; Katz, 1992): star formation occurs only in star-forming gas, defined using some conditions, e.g., that gas density (temperature) is larger (smaller) than some threshold, that gas within some region is gravitationally bound, that gas is in molecular phase, etc. (see, e.g., Hopkins et al., 2013a). Star-forming gas is then converted into stellar particles using a stochastic Poisson process with the rate

$$\dot{\rho}_\star = \frac{\rho}{t_\star}, \tag{1.3}$$

where ρ is the density of the gas that is deemed to be star-forming according to the adopted criteria, and $t_\star$ is its *local* depletion time. In most of the recent studies, this time is parameterized as $t_\star = t_{\rm ff}/\epsilon_{\rm ff}$, where $\epsilon_{\rm ff}$ is the star formation efficiency per freefall time, $t_{\rm ff} \equiv \sqrt{3\pi/32G\rho}$. Likewise, the stellar feedback is modeled by simply injecting thermal

and kinetic energy and momentum into gas resolution elements adjacent to a young star particle (e.g., Hopkins et al., 2011, 2017b; Agertz et al., 2013; Simpson et al., 2015) or using a subgrid prescription with a specific model of ISM on scales below resolution (e.g., Yepes et al., 1997; Springel & Hernquist, 2003; Braun & Schmidt, 2012).

Despite a rather simplistic modeling of star formation and feedback on scales close to the spatial resolution, modern galaxy formation simulations generally predict τ and the KSR on kiloparsec and larger scales in a reasonable agreement with observations (e.g., Governato et al., 2010; Stinson et al., 2013; Hopkins et al., 2014, 2017a; Agertz & Kravtsov, 2015, 2016; Grand et al., 2017; Orr et al., 2018). Although in certain regimes the normalization and slope of the KSR on galactic scales simply reflect the adopted value of $t_\star$ on small scales and its assumed density dependence (Schaye & Dalla Vecchia, 2008; Gnedin et al., 2014), in other regimes there is no direct connection between $t_\star$ and the global KSR (Hopkins et al., 2017a; Orr et al., 2018).

An intriguing example of the behavior in the latter regime is the insensitivity of the global depletion time to the star formation efficiency $\epsilon_{\rm ff}$ assumed on the scales of individual star-forming regions. This phenomenon is usually described as "self-regulation" (e.g., Dobbs et al., 2011a; Agertz et al., 2013; Hopkins et al., 2013a, 2017a; Agertz & Kravtsov, 2015; Benincasa et al., 2016; Orr et al., 2018). The fact that simulations in such self-regulated regime still result in the global depletion time close to the observed values is nontrivial. This agreement indicates that such simulations can be used to shed light on the physical processes connecting local parameters of star formation and feedback to the global star formation in galaxies.

This connection and associated processes are the focus of this dissertation, and one of our goals is to extend and make sense of the results of other recent studies of this issue (see, e.g., Hopkins et al., 2011, 2017a; Agertz et al., 2013; Agertz & Kravtsov, 2015; Benincasa et al., 2016; Li et al., 2017a,b).

1.3 The linear slope of molecular Kennicutt–Schmidt relation

Yet another part of the puzzle is the near-linear slope of the molecular KSR observed in normal star-forming (non-starburst) galaxies (Wong & Blitz, 2002; Bigiel et al., 2008, 2011; Leroy et al., 2008, 2013; Bolatto et al., 2017; Utomo et al., 2017; Colombo et al., 2018). In other words, the depletion time of molecular gas in kiloparsec-scale patches of the ISM, $\tau_{\mathrm{H_2}} = \Sigma_{\mathrm{H_2}}/\dot{\Sigma}_\star \approx 2 \pm 1$ Gyr, is independent of the molecular gas surface density $\Sigma_{\mathrm{H_2}}$.

The existence of some correlation between SFR and molecular gas surface densities is expected because both SFR and molecular gas trace dense ISM gas. What is surprising, however, is that the observed correlation is close to linear. Given that dynamical time scales as $t_{\mathrm{dyn}} \propto 1/\sqrt{G\rho}$, where ρ is the average density of a region, naïvely we could expect a superlinear KSR: $\dot{\rho}_\star \propto \rho/t_{\mathrm{dyn}} \propto \rho^{1.5}$. Therefore, the linear slope indicates that the origin of molecular KSR is more nuanced and is not shaped by gas self-gravity alone.

The mechanism responsible for the linear slope must be rather universal and operate in a range of environments and for different states of dense gas. Indeed, the near-linear slope in the molecular KSR persists in diverse galactic environments, from the average ISM of various Hubble types of disk galaxies (e.g., Utomo et al., 2017; Colombo et al., 2018) to low-density disk outskirts (Schruba et al., 2011) and even in low-metallicity dwarf galaxies (Bolatto et al., 2011; Jameson et al., 2016). A close-to-linear relation is also observed for dense gas visible in HCN and $\mathrm{HCO^+}$ over 8 orders of magnitude in mass and on a wide range of spatial scales, from ~ 10 pc scales to scales of entire galaxies (Gao & Solomon, 2004b,a; Wu et al., 2005). However, the relation for molecular gas is not always linear: it steepens on small, $\lesssim 10$ parsec, scales (e.g., Evans et al., 2009, 2014; Heiderman et al., 2010; Gutermuth et al., 2011) and in extreme dense environments such as starburst galaxies (Genzel et al., 2010, 2015) and galactic centers (e.g., Leroy et al., 2013). Moreover, the depletion time exhibits mild trends with redshift and deviation of galaxies from the mean star formation sequence (e.g., Tacconi et al., 2018). To explain the origin of the molecular KSR slope, both

its universality at moderate and low surface densities and its steepening in more extreme dense environments must be understood.

One of the most popular explanations for the close-to-linear slope of the molecular KSR is the so-called "counting argument," which was first introduced by Wu et al. (2005) to interpret the linear relation observed for the dense gas traced by HCN and later extended to more diffuse molecular gas states. This argument posits that all molecular gas resides in star-forming units that have approximately the same properties and depletion times regardless of the galactic environment. In this case, both $\Sigma_{\mathrm{H_2}}$ and $\dot{\Sigma}_\star$ of an ISM patch result from counting these units in this patch, and therefore, $\Sigma_{\mathrm{H_2}}$ and $\dot{\Sigma}_\star$ become linearly related. However, the observed properties of molecular regions do vary with $\gtrsim 1$ kpc galactic environment (e.g., Miville-Deschênes et al., 2017), and therefore, the explanation of the linear slope must be more nuanced.

Elucidating the origin of the linear slope of molecular KSR will be another goal of this dissertation.

1.4 Dissertation outline

To address above questions and elucidate the origin of depletion times in galaxies, we introduce a simple physical framework that connects galactic star formation on large scales with the processes driving gas evolution on small scales. Our model is based on the mass conservation equations relating the star-forming and non-star-forming components of highly dynamic ISM and the idea of gas cycling between these components on certain characteristic timescales under the influence of dynamical and feedback processes (such gas cycling was also envisioned by Madore, 2010; Kruijssen & Longmore, 2014; Elmegreen, 2015, 2018).

We illustrate our model using a suite of isolated $L_\star$-galaxy simulations that is able to reproduce the observed KSR and depletion times for both total and molecular gas. We show that the model explains the origin of depletion times in our simulations and their

dependence on the parameters of star formation and feedback assumed on the resolution scale. In particular, our simulations are able to reproduce the self-regulated behavior, in which global depletion time becomes independent of local star formation efficiency, and our framework can explain the physical origin of this effect. In addition, we also show that our framework provides major insights into the physics that shapes the slope of the molecular KSR and makes it near-linear in normal star-forming galaxies.

The dissertation is structured as follows. In Chapter 2, we present our analytical model for gas depletion times in galaxies. In Chapter 3, we describe our simulation suite and analysis methods. In Chapter 4, we illustrate our framework using the fiducial simulation from our suite and explore the processes that drive gas evolution in the ISM and their corresponding timescales. In Chapter 5, we explore the effects of star formation and feedback parameters on global star formation in our simulations and show that our analytical model successfully explains the obtained behavior. In Chapter 6, we use our simulations and analytical framework to gain insights into the origin of the slope of molecular KSR.

CHAPTER 2

ANALYTIC MODEL FOR GAS DEPLETION TIME IN GALAXIES

2.1 The connection between the depletion time and evolution timescales of a single gas parcel

The interstellar gas in galaxies is a multiphase, dynamic medium spanning several orders of magnitude in density and temperature. To get a sense of the processes affecting the gas evolution in such a medium, we consider the evolution of individual gas parcels, massless tracers of gas flows in the ISM. One can think of a representative set of the ISM atoms as such tracers. At any given time, the local environment of such tracers can be estimated by averaging gas properties on some scale l around the position of each tracer. The gas around tracers will expand and contract under the influence of dynamical processes, such as turbulence driven by gravitational instabilities and stellar feedback. Therefore, during the evolution over a sufficiently long timescale, the conditions around each gas parcel can evolve between the states of long and short depletion time, $t_\star$, once or over many transition cycles. Such cycling of a gas parcel is schematically shown in Figure 2.1.

The probability density per unit time for a parcel to be converted into a star is given by $1/t_\star$ and one can define the depletion time for a single parcel as the time required for the integrated probability to reach unity. In what follows, for conceptual simplicity, we will adopt a sharp threshold, $t_{\star,\max}$, separating non-star-forming, $t_\star > t_{\star,\max}$, and actively star-forming, $t_\star < t_{\star,\max}$, gas states. For a given distribution of $t_\star$, this threshold can be chosen in such a way that regions with $t_\star < t_{\star,\max}$ include most of the total star formation.

The duration of a single cycle between the successive stages when the parcel's environment is in the star-forming state equals to the sum of the time spent in the non-star-forming, $t_{\rm nsf}$, and star-forming, $t_{\rm sf}$, stages. If we denote the average depletion time of the parcel during

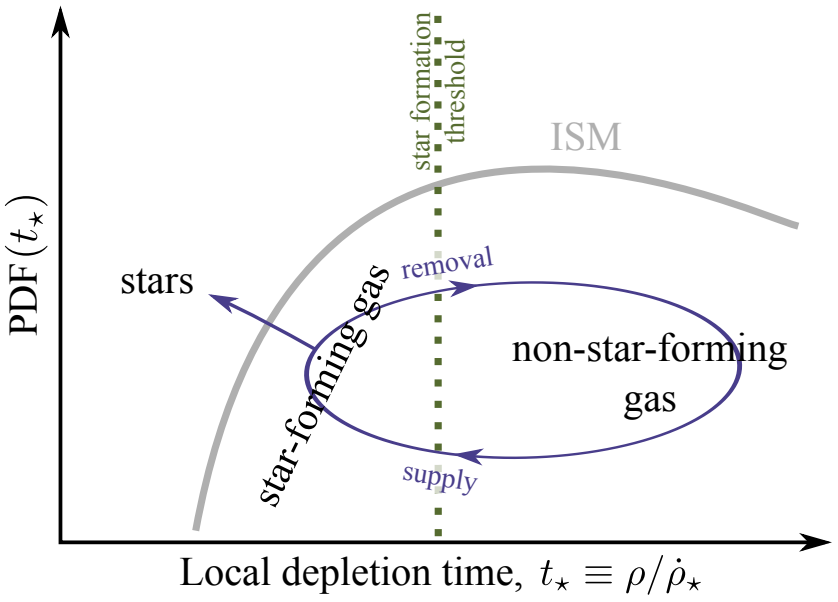

Figure 2.1: Schematic illustration of ISM gas evolution between non-star-forming and star-forming states. The thick gray line depicts the mass-weighted PDF of local gas depletion times, $t_\star \equiv \rho/\dot{\rho}_\star$, where ρ and $\dot{\rho}_\star$ are the local densities of gas and SFR. The vertical dotted line corresponds to the threshold depletion time, $t_{\star,\mathrm{max}}$, separating star-forming and non-star-forming gas. The blue loop illustrates cycling of a gas parcel between these states under the influence of dynamical and feedback processes that supply and remove star-forming gas.

the star-forming stage as $\tau_\star$, the parcel will have a probability of $t_{\rm sf}/\tau_\star$ to be converted into a star during the entire cycle. In other words, $N_{\rm c} = \tau_\star/t_{\rm sf}$ such cycles would be needed for the parcel to be incorporated into a star. Its depletion time can thus be written as

$$t_{\rm dep} = N_{\rm c}(t_{\rm nsf} + t_{\rm sf}) = N_{\rm c} t_{\rm nsf} + \tau_\star = \left(\frac{t_{\rm nsf}}{t_{\rm sf}} + 1\right) \tau_\star. \tag{2.1}$$

Hence, the depletion time of a gas parcel is always longer than $\tau_\star$ and it can be long because star formation during $t_{\rm sf}$ is inherently inefficient, i.e., $\tau_\star$ is long, and/or because only a small fraction of the evolution cycle is spent in the star-forming state, i.e., $t_{\rm nsf}/t_{\rm sf}$ is large.

2.2 The depletion time of an ISM patch or entire galaxy

The depletion time of an ISM patch, entire galaxy, or any larger region of the universe results from the averaging the depletion times of gas parcels constituting these regions. Such a collection of parcels has a distribution of $\tau_\star$, $t_{\rm sf}$, $t_{\rm nsf}$ and the collective depletion time of the group is the average $\tau = \langle 1/t_{\rm dep}\rangle^{-1}$ over these distributions. It is clear that if the depletion times of individual parcels are long, τ will also be long.

In practice, the depletion time τ of an ISM patch or entire glaxy is estimated from the instantaneous mass of gas, $M_{\rm g}$, and young stars formed over a time interval Δt, $M_\star(<\Delta t)$, such that the average star formation rate is $\langle \dot{M}_\star\rangle_{\Delta t} = M_\star(<\Delta t)/\Delta t$ and the depletion time is defined as $\tau \equiv M_{\rm g}/\langle \dot{M}_\star\rangle_{\Delta t}$. This estimate of τ can be related to the dynamics of individual gas parcels within the patch by noting that due to mass conservation, the instantaneous total mass of the gas parcels in the star-forming state, $M_{\rm sf}$, evolves as $\dot{M}_{\rm sf} = F_{\rm sf} - \dot{M}_\star$, where $F_{\rm sf}$ is the net instantaneous flux of the gas parcels through the star formation threshold and $\dot{M}_\star$ is the instantaneous SFR of all parcels. After averaging this expression over the time interval Δt, we get

$$\tau \equiv \frac{M_{\rm g}}{\langle \dot{M}_\star\rangle_{\Delta t}} = \frac{M_{\rm g}}{\langle F_{\rm sf}\rangle_{\Delta t} - \langle \dot{M}_{\rm sf}\rangle_{\Delta t}}. \tag{2.2}$$

For brevity, in the following derivation, we omit explicit averaging, $\langle ... \rangle_{\Delta t}$, but assume all fluxes and rates to be averaged over Δt.

In general, the average net flux of gas through the star formation threshold can be decomposed into positive and negative contributions,

$$F_{\rm sf} = F_+ - F_-, \tag{2.3}$$

which correspond to the supply and removal of star-forming gas illustrated in Figure 2.1.

The positive flux F_+ is controlled by a combination of global dynamical processes, e.g., gravitational instabilities, turbulence, cooling, etc., with a significant contribution from stellar feedback. The latter comes in the form of turbulence stirred by interactions of supernova-driven bubbles and by fountain outflows of gas from star-forming regions. The negative flux $F_- = F_{-,\rm fb} + F_{-,\rm d}$ results from the destruction of star-forming regions both by feedback from young stars formed inside the regions, $F_{-,\rm fb}$, and by shearing due to large-scale turbulence or differential rotation, expansion of gas behind galactic spiral arms, and other dynamical processes not directly related to star formation inside the regions, $F_{-,\rm d}$. All fluxes can be parameterized with the characteristic timescales, i.e., τ_+, $\tau_{-,\rm fb}$ and $\tau_{-,\rm d}$, on which gas is supplied to and removed from the star-forming state by the corresponding processes,

$$F_+ \equiv \frac{M_{\rm nsf}}{\tau_+} = M_{\rm g}\frac{1-f_{\rm sf}}{\tau_+}, \tag{2.4}$$

$$F_{-,\rm fb} \equiv \frac{M_{\rm sf}}{\tau_{-,\rm fb}}, \tag{2.5}$$

$$F_{-,\rm d} \equiv \frac{M_{\rm sf}}{\tau_{-,\rm d}}, \tag{2.6}$$

$$F_- \equiv \frac{M_{\rm sf}}{\tau_-} = F_{-,\rm fb} + F_{-,\rm d} = M_{\rm g} f_{\rm sf}\left(\frac{1}{\tau_{-,\rm fb}} + \frac{1}{\tau_{-,\rm d}}\right), \tag{2.7}$$

where $f_{\rm sf} \equiv M_{\rm sf}/M_{\rm g}$ is the star-forming mass fraction.

To make the relation between star formation and stellar feedback explicit, we can also

parameterize $F_{-,\mathrm{fb}}$ in a way similar to the parameterization of the mass outflow rate of feedback-driven galactic winds,

$$F_{-,\mathrm{fb}} \equiv \xi \dot{M}_\star = M_\mathrm{g} f_\mathrm{sf} \frac{\xi}{\tau_\star}, \tag{2.8}$$

where ξ is the *mass-loading factor* and we used the definition of the average depletion time of *star-forming gas*, $\tau_\star \equiv M_\mathrm{sf}/\dot{M}_\star$. In the context of Equation (2.7) the mass-loading factor can also be interpreted as a relative rate of gas removal by feedback compared to the rate of star formation, i.e., $\xi \equiv \tau_\star/\tau_{-,\mathrm{fb}}$.

An imbalance between the net gas flux into the star-forming state, F_sf, and the average SFR may result in the evolution of the star-forming mass, which we also parameterize with the characteristic timescale, $\tau_\mathrm{e,sf}$:

$$|\dot{M}_\mathrm{sf}| \equiv \frac{M_\mathrm{sf}}{\tau_\mathrm{e,sf}}. \tag{2.9}$$

The final expression for the global depletion time can be readily derived by substituting Equations (2.3–2.9) and $f_\mathrm{sf} = \tau_\star/\tau$ (Equation 1.1) into Equation (2.2),

$$\tau = \left(1 + \xi + \frac{\tau_\star}{\tau_{-,\mathrm{d}}} \pm \frac{\tau_\star}{\tau_\mathrm{e,sf}}\right) \tau_+ + \tau_\star, \tag{2.10}$$

where the sign in front of $\tau_\star/\tau_\mathrm{e,sf}$ reflects the sign of $\dot{M}_\mathrm{sf}$.

If we compare the terms in this equation with those in Equation (2.1) for the depletion time of a single gas parcel, $t_\mathrm{dep} = N_\mathrm{c} t_\mathrm{nsf} + \tau_\star$, their physical meaning becomes clear. The timescale τ_+ is analogous to the time t_nsf that a gas parcel spends in the non-star-forming state, while the expression in parentheses is analogous to $N_\mathrm{c} = \tau_\star/t_\mathrm{sf}$, i.e., the average number of evolution cycles it would take for a single parcel to deplete its gas. Indeed, Equation (2.4) gives $M_\mathrm{nsf} = F_+ \tau_+$, which means that τ_+ is the time over which all of the non-star-forming gas will reach the star-forming state. Thus, τ_+ is analogous to the

average $t_{\rm nsf}$ timescale for a collection of parcels. Likewise, the average rate at which the gas mass in the star-forming state is decreasing due to star formation, dispersal, and the overall evolution of the gas PDF during Δt is given by $M_{\rm sf}/\tau_\star + M_{\rm sf}/\tau_- \pm M_{\rm sf}/\tau_{\rm e,sf}$, and the associated timescale $(1/\tau_\star + 1/\tau_- \pm 1/\tau_{\rm e,sf})^{-1}$ corresponds to the average time that gas spends in this state. Thus, on average, gas will have to reach the star-forming state

$$N_{\rm c} = \tau_\star \left(\frac{1}{\tau_\star} + \frac{1}{\tau_-} \pm \frac{1}{\tau_{\rm e,sf}} \right) = 1 + \xi + \frac{\tau_\star}{\tau_{-,\rm d}} \pm \frac{\tau_\star}{\tau_{\rm e,sf}}, \tag{2.11}$$

times, where we used Equation (2.7) and the definition of the mass-loading factor, $\xi \equiv \tau_\star/\tau_{-,\rm fb}$.

2.3 Implications for depletion times in observed and simulated galaxies

Equation (2.10) is the key expression of our framework. It states that *the global depletion time is the sum of the total time that gas spends in the non-star-forming state over $N_{\rm c}$ cycles and the total time over which star-forming regions convert this gas into stars, $\tau_\star$.*

This equation elucidates how long τ values can be reconciled with the relatively short local depletion times, $\tau_\star$, and even shorter dynamical timescales, τ_+, discussed in Section 1.1. The global depletion time is longer than the depletion time in star-forming regions, $\tau_\star$, due to the significant fraction of time that gas spends in the non-star-forming state. The global depletion time is longer than the timescale associated with dynamical processes supplying star-forming gas, τ_+, because gas must evolve through the non-star-forming state $N_{\rm c}$ times, and $N_{\rm c}$ is large due to either efficient feedback, i.e., large ξ, or fast dynamical processes destroying star-forming regions, i.e., short $\tau_{-,\rm d}$ (see Equation 2.11).

When feedback dominates the removal of gas from the star-forming state, the number of cycles becomes $N_{\rm c} \sim \tau_\star/\tau_{-,\rm fb}$. This clarifies how feedback can self-regulate star formation,

i.e., how τ can become insensitive to $\tau_\star$. Indeed, the timescale $\tau_{-,\rm fb}$ is proportional to the rate of energy and momentum injection by feedback, which, in turn, is set by the local rate of star formation, i.e., $\tau_\star$. Hence, $\tau_{-,\rm fb} \propto \tau_\star$, which renders $N_{\rm c}$ insensitive to $\tau_\star$. Thus, when $N_{\rm c}\tau_+ \gg \tau_\star$, the depletion time, $\tau \approx N_{\rm c}\tau_+$, will be insensitive to $\tau_\star$.

In a nonequilibrium state, in which $\dot{M}_{\rm sf} > 0$ (< 0) during Δt, the term $\pm\tau_\star/\tau_{\rm e,sf}$ in Equation (2.10) accounts for the correction of the average rates estimated using the star-forming gas fraction, $f_{\rm sf}$, defined for the instantaneous masses $M_{\rm sf}$ and $M_{\rm g}$. This correction appears because, when $\dot{M}_{\rm sf} > 0$ (< 0), the actual average fraction of Δt that gas spends in the star-forming state is smaller (higher) than $f_{\rm sf}$ and therefore more (fewer) transition cycles are required for depletion.

In a steady state, on the other hand, the gas distribution is stationary and the star formation rate is in equilibrium with the gas fluxes into and out of the star-forming state: $\dot{M}_{\rm sf} = F_{\rm sf} - \dot{M}_\star \approx 0$. In this case, $\tau_{\rm e,sf} \rightarrow \infty$ and the term $\tau_\star/\tau_{\rm e,sf}$ can be neglected in Equation (2.10). In such a steady state, $\tau = M_{\rm g}/F_{\rm sf}$ (see Equation 2.2), and depletion time is determined by the *net* rate of gas inflow into the star-forming state, $F_{\rm sf}$. When $F_{\rm sf}$ is small, the depletion time is long. Galaxies as a whole reach the steady state with $\dot{M}_{\rm sf} \approx 0$ on the shortest of the timescales that control the global depletion time in Equation (2.10). Thus, globally, such an assumption is justified. However, individual ISM patches may deviate from the steady state, and the $\tau_\star/\tau_{\rm e,sf}$ term will be one of the sources of the scatter in depletion times.

In Chapters 4–6, we use the framework described above and the results of isolated galaxy simulations to illustrate the mechanism controlling depletion times in galaxies, their dependence on the parameters of star formation and feedback on the scales of star-forming regions, and the independence of molecular gas depletion time of its surface densities on $\gtrsim$kiloparsec scales. Although the simulations adopt specific choices for many parameters, including resolution and prescriptions for star formation and feedback, the overall features and implications

of our model do not depend on these specific choices. In general, our framework relates the depletion time on a large scale, e.g., ∼kiloparsec scale or the scale of an entire galaxy, to the star formation and feedback model that operates on a smaller scale, e.g., the resolution scale of a simulation, where the distribution of local depletion times, $t_\star$, is defined.

CHAPTER 3

SIMULATION SUITE AND ANALYSIS

3.1 Simulation code overview and isolated galaxy model

To illustrate the framework outlined above and elucidate the physical processes that give rise to long global depletion times and linear molecular KSR, we use simulations of an isolated $\sim L_\star$-sized galaxy. We carried out our simulations using the Adaptive Refinement Tree (ART) N-body and gas dynamics code (Kravtsov, 1999; Kravtsov et al., 2002; Rudd et al., 2008; Gnedin & Kravtsov, 2011; Semenov et al., 2016). The ART code is a Eulerian code that employs Adaptive Mesh Refinement (AMR) technique with the Fully Threaded Tree data structure (Khokhlov, 1998) and a shock-capturing second-order Godunov-type method (Colella & Glaz, 1985) with piecewise linear reconstruction (van Leer, 1979) to compute hydrodynamical fluxes.

In our simulations we followed the evolution of an isolated gaseous disk in a live potential of a dark matter halo, stellar bulge, and stellar disk that are modeled with collisionless particles. We adopt the initial conditions that were used in the AGORA code comparison project (Kim et al., 2016) and also in the study of Agertz et al. (2013). Specifically, the isolated disk is initialized inside a dark matter halo with $v_{\rm c,200} = 150$ km s^{-1} and an initial concentration of $c = 10$. The initial disk of old stars has an exponential density profile with a radial scale length of $r_{\rm d} \approx 3.4$ kpc and a vertical scale height of $h_{\rm d} = 0.1 r_{\rm d}$ with a total mass of $M_{\star,{\rm d}} \approx 3.4 \times 10^{10}$ M$_\odot$. The stellar bulge has an initial mass of $M_{\star,{\rm b}} \approx 4.3 \times 10^9$ M$_\odot$ that is distributed with a Hernquist density profile with $a = 0.1 r_{\rm d}$ (Hernquist, 1990). The initial exponential gaseous disk has the same $r_{\rm d}$ and $h_{\rm d}$ as the stellar disk; its total mass is $M_{\rm g} \approx 8.6 \times 10^9$ M$_\odot$, which corresponds to the disk gas fraction of $f_{\rm g} \equiv M_{\rm g}/(M_{\star,{\rm d}} + M_{\rm g}) = 20\%$. We adaptively resolve cells where the total gas mass exceeds $\sim 8\,300$ M$_\odot$ and reach a maximum resolution of $\Delta = 40$ pc. Such a Δ is sufficient to resolve ISM structure down

to densities of $n \sim 100$–$1\,000$ cm^{-3}, and therefore we do resolve the dynamical build-up of high-density regions that is sometimes claimed to limit the star-forming gas supply from the general ISM with average density of $n \sim 1$ cm^{-3}. At the highest resolution level, we do not apply an artificial pressure floor in cold gas. Thus, the densities of star-forming regions are limited only by the effects of stellar feedback and the effective pressure due to thermal and both subgrid and resolved turbulent motions discussed below.

The Poisson equation for the gravity of gas and stellar and dark matter particles is solved using a Fast Fourier Transform on the zeroth uniform level of the AMR grid and using the relaxation method on all refinement levels. The resolution for gravity is therefore also set by the local resolution of the AMR grid, and in the ART code it corresponds to ~ 2 grid cells (see Figure 6 in Kravtsov et al., 1997). Gravitational potential and accelerations are used to update positions and velocities of collisionless particles and are also applied in the gas momentum and energy equations as source terms.

Gas evolution is governed by modified hydrodynamical equations that include terms related to cooling and heating, dynamical effects of subgrid turbulence (Section 3.2), gas consumption by star formation, and injection of mass, momentum, and energy by feedback from young stars (Section 3.3). Cooling in the optically thin limit is implemented following the model of Gnedin & Hollon (2012). We assume a fixed metallicity of $Z = Z_\odot$ and constant background heating by interstellar radiation in the Lyman-Werner bands with the photodissociation rate of 10^{-10} s^{-1} (Stecher & Williams, 1967). To model temperatures in dense self-shielded gas, we assume that extinction is proportional to the local column density of atomic gas, which we approximate as $nL_{\rm J,40}$, where n is the gas number density in a cell and $L_{\rm J,40}$ is the local Jeans length with an applied temperature ceiling of 40 K (model "L1a" in Safranek-Shrader et al., 2017).

3.2 Subgrid-scale turbulence

A key novel element of the simulations presented in this dissertation is the explicit dynamical modeling of gas turbulence on unresolved scales. Subgrid models to track unresolved turbulence have been developed and extensively used in aerospace engineering and simulations of terrestrial subsonic and supersonic turbulent flows (see, e.g., Sagaut, 2006; Garnier et al., 2009, for review). In the context of galaxy formation simulations the exploration of such type of models has only started (Latif et al., 2013; Braun et al., 2014; Braun & Schmidt, 2015; Semenov et al., 2016).

To model subgrid turbulence we employ the scale separation technique, where a large-scale flow is governed by filtered hydrodynamical equations, whereas small-scale motions are described by an additional hydrodynamical field. In our simulations, we use the subgrid model described by Schmidt et al. (2014) for application in cosmological AMR simulations. Here we briefly outline the main components and properties of this model. A more extensive description can be found in the original paper by Schmidt et al. (2014).

Model equations follow from applying a spatial filter of scale Δ, which we take to correspond to the grid cell scale, to ordinary hydrodynamical equations. The resulting set of equations governs gas flows on resolved scales ($> \Delta$) and contains additional terms and a new equation for subgrid turbulent energy density, K:

$$\frac{\partial}{\partial t}K + \nabla_i(u_i K) = -P_K \nabla_i u_i - \varepsilon + \tau_{ij}\nabla_i u_j + \nabla_i F_i + S_{\rm SN}, \tag{3.1}$$

where u_i is resolved gas velocity, $P_K = 2K/3$ is turbulent pressure, ε is the rate of turbulence decay into thermal energy, $\tau_{ij}\nabla_i u_j$ is viscous production by cascade from resolved scales, $\nabla_i F_i$ is turbulent diffusion. The source term $S_{\rm SN}$ enables us to directly inject some fraction of supernovae energy into subgrid turbulence, however, in the simulations presented in Chapters 4–6 we set $S_{\rm SN} = 0$ so that the subgrid turbulence is produced only via the

interaction with the resolved flow. The total velocity dispersion of gas motions on unresolved scales is then derived from K as $\sigma_{\rm t} = \sqrt{2K/\rho}$.

Note that the subgrid turbulent energy is very similar to thermal energy, as the latter results from integrating particles kinetic energies over the velocity space in the derivation of hydrodynamical equations from the Boltzmann equation. For instance, the first term on the right-hand side of Equation (3.1) is equivalent to the PdV work term in the equation for thermal energy. This term implies that as gas contracts (expands) P_K does work and turbulent energy increases (decreases) similarly to thermal energy (Robertson & Goldreich, 2012). The change of K in this process depends on the local compression rate ($-\nabla_i u_i$).

Likewise, the ε and $\tau_{ij}\nabla_i u_j + S_{\rm SN}$ terms are equivalent to the cooling and heating terms in the thermal energy equation, respectively. We follow Schmidt et al. (2014) and assume an exponential decay of K into thermal energy over the time scale close to the turbulent cell-crossing time, $\varepsilon = K/t_{\rm dec}$, where $t_{\rm dec} \sim \Delta/\sigma_{\rm t}$. Numerical studies of decaying MHD turbulence generally confirm fast dissipation over a crossing time both in subsonic and supersonic regimes (e.g., Gammie & Ostriker, 1996; Mac Low et al., 1998; Stone et al., 1998; Kim & Basu, 2013).

Equations for resolved gas momentum and energy also include terms related to non-thermal pressure (P_K), turbulent viscosity (τ_{ij}) and diffusion (similar to $\nabla_i F_i$). The latter two terms are analogous to molecular viscosity and thermal conduction that appear in the hydrodynamical equations when different moments of the Boltzmann equation are integrated over the velocity space.

The equations of viscous hydrodynamics and subgrid turbulence both require closure relations for these transport terms in order to become solvable. In both cases, these closure relations cannot be derived from the first principles and are chosen empirically. One of the common choices for the subgrid turbulence is to adopt the closure relations similar to those used for usual viscosity and thermal conduction. Physically, this approach assumes that

energy and momentum are transported on the filtering scale Δ mainly by the eddies of size Δ, i.e. the largest unresolved eddies. Models that employ this assumption are known as the Large-Eddy Simulations (LES) and are widely used for simulations of both incompressible (Sagaut, 2006) and supersonic (Garnier et al., 2009) turbulent flows (see also Schmidt, 2014, for a recent overview in the astrophysical context).

In our simulation for the turbulent stress tensor τ_{ij} we use the large-eddy viscosity closure, given by Equation (8) of Schmidt & Federrath (2011) with $C_2 = 0$ and $C_1 = 0.095$, appropriate for sub- and transonic regime. Our choice is justified by the fact that viscous production of turbulence in our simulated disk is important mainly in warm diffuse gas where subgrid turbulence is subsonic and gas is only weakly compressible (see Section A.3). We checked that our implementation of the subgrid model with such a closure reproduces the distribution of K in a low-resolution isotropic developed turbulence box simulation, when compared to a high-resolution direct simulation.

In the adopted closure, τ_{ij} depends on the local gradients of the resolved velocity field, and these gradients are interpreted as the onset of turbulent cascade on scale Δ. Therefore, in this model, turbulence can be artificially produced by large-scale velocity gradients, such as differential rotation, disk–halo interface, etc. To suppress this spurious production, Schmidt et al. (2014) suggest temporal averaging of simulated flow, so that τ_{ij} depends only on the gradients of fluctuating velocity part, in the so-called "shear-improved" closure, first introduced by Lévêque et al. (2007). In our simulation we adopt exponential temporal filtering with a time window $t_{\rm si} = 10$ Myr, i.e., turbulent energy is produced by the cascade from velocity perturbations that develop faster than $t_{\rm si}$. We choose the value $t_{\rm si} = 10$ Myr to filter out the differential rotation, on the one hand, and to capture various developing disk instabilities, on the other hand. We checked that our results are not sensitive to a change of $t_{\rm si}$ by a factor of 2.

Although the subgrid turbulence model has a number of parameters, as described above,

these parameters are calibrated using turbulence simulations and are not varied in our galaxy formation simulations. In this sense, they do not really add tunable free parameters in such simulations. They do affect the solution, however, as a particular choice of the closure relation forms and their parameters controls all interactions between resolved and unresolved scales and may depend on the flow configuration and turbulent Mach number. Generally, this might be considered as an important limitation of our model, as the specific closure adopted for our simulation was calibrated to reproduce the results of high-resolution simulations of developed isotropic transonic turbulence, while we apply it to a sheared gas flow in a stratified disk. However, we argue that this approach is still viable for prediction of the turbulent velocities in cold star-forming gas. Specifically, we checked that the resulting distribution of turbulent energy *in cold gas* is not sensitive to a particular choice of τ_{ij} parametrization. This is because the turbulent energy in this gas is mostly determined by the interplay between heating by compression and viscous dissipation into heat (see Section A.3). Both these effects are insensitive to turbulent Mach number as indicated by numerical simulations of developed turbulence (Mac Low et al., 1998; Robertson & Goldreich, 2012).

One important limitation of the model is an assumption that the unresolved turbulence on scale Δ is in the inertial regime. This assumption is made implicitly, because the direct simulations of developed turbulence, which were used to calibrate this model, do resolve the inertial range. However, resolving inertial scales in a galactic disk simulation is computationally challenging as it requires high spatial resolution, because turbulence is generated on scales comparable to the disk scale height, $h_{\rm d} \sim 100$ pc, while numerical viscosity affects gas flows in AMR-based codes on scales up to $\sim$ 10–20 cells (e.g., Kritsuk et al., 2011). Thus, resolving the inertial scales unaffected by numerical viscosity requires minimal cell sizes of $<$ 5–10 pc. Therefore, our resolution is not quite within the regime in which the subgrid turbulence model was calibrated. However, this problem is mitigated by the insensitivity of the subgrid turbulence properties in star-forming gas to the parametrization of τ_{ij}, which is

the part that depends on the Δ being within the inertial range. Thus, we believe the use of the subgrid turbulence model in simulations with moderate resolution is justified.

3.3 Star formation and feedback

We stress that the scenario of gas depletion described in Chapter 2 remains valid for any choice of star formation prescription, although the results of Chapters 5 and 6 show that such a prescription should be chosen carefully, as it is important for the prediction of realistic ISM properties. In this work, we adopt a usual parameterization of the local star formation rate with a star formation efficiency per freefall time, $\epsilon_{\rm ff}$,

$$\dot{\rho}_\star = \epsilon_{\rm ff} \frac{\rho}{t_{\rm ff}}, \tag{3.2}$$

and systematically vary $\epsilon_{\rm ff}$ as will be explained at the end of this section. We allow star formation to occur only in the gas that satisfies a chosen criterion. To explore the effects of such a criterion, we adopt thresholds in either the gas virial parameter, $\alpha_{\rm vir,sf}$, or the density, $n_{\rm sf}$, and also vary the values of $\alpha_{\rm vir}$ and $n_{\rm sf}$.

As our fiducial star formation criterion, we adopt a threshold in $\alpha_{\rm vir}$ and define all gas with $\alpha_{\rm vir} < \alpha_{\rm vir,sf}$ as star-forming. For a computational cell with a side Δ, the local virial parameter is defined as for a uniform sphere of radius $R = \Delta/2$ (Bertoldi & McKee, 1992):

$$\alpha_{\rm vir} \equiv \frac{5\sigma_{\rm tot}^2 R}{3GM} \approx 9.35 \frac{(\sigma_{\rm tot}/10 \text{ km s}^{-1})^2}{(n/100 \text{ cm}^{-3})(\Delta/40 \text{ pc})^2}, \tag{3.3}$$

where $\sigma_{\rm tot} = \sqrt{\sigma_{\rm t}^2 + c_{\rm s}^2}$ is the total subgrid velocity dispersion due to turbulent and thermal motions, and subgrid turbulent velocities, $\sigma_{\rm t} = \sqrt{2K/\rho}$, are dynamically followed in each cell using the Schmidt et al. (2014) model.

The choice of the star formation threshold in $\alpha_{\rm vir}$ is motivated by theoretical models

of star formation in turbulent giant molecular clouds (GMCs), which generically predict an exponential increase of $\epsilon_{\rm ff}$ with decreasing $\alpha_{\rm vir}$ (see Padoan et al., 2014, for a review). For example, Padoan et al. (2012) found that the star formation efficiency of a turbulent cloud increases exponentially with a decreasing virial parameter, $\epsilon_{\rm ff} \approx \exp(-\sqrt{\alpha_{\rm vir}/0.53})$. Even though we are able to model $\epsilon_{\rm ff}$ following the Padoan et al. (2012) formula (see Appendix A), in the simulations used here, we approximate the continuous exponential dependence of $\epsilon_{\rm ff}$ on $\alpha_{\rm vir}$ assuming a constant $\epsilon_{\rm ff}$ and a sharp $\alpha_{\rm vir,sf}$ threshold. This makes the interpretation of simulation results easier. We explicitly checked that the global depletion times and the KSR are similar in runs where $\epsilon_{\rm ff}$ follows the Padoan et al. (2012) fit and where we approximate this fit with a threshold (see Appendix C.2).

We set our fiducial values of parameters to $\epsilon_{\rm ff} = 1\%$ and $\alpha_{\rm vir,sf} = 10$, as supported by the observed efficiencies and virial parameters of star-forming GMCs (e.g., Evans et al., 2009, 2014; Heiderman et al., 2010; Lada et al., 2010, 2012; Lee et al., 2016; Vutisalchavakul et al., 2016; Miville-Deschênes et al., 2017), and also consistent with the results of high-resolution GMC simulations (e.g., Padoan et al., 2012, 2017), which show a sharp increase of $\epsilon_{\rm ff}$ below $\alpha_{\rm vir} \sim 10$. Note also that the threshold in $\alpha_{\rm vir}$ is equivalent to a threshold in the local Jeans length that accounts for both the thermal and turbulent pressure support: $\lambda_{\rm J} = \sigma_{\rm tot}\sqrt{\pi/G\rho} = \pi\Delta\sqrt{\alpha_{\rm vir}/5}$, and thus $\alpha_{\rm vir,sf} = 10$ implies that gas becomes star-forming when the local Jeans length is resolved by less than $\lambda_{\rm J}/\Delta \approx 4.5$ cells. A qualitatively similar star formation prescription but with a different choice of parameters was studied by Hopkins et al. (2013a).

In galaxy simulations that do not track subgrid turbulence, the GMC-scale $\alpha_{\rm vir}$ is not readily available owing to insufficient resolution. Instead, such simulations often adopt a star formation threshold in gas density, n, and define star-forming gas as the gas with $n > n_{\rm sf}$. For comparison, we also explore models with varied density-based thresholds in addition to our fiducial $\alpha_{\rm vir}$-based threshold.

Our default star formation prescription (Equation 3.2) implies a superlinear scaling of local SFR with gas density: $\dot{\rho}_\star \propto \rho^{1.5}$. To explore the effect of this local dependence on the slope of the molecular KSR, we also adopt a more general recipe:

$$\dot{\rho}_\star = \epsilon_{\rm ff} \, \frac{\rho_0}{t_{\rm ff,0}} \left(\frac{\rho}{\rho_0} \right)^\beta , \tag{3.4}$$

where $t_{\rm ff,0} = \sqrt{3\pi/32G\rho_0}$ is the freefall time at $\rho_0 = 100 \ m_{\rm p} \ {\rm cm}^{-3}$ and β is a variable parameter. For $\beta = 1.5$, this expression is equivalent to Equation (3.2).

The feedback from young stars is implemented by injection of thermal energy and radial momentum generated during supernova (SN) remnant expansion in a nonuniform medium in the amounts calibrated against simulations by Martizzi et al. (2015).

The explicit injection of the generated radial momentum allows one to partially resolve the overcooling problem and efficiently couple the feedback energy to the resolved dynamics of gas, which explains the growing popularity of the method (e.g., Simpson et al., 2015; Grisdale et al., 2017; Hopkins et al., 2017b). However, the injected momentum is still partially lost as a result of advection errors (see, e.g., Agertz et al., 2013), and to compensate for this loss, we boost the momentum predicted by Martizzi et al. (2015) by a factor of 5. This value is motivated by our idealized tests of a stellar particle exploding in a uniform medium with additional translational motion at velocity 200 km s^{-1}, which is comparable to the rotational velocity of the simulated galaxy. Such a fiducial boosting factor also absorbs uncertainties related to SNe clustering (Gentry et al., 2017, 2019), the presence of cosmic rays (Diesing & Caprioli, 2018), and the total energy of a single SN. To explore the effects of the feedback strength on the global depletion times, in addition to this fiducial boosting, we multiply the injected momentum by a factor b, which is systematically varied. The resulting radial momentum is distributed among all immediate neighbors[1] of the cell hosting the supernova.

1. For a uniform grid, the number of neighbors receiving momentum is 26, but it can be larger depending on the local refinement structure of the grid.

The total number of SNe exploded in a single stellar particle is computed assuming the Chabrier (2003) initial mass function. In the simulations presented in Section 4.1 and Chapter 4, the energy and momentum of these supernovae are injected at a uniform rate between 3 and 43 Myr after the formation of a stellar particle. In the simulations with high $\epsilon_{\rm ff}$ explored in Chapters 5 and 6, a significant fraction of gas can be converted into stars before the first SNe explode because local gas depletion time is comparable to the lag before the first SN. Thus, to mimic the effects of pre-SN feedback, such as radiation pressure and winds from massive young stars, in all simulations presented in Chapters 5 and 6 the momentum injection commences at the moment when a stellar particle is created and continues for 40 Myr.

In addition to SNe type II feedback, we also account for the mass loss by stellar particles following Leitner & Kravtsov (2011) and inject mass and the corresponding momentum resulting from the motion of the stellar particle with respect to the gas into the cell hosting the stellar particle.

In the end, in our simulations, star formation and feedback are parameterized by four numbers: the star formation efficiency, $\epsilon_{\rm ff}$, the star formation threshold, $\alpha_{\rm vir,sf}$ or $n_{\rm sf}$, the slope of local SFR dependence on density, β, and the feedback boost factor, b, which we vary in order to explore their effects on the global star formation. To assess the effect of the local star formation efficiency, we vary $\epsilon_{\rm ff}$ from 0.01% to 100%, i.e., by four orders of magnitude around our fiducial value of $\epsilon_{\rm ff} = 1\%$. To explore the effects of the star-forming gas definition, we vary $\alpha_{\rm vir,sf}$ between 10 and 100 and $n_{\rm sf}$ between 10 cm^{-3} and 100 cm^{-3}. We expect that such $\alpha_{\rm vir}$ and n are well resolved in our simulations, because they are sufficiently far from the resolution-limited values of $\alpha_{\rm vir} \sim 2$ and $n \sim 10^4$ cm^{-3} in a simulation with $\epsilon_{\rm ff} = 0.01\%$, in which gas contraction is not inhibited by stellar feedback (see the bottom left panel of Figure 5.4 below). Next, β is set to fiducial 1.5 in the simulations presented in Chapters 4–5 and is varied between 1 and 2.5 in Chapter 6. Finally, in order to explore the effect of

the feedback strength, in addition to the fiducial case of $b = 1$, we also consider the 5 times stronger feedback ($b = 5$), the 5 times weaker feedback ($b = 0.2$), and the case of no feedback at all ($b = 0$). Such wide variation of model parameters allows us to explore the connection between the subgrid scale and the global star formation in the simulated galaxy.

3.4 Analysis overview

Analysis of time evolution shows that all our simulations exhibit a short ($\lesssim 300$ Myr) initial transient stage, after which the simulated galaxy settles into a quasi-equilibrium state with approximately constant global galaxy parameters, such as gas depletion time, τ (see, e.g., Figure 5.1 below). Thus, in our subsequent analysis we average the galaxy properties of interest over either 200 or 300 Myr after the initial 300 Myr of evolution with the actual averaging interval indicated in figure captions. A 200–300 Myr time interval is sufficiently long to average out the temporal variability of galaxy properties, but it is also shorter than τ, and hence the galaxy maintains the approximate equilibrium over this time interval. The only exceptions are the runs without feedback and with high local star formation efficiency of $\epsilon_{\rm ff} \geq 10\%$, in which τ is very short and the total gas mass decreases appreciably between 300 and 600 Myr. The equilibrium assumption is also violated for the central region in simulations with $\epsilon_{\rm ff} \leq 0.1\%$, where the central density keeps increasing owing to continuous accretion. However, outside the central 1 kpc the total gas mass and the value of τ remain approximately constant, and therefore we exclude gas in the central 1 kpc region when computing quantities in our analysis.

Some of the results presented below relate to molecular gas content of our simulated galaxies. To measure molecular gas mass fractions, we estimate the molecular gas density in each cell using the KMT model (Krumholz et al., 2008, 2009a; McKee & Krumholz, 2010): $\rho_{\rm H_2} = \max[0, (1 - 0.75s/(1 + 0.25s))\rho]$, where at solar metallicity $s \approx 1.8/\tau_{\rm c}$ and $\tau_{\rm c} = 320(\rho\Delta/{\rm g\ cm^{-2}})$. Molecular gas surface density, $\Sigma_{\rm H_2}$, is measured by integrating

molecular density in all cells along the direction perpendicular to the disk. Note that the result presented in different chapters differ by the correction due to the helium fraction: in Chapters 4 and 5 helium is excluded from the molecular mass while in Chapter 6 it is included leading to ~ 1.33 times larger molecular mass assuming 25% helium mass fraction.

For a consistent comparison with the observed KSR for H I + H_2 gas in Section 4.1, we defined neutral hydrogen to be all nonmolecular gas denser than $n_{\rm H,SSh}$, given by Equation (13) in Rahmati et al. (2013). This threshold corresponds to the gas self-shielded from the far ultraviolet (FUV) background with the adopted photoionization rate $\Gamma = 10^{-10}$ s^{-1}. We also excluded all neutral hydrogen that is colder than 1000 K assuming that it constitutes the optically thick cold neutral medium (CNM) not included into the observed measurements of $\Sigma_{\rm HI}$. Our temperature threshold is somewhat higher than the CNM temperature estimated in real galaxies ($\lesssim 300$ K, e.g., Wolfire et al., 2003) because, in our simulation, we do not resolve the transition between warm and cold neutral gas phases, which results in intermediate gas temperatures on the resolution scale. The particular value of the temperature threshold was chosen to select $\sim 40\%$ of the neutral hydrogen mass, which is close to the CNM mass fractions estimated in the Milky Way and nearby galaxies (e.g., Heiles & Troland, 2003; Braun, 2012; Pineda et al., 2013; Sofue, 2017).

To obtain the $\dot{\Sigma}_\star$–$\Sigma_{\rm H_2}$ relation in Chapter 6, we measure the SFR surface density from the distribution of stars younger than 10 Myr. This time interval is chosen to approximate the temporal averaging of SFR used in the extragalactic observations to which we will compare our results.[2]

To study the detailed dynamics of individual gas parcels, we use gas tracer particles that are passively advected with the local gas flow. The results presented in the following chapters differ by the implementation and initialization of these tracer particles.

2. Specifically, 10 Myr corresponds to the Hα star formation indicator (see, e.g., Table 1 in Kennicutt & Evans, 2012). Extragalactic observations usually adopt a combination of Hα and infrared indicators, which corresponds to the SFR averaged over a somewhat longer time interval. However, we checked that our results remain almost unchanged when we average SFRs over 30 Myr instead of 10 Myr.

In Chapter 4, we use classical tracers that are moved at each step with the local gas velocity interpolated to the positions of the particles using the cloud-in-cell scheme. We populate the disk with 10^5 tracer particles uniformly initialized within $R < 8\,\mathrm{kpc}$ after 300 Myr of disk evolution when the transients related to the initial off-equilibrium state had dissipated away. After initialization, we wait for 100 Myr to let the tracers equilibrate with the gas density distribution. At that point, the distributions of tracer densities in radial annuli approximates the gas density PDF in computational cells.

In mesh-based codes, the classical implementation of tracer particles is known to follow gas density imperfectly (Genel et al., 2012). Therefore, for the analysis presented in Chapters 5 and 6 we implemented the scheme proposed by Genel et al. (2012) to accurately follow gas density, modulo the Poison noise introduced by the finite number of tracers in a cell. In this scheme, gas-tracer particles that are exchanged between adjacent computational cells stochastically, with the probability proportional to the gas mass flux between the cells. We initialize tracer particles proportionally to the local gas density after 400 Myr of disk evolution.

We average the distribution of tracers to construct statistics, such as their PDF and fluxes in the n–σ_{tot} phase diagram, between 400 and 600 Myr. We checked that at every moment between 400 and 600 Myr phase distributions of gas and tracer particles resembled their averaged versions, which confirms that the galaxy remained in approximate equilibrium over the considered period of time.

We focus on the evolution of gas tracers in the n–σ_{tot} phase plane because the position of a gas parcel in this plane determines its internal consumption time, $t_\star$, according to our star formation prescription. To accurately quantify gas motions in the n–σ_{tot} plane, we output positions, n, and σ_{tot} for each gas tracer every 1 Myr. The instantaneous contributions of each tracer into the gas fluxes, $d\log n/dt$ and $d\log\sigma_{\mathrm{tot}}/dt$, are measured as the second-order time derivatives between the previous and subsequent snapshots. To estimate the average

local flow rates of gas, we accumulate fluxes corresponding to these derivatives and normalize them by the local density of tracers in the n–$\sigma_{\rm tot}$ plane. To account for gas consumption, whenever a stellar particle is formed, relative weights of all tracers inside the host cell are decreased correspondingly.

To characterize actual fluxes that supply and remove star-forming gas, in addition to the total flux of tracers, we separately track the fluxes of tracers with decreasing or increasing $\alpha_{\rm vir}$. We quantify the magnitudes of these fluxes with the characteristic evolution timescale, on which $\alpha_{\rm vir}$ changes by an order of magnitude at a given rate,

$$\tau_{\alpha,\gtrless 0} \equiv \left\langle \left| \frac{d \log_{10} \alpha_{\rm vir}}{dt} \right| \right\rangle_{\gtrless 0}^{-1}, \tag{3.5}$$

where we average the derivative of $\log_{10} \alpha_{\rm vir}$ taking into account only tracers with decreasing (increasing) $\alpha_{\rm vir}$ to compute $\tau_{\alpha,<0}$ ($\tau_{\alpha,>0}$).

For the analysis presented in Chapter 6, we define the duration of a single molecular stage of a gas tracer as

$$t_{\rm H_2} = \int_{t_1}^{t_2} f_{\rm H_2}(t)\, dt, \tag{3.6}$$

where $f_{\rm H_2}$ is the molecular mass fraction of the cell hosting the gas tracer at a given time step, and t_1 and t_2 are the subsequent moments when the gas tracer crosses the $n = 10$ cm^{-3} threshold[3]. We also accumulate integral star formation efficiency over $t_{\rm H_2}$ as

$$\epsilon = \int_{t_1}^{t_2} \frac{\Theta_{\rm sf}(t)}{t_\star(t)}\, dt, \tag{3.7}$$

where at each time step $\Theta_{\rm sf} = 1$ if a gas tracer resides in a cell that satisfies the star formation criterion, and $\Theta_{\rm sf} = 0$ otherwise; $t_\star = \rho/\dot{\rho}_\star$ is the local depletion time in star-forming gas;

3. For our choice of parameters, the Krumholz et al. (2008) model predicts that the molecular mass fraction is 0 for $n < 10$ cm^{-3} and it sharply increases for $n > 10$ cm^{-3}

$t_\star = t_{\rm ff}/\epsilon_{\rm ff}$ for our fiducial $\beta = 1.5$ in Equation (3.4).

CHAPTER 4

THE PHYSICAL ORIGIN OF LONG GAS DEPLETION TIMES

In this chapter, we illustrate our framework using our fiducial simulation of a galactic disk that reproduces the observed depletion time and the Kennicutt-Schmidt relation. We start from a brief review of the results of our simulation in Section 4.1. In Section 4.2 we demonstrate that the long global depletion time in our simulation originates from the rapid cycling of ISM gas between non-star-forming and star-forming states on timescales $\sim$ 20–100 Myr, in accord with the estimates discussed in the Introduction and with the results of previous galactic disk simulations. On each evolution cycle, only a small fraction of the gas mass is converted into stars and thus τ is long because a large number of such cycles would be required to deplete all available gas. In Sections 4.3 and 4.4, we analyze the processes driving the rapid gas evolution and estimate the timescales of gas evolution using gas tracer particles. We discuss our results and summarize our conclusions in Sections 4.5 and 4.6.

This chapter is based on the work published in Semenov et al. (2017).

4.1 Gas distribution and the KSR in the fiducial simulations

Figure 4.1 shows the spatial distribution of gas number density, temperature, and subgrid turbulent velocity in our fiducial simulation with $\epsilon_{\rm ff} = 1\%$ for $\alpha_{\rm vir} < \alpha_{\rm vir,sf} = 10$ and $b = 1$ at $t = 500$ Myr. The figure highlights the multiphase, dynamic structure of the ISM. Comparison with a simulation weak feedback (see, e.g., the top left panel of Figure 5.4 below) shows that the structure of the ISM is significantly affected by stellar feedback. Its effect is manifested in the ubiquitous regions of hot, turbulent gas and in the overall flocculent nature of the spiral pattern.

Subgrid turbulent velocities, $\sigma_{\rm t}$, range from $\lesssim 3$ km s^{-1} in the diffuse ISM between the spiral arms to $\sim$ 30–300 km s^{-1} in hot SNe bubbles. In this simulation, supernovae do not

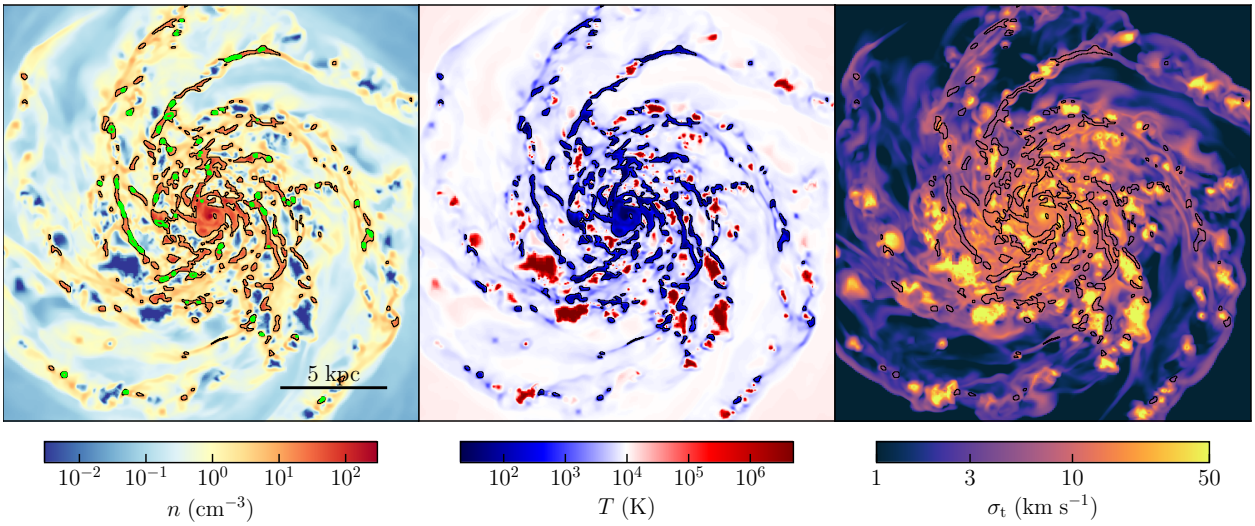

Figure 4.1: Midplane slices of gas number density, n, temperature, T, and subgrid turbulent velocity, $\sigma_{\rm t} = \sqrt{2K/\rho}$, after 500 Myr of evolution. To make comparison easier, the black contours in all panels indicates $n = 10$ cm^{-3}, above which the molecular mass fraction rapidly increases at solar metallicity. Green contours in the left panel show gas that satisfies our star formation criterion, $\alpha_{\rm vir} < \alpha_{\rm vir,sf} = 10$.

explicitly inject turbulent energy, and high $\sigma_{\rm t}$ in hot bubbles are generated by the subgrid turbulence model. In the cold dense gas, turbulent velocities are supersonic and also vary significantly, $\sigma_{\rm t} \sim 5$–15 km s^{-1}. Strong subgrid turbulence in cold gas results in high values of $\alpha_{\rm vir}$ and, according to our star formation criterion, $\alpha_{\rm vir} < \alpha_{\rm vir,sf} = 10$, only $\sim 40\%$ of all molecular gas mass is star-forming at any given moment. Such star-forming regions are shown in the left panel of Figure 4.1 with green contours.

The total SFR of our model galaxy is $\dot{M}_\star \sim 1$–2 M$_\odot$ yr^{-1}, which translates to global depletion times for the total and molecular gas of $\tau \sim 4$–8 Gyr and $\tau_{\rm H_2} \sim 1$–2 Gyr. These values are in the ballpark of the typical values observed in nearby spiral galaxies (e.g., Wong & Blitz, 2002; Bigiel et al., 2008; Leroy et al., 2013). The average depletion time of star-forming gas only is $\tau_\star \sim 300$–500 Myr which is also consistent with observational estimates of depletion times in actively star-forming regions (e.g., Evans et al., 2009, 2014; Lada et al., 2010, 2012; Heiderman et al., 2010; Gutermuth et al., 2011; Schruba et al., 2017).

Figure 4.2 compares the Kennicutt-Schmidt relation between the surface densities of the

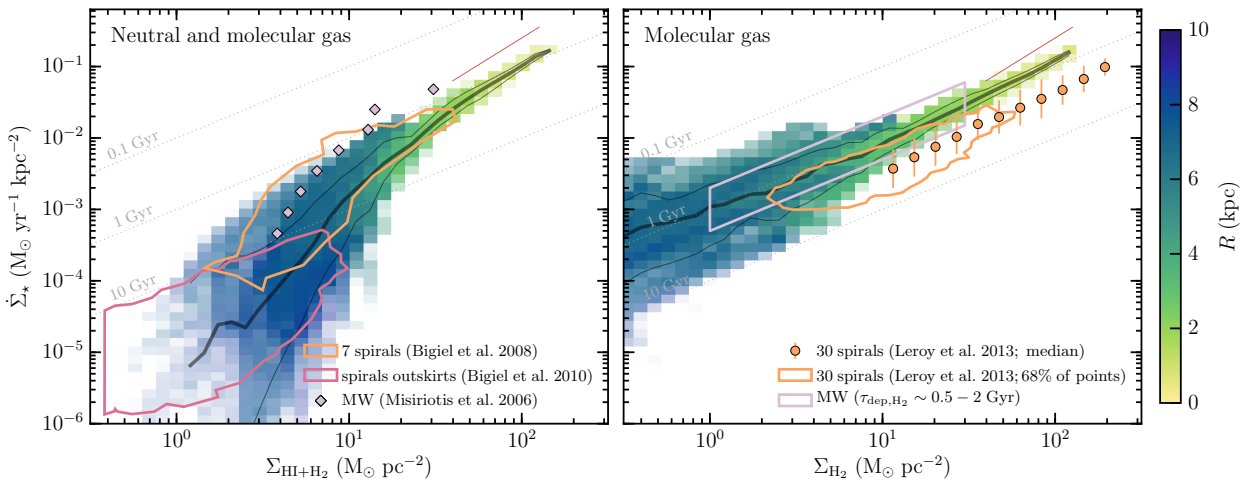

Figure 4.2: Relation between the surface density of the SFR and the total (left panel) and molecular gas (right panel) in our simulation and in observations. To match the typical spatial scales on which this relation is usually measured, we smooth 2D maps of $\dot{\Sigma}_\star$, Σ_{HI+H_2} and Σ_{H_2} obtained at 500 Myr with a Gaussian filter with a width of 1 kpc and plot the median, 16th, and 84th percentiles of the resulting pixel distribution (thick and thin gray lines). The distributions are colored according to the average galactic radius, R, of pixels in a given bin. To match the averaging timescales of the star formation indicators, we measure the surface density of stars that are younger than 30 Myr and define $\dot{\Sigma}_\star$ as $\Sigma_\star(< 30$ Myr$)/30$ Myr. The thin red line at high Σ indicates the slope adopted in our star formation prescription, $\dot{\rho}_\star \propto \rho^{1.5}$. Thin dotted lines correspond to the constant depletion times of 0.1, 1, and 10 Gyr (from top to bottom). We compare our results to the observed relations in nearby spiral galaxies (Bigiel et al., 2008, 2010; Leroy et al., 2013) and in the Milky Way (Misiriotis et al., 2006). The violet contour in the right panel shows the range of $\tau_{H_2} \sim 0.5$–2 Gyr estimated using the radial profiles of $\dot{\Sigma}_\star$ and Σ_{H_2} for the Milky Way from Figure 7 in Kennicutt & Evans (2012).

SFR and H I + H_2 and H_2 gas in our simulation[1] to the observed relations in the Milky Way and nearby spiral galaxies. Our results are in a good agreement in both normalization (i.e., the depletion time value) and slope. Note, in particular, that the linear relation between $\dot{\Sigma}_\star$ and Σ_{H_2} emerges from the nonlinear star formation prescription adopted in our simulation: $\dot{\rho}_\star \propto \rho^{1.5}$. In Chapter 6, we consider the origin of the linear relation and show that it results from the particular behavior of the gas density distribution shaped by stellar feedback. In the remainder of this chapter we focus on the physical origin of the KSR normalization and explain why global depletion times in galaxies are long.

4.2 Long global depletion times as a result of rapid gas cycling

As we discussed at the end of Section 2, in a steady state, when $\langle \dot{M}_{\rm sf} \rangle_{\Delta t} \approx 0$ on the timescale Δt over which the SFR is estimated, long global depletion times, $\tau \equiv M_{\rm g}/\dot{M}_\star = M_{\rm g}/F_{\rm sf}$, originate from a small *net* flux of gas into the star-forming state, $F_{\rm sf}$. In principle, $F_{\rm sf}$ could be small if the rate at which gas evolves toward the star-forming state were set by a slow "bottleneck" process. However, as Figure 4.3 shows, in simulations with efficient feedback, gas rapidly transitions between the star-forming and non-star-forming states, and a small $F_{\rm sf}$ results from a near-cancellation of large opposite fluxes into and out of the star-forming state.

In this figure, we plot the distribution of gas tracer particles within the disk in the plane of gas number density, n, and $\sigma_{\rm tot} = \sqrt{\sigma_{\rm t}^2 + c_{\rm s}^2}$, that can be viewed as an effective temperature including both thermal and turbulent gas motions on subgrid scales. The gas distribution spans a wide range of densities, $\sigma_{\rm tot}$, and temperatures and has two distinct peaks. The peak at low densities, $n \sim 1$ cm^{-3}, corresponds to diffuse, warm, subsonic ($\sigma_{\rm t} \lesssim c_{\rm s}$) gas at temperature $T \sim 10^4$ K. The gas in the second peak at $n > 10$ cm^{-3}, on the other hand, is cold ($T \lesssim 100$ K) and supersonic ($\sigma_{\rm t} > c_{\rm s}$).

1. The definition of H I and H_2 gas in our simulations is explained in Section 3.4.

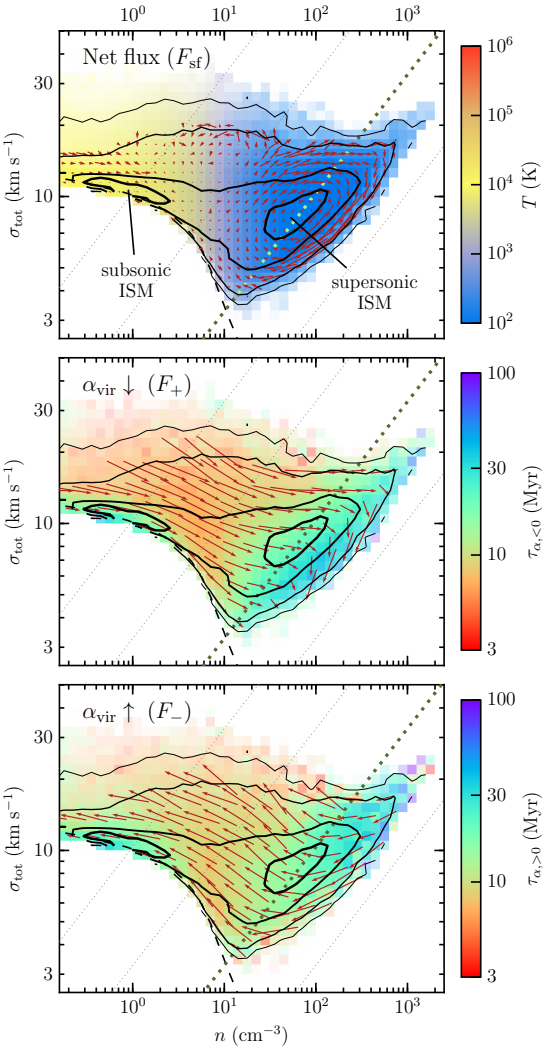

Figure 4.3: Distribution of gas tracer particles in the plane of gas number density, n, and total velocity dispersion, $\sigma_{\rm tot} = \sqrt{\sigma_{\rm t}^2 + c_{\rm s}^2}$, averaged between 400 and 600 Myr. The black contours in all panels indicate the average PDF of tracers and correspond to 20, 68, 95, and 99% of all tracers. The diagonal dotted lines indicate constant values of $\alpha_{\rm vir}$ from left to right: 1000, 100, 10, and 1, with $\alpha_{\rm vir} = \alpha_{\rm vir,sf} = 10$ shown by the thick green dotted line. The dashed line along the lower envelope of the PDF at $n < 10$ cm^{-3} indicates the median sound speed, $c_{\rm s}$, in each density bin. Colors in the top panel show the average gas temperature in each bin, while arrows indicate the average total fluxes of gas tracers measured as described at the end of Section 3. Arrows in the middle and bottom panels correspond to the fluxes of gas tracers with decreasing and increasing $\alpha_{\rm vir}$ respectively. Colors in these panels show the distribution of the characteristic evolution timescales, $\tau_{\alpha,\gtrless 0}$, defined by Equation (3.5). The normalizations of the arrows are the same in all three panels and correspond to the distances that tracers would traverse at a given rate over 5 Myr.

According to our star formation prescription, the star-forming gas has $\alpha_{\rm vir} < \alpha_{\rm vir,sf} = 10$. Such gas in Figure 4.3 resides below the thick green dotted line. The net mass flux of gas in the n–$\sigma_{\rm tot}$ plane is visualized by the arrows in the top panel of Figure 4.3, where the length of the arrows is equal to the distance tracers would traverse in 5 Myr for a given flux. The figure shows that arrows are rather small throughout most of the phase space occupied by tracers and are particularly small near the thick green dotted line. This means that the *net* evolution of gas in the n–$\sigma_{\rm tot}$ plane is slow and the net flux through the star formation threshold, $F_{\rm sf}$, is small. This small net flux results in the long global depletion timescales exhibited by our simulated galaxy, $\tau \sim 5$ Gyr and $\tau_{\rm H_2} \sim 1$ Gyr (see Section 4.1 and Figure 4.2).

However, the middle and bottom panels of Figure 4.3 show that the small net $F_{\rm sf}$ results from the near-cancellation of two opposite fluxes. These panels show the fluxes of only those tracers in which $\alpha_{\rm vir}$ is decreasing, F_+, or increasing, F_-, and these fluxes are significantly stronger than the net flux in the top panel. A typical tracer evolves toward and away from the star-forming state on a timescale of order $\tau_{\alpha,\gtrless 0} \sim$ 5–30 Myr, consistent with the estimates of the timescales of relevant processes in Section 1.1. Thus, the rate of gas supply from the warm, diffuse ISM to the star-forming state cannot be the factor limiting the global star formation rate, as envisioned by Saitoh et al. (2008). Instead, gas generally evolves from the diffuse to the star-forming state on a timescale of tens of Myr, much shorter than the global depletion time. The latter is long because gas rapidly leaves the star-forming state at the rate that nearly cancels the rate at which gas is reaching this state. In the next section, we consider the processes that drive the fast gas evolution in more detail.

4.3 Dynamical processes shaping ISM

The average gas flow patterns shown with arrows in Figure 4.3 result from the statistical averaging of the complicated trajectories of individual tracer particles. The particular shapes

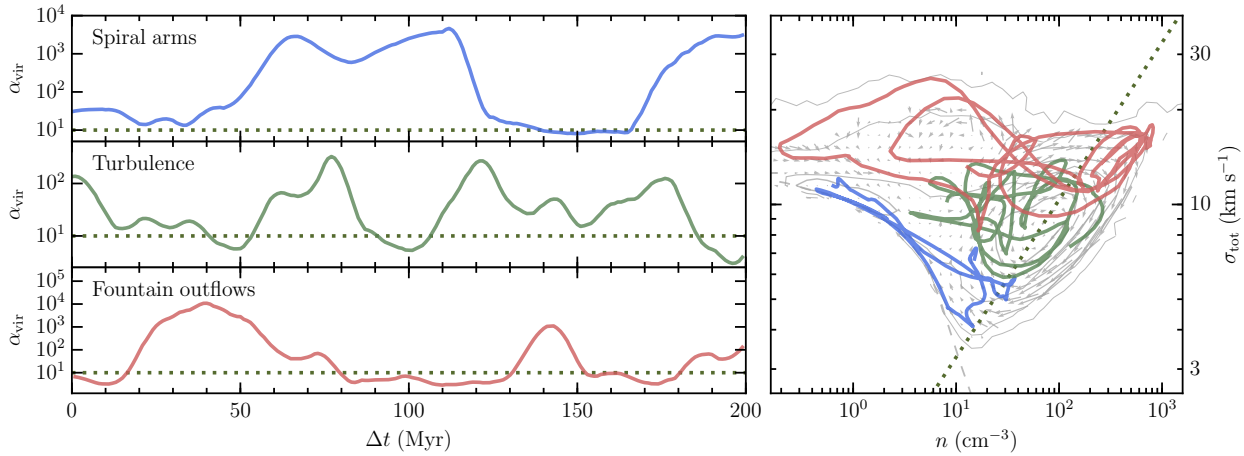

Figure 4.4: Trajectories of three illustrative tracers followed for 200 Myr. The left set of panels shows the evolution of $\alpha_{\rm vir}$ for each of the three tracers. The right panel shows the trajectories in the n–$\sigma_{\rm tot}$ plane with the corresponding colors. The gray contours and arrows indicate the average tracer PDF and their net fluxes, as in the top panel of Figure 4.3. The thick dotted lines in all panels correspond to the adopted star formation threshold, $\alpha_{\rm vir} = \alpha_{\rm vir,sf} = 10$. For presentation purposes, small fluctuations of actual tracer trajectories on timescales $\lesssim 5$ Myr were smoothed using Savitzky-Golay filter.

of such trajectories vary depending on local conditions and specific physical processes that govern gas evolution.

In our simulation, gas evolution between diffuse, warm, subsonic and dense, cold, supersonic ISM phases is governed by large-scale disk instabilities and the turbulent flows generated by them. The evolution of gas in the dense phase is largely affected by stellar feedback that disperses star-forming regions, drives large-scale ISM turbulence, and launches fountain-like outflows.

In the following subsections, we consider these processes using three illustrative tracer trajectories integrated over 200 Myr that are shown in Figure 4.4. We chose these particular tracers because their evolution over the considered period of time is governed predominantly by the same process over several consequential cycles of compression and expansion.

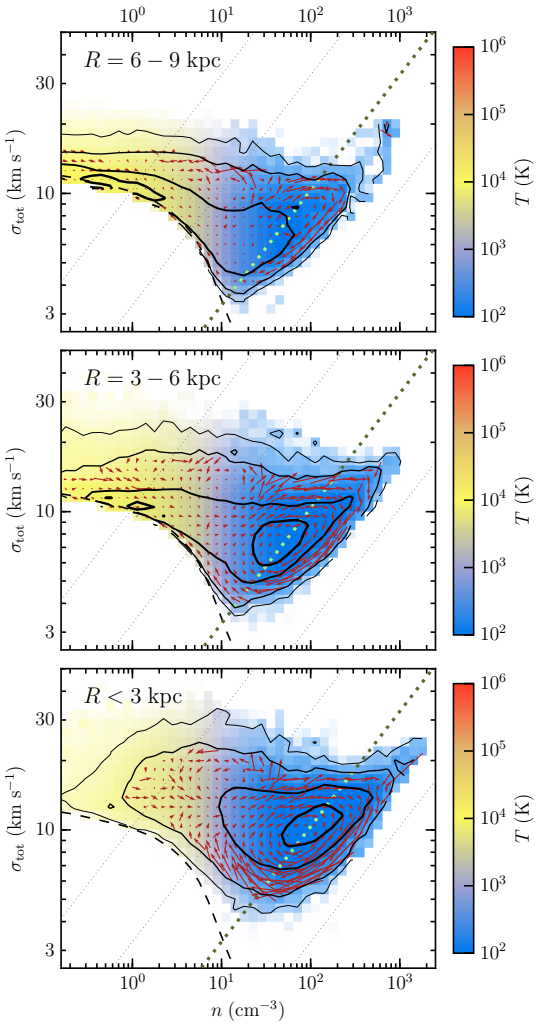

Figure 4.5: Distributions and average fluxes of tracers residing at different galactocentric radii, R (shown in the top left corner of each panel). Notation follows that of the top panel of Figure 4.3. Comparison with the right panel of Figure 4.4 hints that the distribution of tracers on the disk outskirts (top panel) is predominantly shaped by gas compression and expansion due to the spiral arms, while close to the disk center (bottom panel), the distribution is shaped by feedback-driven turbulence and outflows. Whirl-like patterns of velocities in the cold, supersonic phase indicate that the distribution of dense gas at all radii is affected by star formation feedback (see text for details).

4.3.1 Compression and expansion due to spiral arms

The blue line in the top left panel of Figure 4.4 shows an example of the $\alpha_{\rm vir}$ evolution followed by a tracer that swings between the subsonic and supersonic phases during cycles of compression and expansion as it enters and exits the spiral arms. The trajectory of this tracer in the n–$\sigma_{\rm tot}$ plane is shown with the same color in the right panel.

Due to strong compression, gas entering a spiral arm rapidly cools down and loses the thermal support that initially dominates in the subsonic ISM. At the same time, initially low subgrid turbulent velocities of the subsonic ISM, $\sigma_{\rm t} \lesssim 3\,{\rm km\,s^{-1}}$, rapidly grow due to compressional heating (see the detailed discussion in Appendix A.3 and also Robertson & Goldreich 2012). At $n \sim 10\,{\rm cm^{-3}}$, when subgrid turbulent velocities become comparable to the thermal speed, gas detaches from the lower envelope of the distribution shown in Figure 4.3 and enters the supersonic ISM phase. Similarly, when gas leaves a spiral arm, it expands, and subgrid turbulent velocities decrease. Eventually, under the influence of expansion and interstellar FUV heating, gas returns to the subsonic ISM phase with $n \sim 1\,{\rm cm^{-3}}$ and $T \sim 10^4$ K.

The actual transition of gas between the subsonic and supersonic phases is fast, as it is controlled by a strong compression rate in the spiral arms and short cooling times at $n > 1\,{\rm cm^{-3}}$. Hence, the rate at which diffuse gas is promoted into the dense phase is mostly determined by the time that gas waits between subsequent passages of the spiral arms,

$$\tau_{\rm arm} \sim \frac{2\pi R}{m V_{\rm gas}} \sim 80\,{\rm Myr} \frac{(R/8\,{\rm kpc})}{(m/6)(V_{\rm gas}/100\,{\rm km\,s^{-1}})}, \tag{4.1}$$

where $V_{\rm gas} \equiv v_{\rm gas} - v_{\rm pat}$ is the speed of gas relative to the spiral waves pattern, and we set $m = 6$, as our simulated galaxy develops six spiral arms.

The typical time that gas spends inside a spiral arm before expansion contributes to the dynamical rate of gas removal from the star-forming state, $\tau_{-,{\rm d}}$. This timescale depends on the spiral arm width, gas velocity, and the angle at which gas flows inside the arm.

Depending on local conditions, this timescale can be as long as a few tens of Myr.

In Figure 4.5 we plot distributions of n and $\sigma_{\rm tot}$ separately for tracers residing at different galactic radii and therefore experiencing different ISM conditions. The distribution in the outer disk (top panel) is shaped predominantly by the compression and expansion due to the spiral arms. Specifically, most of the gas mass in the outer disk resides in the diffuse subsonic phase and forms a peak at $n \sim 1$ cm^{-3} and $T \sim 10^4$ K. The tail extending along the lower envelope of the distribution toward the dense supersonic phase corresponds to the gas currently being compressed in the spiral arms. As the figure also shows, the compression of diffuse gas in the spiral arms is only relevant at large radii, whereas closer to the disk center, less gas remains in the diffuse phase, and this process becomes much less important.

4.3.2 SNe-induced shocks and ISM turbulence

We find that the evolution of dense, supersonic gas in the n–$\sigma_{\rm tot}$ plane is dominated by the turbulence that is driven by stellar feedback. Injection of momentum by SNe in a star-forming region results in a rapid expansion of gas until the region is eventually dispersed. Shocks associated with expanding bubbles compress gas in the disk plane, which may induce new episodes of star formation and subsequent SN explosions. The turbulence resulting from overlapping and interacting bubbles makes gas parcels oscillate in fast cycles, as illustrated by the green trajectory in Figure 4.4.

The characteristic timescale between subsequent compressions of ISM gas by such expanding SN shocks corresponds to

$$\tau_{\rm shell} \sim \frac{L}{v_{\rm shell}} \sim 50 \text{ Myr} \frac{(L/1 \text{ kpc})}{(v_{\rm shell}/20 \text{ km s}^{-1})}, \tag{4.2}$$

where L is a typical separation between bubbles (see, e.g., the temperature map in the middle panel of Figure 4.1) and $v_{\rm shell}$ is a typical velocity of shells on a scale L.

Compression and expansion of gas in the turbulent ISM is accompanied by the increase and decrease of turbulent velocity dispersion. As a result, averaging of such large-scale turbulent motions over many tracers results in a prominent clockwise whirl-like pattern of arrows around the peak of the PDF in the cold (blue) part of the diagram (see Figures 4.3 and 4.5). Closer to the peak center, the net flux magnitude decreases due to the averaging between fast motions of many tracers at the different stages of their turbulent compression-expansion cycles.

As Figure 4.5 shows, such a whirlwind pattern is most prominent at $R \leq 6$ kpc. Thus, the feedback-driven turbulence and associated compression and expansion of gas are dominant processes at these radii in the cold, supersonic gas. The ISM at these radii has a complex structure (see Figure 4.1) reflecting the chaotic turbulent nature of the gas.

4.3.3 Feedback-driven fountain outflows

Supernova feedback also affects some of the gas by accelerating it in the direction perpendicular to the disk plane. Such gas expands in fountain-like outflows but eventually cycles back to the ISM under the influence of the disk potential. Interactions of such outflows with the halo gas adjacent to the disk result in an increase of small-scale turbulent velocities that quickly dissipate when the gas falls back onto the disk.

An example of a tracer trajectory during expansion and subsequent recycling of a fountain outflow is shown with the red lines in Figure 4.4. This particular tracer was ejected and recycled twice, at $\sim$ 20–80 and $\sim$ 130–150 Myr. In each event, after its star-forming region was dispersed by feedback, this tracer acquired a moderate vertical velocity of $v_z \sim 50$ km s^{-1} and elevated as high as $\sim$ 400 pc above the disk plane, i.e., a few scale heights, before falling back onto the disk. At the highest elevation point, the gas in these outflows expands only to the densities comparable to those of the diffuse subsonic ISM phase, $n \sim 0.2$–2 cm^{-3} and its virial parameter reaches the values of $\alpha_{\rm vir} \sim 10^3$–$10^4$ due to the strong turbulence generated

by the interaction of the expanding outflow with the surrounding gas. Outflows launched by feedback from regions of more vigorous star formation reach even lower n and higher $\alpha_{\rm vir}$.

The timescale of the fountain cycle can be estimated as a dynamical time in the gravitational field of a massive infinite sheet of constant surface density $\Sigma_{\rm tot}$, corresponding to the local total surface density of the disk,

$$\tau_{\rm grav} \sim \frac{v_z}{\pi G \Sigma_{\rm tot}} \sim 20 \text{ Myr} \frac{(v_z/50 \text{ km s}^{-1})}{(\Sigma_{\rm tot}/200 \text{ M}_\odot \text{ pc}^{-2})}, \tag{4.3}$$

where v_z is the initial vertical velocity of gas in the outflow and $\Sigma_{\rm tot} = \Sigma_\star + \Sigma_{\rm g} \sim 200 \text{ M}_\odot \text{ pc}^{-2}$ is the typical total surface density of gas and stars in our simulated galaxies.

The averaging of trajectories between many gas parcels constituting fountain-like outflows results in a tail of the distribution directed from the star-forming state toward the lower densities and higher $\sigma_{\rm tot}$. The total flux of tracers forms a prominent counterclockwise vortex inside this tail that is clearly seen in Figures 4.3 and 4.5.

Figure 4.5 shows that at all radii within the disk, some fraction of gas evolves in the manner discussed above, which indicates the existence of fountain-like outflows. At larger radii, where the SFR is slower, the outflows are less prominent but still visible as a net flux of tracers directed toward lower densities along the top envelope of the distribution shown in the upper panel. Gas in such outflows at large radii usually returns to the diffuse, warm, subsonic ISM between the spiral arms. Closer to the center, outflows are ubiquitous, and, after falling back, their gas directly rejoins the tumultuous large-scale turbulent motions of dense, supersonic gas.

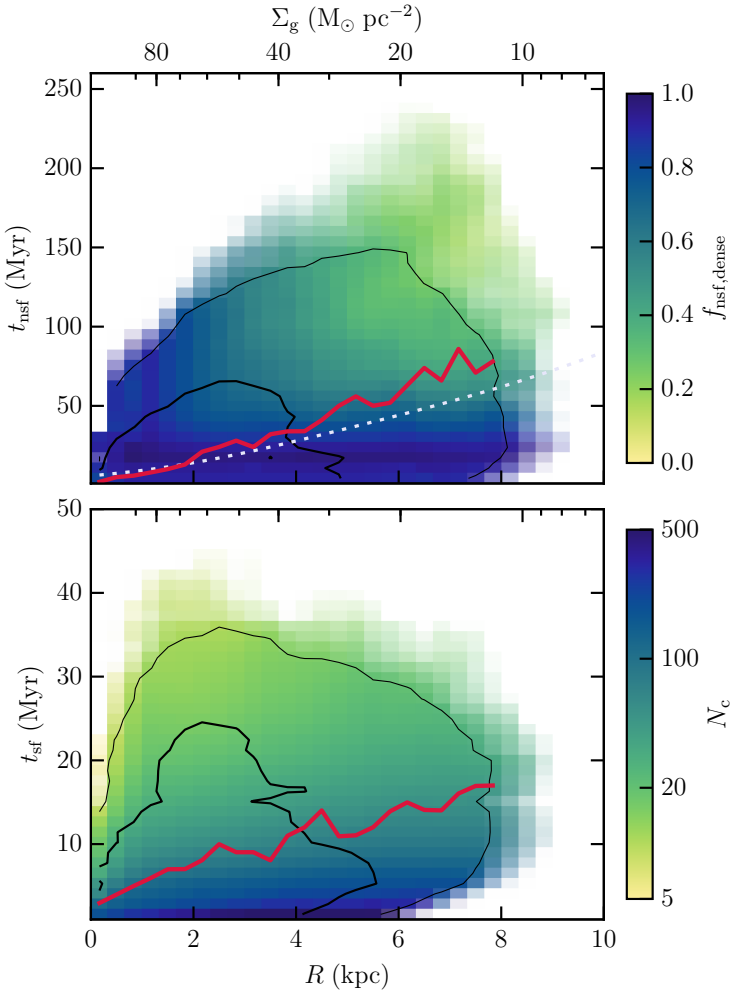

Figure 4.6: Distribution of times that tracers spend in non-star-forming ($t_{\rm nsf}$, top panel) and star-forming ($t_{\rm sf}$, bottom panel) states between successive crossings of the star formation threshold. Distributions of $t_{\rm nsf}$ and $t_{\rm sf}$ are shown as a function of galactic radius, R. The top axis in each panel also indicates the average surface density of gas at a given radius, $\Sigma_{\rm g} \propto \exp(-R/r_{\rm d})$, where $r_{\rm d}$ is the initial scale radius of the disk. Contours indicate 68% and 95% of trajectories. The thick red lines show the median timescales at every radius. The dotted line in the top panel corresponds to the free-fall time at the average midplane density at a given radius. Colors in the top panel show the average fraction of time spent in the dense phase with $n > 10\,{\rm cm}^{-3}$: $f_{\rm nsf,dense} \equiv t_{\rm nsf,dense}/t_{\rm nsf}$. Colors in the bottom panel show the average number of passages through the star-forming state required for complete depletion, $N_{\rm c}$ (Equation 4.4). To increase the statistics for long cycles, we follow tracers between 400 and 1 000 Myr of the disk evolution. For presentation purposes, we smooth the resulting distributions, preserving their main features.

4.4 Duration and number of evolution cycles

Typical tracer trajectories considered in the previous section explicitly confirm that during the evolution, gas parcels perform many fast cycles and rapidly explore a significant portion of the PDF, frequently switching between non-star-forming and star-forming states. As we discussed in Section 2, the distribution of the time that the gas parcels spend on each cycle in these states, $t_{\rm nsf}$ and $t_{\rm sf}$, determines the global depletion time of the galaxy.

In Figure 4.6 we plot the distribution of $t_{\rm nsf}$ and $t_{\rm sf}$ directly measured from the trajectories of all tracers as the time between consequential crossings of the star formation threshold. The results in the previous section indicate that the mix of the processes governing gas evolution may change with the galactic radius, R, and surface density, $\Sigma_{\rm g}$. Thus, to explore possible trends, we plot the distributions of timescales as a function of R and $\Sigma_{\rm g}$.

The distribution of $t_{\rm nsf}$ shown in the top panel indicates that the majority of tracers spend less than 100 Myr in the non-star-forming stage of evolution during each cycle. At higher average surface densities closer to the disk center, this time is even shorter, $t_{\rm nsf} \lesssim 50$ Myr, with a very low median value (thick red line).

Colors in the top panel show the average fraction of time that gas tracers spend in the dense phase, $n > 10\,{\rm cm}^{-3}$, over the non-star-forming stage of evolution. A blue color at small radii implies that gas preferentially stays in the dense, molecular phase even when it does not form stars. This is also evident from the bottom panel of Figure 4.5, which shows that only a small fraction of gas expands to $n < 10\,{\rm cm}^{-3}$ and it does so as a part of fountain outflows.

At larger radii, the relatively slow rate of star-forming gas replenishment via compression in the spiral arms becomes important, and the median $t_{\rm nsf}$ increases to ~ 80 Myr. Gas governed by this process spends significant time in the diffuse subsonic ISM, and such tracer trajectories occupy the areas of the longest $t_{\rm nsf}$ at $R > 4$ kpc (green color in Figure 4.6). However, as indicated by the blue color, at such radii many tracers still perform short cycles

with $t_{\rm nsf} < 50$ Myr without leaving the dense phase.

The increase of the $t_{\rm nsf}$ median value is consistent with the scaling proportional to the free-fall time at the mean or midplane density at a given radius, $t_{\rm ff,0} \propto \rho_0^{-1/2} = (\Sigma_{\rm g}/2h_{\rm d})^{-1/2}$, shown by the dotted line in Figure 4.6 (see also Saitoh et al., 2008). Such scaling is sometimes adopted in analytical models of galactic star formation to define the timescale on which star-forming regions are created (e.g., Krumholz et al., 2012a; Elmegreen, 2015). As we discussed above, $t_{\rm nsf}$ in our simulations is set by both stellar feedback that drives turbulence and dynamical processes within the ISM. The scaling of the median $t_{\rm nsf}$ with density indicates that gravity and the associated timescale plays at least some role in setting the time that gas spends in the non-star-forming state. For example, the fall of the gas driven out in a fountain outflow back to the disk will occur on a timescale of order $\sim t_{\rm ff,0}$.

The bottom panel of Figure 4.6 shows the distribution of time spent by tracers in the star-forming state on each cycle. This timescale is close to the typical "lifetime" of star-forming regions and is quite short: $t_{\rm sf} \lesssim 20$ Myr or 2–4 free-fall times at the typical densities of star-forming regions. The fact that $t_{\rm sf}$ is, on average, significantly shorter than $t_{\rm nsf}$ is consistent with the small mass fraction of star-forming gas.

As we discussed in Section 2, the average time that a gas parcel spends in the star-forming state on a single cycle determines the total number of such cycles required for complete depletion as $N_{\rm c} = \tau_\star/t_{\rm sf}$. For every tracer on each passage through the star-forming stage, we estimate this number as the inverse fraction of mass depleted during the passage,

$$N_{\rm c}^{-1} = \int \frac{dt}{t_\star} = \int \epsilon_{\rm ff} \frac{dt}{t_{\rm ff}}, \tag{4.4}$$

where the integral is accumulated for each tracer particle while it is in the star-forming state between subsequent crossings of the star formation threshold. The resulting distribution of $N_{\rm c}$ is shown by the colors in the bottom panel of the figure.

In agreement with our model, typical $N_{\rm c} \sim 50$ and the lifetimes of gas in the star-forming

state, $t_{\rm sf} \sim$ 10–20 Myr, are consistent with the range of the star-forming gas depletion times, $\tau_\star \sim N_{\rm c} t_{\rm sf} \sim$ 300–500 Myr, obtained in our simulation. In addition, assuming $t_{\rm nsf} \sim$ 50–100 Myr, Equation (2.1) for the typical depletion time of a gas parcel gives a value of $\sim$ 2–5 Gyr, which is consistent with the actual global depletion time obtained in our simulation (see Section 3).

4.5 Discussion

4.5.1 Comparison with previous studies

The short, $\sim$ 10–100 Myr, timescales of the physical processes driving the evolution of gas in the ISM (see the top panel of Figure 4.6) indicate that the ISM is vigorously "boiling" when considered on the global depletion timescale. During this vigorous evolution, gas cycles between non-star-forming and star-forming stages and spends only $t_{\rm sf} \sim$ 5–15 Myr in the star-forming stage on each cycle (see the bottom panel of Figure 4.6), which is consistent with the short lifetimes derived for observed GMCs (e.g., Kawamura et al., 2009; Murray, 2011; Schruba et al., 2017).

Observational estimates of the integral star-formation efficiency during a star-forming stage, defined for a given star-forming region containing a gas mass of $m_{\rm g}$ and a mass of formed young stars of $m_\star$ as $\epsilon \equiv m_\star/(m_{\rm g} + m_\star)$, give $\epsilon \sim$ 1–20% (e.g., Evans et al., 2009; Lada et al., 2010). This fraction is even smaller in less-efficient clouds (e.g., Rebolledo et al., 2015; Lee et al., 2016; Vutisalchavakul et al., 2016). A similar range of ϵ is also obtained in simulations of star cluster formation (Gavagnin et al., 2017), models of star formation in GMCs (e.g., Zamora-Avilés & Vázquez-Semadeni, 2014), and cosmological simulations of a Milky Way-sized galaxy that resolve the growth of globular clusters and self-consistently capture its termination by stellar feedback (Li et al., 2017b).

Such values of ϵ imply that gas parcels must undergo $N_{\rm c} \sim \epsilon^{-1} \sim$ 5–100 cycles transition-

ing from the non-star-forming to star-forming state before they convert their gas into stars. This number of cycles is also consistent with the typical depletion times of star-forming gas, $\tau_\star \equiv \langle 1/t_\star \rangle_{\rm sf}^{-1}$, and lifetimes, $t_{\rm sf}$, derived for observed star-forming regions, $N_{\rm c} = \tau_\star / t_{\rm sf}$. Specifically, depletion times of gas in observed star-forming regions are estimated to be $t_\star \sim$ 50–500 Myr (e.g., Evans et al., 2009, 2014; Lada et al., 2010, 2012; Heiderman et al., 2010; Gutermuth et al., 2011; Schruba et al., 2017); for $t_{\rm sf} \sim$ 5–15 Myr quoted above, these $t_\star$ give $N_{\rm c} \sim$ (50–500)/(5–15) $\sim$ 3–100. Such $N_{\rm c}$ are in the ballpark of the $N_{\rm c}$ range that we estimate for the gas in our simulations (see the bottom panel of Figure 4.6), although we note that the number of cycles in our simulation can be somewhat overestimated due to the artificially sharp threshold in the definition of star-forming gas.

Note that specific values of $t_{\rm nsf}$, $t_{\rm sf}$ and $N_{\rm c}$ depend on the scale, l, on which the small-scale distribution of $t_\star$ is defined. Clearly, if we consider the evolution of gas parcels on the scale of protostellar cores, $\sim$ 0.01 pc, the star-forming stage of evolution will correspond to the formation of one or a handful of stars, which will consume most of the gas in a single event. The gas parcels on this scale will spend a long time in the non-star-forming stage and will consume their gas in one or a few cycles, $N_{\rm c} = 1 + \xi$, where ξ corresponds to the ratio of the protostellar core mass returned back to the ISM to the mass of the formed star.

The key expression of our model (Equation 2.10) was derived by applying the mass conservation law to all star-forming gas in a galaxy or in a given ISM patch. Mass conservation can also be invoked to build a model for the formation, evolution, and destruction of individual GMCs (e.g., Feldmann & Gnedin, 2011; Zamora-Avilés et al., 2012; Lee et al., 2016).

Our model is based on mass conservation alone, and thus the overall physical explanation for long gas depletion times presented in Chapter 2 does not require the assumption of dynamical equilibrium. Indeed, when a gas parcel undergoes some inherently nonequilibrium process, such as compression in a spiral arm, the parcel's depletion time will still be given by

$t_{\rm dep} = (\tau_\star/t_{\rm sf})(t_{\rm nsf}+t_{\rm sf}) = \tau_\star(t_{\rm nsf}/t_{\rm sf}+1)$, and therefore $t_{\rm dep}$ will be long if $t_{\rm nsf} \gg t_{\rm sf}$ and/or $\tau_\star$ is long. The absence of a long-term equilibrium requirement is an essential difference of our framework from the models for the Kennicutt-Schmidt relation that rely on the assumption of self-regulation to the vertical or Toomre (1964) equilibrium state (e.g., Ostriker & Shetty, 2011; Faucher-Giguère et al., 2013).

In fact, our model explicitly accounts for the deviations from the equilibrium state in which $\dot{M}_{\rm sf} \approx 0$. Such deviations, along with fluctuations of other quantities that enter Equation (2.10), can be important sources of the depletion time scatter. These deviations can be substantial for individual ISM patches, which generally will not be in equilibrium, even if a galaxy as a whole is. Additional scatter can arise due to observational tracers sampling different stages of gas evolution incompletely (Kruijssen & Longmore, 2014).

We note, however, that unlike the models of Ostriker & Shetty (2011) and Faucher-Giguère et al. (2013), our conceptual framework cannot quantitatively predict the depletion time by itself. It only elucidates how the depletion time is related to the timescales of the processes driving gas evolution. The variables through which this relation is parameterized can be either calibrated in simulations, as is done in this study, or be derived in analytical models (e.g., Zamora-Avilés et al., 2012). Nevertheless, as detailed in the next subsection and Chapters 5 and 6, our framework is very useful for interpreting and explaining a number of puzzling facts about star formation in both observed and simulated galaxies.

4.5.2 Implications for observations

Rapid cycling of gas between non-star-forming and star-forming states explains the large discrepancy between long global depletion times of $\gtrsim 1$ Gyr and short, $\sim$ 10–100 Myr, timescales associated with the dynamical processes in the ISM. Only a small fraction of gas is converted into stars during each cycle, and therefore gas would have to go through a large number of cycles to be depleted.

Our model also naturally explains the difference between observed local depletion times of (mostly molecular) gas in star-forming regions, $t_\star \sim 50$–$500\,\mathrm{Myr}$, and global depletion times of both total gas, $\tau \sim 2$–$10\,\mathrm{Gyr}$, and molecular gas, $\tau_{\mathrm{H_2}} \sim 1$–$3\,\mathrm{Gyr}$. The global depletion times, τ and $\tau_{\mathrm{H_2}}$, are longer than the average gas depletion time in star-forming regions, $\tau_\star$, due to the significant fraction of time that gas spends in the non-star-forming state (see Equation 2.1). This implies that only a fraction of total and molecular gas is forming stars at any given moment. For example, the observed values of $t_\star$ and $\tau_{\mathrm{H_2}}$ indicate that only $f_{\mathrm{sf,H_2}} \equiv M_{\mathrm{sf}}/M_{\mathrm{H_2}} = \tau_\star/\tau_{\mathrm{H_2}} \sim 5\%$–$50\%$ of molecular gas is forming stars. The range of $f_{\mathrm{sf,H_2}}$ in our simulation is consistent with this estimate, with the non-star-forming molecular gas state corresponding to strongly turbulent cold gas. Diffuse, non-star-forming molecular gas is also observed in the Milky Way, but its mass fraction ($\sim 25\%$ from Roman-Duval et al., 2016) is a factor of ~ 2–4 too low to explain the discrepancy between global and local depletion times of molecular gas. Thus, a substantial fraction of non-star-forming molecular gas must be missed in such observations.

As pointed out by Kruijssen & Longmore (2014), a model considering different evolutionary stages and corresponding chemical phases of the ISM gas can be used to interpret the dependence of the depletion time and its scatter on the averaging scale (see, e.g., Schruba et al., 2017). This dependence in observed galaxies can also be used as a stringent test of the star formation and feedback implementation in galaxy formation models.

Our model for gas depletion time provides a natural framework for predicting and interpreting trends with galaxy properties and redshift. For instance, we show that the duration of cycles decreases with increasing surface density as $t_{\mathrm{nsf}} \propto \Sigma_{\mathrm{g}}^{-0.5}$. As we will also show in Section 6.1, this trend is accompanied by a milder but nevertheless nonnegligible decrease in $\tau_\star$. This means that the observed decrease in global depletion times in high-redshift and starburst galaxies (e.g., Kennicutt, 1998; Bouché et al., 2007; Genzel et al., 2010; Tacconi et al., 2018) can be explained by shorter dynamical timescales, t_{nsf}, and star-forming gas

depletion times, $\tau_\star$, associated with high-density environments. In addition, the nonequilibrium state of starburst galaxies may result in short τ due to the contribution of the $\tau_\star/\tau_{\rm e,sf}$ term in Equation (2.10).

The described mechanism controlling depletion time remains qualitatively the same in the presence of cosmological accretion of gas. Indeed, the cycling of the ISM gas between star-forming and non-star-forming states happens on short, $\lesssim 100$ Myr, dynamical timescales, while the accretion of intergalactic gas proceeds on a much longer timescale, comparable with Gyrs-long gas depletion times. As new gas is added to the galaxy, the timescales that control ISM gas cycling—$t_{\rm nsf}$, $t_{\rm sf}$, and $\tau_\star$—can slowly change because they depend on the global properties of galaxy, such as its total mass. However, at any moment, the depletion time will still be set by the dynamical gas cycling in the ISM even though the typical duration of a cycle can slowly change with time. Cosmological accretion can significantly affect gas cycling only when it happens on a timescale comparable with the duration of a cycle, $\lesssim 100$ Myr, e.g., during galaxy mergers.

Our framework also predicts the dependence of depletion times and KSR shape on metallicity. Gas must be shielded by a certain column density in order to become cold and molecular. This column density has a corresponding number density at which such a transition occurs, as can be seen in the phase diagrams in Figure 4.5, that show the sharp change from the warm, transonic phase (yellow) to the cold, supersonic phase (blue) at $n \sim 10\ {\rm cm}^{-3}$. At lower metallicities, both the characteristic number density and column density of the transition increase, leading to the decrease of $f_{\rm H_2}$, $f_{\rm sf}$ and $\tau_\star$. Thus, the overall gas depletion time, τ, increases.

The higher characteristic density of the transition at lower metallicity also results in the shift of the turnover in the KSR for total gas to higher surface densities. This shift is qualitatively similar to that predicted by the Gnedin & Kravtsov (2011) models, where star formation is tied to molecular gas. We have confirmed this explicitly by resimulating our

model galaxy at a lower metallicity and will present these results in a forthcoming paper.

4.6 Summary

In this chapter we explored our physical model that elucidates why gas depletion times in galaxies are long compared to the timescales of the processes driving the evolution of the interstellar medium. We show that the depletion time is long not because some bottleneck in the formation of star-forming regions imposes a long evolutionary timescale, but because only a small fraction of the gas mass is converted into stars during a single star-forming stage in the evolution of a gas parcel. This fraction is small due to both the short duration of the star-forming stage, as dynamical processes and stellar feedback efficiently disperse star-forming regions, and the low intrinsic star formation efficiency of dense molecular gas. A gas parcel thus must go through many cycles transitioning between non-star-forming and star-forming states before it becomes converted into stars. Hence, even though the duration of each cycle can be short, the global depletion time is long because the number of cycles is large.

Furthermore, the difference between the global and local depletion times of molecular gas in our model arises because not all of the molecular gas is actively forming stars. Non-star-forming molecular gas appears naturally if local star formation efficiency is a strong function of the virial parameter of a region, while the molecular fraction of gas is set by its ability to shield against FUV radiation and is a function of mainly gas number density and metallicity.

We illustrate our model using the results of an isolated $L_\star$-sized disk galaxy simulation that reproduces the observed Kennicutt-Schmidt relation for both molecular and atomic gas. Our results and conclusions can be summarized as follows.

1. Analysis of our simulation shows that the properties of gas parcels in the ISM evolve on timescales of $\sim$ 10–100 Myr under the influence of compression by the spiral arms, ISM turbulence, and SNe-driven shocks. The relative importance of these processes varies

with galactocentric radius, R, and average surface density. At $R \gtrsim 5$ kpc, the evolution from a warm, diffuse state to a dense, cold phase is driven mainly by compression in the spiral arms, while SNe-driven shocks and large-scale ISM turbulence dominate at smaller radii.

2. During an evolutionary cycle, gas spends most of the time in the non-star-forming state, $t_{\rm nsf} > t_{\rm sf}$, whereas the time spent in the star-forming state, $t_{\rm sf}$, is limited by stellar feedback and dynamical processes to $t_{\rm sf} \sim 5$–15 Myr. We find that the median $t_{\rm nsf}$ varies with gas surface density as $t_{\rm nsf} \propto \Sigma_{\rm g}^{-0.5}$.

3. On the resolution scale of our simulation, 40 pc, the typical range of densities in star-forming regions is limited to $n \sim 10$–10^3 cm^{-3} by the interstellar FUV background and stellar feedback. We find that the resulting depletion times of star-forming gas $\tau_\star \sim 300$–500 Myr are consistent with the depletion times estimated for observed GMCs on these scales.

4. The distributions of depletion times and lifetimes of star-forming regions in our simulations imply that a typical gas parcel has to undergo 5–100 cycles transitioning between non-star-forming and star-forming states before converting its mass into stars.

CHAPTER 5

EFFECTS OF STAR FORMATION AND FEEDBACK PARAMETERS ON GLOBAL STAR FORMATION IN GALAXIES

Recent simulations of galaxy formation revealed several nontrivial dependencies of global star formation on the parameters of star formation and feedback adopted on the resolution scale of simulations. One of the most intriguing results is that in simulations with strong feedback, the galaxy-scale star formation rate—and hence the global depletion time—is insensitive to the local star formation efficiency (e.g., Dobbs et al., 2011a; Agertz et al., 2013; Hopkins et al., 2013a, 2017a; Agertz & Kravtsov, 2015; Benincasa et al., 2016; Orr et al., 2018). This behavior is thought to be due to "self-regulation" of star formation by feedback (e.g., Dobbs et al., 2011a).

In this chapter, we focus on explaining the connection between the local parameters of star formation and feedback and global star formation and galaxies, and our goal is to extend and make sense of the results of other recent studies of this issue. In Section 5.1, we use the simulation suite presented in Chapter 3 where we systematically varied $\epsilon_{\rm ff}$ value, star formation threshold, and feedback strength to show that the global depletion time and the star-forming gas mass fraction in simulated galaxies exhibit systematic and well-defined trends as a function of these parameters. In Section 5.2, we demonstrate that these trends can be reproduced both qualitatively and quantitatively using the physical model presented in Chapter 2 that explains the origin of long gas depletion times in galaxies.

In Section 5.3, we compare our simulation results and model predictions to the observed star-forming properties of real galaxies. We also discuss how the trends identified in simulations and our analytic model can be used to guide the choice of star formation and feedback parameters in high-resolution galaxy simulations. In particular, we show that both the

global depletion times and the star-forming gas mass fractions of observed galaxies should be used on kiloparsec and larger scales, while the measurements of the depletion time and its scatter on smaller spatial scales provide additional constraints on the local efficiency of star formation.

In Section 5.4, we compare our predictions with the results of previous recent studies and interpret their results in the context of our model, and in Section 5.5, we summarize our results and conclusions.

This chapter is based on the work published in Semenov et al. (2018).

5.1 Overview of simulation results

The analysis presented in this section focuses on the quantities that characterize the global star formation of the simulated galaxy: the global gas depletion time,

$$\tau \equiv \frac{M_{\rm g}}{\dot{M}_\star}, \tag{5.1}$$

as well as the mass fraction of star-forming gas, $f_{\rm sf} = M_{\rm sf}/M_{\rm g}$, and the mean freefall time of star-forming gas, $\tau_{\rm ff} = \langle 1/t_{\rm ff} \rangle_{\rm sf}^{-1}$. Here the star-forming gas mass, $M_{\rm sf}$, is the total mass of all gas in the galaxy that satisfies the adopted star formation criterion. Consequently, the average freefall time is defined by analogy with Equation (3.2), $\dot{M}_\star = \epsilon_{\rm ff} M_{\rm sf}/\tau_{\rm ff}$, and thus $\tau_{\rm ff}$ depends on the local $t_{\rm ff}$ via $\epsilon_{\rm ff}/\tau_{\rm ff} = \dot{M}_\star/M_{\rm sf} = \int (\epsilon_{\rm ff}/t_{\rm ff}) \rho dV / \int \rho dV = \epsilon_{\rm ff} \langle 1/t_{\rm ff} \rangle_{\rm sf}$, where the integrals are taken over all star-forming gas. The values of τ, $f_{\rm sf}$, and $\tau_{\rm ff}$ are closely related. For example, the global depletion time can be expressed as

$$\tau \equiv \frac{M_{\rm g}}{\dot{M}_\star} = \frac{M_{\rm sf}}{\dot{M}_\star} \frac{M_{\rm g}}{M_{\rm sf}} = \frac{\tau_{\rm ff}}{\epsilon_{\rm ff} f_{\rm sf}}. \tag{5.2}$$

Below, we describe the trends of τ, $f_{\rm sf}$, and $\tau_{\rm ff}$ with the main parameters of the star formation and feedback prescriptions in our $L_\star$-sized galaxy simulations: efficiency $\epsilon_{\rm ff}$, the

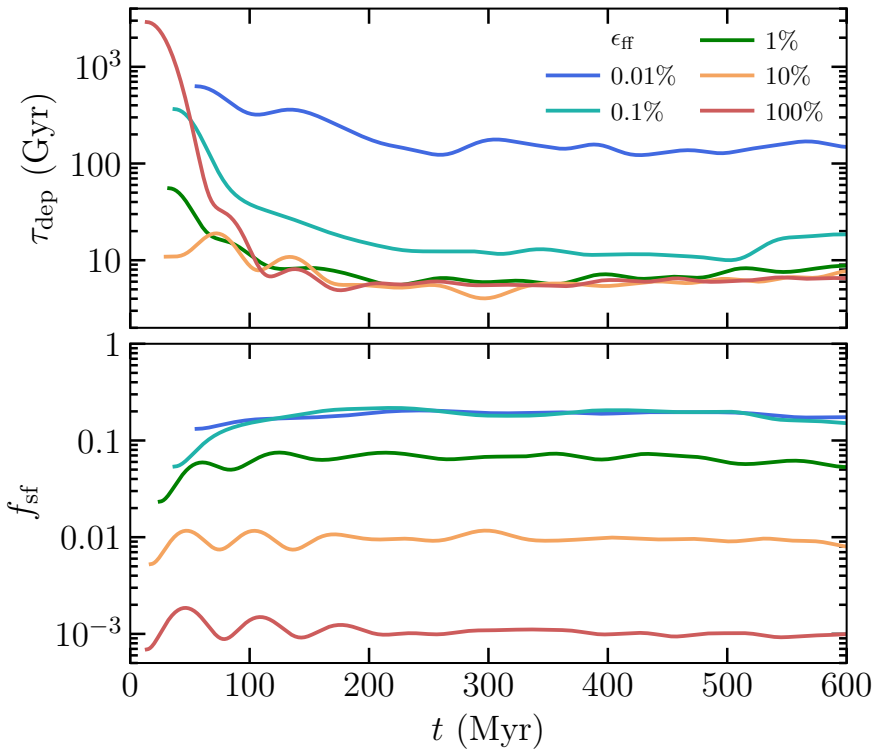

Figure 5.1: Evolution of the global depletion time, τ, and the star-forming mass fraction, $f_{\rm sf}$, in the simulations with varying $\epsilon_{\rm ff}$ at the fiducial feedback strength ($b = 1$) and star formation threshold ($\alpha_{\rm vir,sf} = 10$). To compare different runs at the same temporal resolution, all curves are smoothed using a Gaussian filter with a width of 30 Myr. All quantities are measured in a cylindrical volume centered at the disk center with $|z| < 2$ kpc and $1 < R < 20$ kpc.

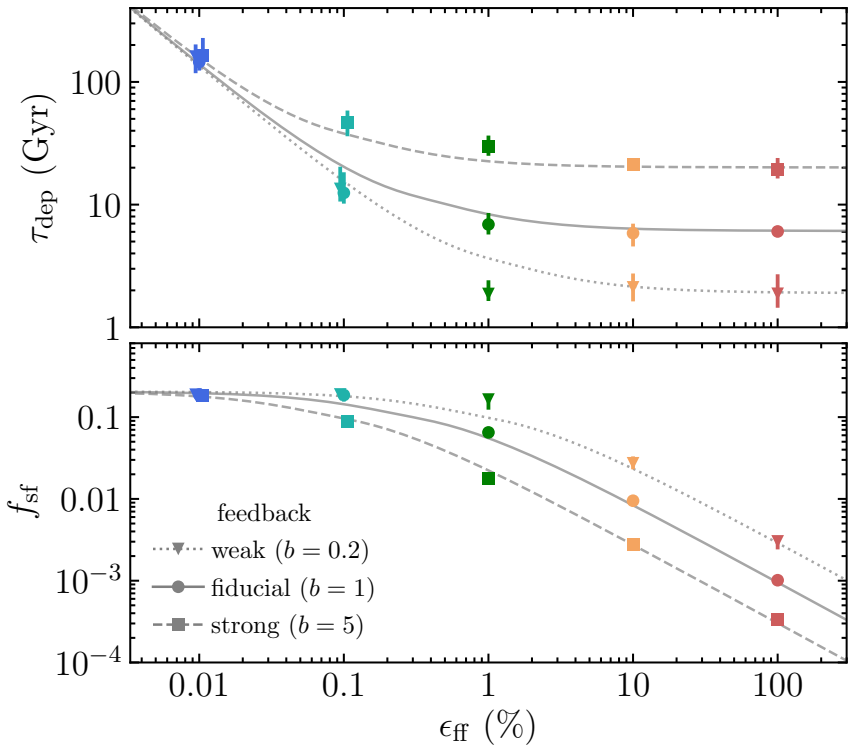

Figure 5.2: Dependence of the equilibrium τ and $f_{\rm sf}$ values on the $\epsilon_{\rm ff}$ value in our simulations with fiducial star formation threshold ($\alpha_{\rm vir,sf} = 10$) and different feedback boosts: weak ($b = 0.2$; triangles), fiducial ($b = 1$; circles), and strong ($b = 5$; squares). The values of τ and $f_{\rm sf}$ are time-averaged between 300 and 600 Myr, with error bars indicating $5^{\rm th}$ and $95^{\rm th}$ percentiles over this time interval. The choice of the averaging interval is explained in Section 3.4. Gray lines show the predictions of our model, which will be explained in Section 5.2. The figure illustrates qualitatively different behavior of τ and $f_{\rm sf}$ at low and high $\epsilon_{\rm ff}$.

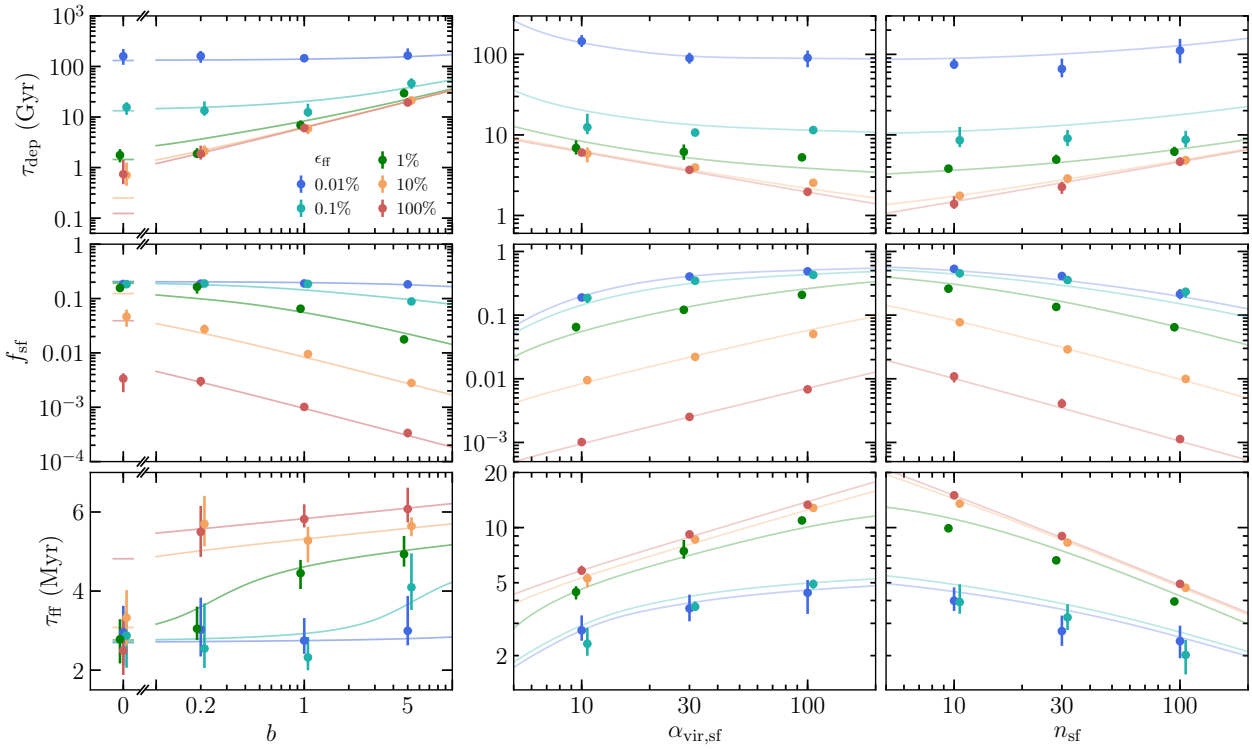

Figure 5.3: Equilibrium values of τ, $f_{\rm sf}$, and $\tau_{\rm ff}$, in simulations with varying $\epsilon_{\rm ff}$ and different feedback strengths (b; left column) and star formation thresholds set in virial parameter ($\alpha_{\rm vir} < \alpha_{\rm vir,sf}$; middle columns) and gas density ($n > n_{\rm sf}$; right column). The feedback strength is varied at the fiducial threshold value ($\alpha_{\rm vir,sf} = 10$), whereas the threshold is varied at the fiducial feedback strength ($b = 1$). Points indicate the values of τ, $f_{\rm sf}$, and $\tau_{\rm ff}$ time-averaged between 300 and 600 Myr, with error bars indicating 5$^{\rm th}$ and 95$^{\rm th}$ percentiles over this time interval. To avoid overlap, points for $\epsilon_{\rm ff} = 0.1\%$, 1%, and 10% are slightly shifted horizontally around the actually used values of b, $\alpha_{\rm vir,sf}$, and $n_{\rm sf}$. Lines show our analytical model detailed in Section 5.2 and summarized in Appendix B.1.

feedback strength parameter b, and the star formation threshold $\alpha_{\rm vir,sf}$ or $n_{\rm sf}$. The efficiency $\epsilon_{\rm ff}$ affects local star formation in the most direct way, while the feedback strength b affects the *integral* local star formation efficiency by controlling the time that gas spends in the star-forming state. The interplay between star formation and feedback also affects the overall distribution of gas in a galaxy. For a given distribution, the star formation thresholds control the mass fraction, $f_{\rm sf}$, and the mean density of star-forming gas, and thus its mean freefall time, $\tau_{\rm ff}$.

Figure 5.1 shows the evolution of τ and $f_{\rm sf}$ in simulations with varying $\epsilon_{\rm ff}$ at the fixed fiducial feedback strength ($b = 1$) and the star formation threshold ($\alpha_{\rm vir,sf} = 10$). After the initial transient stage, τ and $f_{\rm sf}$ become approximately constant in time at values that depend on the choice of $\epsilon_{\rm ff}$. To explore this dependence on $\epsilon_{\rm ff}$, we average the equilibrium values of τ and $f_{\rm sf}$ between 300 and 600 Myr[1] and show them in Figure 5.2 with error bars indicating temporal variability around the average. In addition to simulations with fiducial feedback (circles), the figure also shows the results for 5 times weaker (triangles) and 5 times stronger feedback (squares). Star formation histories in these and all other our simulations are qualitatively similar to those shown above, and thus for quantitative comparison from now on we will consider only the equilibrium values of τ and $f_{\rm sf}$. Gray lines in this figure show the predictions of our analytic model that will be detailed in Section 5.2.

Figure 5.2 clearly shows that the dependence of τ and $f_{\rm sf}$ on $\epsilon_{\rm ff}$ is qualitatively different when $\epsilon_{\rm ff}$ is low and when it is high. When $\epsilon_{\rm ff}$ is low, $\leq 0.01\%$, τ scales as $\epsilon_{\rm ff}^{-1}$, whereas the star-forming mass fraction remains independent of $\epsilon_{\rm ff}$. When $\epsilon_{\rm ff}$ is high, $\epsilon_{\rm ff} \geq 1\%$, the trends are reversed: τ is independent of $\epsilon_{\rm ff}$, whereas $f_{\rm sf}$ scales as $\epsilon_{\rm ff}^{-1}$. It is this independence of τ from $\epsilon_{\rm ff}$ that has been referred to as *self-regulation* in the literature.

The figure also shows that the dependence on $\epsilon_{\rm ff}$ remains qualitatively similar at different feedback strengths, and the limiting regimes of low and high $\epsilon_{\rm ff}$ exist at all b. However,

1. The choice of this time interval is explained in Section 3.4.

for stronger feedback, the transition to the self-regulation regime occurs at smaller $\epsilon_{\rm ff}$ and depletion time in this regime increases.

This increase of τ with feedback strength at high $\epsilon_{\rm ff}$ is easier to quantify in the top left panel of Figure 5.3, which shows τ as a function of feedback boost b at different $\epsilon_{\rm ff}$. As before, the error bars indicate temporal variability around the average, and lines show the predictions of our model that will be detailed in Section 5.2. From the figure, depletion time at high $\epsilon_{\rm ff}$ increases almost linearly with b: $\tau \sim (6\ {\rm Gyr})\ b^{0.75}$. The middle left panel shows that $f_{\rm sf}$ exhibits the opposite trend with b. The bottom left panel also shows that despite wide variation of $\epsilon_{\rm ff}$ and b, the average freefall time in star-forming gas varies only mildly, from $\tau_{\rm ff} \sim 3$ Myr at low $\epsilon_{\rm ff}$ to $\tau_{\rm ff} \sim 5$–6 Myr at high $\epsilon_{\rm ff}$.

The middle column of panels in Figure 5.3 shows the variation of τ, $f_{\rm sf}$, and $\tau_{\rm ff}$ in the runs with different $\epsilon_{\rm ff}$ and values of the adopted star formation threshold: $\alpha_{\rm vir,sf} = 10$, 30, and 100. Again, for every value of $\alpha_{\rm vir,sf}$, the dependence on $\epsilon_{\rm ff}$ is qualitatively similar to the fiducial case. In the high-$\epsilon_{\rm ff}$ regime, τ decreases at higher $\alpha_{\rm vir,sf}$, i.e., when the threshold becomes less stringent and makes more gas eligible to star formation. At a less stringent threshold, $f_{\rm sf}$ and $\tau_{\rm ff}$ both increase, and this increase is stronger in the high-$\epsilon_{\rm ff}$ regime. In the right panels of Figure 5.3, the star formation threshold is set in the gas density rather than in $\alpha_{\rm vir}$, and the behavior of τ, $f_{\rm sf}$, and $\tau_{\rm ff}$ remains qualitatively the same, but the direction of all trends is opposite since a density-based threshold becomes less stringent at smaller $n_{\rm sf}$.

The presented results show that the key global star formation properties of our simulated galaxies change systematically with changing parameters of the local star formation and feedback. The trends are well defined and exhibit distinct behavior in the low-$\epsilon_{\rm ff}$ and high-$\epsilon_{\rm ff}$ regimes. In the latter, the global star formation rate and the gas depletion time become insensitive to the variation of $\epsilon_{\rm ff}$, while the mass fraction of the star-forming gas, $f_{\rm sf}$, is inversely proportional to $\epsilon_{\rm ff}$. In the low-$\epsilon_{\rm ff}$ regime, the trends are reversed: τ scales inversely

with $\epsilon_{\rm ff}$, while $f_{\rm sf}$ is almost insensitive to it. The dependence of τ on the feedback strength parameter b is the opposite to the dependence on $\epsilon_{\rm ff}$: in the low-$\epsilon_{\rm ff}$ regime, τ is insensitive to b, while in the high-$\epsilon_{\rm ff}$ regime τ exhibits a close-to-linear scaling with b.

5.2 Interpretation of the results using the analytic model

As solid lines in Figures 5.2 and 5.3 show, the trends of τ, $f_{\rm sf}$, and $\tau_{\rm ff}$ are well described by a physical model of gas cycling in the interstellar medium formulated in Chapter 2. This model is based on the basic mass conservation between different parts of the interstellar gas. In this section, we summarize the main equations of our model and its predictions for the regimes of star formation regulation in galaxies. We then discuss the qualitative predictions of the model for the trends of τ, $f_{\rm sf}$, and $\tau_{\rm ff}$ in simulations and provide a physical interpretation of these trends. We then show that with a minimal calibration, our model can reproduce these trends *quantitatively*. For convenience, the meanings of quantities used in our model are summarized in Table B.1 in Appendix B.1.

5.2.1 Two regimes of star formation regulation

To interpret the results presented above, we will use the main Equation (2.10) of our model for depletion times. This equation was derived from the conservation of star-forming mass in a galaxy or ISM patch,

$$\dot{M}_{\rm sf} = F_{+} - F_{-,\rm d} - F_{-,\rm fb} - \dot{M}_{\star}, \tag{5.3}$$

adopting the following parametrization of fluxes and SFR:

$$F_{+} = \frac{M_{\rm nsf}}{\tau_{+}}, \qquad F_{-,\rm d} = \frac{M_{\rm sf}}{\tau_{-,\rm d}}, \qquad F_{-,\rm fb} = \xi\frac{M_{\rm sf}}{\tau_{\star}}, \qquad \dot{M}_{\star} = \frac{M_{\rm sf}}{\tau_{\star}}. \tag{5.4}$$

As our simulated galaxy quickly settles into a quasi-steady regime with approximately constant τ, $f_{\rm sf}$, and $\tau_{\rm ff}$, we will ignore the non-equilibrium term that reflects the variation of star-forming mass by setting $\dot{M}_{\rm sf} = 0$, i.e. $\tau_{\rm e,sf} \to \infty$ in Equation (2.10).[2] For our subsequent discussion, it is also convenient to rearrange terms in the resulting Equation (2.10) as

$$\tau = (1+\xi)\tau_+ + \left(1 + \frac{\tau_+}{\tau_{-,\rm d}}\right)\frac{\tau_{\rm ff}}{\epsilon_{\rm ff}}, \tag{5.5}$$

where we have substituted the parametrization of local depletion time, $\tau_\star = \tau_{\rm ff}/\epsilon_{\rm ff}$. Similarly, star-forming mass fraction can be expressed using Equation (5.2):

$$f_{\rm sf} = \frac{\tau_{\rm ff}}{\epsilon_{\rm ff}\,\tau} = \left[(1+\xi)\tau_+\frac{\epsilon_{\rm ff}}{\tau_{\rm ff}} + 1 + \frac{\tau_+}{\tau_{-,\rm d}}\right]^{-1}. \tag{5.6}$$

As was shown in Figures 5.2 and 5.3 and as we will discuss in more detail below, Equations (5.5) and (5.6) can predict the trends of τ and $f_{\rm sf}$ observed in our simulations with varied star formation efficiency $\epsilon_{\rm ff}$, star formation threshold, and feedback strength b. We note that the latter is closely related to the ξ parameter of the model. Both these parameters reflect the strength of feedback per unit stellar mass formed and its efficacy in dispersing star-forming regions. However, these parameters are not identical: b is a relative strength of the momentum injection in our implementation of feedback, while $\xi = F_{-,\rm fb}/\dot{M}_\star$ is an average "mass-loading factor" that characterizes the efficacy of gas removal from star-forming regions by feedback (see Chapter 2). We also note that in equations for τ and $f_{\rm sf}$ the average freefall time in the star-forming gas, $\tau_{\rm ff}$, is a model parameter, but, as we will show in Section 5.2.2 and Appendix B.1, its trends with simulation parameters discussed in Section 5.1

2. We stress that an assumption of the quasi-equilibrium is not required in general and is made here only to simplify notation. As was discussed in Section 4.5, the term $\pm\tau_\star/\tau_{\rm e,sf}$ contributes to the scatter of the depletion time in galaxies or ISM patches. For normal star-forming galaxies, this term is small and can become significant only if the global dynamical properties of the galaxy change on a timescale much shorter than the local depletion time $\tau_\star$. Thus, in case of, e.g., starburst mergers, a more general Equation (2.10) should be used.

can also be understood using our model predictions.

Equation (5.5) readily shows that the global depletion time is a sum of two terms, one of which may dominate depending on the parameters. For example, the first term, $(1+\xi)\tau_+$, will dominate when feedback is sufficiently strong, i.e. ξ is large, or star formation efficiency $\epsilon_{\rm ff}$ is sufficiently high so that the second term, $(1+\tau_+/\tau_{-,\rm d})\tau_{\rm ff}/\epsilon_{\rm ff}$, is subdominant. Conversely, the second term may dominate if feedback is inefficient or $\epsilon_{\rm ff}$ is low. In these two regimes, the dependence of depletion time on the parameters of star formation and feedback will be qualitatively different. Specifically, when the first term in the equation dominates, τ is insensitive to $\epsilon_{\rm ff}$ and scales with feedback strength ξ. Conversely, when the second term dominates, τ scales as $\epsilon_{\rm ff}^{-1}$ and is independent of feedback strength.

Physically, these two regimes reflect the dominance of different negative terms in the mass conservation Equation (5.3) and thus different mechanisms that limit lifetimes of star-forming regions. In the first regime, $\tau \approx (1+\xi)\tau_+$ and the lifetime of gas in the star-forming state is limited by feedback and star formation itself. We therefore will refer to this case as the *"self-regulation regime"* because this was the term used to indicate insensitivity of τ to $\epsilon_{\rm ff}$ in previous studies. In the second regime, $\tau \approx (1+\tau_+/\tau_{-,\rm d})\tau_{\rm ff}/\epsilon_{\rm ff}$ and star-forming gas lifetime is limited by dynamical processes dispersing star-forming regions, such as turbulent shear, differential rotation, and expansion behind spiral arms, operating on timescale $\tau_{-,\rm d}$. We will refer to this case as the *"dynamics-regulation regime,"* as star formation passively reflects the distribution of ISM gas regulated by gas dynamics, rather than actively shaping it by gas consumption and associated feedback.

In the next section, we will consider dynamics- and self-regulation regimes in more detail. We will illustrate these regimes using our simulations with the fiducial feedback strength and star formation threshold but varying $\epsilon_{\rm ff}$ from a low value of 0.01%, corresponding to the dynamics-regulation regime, to a high value of 100%, corresponding to the self-regulation regime. As Figure 5.4 shows, in different regimes the quasi-equilibrium ISM gas distribution

is qualitatively different. The figure shows the midplane density slices and n–$\sigma_{\rm tot}$ diagrams (like the one in Figure 4.3) colored according to the average gas temperature, with arrows indicating average gas fluxes. In agreement with the results of Chapter 4, small net fluxes through the star formation threshold result from the near cancellation of strong positive and negative fluxes, F_+ and F_-, whose typical magnitudes are shown with the thick blue and red arrows, respectively, in the lower right corner of each diagram. Depending on the $\epsilon_{\rm ff}$ value, the negative flux can be dominated by either dynamical or feedback-driven flux, $F_{-,\rm d}$ or $F_{-,\rm fb}$, which in turn results in qualitatively different behavior of Equation (5.5).

5.2.2 Predictions for trends of τ, $f_{\rm sf}$, and $\tau_{\rm ff}$

Interpretation of scalings in the dynamics-regulation regime

As discussed above, dynamics-regulation occurs when $\epsilon_{\rm ff}$ or ξ are small, so that the second term on the right-hand side of Equation (5.5) dominates. In this case, τ scales inversely with $\epsilon_{\rm ff}$:

$$\tau \approx \left(1 + \frac{\tau_+}{\tau_{-,\rm d}}\right) \frac{\tau_{\rm ff}}{\epsilon_{\rm ff}}. \tag{5.7}$$

The star-forming mass fraction, on the other hand, remains independent of $\epsilon_{\rm ff}$ because, according to Equation (5.6),

$$f_{\rm sf} \approx \left(1 + \frac{\tau_+}{\tau_{-,\rm d}}\right)^{-1}. \tag{5.8}$$

Such scalings, $\tau \propto \epsilon_{\rm ff}^{-1}$ and $f_{\rm sf} \approx$ const, indeed persist in our simulations with low $\epsilon_{\rm ff}$ values (see $\epsilon_{\rm ff} = 0.01\%$ and 0.1% in Figures 5.1–5.3).

Physically, these scalings arise because at low $\epsilon_{\rm ff}$ and ξ the contributions of star formation ($\dot{M}_\star$) and feedback ($F_{-,\rm fb}$) terms to the overall mass flux balance in Equation (5.3) become small. As a result, the steady state is established with $F_{-,\rm d} \approx F_+$, which yields Equations (5.7) and (5.8). In our simulated galaxy, such a state is established as gas is

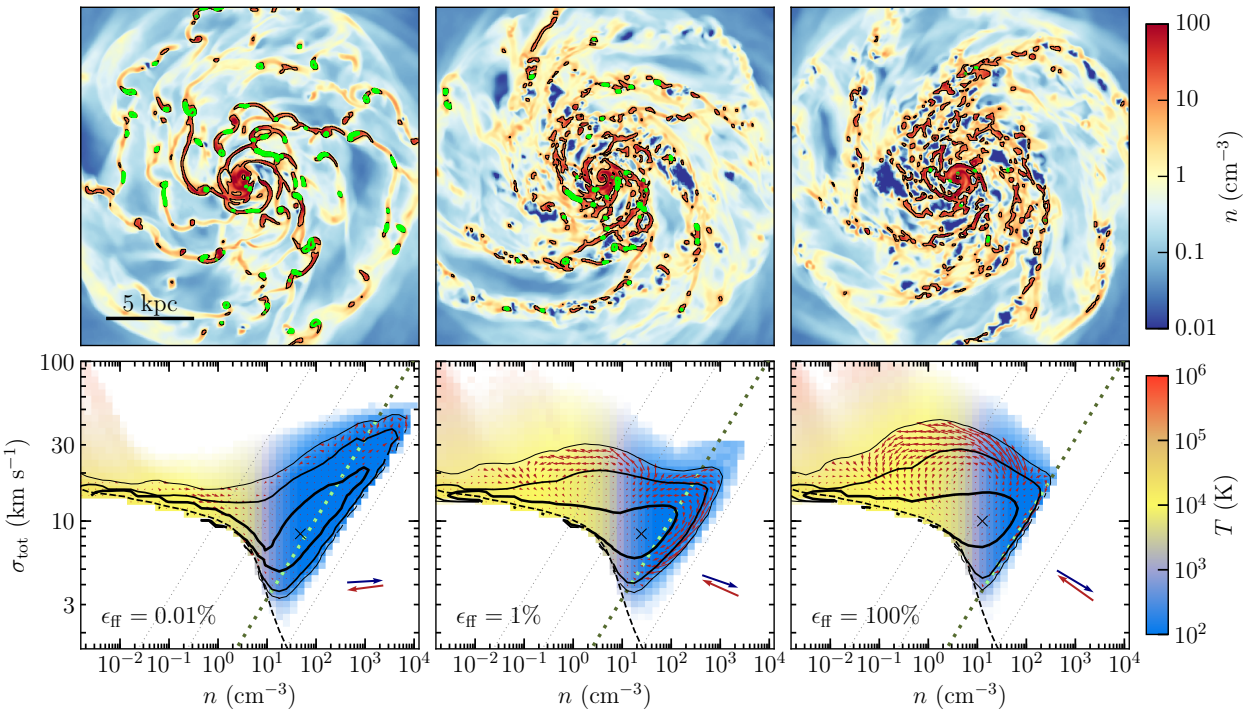

Figure 5.4: Effect of $\epsilon_{\rm ff}$ on the spatial gas distribution and the gas distribution in the phase space of the gas density, n, and the total subgrid velocity dispersion, $\sigma_{\rm tot}$. The adopted value for $\epsilon_{\rm ff}$ changes from left to right: 0.01%, 1%, and 100%. The top row of panels shows the midplane density slices at $t = 500$ Myr, with black contour indicating cold dense gas, $n > 10$ cm^{-3}, and green contour indicating star-forming regions, $\alpha_{\rm vir} < \alpha_{\rm vir,sf} = 10$. The bottom row of panels shows n–$\sigma_{\rm tot}$ diagrams colored with the mass-weighted temperature in each bin. The distribution is time averaged between 400 and 600 Myr using gas-tracer particles at $R > 1$ kpc (see Section 3.4). Black contours indicate 68%, 95%, and 99% of resulting gas tracers' PDF. Thin red arrows throughout the diagram show the average net flux of gas tracers, while the thick blue and red arrows in the corner of each panel illustrate magnitudes and directions of the average positive and negative gas fluxes, respectively, measured at the point indicated with a cross. All arrows can be directly compared to each other because their normalization is the same: the arrow extent corresponds to the distance that a tracer traverses over 5 Myr. Star-forming gas in each n–$\sigma_{\rm tot}$ diagram resides below the thick dotted line, which corresponds to the star formation threshold of $\alpha_{\rm vir,sf} = 10$. Thin dotted lines parallel to the star formation threshold show constant values of $\alpha_{\rm vir} = 1000$, 100, and 1 (from left to right).

compressed into new star-forming clumps at the same rate at which old clumps are dispersed by differential rotation and tidal torques, and neither of these processes depends on $\epsilon_{\rm ff}$. The interplay between compression and dynamical dispersal determines the steady-state distribution of gas in the n–$\sigma_{\rm tot}$ diagram (the bottom left panel of Figure 5.4), which is also insensitive to $\epsilon_{\rm ff}$. As a consequence, the star-forming mass fraction, $f_{\rm sf}$, and the mean freefall time in star-forming gas, $\tau_{\rm ff}$, also do not depend on $\epsilon_{\rm ff}$ and are determined solely by the definition of the star-forming gas. The global depletion time, however, does depend on $\epsilon_{\rm ff}$ as is evident from Equation (5.7).

As $F_{-,\rm fb}$ is subdominant in this regime, τ, $f_{\rm sf}$, and $\tau_{\rm ff}$ are also insensitive to the feedback strength, but they do depend on the star formation threshold. Indeed, as blue lines in the left column of Figure 5.3 show, τ, $f_{\rm sf}$, and $\tau_{\rm ff}$ remain approximately constant when feedback boost factor, b, is varied from 0 to 5. At the same time, when star formation threshold is varied such that more gas is included in the star-forming state, both $f_{\rm sf}$ and $\tau_{\rm ff}$ increase because more low-density gas is added, while τ decreases as additional star-forming gas increases SFR. It is worth noting that these dependencies on star formation threshold are rather weak when the threshold encompasses significant fraction of the ISM gas, but they become stronger when the threshold selects gas only from the high-density tail of distribution, because it is this high-density gas that mostly determines τ, $f_{\rm sf}$, and $\tau_{\rm ff}$.

Finally, it is also worth noting that for some galaxies, or certain regions within galaxies, equilibrium may not be achievable, so that $F_+ > F_{-,\rm d}$ or $F_+ < F_{-,\rm d}$. In this case distribution of gas evolves, and thus τ, $f_{\rm sf}$, and $\tau_{\rm ff}$ also change with time. This occurs in the central regions of galaxies in simulations with $\epsilon_{\rm ff} = 0.1\%$ and 0.01%, where the central gas concentration grows owing to accretion, and which we thus exclude from our analysis (see Section 3.4).

Interpretation of scalings in the self-regulation regime

Self-regulation occurs when $\epsilon_{\rm ff}$ or ξ are sufficiently large, so that the first term on the right-hand side of Equation (5.5) dominates and depletion time is given by

$$\tau \approx (1+\xi)\tau_+, \tag{5.9}$$

and is thus independent of $\epsilon_{\rm ff}$, but scales almost linearly with ξ. In this regime, the star-forming mass fraction scales inversely with $\epsilon_{\rm ff}$ (see Equation 5.6):

$$f_{\rm sf} \approx \frac{1}{(1+\xi)\epsilon_{\rm ff}}\frac{\tau_{\rm ff}}{\tau_+}, \tag{5.10}$$

which also implies $f_{\rm sf} \ll 1$ because $\tau_{\rm ff}/\epsilon_{\rm ff} \ll (1+\xi)\tau_+$ is required for the subdominance of the terms proportional to $\epsilon_{\rm ff}^{-1}$ in Equation (5.5).

The scalings of Equations (5.9) and (5.10) are consistent with the results of our simulations with large $\epsilon_{\rm ff}$ values (Figures 5.1–5.3). The insensitivity of τ to $\epsilon_{\rm ff}$ and its scaling with feedback strength have also been observed in other simulations with high $\epsilon_{\rm ff}$ and efficient feedback (e.g., Agertz & Kravtsov, 2015; Hopkins et al., 2017a; Orr et al., 2018). In the literature, these phenomena are also usually referred to as "self-regulation."

As was already mentioned in Section 2.3, self-regulation occurs when gas spends most of the time in non-star-forming stages, $f_{\rm sf} \ll 1$, and the rate of star-forming gas supply, F_+ in Equation (5.3), is balanced by rapid gas consumption and strong feedback-induced gas dispersal: $F_+ \approx \dot{M}_\star + F_{-,\rm fb}$. In this case, global depletion time is given by $\tau \approx N_{\rm c}\tau_+$, where $N_{\rm c}$ is the total number of cycles between non-star-forming and star-forming states. Due to large $\dot{M}_\star + F_{-,\rm fb} \propto (1+\xi)\epsilon_{\rm ff}$, the duration of star-forming stages, $t_{\rm sf}$, is regulated by star formation and feedback: when $\epsilon_{\rm ff}$ or ξ are increased, the lifetime of gas in the star-forming state shortens as $t_{\rm sf} \propto [(1+\xi)\epsilon_{\rm ff}]^{-1}$. However, the *total* time spent in the star-forming state before complete depletion depends on $\epsilon_{\rm ff}$ but not on ξ: $\tau_\star \propto \epsilon_{\rm ff}^{-1}$. The dependence on $\epsilon_{\rm ff}$

thus cancels out in $N_{\rm c} = \tau_\star / t_{\rm sf}$ and global depletion time becomes independent of $\epsilon_{\rm ff}$ but maintains scaling with ξ.

Therefore, in the self-regulation regime, star formation regulates itself by controlling the timescale on which feedback disperses star-forming regions and the timescale on which gas is converted into stars in these regions. The relative importance of these processes is determined by the feedback strength per unit of formed stars, i.e. the ξ value.

When feedback is efficient, $\xi \gg 1$, as is the case in our simulations[3] shown in Figure 5.4, the ISM gas distribution at high $\epsilon_{\rm ff}$ is shaped by feedback-induced gas motions, $F_+ \approx F_{-,{\rm fb}}$. Specifically, as the top panels show, at $\epsilon_{\rm ff} = 1\%$ and 100%, efficient feedback makes ISM structure flocculent and devoid of dense star-forming clumps, which are typical in the $\epsilon_{\rm ff} = 0.01\%$ simulation. The bottom panels show that at high $\epsilon_{\rm ff}$ efficient feedback keeps most of the dense gas above the star formation threshold or close to it. This results in a significant decrease of $f_{\rm sf}$ and increase of $\tau_{\rm ff}$ in this regime, compared to the dynamics-regulated regime.

When feedback is inefficient, $\xi \ll 1$, or even completely absent, $\xi = 0$, the gas consumption dominates at high $\epsilon_{\rm ff}$, $F_+ \approx \dot{M}_\star$. In this regime, all available star-forming gas is rapidly converted into stars and the global depletion time is determined by the timescale on which new star-forming gas is supplied, i.e. $\tau \sim \tau_+$. Thus, this regime is analogous to the "bottleneck" scenario envisioned by Saitoh et al. (2008). Our simulations with $b = 0$ and $\epsilon_{\rm ff} \geq 10\%$ operate in this regime, and because τ_+ is short, τ is also short, so that gas is rapidly consumed and the simulated galaxy cannot settle into a quasi-equilibrium state.

Dependence of τ, $f_{\rm sf}$, and $\tau_{\rm ff}$ on the choice of the star formation threshold can also be understood as follows. As $\epsilon_{\rm ff}$ and ξ increase, the average density of the star-forming gas decreases, which increases $\tau_{\rm ff}$. For the density-based threshold, the value of $\tau_{\rm ff}$ becomes independent of $\epsilon_{\rm ff}$ and ξ as the star-forming gas is kept at the density close to the threshold, $n \sim n_{\rm sf}$. Larger $\alpha_{\rm vir,sf}$ (or smaller $n_{\rm sf}$) in Figure 5.3 results in shorter $\tau \propto \tau_+$, because τ_+

3. Our results in Section 5.2.2 and Appendix B.1 suggest that $\xi \sim 60$ in our simulations with fiducial feedback and star formation threshold.

decreases as it takes less time for gas to evolve from the typical ISM density and $\alpha_{\rm vir}$ to the values of the star-forming gas. As typical densities of the star-forming gas decrease, $\tau_{\rm ff}$ increases and thus $f_{\rm sf} \propto \tau_{\rm ff}/\tau_{+}$ (Equation 5.10) also increases because of both longer $\tau_{\rm ff}$ and shorter τ_{+}.

In the above discussion, the dynamical time τ_{+} was assumed to be independent of $\epsilon_{\rm ff}$ and the feedback strength. This is certainly a simplification, as τ_{+} can be determined by feedback, which can limit the lifetime of star-forming regions, drive large-scale turbulence in the ISM, inflate low density hot bubbles, launch fountain-like outflows, and sweep gas into new star-forming regions. These processes are reflected in the complicated pattern of the net gas flux in the n–$\sigma_{\rm tot}$ plane in the bottom middle panel of Figure 5.4, which shows a prominent clockwise whirl near the star formation threshold and a counterclockwise whirl in the lower-density gas. The clockwise whirl originates from the ISM gas being swept by SN shells, while the counterclockwise whirl is shaped by the gas in freely expanding shells (see Section 4.3 for a more detailed discussion). Nevertheless, we find that the dependence of τ_{+} on the feedback strength variation is much weaker than the linear scalings of τ and $f_{\rm sf}$ with ξ and $\epsilon_{\rm ff}$ (see the quantitative predictions below), and thus our simplification is warranted.

Transition between the regimes

Self-regulation or dynamics-regulation regimes occur when the first or second term in Equation (5.5) dominates. In Section 5.1, we illustrated these regimes using simulations in which $\epsilon_{\rm ff}$, feedback strength, and star formation threshold are varied in a wide range. The transition between the two regimes depends on all of these parameters. For example, the dependence of transition on the feedback strength is evident from Figure 5.2: at stronger feedback, the transition occurs at smaller $\epsilon_{\rm ff}$. As a result, the run with $\epsilon_{\rm ff} = 1\%$ and weak feedback, $b = 0.2$, exhibits behavior of the dynamics-regulation regime, while the galaxy in the run with the same $\epsilon_{\rm ff}$ but with much stronger feedback, $b = 5$, is in the self-regulation regime.

Similarly, from the middle and right panels of Figure 5.3, when $\epsilon_{\rm ff} = 1\%$ and threshold defines a significant fraction of gas as star-forming (e.g., $\alpha_{\rm vir,sf} = 100$ or $n_{\rm sf} = 10\ {\rm cm}^{-3}$), simulated galaxies are in the dynamics-regulation regime. On the other hand, when threshold defines only a small fraction of gas as star-forming (e.g., $\alpha_{\rm vir,sf} = 10$ or $n_{\rm sf} = 100\ {\rm cm}^{-3}$), galaxies are in the self-regulation regime.

Note, however, that achieving self-regulation with the threshold variation is not always possible, because the threshold affects both terms in Equation (5.5), and thus the value of the threshold at which the first term dominates does not always exist. For example, in the top middle panel of Figure 5.3, when $\epsilon_{\rm ff} < 1\%$, depletion time bends upward at $\alpha_{\rm vir,sf} < 10$ and remains inversely proportional to $\epsilon_{\rm ff}$ and therefore never reaches the self-regulation regime.

In the transition between dynamics-regulated and self-regulated regimes, the relation between our model parameters follows from the condition that the terms in Equation (5.5) are comparable:

$$(1+\xi)\epsilon_{\rm ff} \sim \left(1 + \frac{\tau_+}{\tau_{-,\rm d}}\right)\frac{\tau_{\rm ff}}{\tau_+}. \tag{5.11}$$

Notably, in this case a given galaxy has the same star-forming mass fraction independent of $\epsilon_{\rm ff}$ or the feedback strength. Indeed, after substituting condition (5.11) into Equation (5.6), we get

$$f_{\rm sf} \sim \frac{1}{2}\left(1 + \frac{\tau_+}{\tau_{-,\rm d}}\right)^{-1}, \tag{5.12}$$

i.e., the star-forming mass fraction at the transition is half of that in the dynamics-regulation regime (Equation 5.8).

Quantitative predictions as a function of $\epsilon_{\rm ff}$ and feedback strength

So far, we described how the model presented above can qualitatively explain the trends and regimes revealed by our simulations. Here we will show that the model can also describe the simulation results *quantitatively.*

To predict τ and $f_{\rm sf}$ in the simulations using Equations (5.5) and (5.6), we note that the unknown parameters enter these equations only in three different combinations: $(1+\xi)\tau_+$, $\tau_+/\tau_{-,\rm d}$, and $\tau_{\rm ff}/\epsilon_{\rm ff}$. These can be calibrated against a small subset of the simulations in the dynamics- and self-regulation regimes using scalings discussed above as a guide. Quantitative predictions of the model with calibrated parameters for the trends of τ and $f_{\rm sf}$ can then be compared with the results of other simulations, not used in the calibration.

Specifically, using two runs in the self-regulated regime with $\epsilon_{\rm ff}=100\%$, we measure the normalization of $(1+\xi)\tau_+$ and its scaling with the feedback boosting factor b. Equation (5.9) gives the normalization of the global depletion time in the high-$\epsilon_{\rm ff}$ run with $b=1$: $[(1+\xi)\tau_+]_0 \approx \tau(b=1) \sim 6\,{\rm Gyr}$. Adopting $(1+\xi)\tau_+ \propto b^{\beta}$ for the scaling with b, the slope $\beta = \Delta\log\tau/\Delta\log b \approx 0.75$ is measured using the second run with $b=5$, and thus the final relation is

$$(1+\xi)\tau_+ \approx 6\,b^{0.75}\ \ {\rm Gyr}, \tag{5.13}$$

i.e. $(1+\xi)\tau_+$ is long and increases almost linearly with b.

Using a simulation with $\epsilon_{\rm ff}=0.01\%$ (i.e., the dynamics-regulation regime) and Equation (5.8), we estimate the ratio of dynamical times $\tau_+/\tau_{-,\rm d}$ from the value of star-forming mass fraction, $f_{\rm sf}\approx 0.2$, measured in this simulation:

$$\frac{\tau_+}{\tau_{-,\rm d}} \approx \frac{1}{f_{\rm sf}} - 1 \sim 4, \tag{5.14}$$

which implies that in the absence of feedback the star-forming gas is supplied 4 times more slowly than it is dispersed by dynamical effects.

Finally, the last unknown parameter is the average freefall time in the star-forming gas, $\tau_{\rm ff}$. In our simulations, $\tau_{\rm ff}$ varies only mildly, from $\tau_{\rm ff}\approx 2$–3 Myr in the dynamics-regulation regime to $\tau_{\rm ff}\approx 5$–6 Myr in the self-regulation regime. In the simplest case, we can make predictions assuming a constant $\tau_{\rm ff}=4$ Myr, which is representative of the freefall time in

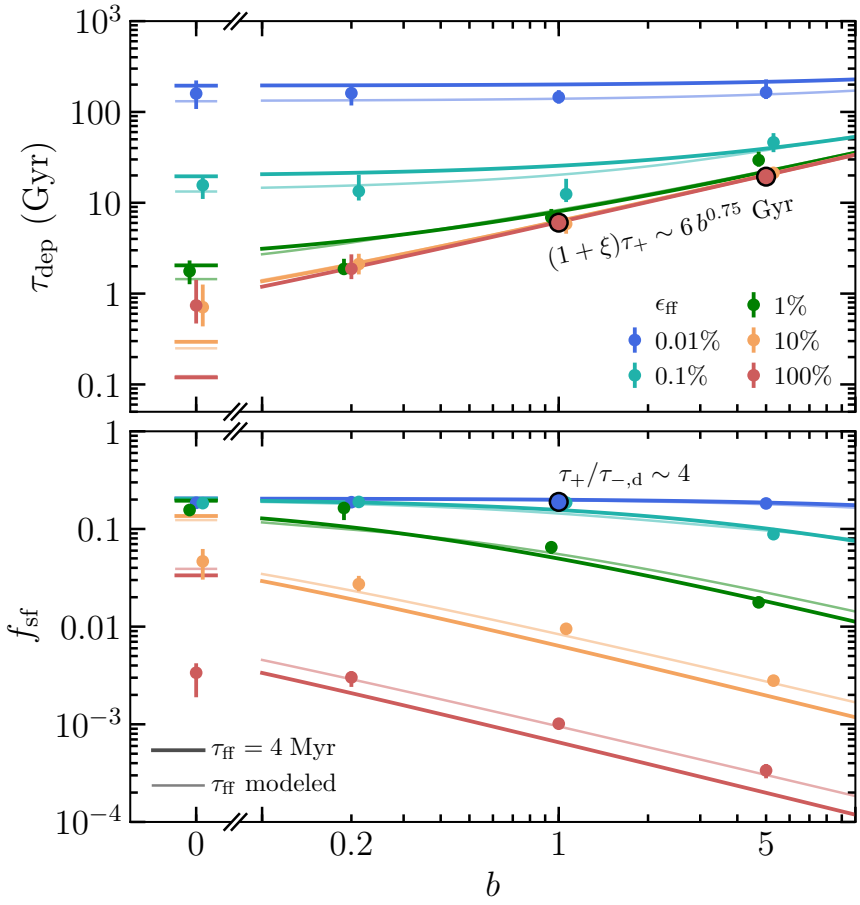

Figure 5.5: Comparison of our model predictions (shown with lines) for the global depletion time (τ; top panel) and the star-forming mass fraction ($f_{\rm sf}$; bottom panel) with the results of our simulations with varying $\epsilon_{\rm ff}$ and the feedback boost factor, b, assuming the fiducial star formation threshold, $\alpha_{\rm vir,sf} = 10$ (notation repeats that of Figure 5.3). To fix the model parameters, we use τ in two high-$\epsilon_{\rm ff}$ runs (red circled points in the top panel), which give $(1+\xi)\tau_+ \sim (6\ {\rm Gyr})\ b^{0.75}$, and $f_{\rm sf}$ from a low-$\epsilon_{\rm ff}$ run (blue circled point in the bottom panel), which gives $\tau_+/\tau_{-,\rm d} \sim 4$. As thick lines show, if we neglect variation of $\tau_{\rm ff}$ and assume the average $\tau_{\rm ff} = 4$ Myr, our model correctly predicts the overall behavior of τ and $f_{\rm sf}$. As thin lines show, predictions of our model are improved if the variation of $\tau_{\rm ff}$ is also modeled as explained in Appendix B.1. To avoid clutter, simulation points for $\epsilon_{\rm ff} = 0.1\%$, 1%, and 10% are slightly shifted horizontally around the actually used values of $b = 0$, 0.2, 1, and 5.

star-forming regions both in our simulations and in observations.

Figure 5.5 compares the simulation results for τ and $f_{\rm sf}$ as a function of the feedback strength, b, with the predictions of our model with constant $\tau_{\rm ff} = 4$ Myr (thick lines). Of the 20 simulation results shown by points in the figure, only three were used to calibrate the four model parameters, $[(1+\xi)\tau_+]_0$, β, $\tau_+/\tau_{-,\rm d}$, and $\tau_{\rm ff}$, as described above; these simulations are shown by the large circled points. For the other 17 simulations, the lines show *predictions* of the model. Figure 5.5 shows that the model correctly predicts a wide variation of τ and $f_{\rm sf}$ with $\epsilon_{\rm ff}$ and the feedback strength b in the entire suite of simulations.

Moreover, τ and $f_{\rm sf}$ involve two independent quantities, $\dot{M}_\star$ and $M_{\rm sf}$, measured in the simulations. Thus, our four-parameter model calibrated using three simulations describes well $17 \times 2 = 34$ independent data points. The fact that our model closely agrees with the simulations when we treat $\tau_{\rm ff}$ as a fixed parameter and τ_+ as independent of ξ and $\epsilon_{\rm ff}$ indicates that most of the variation of τ and $f_{\rm sf}$ is driven by their explicit dependence on $\epsilon_{\rm ff}$ and ξ in Equations (5.5) and (5.6), whereas any variation of $\tau_{\rm ff}$ and τ_+ with $\epsilon_{\rm ff}$ and ξ is secondary.

Nevertheless, accounting for $\tau_{\rm ff}$ variations can somewhat improve the accuracy of our model. Thin lines in Figure 5.5 and in the left panels of Figure 5.3 show our model predictions incorporating $\tau_{\rm ff}$ variation with $\epsilon_{\rm ff}$ and ξ values. To model this variation, we note that the increase of $\tau_{\rm ff}$ during the transition from the dynamics-regulation regime to the self-regulation regime is controlled by the total rate of the star-forming gas removal by gas consumption and feedback: $\dot{M}_\star + F_{-,\rm fb} \propto (1+\xi)\epsilon_{\rm ff}$. Thus, we calibrate the values of $\tau_{\rm ff}$ in these regimes using the same three simulations as before, and we interpolate $\tau_{\rm ff}$ as a function of $(1+\xi)\epsilon_{\rm ff}$ for all other simulations. The details of this calibration and the adopted interpolation function are presented in Appendix B.1.

Quantitative predictions as a function of the star formation threshold

To predict how τ, $f_{\rm sf}$, and $\tau_{\rm ff}$ depend on the star formation threshold, $\alpha_{\rm vir,sf}$, we need to calibrate model parameters as a function of $\alpha_{\rm vir,sf}$. Analogously to the previous section, we constrain these dependencies using runs in the limiting regimes and use our model to predict τ, $f_{\rm sf}$, and $\tau_{\rm ff}$ in the other simulations. Our model predictions are shown with lines in the middle column of panels in Figure 5.3 using calibrations done as follows.

First, the dependence of $(1+\xi)\tau_+$ and $\tau_{\rm ff}$ in the self-regulation regime on $\alpha_{\rm vir,sf}$ can be assessed using a run with $\epsilon_{\rm ff} = 100\%$ and fiducial $\alpha_{\rm vir,sf} = 10$ and an additional run with $\alpha_{\rm vir,sf} = 100$ to obtain the following scalings:

$$(1+\xi)\tau_+ \propto \alpha_{\rm vir,sf}^{-0.5}, \tag{5.15}$$

$$\tau_{\rm ff} \propto \alpha_{\rm vir,sf}^{0.4}. \tag{5.16}$$

The scaling of $(1+\xi)\tau_+$ is measured as the slope of τ in the top middle panel of the figure. For the typical density of the star-forming gas $\bar{n}$, the freefall time is $\tau_{\rm ff} \propto \bar{n}^{-0.5}$ and the slope of 0.4 in Equation (5.16) thus indicates that $\bar{n} \propto \alpha_{\rm vir,sf}^{-0.8}$. Given that $\alpha_{\rm vir} \propto \sigma_{\rm t}^2/n$, this means that the typical velocity dispersion in the star-forming gas scales as $\bar{\sigma}_{\rm t} \propto \alpha_{\rm vir,sf}^{0.1}$.

Second, we note that to constrain the behavior of $\tau_+/\tau_{-,\rm d}$ and $\tau_{\rm ff}$ in the dynamics-regulated regime, no extra runs are needed, and all the required information can be obtained directly from the simulation with $\epsilon_{\rm ff} = 0.01\%$ and $b = 1$, which has been already used in the previous section. This is because in the dynamics-regulated regime the gas distribution in the n–$\sigma_{\rm tot}$ plane is not affected by star formation and feedback, and thus we expect it to be the same as in the bottom left panel of Figure 5.4. Therefore, $f_{\rm sf}$—which yields $\tau_+/\tau_{-,\rm d}$ from Equation (5.8)—and $\tau_{\rm ff}$ as a function of the star formation threshold can be directly measured from this distribution. We spline $f_{\rm sf}(\alpha_{\rm vir,sf})$ and $\tau_{\rm ff}(\alpha_{\rm vir,sf})$ in the low-$\epsilon_{\rm ff}$ simulation with fiducial $\alpha_{\rm vir,sf}$ and show these functions with blue lines in the bottom two

panels of the middle column in Figure 5.3.

These two steps fix the dependencies of $(1+\xi)\tau_+$, $\tau_+/\tau_{-,\mathrm{d}}$, and τ_{ff} on the star formation threshold, and thus we can predict how τ, f_{sf}, and τ_{ff} depend on the threshold at different ϵ_{ff} and our predictions closely agree with the results of simulations, as shown in the middle column of panels in Figure 5.3. To test our model, we repeated the above steps for the simulations with the star formation threshold in the gas density rather than in α_{vir}. As the right column of Figure 5.3 shows, our predictions again closely agree with the results of the simulations, although the values of the parameters are of course different (see Appendix B.1).

5.2.3 Generic approach to calibrating the star formation and feedback parameters in simulations

Galaxy simulations can differ significantly in numerical methods used to handle hydrodynamics and in specific details of the implementation of star formation and feedback processes. The implementations can also be applied at different resolutions, so that the values and sometimes even the physical meaning of the parameters change. Thus, the parameter values of our model that we calibrated above should be used with caution and applied only when similar numerical techniques, resolutions, and implementations of star formation and feedback are used.

Nevertheless, the overall calibration approach can still be used in all cases to choose the values of the star formation and feedback parameters. For example, one can calibrate τ and f_{sf} dependence on the parameters in the dynamics-regulation regime using one simulation with a very low (or even zero) value of ϵ_{ff}, as was done in Section 5.2. Then, the τ and f_{sf} behavior in the self-regulation regime can be anchored using several simulations with varying feedback strength and star formation threshold at sufficiently high ϵ_{ff}. The value of ϵ_{ff} appropriate for this second step can be chosen from the condition that the local depletion

time at typical densities of the star-forming gas must be much shorter than the global depletion time, which thus implies $\epsilon_{\rm ff} \gg \tau_{\rm ff}/\tau$. The appropriately high value of $\epsilon_{\rm ff}$ will also result in $f_{\rm sf}$ much smaller than the $f_{\rm sf}$ in the simulation with low $\epsilon_{\rm ff}$.

5.3 Comparisons with observations

Results presented in the previous section demonstrate that our general theoretical framework for star formation in galaxies can describe and explain the results of galaxy simulations both qualitatively and quantitatively. The model can thus be also used to interpret and explain observational results, in particular the observed long gas depletion times in galaxies, as we showed in Chapter 4. In this section, we use the observations to constrain the parameters of our model, in particular, the efficiency of star formation per freefall time, $\epsilon_{\rm ff}$. We also use the model to infer whether observed galaxies are in the dynamics- or self-regulation regime.

Specifically, we use the observed values of the depletion time of atomic+molecular and just molecular gas at different scales—from global galactic values to the scales comparable to our resolution limit of ~ 40 pc—as well as the mass fraction of gas in star-forming regions and in the molecular phase. Comparisons and inferences from observations on different scales are presented in separate sections below. In most of the comparisons, we use observations in the Milky Way, where star formation is studied most extensively. However, whenever possible, we also use recent observations of other nearby galaxies. Note that we focus here on the inferences specific to $\sim L_\star$-sized galaxies, as our simulated galaxy model has structural parameters typical for such galaxies.

In what follows, we use the star formation rates in simulations computed differently on different scales, in ways that approximate how corresponding rates are estimated in observations. We compute the local SFR using the total mass of stellar particles younger than some age $t_{\rm sf}$ in the cell: $\dot{M}_\star^{\rm cell} \equiv M_\star^{\rm cell}(< t_{\rm sf})/t_{\rm sf}$, where the choice of $t_{\rm sf}$ is motivated by star formation indicators used in observations. In Sections 5.3.3 and 5.3.5, we compare

our results with extragalactic studies that use Hα and far IR indicators sensitive to the presence of massive young stars, and we thus adopt $t_{\rm sf} = 10$ Myr (see, e.g., Table 1 in Kennicutt & Evans, 2012). In Section 5.3.4 we compare with observations of individual star-forming regions, where SFR is estimated by direct counting of pre-main-sequence young stellar objects, and thus we adopt $t_{\rm sf} = 1$ Myr in this case. To compare our results with the observed distribution of molecular gas, we define molecular gas in our simulations as detailed in Section 3.4.

5.3.1 Global τ and $f_{\rm sf}$

We start our comparisons with observations by comparing our model and simulation predictions as a function of $\epsilon_{\rm ff}$ and the feedback strength b with the global values of the depletion time, τ, and the mass fraction of star-forming gas, $f_{\rm sf}$. To make a fair comparison, τ and $f_{\rm sf}$ in observations must be defined consistently with their definition in the simulations. While τ can be compared directly using the total gas mass and SFR, the comparison of $f_{\rm sf}$ is more nuanced, because one needs to choose which gas in real galaxies corresponds to the star-forming gas in simulations. Our fiducial star formation criterion, $\alpha_{\rm vir} < \alpha_{\rm vir,sf} = 10$, is motivated by $\alpha_{\rm vir}$ in observed GMCs, and it selects molecular gas with the lowest turbulent velocity dispersions on the scale of our resolution, $\Delta = 40$ pc. Such a criterion also results in the average freefall time in star-forming regions of $\tau_{\rm ff} \approx 3$–6 Myr, which is consistent with typical $\tau_{\rm ff}$ values estimated for observed GMCs (see, e.g., Figure 1 in Agertz & Kravtsov, 2015). In simulations with larger $\alpha_{\rm vir,sf}$, $\tau_{\rm ff}$ becomes several times longer than observed in GMCs (see the bottom middle panel of Figure 5.3). Thus, we argue that our fiducial value of $\alpha_{\rm vir} = 10$ corresponds to the definition of the star-forming regions in observations most closely, and we will use the simulations with this value to constrain $\epsilon_{\rm ff}$. We will, however, discuss the dependence on the assumed threshold below, whenever it is relevant.

To compare our model results, we use the global depletion time and the mass fraction

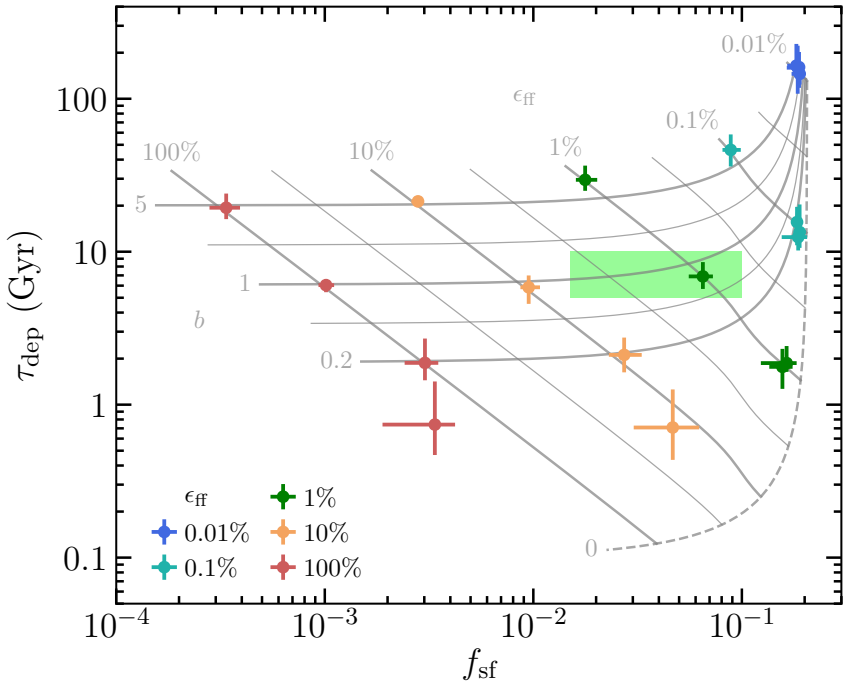

Figure 5.6: Comparison of our simulation results (points) and our model predictions (gray lines) for the star-forming mass fraction, $f_{\rm sf}$, and the global depletion time, τ, with their values in the Milky Way (green rectangle). Notation of points repeats that of Figure 5.3, with color indicating $\epsilon_{\rm ff}$ and the feedback boost factor, b, increasing upward: 0, 0.2, 1, and 5. Solid gray lines show the predictions of our model calibrated in Section 5.2.2 for the constant values of $0.2 < b < 5$ and $0.01\% < \epsilon_{\rm ff} < 100\%$, with thicker lines corresponding to the values used in the simulations and thinner lines showing intermediate values: $b \approx 0.45$ and 2.2 and $\epsilon_{\rm ff} \approx 0.032\%$, 0.32%, 3.2%, and 32%. The dashed line indicates model predictions for runs without feedback ($b = 0$), assuming $\tau_+ = 100$ Myr, as motivated by the results of Section 4.4. The green rectangle indicates the range estimated for the Milky Way, $f_{\rm sf} \sim 1.5\%$–10% and $\tau \sim 5$–10 Gyr, as explained in the text.

of the star-forming gas in the Milky Way, $\tau \sim 5$–10 Gyr and $f_{\rm sf} \sim 1.5\%$–10% estimated as follows. The range of τ follows from $M_{\rm g} \sim 10^{10}$ M$_\odot$ (e.g., Kalberla & Kerp, 2009) and $\dot{M}_\star \sim 1$–2 M$_\odot$ yr^{-1} (e.g., Licquia & Newman, 2015). The upper limit on the star-forming mass fraction follows from the assumption that all molecular gas in the Milky Way is star-forming, and thus $f_{\rm sf} < f_{\rm H_2} = M_{\rm H_2}/M_{\rm g} \sim (10^9\ {\rm M}_\odot)/(10^{10}\ {\rm M}_\odot) \sim 10\%$ (Heyer & Dame, 2015). A conservative lower limit on $f_{\rm sf}$ can be estimated using the total mass in the largest star-forming GMCs in the Milky Way from Murray (2011), with sizes comparable to our resolution of 40 pc. These massive GMCs account for 33% of total SFR in the Milky Way but have a total mass of $\approx 5 \times 10^7$ M$_\odot$. If the rest of star formation in the Milky Way were proceeding in clouds with local depletion times similar to those in the Murray (2011) sample, then the total mass of the star-forming gas would be 3 times larger, or $\approx 1.5 \times 10^8$ M$_\odot$, which would mean $f_{\rm sf} \sim 1.5\%$. However, this estimate is a conservative lower limit because the rest of the star-forming gas probably forms stars with lower efficiency, as it does not host bright radio sources associated with H II regions, used by Murray (2011) to identify the star-forming GMCs.

In Figure 5.6, the above constraints on τ and $f_{\rm sf}$ in the Milky Way (green rectangle) are compared to the results of our simulations (points with error bars) and the predictions of our analytical model (gray lines). The figure shows that only $\epsilon_{\rm ff} \sim 0.5\%$–$5\%$ and $b \sim 0.3$–2 can satisfy the constraints on both τ and $f_{\rm sf}$ simultaneously. It is important to note that this constraint on $\epsilon_{\rm ff}$ is rather generous, due to the rather conservative lower limit estimate of $f_{\rm sf}$ we use for the Milky Way.

This conclusion would not change if we adopted a different star formation threshold. Figure 5.3 shows that $\alpha_{\rm vir,sf}$ values smaller than our fiducial $\alpha_{\rm vir,sf} = 10$ would result in even smaller $f_{\rm sf}$, while even values as large as $\alpha_{\rm vir,sf} = 100$ for $\epsilon_{\rm ff} = 100\%$ would only increase the star-forming gas mass fraction to $f_{\rm sf} \approx 0.7\%$, while decreasing the depletion time to $\tau \approx 2$ Gyr, which is still far outside the range we estimate for the Milky Way.

Note that the figure shows that τ and $f_{\rm sf}$ in the Milky Way have values close to the transition between self-regulation and dynamics-regulation regimes. Indeed, the self-regulation regime corresponds to small $f_{\rm sf} < 0.01$ at which gray lines of constant b are horizontal, the dynamics-regulation regime is manifested by the convergence of these lines to $f_{\rm sf} \sim 0.2$, and $f_{\rm sf}$ in the Milky Way lie in between these two regimes. The conclusion that the Milky Way is in the regime intermediate between dynamics- and self-regulation regimes is also directly supported by the estimate for the second term in Equation (5.5), $(1 + \tau_+/\tau_{-,{\rm d}})\tau_\star$. Indeed, observed local depletion times in the Milky Way's GMCs are $\tau_\star \sim 100 - 500$ Myr (e.g., Evans et al., 2009, 2014; Heiderman et al., 2010; Lada et al., 2010, 2012; Gutermuth et al., 2011; Schruba et al., 2017), and the prefactor in front of $\tau_\star$ is likely similar to that obtained in our simulations, $1 + \tau_+/\tau_{-,{\rm d}} \sim 5$ (Equation 5.14), because we expect that our simulations capture dynamical time scales of star-forming gas supply and dispersal. As a result, $(1 + \tau_+/\tau_{-,{\rm d}})\tau_\star \sim 0.5$–$2.5$ Gyr contributes a sizable fraction to the observed global depletion time in the Milky Way, $\tau_{\rm dep,MW} \sim 5$–10 Gyr, and thus the Milky Way is in the intermediate regime.

5.3.2 Global mass fraction and the depletion time of molecular gas

Figure 5.7 compares the global molecular gas mass fraction, $f_{\rm H_2}$, and its depletion time, $\tau_{\rm H_2}$, estimated for the Milky Way (green rectangle) with their values measured in our simulations (points with error bars) and predicted by our model (gray lines). For the Milky Way, we used $f_{\rm H_2} = (1.0 \pm 0.3) \times 10^9$ M$_\odot$ from Heyer & Dame (2015) and estimated $\tau_{\rm H_2} = (10^9$ M$_\odot)/(1$–2 M$_\odot$ yr$^{-1}) \sim 0.5$–1 Gyr. In the simulations, the total molecular mass, $M_{\rm H_2}$, required to compute $f_{\rm H_2}$ and $\tau_{\rm H_2}$ is derived as a sum of the molecular mass in each cell, computed as explained at the beginning of Section 5.3. The model predictions are obtained using the dependence of $f_{\rm H_2}$ on $\epsilon_{\rm ff}$ and the feedback strength, calibrated at the end of Appendix B.2. The definition of the molecular gas depletion time is $\tau_{\rm H_2} \equiv M_{\rm H_2}/\dot{M}_\star =$

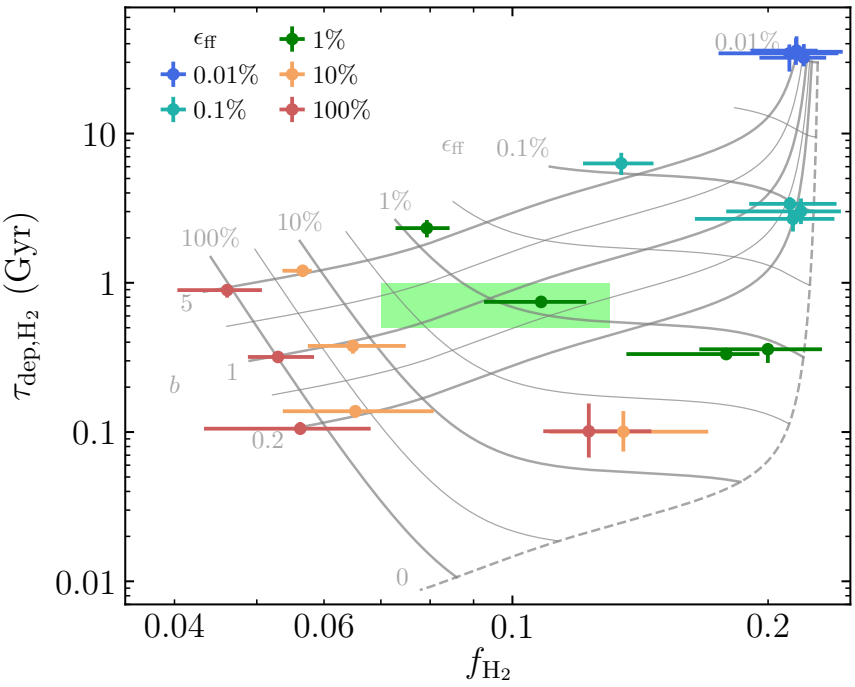

Figure 5.7: Comparison of the simulation results (points) and our model predictions (gray lines) with the total molecular mass fraction, $f_{\rm H_2}$, and the global depletion time of molecular gas, $\tau_{\rm H_2} = f_{\rm H_2}\tau$, in the Milky Way (green rectangle). The symbols and lines are the same as in Figure 5.6. Our model for $f_{\rm H_2}$ is explained in Appendix B.2. For the Milky Way, we adopt $f_{\rm H_2} = (1.0 \pm 0.3) \times 10^9$ M$_\odot$ (Heyer & Dame, 2015) and $\tau_{\rm H_2} = (10^9$ M$_\odot)/(1$–2 M$_\odot$ yr$^{-1}) \sim 0.5$–1 Gyr (e.g., Licquia & Newman, 2015).

$(M_{\rm H_2}/M_{\rm g})(M_{\rm g}/\dot{M}_\star) = f_{\rm H_2}\tau$, with τ given by Equation (5.5).

The figure shows that $f_{\rm H_2}$ and $\tau_{\rm H_2}$ within the observed range can be obtained only in the simulations with $\epsilon_{\rm ff} \sim 0.5\%$–$5\%$ and $b \sim 0.2$–3. Note that this range of parameters is similar to the range constrained by the observed $f_{\rm sf}$ and τ in the previous section. This consistency between different constraints indicates that in our simulations with $\epsilon_{\rm ff} \sim 1\%$ and $b \sim 1$ the overall distribution of the ISM gas in different phases is captured correctly.

Typical values of $f_{\rm H_2}$ estimated in other $L_\star$-sized galaxies are usually even larger than the Milky Way value (e.g., $\sim 10\%$–30% in Leroy et al., 2008). According to Figure 5.7, such $f_{\rm H_2}$, together with somewhat longer depletion times ($\tau_{\rm H_2} \sim 1$–3 Gyr in Bigiel et al., 2008, 2011; Leroy et al., 2013; Utomo et al., 2017), favors small values of $\epsilon_{\rm ff}$. Our model, calibrated on a specific simulation of an $L_\star$-sized galaxy, does not predict values $f_{\rm H_2} > 20\%$. However, according to our model, the values of $f_{\rm H_2} > 20\%$ observed in molecular-rich galaxies can be due to a smaller ratio of dynamical time scales $\tau_+/\tau_{-,\rm d}$ in such galaxies as compared to the value of $\tau_+/\tau_{-,\rm d} \sim 4$ in our simulated galaxy, which sets the upper limit of $f_{\rm H_2} \sim 20\%$ in the dynamics-regulation regime (Equation 5.8).

Figure 5.7 also illustrates three interesting differences in the behavior of $f_{\rm H_2}$ and $\tau_{\rm H_2}$ as compared to that of $f_{\rm sf}$ and τ in the previous section: (1) the range of $f_{\rm H_2}$ variation is substantially narrower than that of $f_{\rm sf}$; (2) in contrast to τ, $\tau_{\rm H_2}$ does depend on $\epsilon_{\rm ff}$ even in the self-regulation regime; and (3) the temporal variation of $\tau_{\rm H_2}$ (shown with vertical error bars) is much smaller than that of τ. The range of $f_{\rm H_2}$ variation is narrow because even at high $\epsilon_{\rm ff}$ and b feedback cannot efficiently clear the non-star-forming molecular gas that piles up above the star formation threshold. When τ is independent of $\epsilon_{\rm ff}$, the sensitivity of $\tau_{\rm H_2}$ to $\epsilon_{\rm ff}$ originates from the weak sensitivity of $f_{\rm H_2}$ to $\epsilon_{\rm ff}$, $\tau_{\rm H_2} = f_{\rm H_2}\tau$, and its temporal variation is small because $f_{\rm H_2}$ anticorrelates with $\tau_{\rm ff}$, as both respond to the dispersal of the dense gas by feedback, and this anticorrelation mitigates the variation of $\tau_{\rm H_2} \propto f_{\rm H_2}\tau_{\rm ff}$. Note that all these effects are due to the definition of the star-forming gas being different from

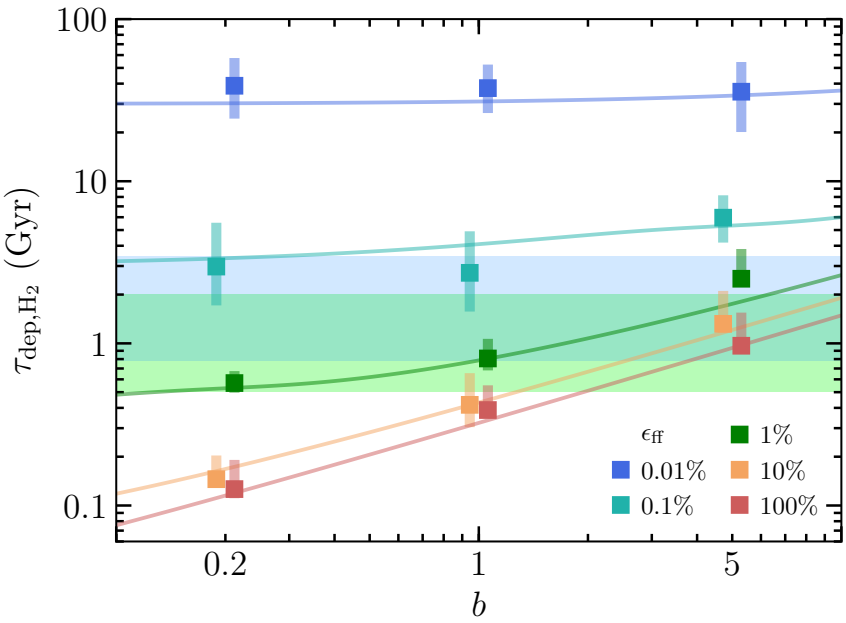

Figure 5.8: Comparison of the molecular gas depletion time, $\tau_{\rm H_2}$, averaged on kiloparsec scale in our simulations (squares with vertical bands), with the observed range shown with horizontal color bands. The blue band indicates the range of $\tau_{\rm H_2} \sim 1.6$ Gyr (excluding correction for helium) with a factor of 2 scatter, which was derived in a number of studies (Bigiel et al., 2008, 2011; Leroy et al., 2013; Bolatto et al., 2017; Utomo et al., 2017; Colombo et al., 2018). The green band indicates the range of kiloparsec scale $\tau_{\rm H_2}$ in the Milky Way, estimated from the profiles of $\Sigma_{\rm H_2}$ and $\Sigma_{\rm H_2}$ in Figure 7 in Kennicutt & Evans (2012). In simulations, $\tau_{\rm H_2}$ is averaged using 10 simulation snapshots between 410 and 500 Myr. Squares indicate the mass-weighted averages $\langle 1/\tau_{\rm H_2} \rangle^{-1}$, and vertical stripes show the range of the running median for gas with $\Sigma_{\rm H_2} > 1$ M$_\odot$ pc^{-2}. For presentation purposes, the simulation points are slightly shifted horizontally around the actually used values of $b = 0.2$, 1, and 5. Colored lines show the predictions of our model for the global depletion time of the molecular gas (see Sections 5.3.2).

the molecular gas and its corollary of the existence of the non-star-forming molecular gas.

5.3.3 Molecular gas depletion times on kiloparsec scales

Over the past two decades, star formation, the distribution of the molecular gas, and its depletion time $\tau_{\rm H_2} = \Sigma_{\rm H_2}/\dot{\Sigma}_\star$ have been studied observationally down to kiloparsec scales in dozens of nearby galaxies (e.g., Wong & Blitz, 2002; Bigiel et al., 2008, 2011; Leroy et al., 2013; Bolatto et al., 2017; Utomo et al., 2017). These observational studies show that

typical observed values of $\tau_{H_2} \sim 2$ Gyr have a factor of ~ 2 scatter and are independent of the local kiloparsec-scale molecular gas surface density, Σ_{H_2}. In the Milky Way, values of kiloparsec-scale τ_{H_2} are somewhat shorter and span a range of $\tau_{H_2} \sim 0.5$–2 Gyr (estimated from Figure 7 in Kennicutt & Evans, 2012).

In Figure 5.8, we compare these values of τ_{H_2} (colored bands) with the results of our simulations (squares with vertical stripes) and our model predictions (thin lines). As the figure shows, the results of our fiducial simulation with $\epsilon_{ff} = 1\%$ and $b = 1$ agree well with the typical values of τ_{H_2} inferred in observations. However, the simulations with, e.g., $\epsilon_{ff} \sim 100\%$ and $b \sim 5$ also agree with the observed range of τ_{H_2} because the dependence of τ_{H_2} on these parameters (and especially on ϵ_{ff}) is relatively weak. Similarly to the global star-forming gas and molecular gas mass fractions considered above in Section 5.3.2, the parameters will be constrained much better when estimates of the molecular gas fraction become available on subgalactic scales in more and more galaxies (e.g., Wong et al., 2013; Leroy et al., 2016, 2017).

To make the comparison presented in Figure 5.8, in the simulations we compute $\tau_{H_2} = \Sigma_{H_2}/\dot{\Sigma}_\star$, where Σ_{H_2} and $\dot{\Sigma}_\star$ are measured by first projecting the local densities of the molecular gas and SFR perpendicular to the disk plane and then smoothing the resulting surface densities using a Gaussian filter with a width of 1 kpc. Squares in Figure 5.8 show the mass-weighted averages $\langle 1/\tau_{H_2} \rangle^{-1}$ on a kiloparsec scale, which are equivalent to the global depletion times of the molecular gas,[4] and these averages are well approximated by our model (colored lines). A vertical band around each square indicates variation of the running median of τ_{H_2} in bins of Σ_{H_2} at surface densities of $\Sigma_{H_2} > 1\ M_\odot\ pc^{-2}$. This variation is rather small because our simulations produce constant τ_{H_2}, even though a density-dependent depletion time is adopted on subgrid scale: $\tau_\star \propto \tau_{ff} \propto \rho^{-0.5}$. Such independence of τ_{H_2} from Σ_{H_2} agrees with the observed constant τ_{H_2}, and its origin in our simulations is discussed

4. By definition, $\langle 1/\tau_{H_2} \rangle^{-1} \equiv [\int dA\ (\Sigma_{H_2}/\tau_{H_2}) / \int dA\ \Sigma_{H_2}]^{-1} = \int dA\ \Sigma_{H_2} / \int dA\ \dot{\Sigma}_\star = M_{H_2}/\dot{M}_\star$.

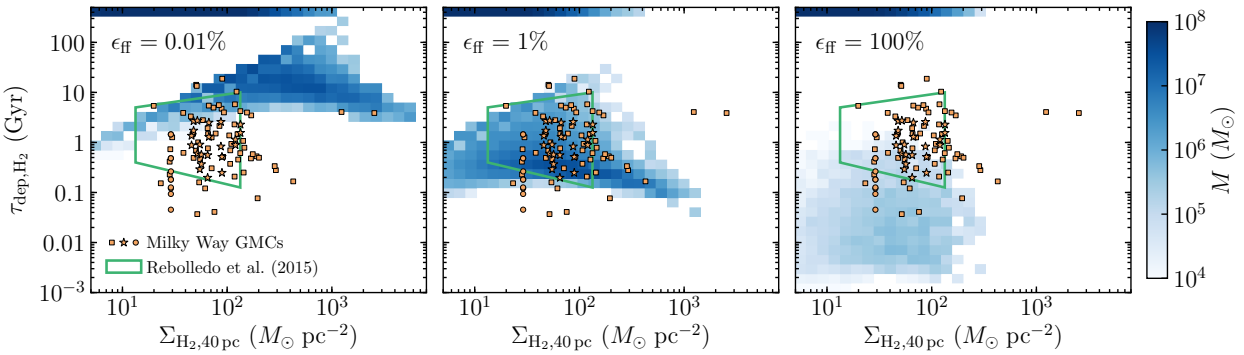

Figure 5.9: Comparison of the molecular gas depletion time and the gas surface densities on GMC scales with their distribution on the resolution scale in our simulations, $\Delta = 40$ pc. Adopted star formation efficiency increases from the left to the right: $\epsilon_{\rm ff} = 0.01\%$, 1%, and 100%. The color map shows the mass-weighted distribution of computational cells for which we define $\Sigma_{\rm H_2,40\,pc} = M^{\rm cell}_{\rm H_2}/\Delta^2$ with molecular mass in a cell, $M^{\rm cell}_{\rm H_2}$, computed using the model of Krumholz et al. (2009a, see the beginning of Section 5.3 above) and $\tau_{\rm H_2} = M^{\rm cell}_{\rm H_2}/\dot{M}^{\rm cell}_\star = M^{\rm cell}_{\rm H_2}/(M^{\rm cell}_\star(< 1\ {\rm Myr})/(1\ {\rm Myr}))$, where in each cell $M^{\rm cell}_\star(< 1\ {\rm Myr})$ is the total mass of stars younger than 1 Myr. Cells containing only a single stellar particle form the diagonal upper boundary of $\tau_{\rm H_2}$ distribution. Cells without young stellar particles are indicated by blue horizontal stripes on top of each axis. Orange points show the observed $\tau_{\rm H_2}$ in the Milky Way GMCs from Lada et al. (2010, circles), Heiderman et al. (2010, stars), and Vutisalchavakul et al. (2016, squares). A green polygon indicates the range of $\Sigma_{\rm H_2}$ and $\tau_{\rm H_2}$ observed in three nearby spiral galaxies by Rebolledo et al. (2015).

in Chapter 6. We also find that the scatter around the running median (not shown in the figure) is consistent with observations as well (see Figure 4.2).

5.3.4 Molecular gas depletion times on tens of parsec scales

Although current observations in most galaxies probe star formation and molecular gas only on scales $\gtrsim 1$ kpc, observations of star-forming regions in the Milky Way allow us to examine these quantities on smaller scales. Furthermore, scales of $\lesssim 100$ pc are increasingly probed in nearby galaxies (Bolatto et al., 2011; Rebolledo et al., 2015; Leroy et al., 2017), and this allows us to compare results of our simulations on these scales as well.

Figure 5.9 shows the variation of $\tau_{\rm H_2}$ in the Milky Way (points; Heiderman et al., 2010; Lada et al., 2010; Vutisalchavakul et al., 2016) and three nearby spiral galaxies (trapezoidal

region; Rebolledo et al., 2015) with the molecular gas depletion time on the scale of 40 pc in our simulations (blue color map) as a function of Σ_{H_2}. For this comparison we only show GMCs in the Milky Way that have sizes of $\gtrsim 10$ pc, to make the scales comparable to the scale probed in our simulations. Different panels show the distribution of the local depletion times in our simulations with different values of the star formation efficiency: $\epsilon_{\rm ff} = 0.01\%$, 1%, and 100%.

As the figure shows, although the observed τ_{H_2} vary substantially, their typical values can be reproduced only in runs with $\epsilon_{\rm ff} \sim 1\%$, while runs with too low (high) $\epsilon_{\rm ff}$ significantly overestimate (underestimate) τ_{H_2} in star-forming regions. Note that in all runs the distribution of τ_{H_2} is bimodal: τ_{H_2} is either finite, which corresponds to star-forming gas, or infinitely long, i.e. the gas is non-star-forming. In the figure, τ_{H_2} in the latter case is artificially set to 500 Gyr for illustration purposes. Different runs differ by the fraction of the molecular gas in the star-forming state and by the average τ_{H_2} of such gas. The fraction of the star-forming gas is the lowest in the run with $\epsilon_{\rm ff} = 100\%$, and this gas has depletion times of only $\sim$ 2–200 Myr. These short depletion times of star-forming H_2 are averaged with large amounts of the non-star-forming molecular gas in this run, so that the depletion time on $\gtrsim 1$ kpc scales in the $\epsilon_{\rm ff} = 100\%$ case is only a factor of two shorter than in the $\epsilon_{\rm ff} = 1\%$ run. This shows that while τ_{H_2} on $\gtrsim 1$ kpc scales is relatively insensitive to $\epsilon_{\rm ff}$, its values on the scales of $\lesssim 100$ pc are quite sensitive to the efficiency and can thus be used to constrain it.

5.3.5 The scale dependence of molecular gas depletion times

Results of the previous two sections clearly show that the distribution of τ_{H_2} depends on the spatial scale. Indeed, τ_{H_2} in a given ISM patch results from averaging over a distribution of gas and stars inside the patch, and thus τ_{H_2} depends on the patch size, L: $\tau_{H_2}(L)$. The quantity that particularly strongly depends on the spatial scale is scatter: when the size

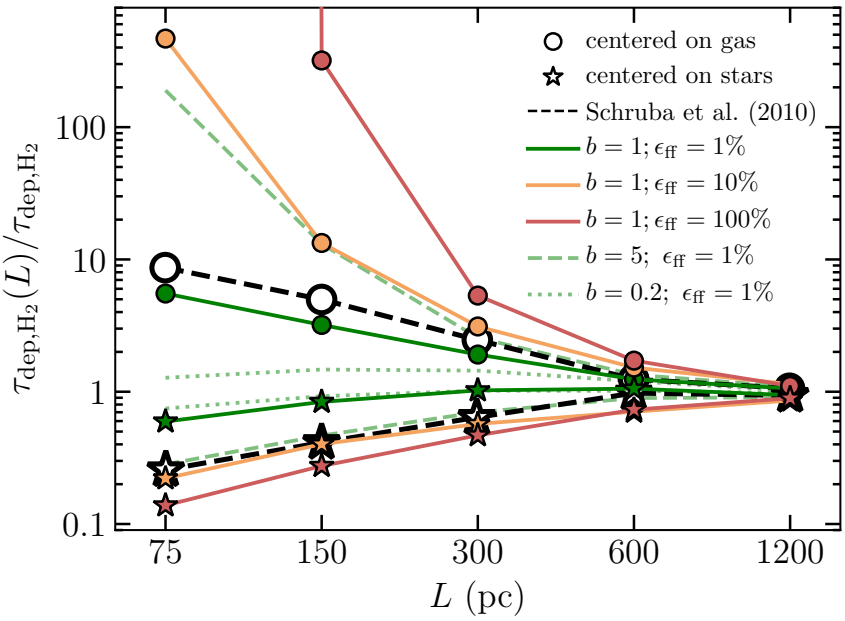

Figure 5.10: Effect of $\epsilon_{\rm ff}$ and the feedback boost factor, b, on the $\tau_{\rm H_2}$ bias as a function of the spatial smoothing scale, L. The depletion time in a given aperture of size L is defined as $\tau_{\rm H_2}(L) \equiv \Sigma_{\rm H_2,L}/\dot{\Sigma}_{\star,L}$, where $\Sigma_{\rm H_2,L}$ and $\dot{\Sigma}_{\star,L}$ are the molecular gas and the SFR surface densities smoothed using a Gaussian filter with a width L. Star symbols indicate the median depletion time measured in the apertures centered on peaks in $\dot{\Sigma}_\star$, while circles correspond to the apertures centered on peaks in $\Sigma_{\rm H_2}$. To factor out the variation of the global molecular gas depletion time with the feedback strength, we divide $\tau_{\rm H_2}(L)$ by global $\tau_{\rm H_2}$. Dashed lines show the results obtained for M33 by Schruba et al. (2010). To match the temporal averaging of the Hα indicator used by Schruba et al. (2010), we estimate $\dot{\Sigma}_\star$ using stars younger than 10 Myr.

of the patch decreases, patch-to-patch variation of gas and stars contained inside a patch becomes stronger, which leads to a stronger variation of the derived depletion time in each patch and thus larger scatter in $\tau_{\rm H_2}$.

Following Schruba et al. (2010), one of the ways to express the dependence of scatter on the spatial scale is to consider the scale dependence of the depletion time, $\tau_{\rm H_2}(L)$, measured in patches centered on the peaks of $\Sigma_{\rm H_2}$, which thus are biased to long $\tau_{\rm H_2}(L)$, versus those measured in patches centered on the peaks of $\dot{\Sigma}_\star$, which are biased to short $\tau_{\rm H_2}(L)$. The difference between these two estimates of $\tau_{\rm H_2}(L)$ is small on large scales, and their values are approximately equal to the global depletion time. At smaller scales, this difference increases, as shown in Figure 5.10, which compares $\tau_{\rm H_2}(L)$ observed in M33 by Schruba et al. (2010) with the results of our simulations.

In simulations, $\tau_{\rm H_2}(L)$ centered on gas or stars strongly depends on $\epsilon_{\rm ff}$ and the feedback boost factor b because stronger feedback-induced gas flux results in more expulsive evacuation of the gas from star-forming regions, which leads to a stronger spatial displacement of $\Sigma_{\rm H_2}$ and $\dot{\Sigma}_\star$ peaks. As Figure 5.10 shows, the fiducial run that satisfied all previous constraints also provides a reasonably good match to the observed $\tau_{\rm H_2}(L)$. Overall, for the fiducial feedback strength, both gas- and star-centered $\tau_{\rm H_2}(L)$ favors $\epsilon_{\rm ff} \lesssim 10\%$. Note, however, that there is a degeneracy between the feedback strength and $\epsilon_{\rm ff}$ value: the simulation with $\epsilon_{\rm ff} = 1\%$ and $b = 5$ produces a relation similar to the simulation with $\epsilon_{\rm ff} = 10\%$ and $b = 1$.

It is also worth noting that $\Sigma_{\rm H_2}$-centered $\tau_{\rm H_2}(L)$ is noticeably more sensitive to $\epsilon_{\rm ff}$ and b values. The sensitivity is stronger because at higher $\epsilon_{\rm ff}$ or b the gas lifetime in the star-forming state is shorter, young stars are more sporadic, and thus it is less probable for a given patch centered on a $\Sigma_{\rm H_2}$ peak to contain young stars. As a result, $\tau_{\rm H_2}(L)$ at high $\epsilon_{\rm ff}$ or b becomes highly biased to very large values. On the contrary, $\dot{\Sigma}_\star$-centered patches almost always contain molecular gas, because its abundance does not significantly decrease at stronger feedback (see Section 5.3.2). As a result, for $\dot{\Sigma}_\star$-centered patches, the bias also

increases with $\epsilon_{\rm ff}$ and b ($\tau_{\rm H_2}(L)$ becomes shorter), but this change is much milder than for $\Sigma_{\rm H_2}$-centered patches.

Such strong dependence of $\Sigma_{\rm H_2}$-centered $\tau_{\rm H_2}(L)$ on star formation and feedback parameters can provide tight constraints on these parameters. These constraints can be improved significantly if the scale dependence of $\tau_{\rm H_2}$ is measured in a larger sample of galaxies. Note, however, that more comprehensive comparison must include the effects of the intrinsic variation of $\epsilon_{\rm ff}$ and the metallicity dependence of the molecular gas fraction on GMC scale, which are not accounted for in our simulations.

5.4 Comparison with previous studies

In previous sections, we showed that our simple theoretical framework presented in Chapter 2 explains how local star formation and feedback parameters affect the global star formation in our $L_\star$-sized galaxy simulations, both qualitatively and quantitatively. Here we illustrate how our framework can also explain the results of other recent galaxy simulations done with different numerical methods and implementations of star formation and feedback, both in isolated setups and in the cosmological context. Specifically, we will use our model to interpret trends (or lack thereof) of the depletion times with the local star formation efficiency, $\epsilon_{\rm ff}$, the feedback strength, and the adopted star formation thresholds.

For example, our framework predicts that in the simulations that adopt high $\epsilon_{\rm ff}$ values and implement efficient feedback the depletion time is almost completely insensitive to the value of $\epsilon_{\rm ff}$. This is because in this regime τ is controlled by the time that gas spends in the non-star-forming state, which does not depend on $\epsilon_{\rm ff}$ explicitly. This explains why τ is insensitive to the variation of $\epsilon_{\rm ff}$ in the simulations of Hopkins et al. (2017a); this behavior is also reproduced in our simulations (see Figures 5.1 and 5.3 above). In this regime, our framework also predicts a nearly linear scaling of τ with the feedback strength parameter ξ, as is indeed observed in simulations (Benincasa et al., 2016; Hopkins et al., 2017a; Orr et al.,

2018).

For smaller values of $\epsilon_{\rm ff} \approx 1$–$10\%$, when the two terms in Equation (5.5) contribute comparably to the total depletion time, the model predicts that τ should scale with $\epsilon_{\rm ff}$ weakly (sublinearly). This was indeed observed in a number of simulations carried out in this regime (Saitoh et al., 2008; Dobbs et al., 2011a; Agertz et al., 2013, 2015; Benincasa et al., 2016). In this case, sublinear scaling is also expected with the strength of feedback, ξ, which is also confirmed by simulations (Hopkins et al., 2011; Agertz et al., 2013, 2015; Benincasa et al., 2016).

For simulations with $\epsilon_{\rm ff} \lesssim 1\%$ or when the feedback implementation is inefficient, $\xi \ll 1$, our model predicts that the depletion time is controlled by the second term in Equation (5.5) and that it scales inversely with $\epsilon_{\rm ff}$: $\tau \sim \epsilon_{\rm ff}^{-1}$. Such scaling was observed in the simulations without feedback by Agertz et al. (2013, 2015), while in the simulations using the same galaxy model but with efficient feedback, τ was found to be only weakly dependent on $\epsilon_{\rm ff}$.

The weak dependence or complete insensitivity of τ to $\epsilon_{\rm ff}$ at intermediate and high $\epsilon_{\rm ff}$ explains why different galaxy simulations with widely different $\epsilon_{\rm ff} \sim 1\%$–$100\%$ all produce realistic global depletion times. However, as our results of Section 5.3 show, these simulations make drastically different predictions for the star-forming and molecular gas mass fractions, which can be used to constrain $\epsilon_{\rm ff}$ in this regime (see Sections 5.3.1 and 5.3.2). A similar idea was reported previously by Hopkins et al. (2012, 2013b), who showed that the fraction of gas in the dense molecular state with $n > 10^4$ cm^{-3} strongly depends on the local efficiency $\epsilon_{\rm ff}$ and the feedback implementation. Specifically, simulations with high $\epsilon_{\rm ff}$ and efficient feedback have a small dense gas mass fraction owing to efficient conversion of dense gas into stars and its dispersal by feedback. This effect can explain why in the simulations with $\epsilon_{\rm ff} = 100\%$ reported by Orr et al. (2018) the Kennicutt–Schmidt relation between the surface densities of SFR and dense and cold gas ($n > 10$ cm^{-3} and $T < 300$ K) is considerably higher than the observed relation for molecular gas. In these simulations, the SFR is likely realistic

because the depletion time of the total gas is expected to be insensitive to $\epsilon_{\rm ff}$. The dense gas fraction, on the contrary, is expected to be small, which leads to the small surface density of such gas and thus high Kennicutt–Schmidt relation as in Orr et al. (2018).

Our model also predicts that τ depends on the star formation threshold differently in different regimes. For low $\epsilon_{\rm ff}$, τ only weakly depends on the threshold value, while at high $\epsilon_{\rm ff}$, τ decreases when the threshold encompasses more gas from a given distribution (see top middle and left panels in Figure 5.3). The former weak trend agrees with the results of Saitoh et al. (2008), who found that for $\epsilon_{\rm ff} \sim 1.5\%$ the value of τ decreased only by a factor of $\sim$ 1.5–2 when the density threshold was varied from $n_{\rm sf} = 100$ to 0.1 cm^{-3}. Similarly, Hopkins et al. (2011) and Benincasa et al. (2016) found almost no dependence of τ on $n_{\rm sf}$. On the contrary, in simulations of Agertz et al. (2015) with $\epsilon_{\rm ff} = 10\%$, τ varied relatively strongly with variation of $n_{\rm sf}$, as expected for high $\epsilon_{\rm ff}$. We note that to observe the effect on τ when a combination of thresholds in different physical variables is used, all thresholds must be varied simultaneously. Varying thresholds one by one may not affect τ if several thresholds define approximately the same gas as star-forming. This is likely why Hopkins et al. (2017a) found that τ is insensitive to variation of star formation thresholds, when thresholds in different variables were changed.

5.5 Summary

Using a simple physical model presented in Chapter 2 and a suite of $L_\star$-sized galaxy simulations, we explored how the global depletion times in galaxies, $\tau = M_{\rm g}/\dot{M}_\star$, and the gas mass fractions in the star-forming and molecular states depend on the choices of the parameters of local star formation and feedback.

In our model, τ is expressed as a sum of contributions from different physical processes, which include dynamical processes in the ISM, the conversion of gas into stars in star-forming regions, and the dispersal of such regions by stellar feedback. Some of these processes

explicitly depend on the parameters of the *local* star formation and feedback model, such as a star formation efficiency per freefall time, $\epsilon_{\rm ff}$, and a feedback boost factor, b. Others do not have such explicit dependence and may be affected by these parameters only indirectly. This leads to two distinct regimes, in which terms with and without such explicit dependence dominate.

We demonstrated these regimes in a suite of $L_\star$-sized galaxy simulations, in which we systematically varied $\epsilon_{\rm ff}$, b, and the thresholds used to define the star-forming gas. We also showed that the trends of τ and the star-forming gas mass fraction exhibited in the simulations can be reproduced by our model both qualitatively and quantitatively after a minimal calibration of the model parameters. The main results of our simulations and the predictions of our model can be summarized as follows:

1. When $\epsilon_{\rm ff}$ or b are large, the contribution of processes without explicit dependence on $\epsilon_{\rm ff}$ dominates and τ is insensitive to $\epsilon_{\rm ff}$, which is usually referred to as "self-regulation" in the literature. However, in this regime, the mass fractions of the star-forming ($f_{\rm sf}$) and the molecular ($f_{\rm H_2}$) gas *do* depend sensitively on $\epsilon_{\rm ff}$ and τ scales almost linearly with the feedback strength factor for $b \gtrsim 1$.

2. Conversely, when $\epsilon_{\rm ff}$ or b are sufficiently small, τ is dominated by the processes that explicitly depend on the local gas depletion time, $t_\star = t_{\rm ff}/\epsilon_{\rm ff}$ in Equation (3.2), and thus on $\epsilon_{\rm ff}$, but not on the feedback strength. In this case, the model predicts $\tau \propto \epsilon_{\rm ff}^{-1}$ and only weak dependence of $f_{\rm sf}$ and $f_{\rm H_2}$ on $\epsilon_{\rm ff}$, the behavior confirmed by our simulations.

3. The star formation threshold controls the mass fraction of the star-forming gas, the extent of star-forming regions, and their average properties, such as the average freefall time. We find that when $\epsilon_{\rm ff}$ is small and the threshold is such that only a small fraction of the ISM gas is star-forming, τ and $f_{\rm sf}$ are sensitive to the threshold value.

4. When $\epsilon_{\rm ff}$ is large or feedback is efficient (i.e., when the first term in Equation 5.5

dominates), $f_{\rm sf}$ is small and most of the star-forming gas has density or virial parameter close to the star formation threshold. In this case global star formation and the molecular mass fraction, $f_{\rm H_2}$, become sensitive to the value of the threshold.

The dependence of global star-forming properties of galaxies on the parameters of the local star formation and feedback model can be used to constrain the values of these parameters using observations of global galaxy properties. For example, the global depletion times of the total and molecular gas constrain the feedback strength but cannot constrain the value of $\epsilon_{\rm ff}$ owing to their weak dependence on this parameter. However, the value of $\epsilon_{\rm ff}$ can be constrained using the mass fraction of gas in the star-forming or molecular state. In addition, we showed that $\epsilon_{\rm ff}$ can be constrained using the distribution of local depletion times in star-forming regions and measurements of $\tau_{\rm H_2}$ for gas patches of different sizes centered on the peaks of the molecular gas surface density.

Using our simulation suite, we demonstrated that it is possible to find a combination of the local star formation and feedback parameters that satisfies all of these observational constraints. Our fiducial run with $\epsilon_{\rm ff} = 1\%$, the fiducial feedback boost $b = 1$, and the star formation threshold based on the virial parameter, $\alpha_{\rm vir} < \alpha_{\rm vir,sf} = 10$, is able to match all considered observations reasonably well. The low values of $\epsilon_{\rm ff} \sim 1\%$ are also consistent with previous inferences (e.g., Krumholz et al., 2012a, and references therein). We admit that the obtained constraints on $\epsilon_{\rm ff}$ and other parameters are specific to the scales close to our resolution, i.e. ~ 40 pc, and an additional study is required to explore the scale dependence of these constraints on smaller spatial scales. We note, however, that the observed depletion times in GMCs on parsec scales also favor $\epsilon_{\rm ff} \sim 1\%$–$10\%$ (e.g., Heiderman et al., 2010; Gutermuth et al., 2011), while simulations with a few parsec resolution adopting higher $\epsilon_{\rm ff}$ seem to underpredict the amount of dense star-forming gas (see the end of Section 5.4).

We also showed that our model explains the results of a number of recent studies that explored the effects of the local star formation and feedback model on the global properties

of simulated galaxies. This broad consistency confirms that our model accurately describes the origin of global star-forming properties in galaxy simulations and thus allows us to understand the role played by gas dynamics, star formation, and feedback in shaping these properties. Understanding the role of these processes in simulations also sheds light on their role in real galaxies, which is an essential step toward understanding how real galaxies form and evolve.

CHAPTER 6

THE SLOPE OF THE MOLECULAR KENNICUTT–SCHMIDT RELATION

One of the most intriguing results of our simulations is the emergence of the linear $\dot{\Sigma}_\star$–$\Sigma_{\rm H_2}$ relation consistent with observations (see the right panel of Figure 4.2), even though on small scales the star formation rate is assumed to scale nonlinearly with the gas density: $\dot{\rho}_\star = \epsilon_{\rm ff}\rho/t_{\rm ff} \propto \rho^{1.5}$. Moreover, as we will show, in our simulations with a star formation threshold in virial parameter, the relation on kiloparsec scales remains near-linear when we vary the slope adopted locally (β in Equation 3.4). This insensitivity is a counterexample to the argument that in simulations, the KSR on kiloparsec scales simply reflects the relation assumed at the resolution scale (Schaye & Dalla Vecchia, 2008; Gnedin et al., 2014). We show instead that the linear slope of the molecular KSR on kiloparsec scales and its insensitivity to small-scale star formation parameters is a result of self-regulation by stellar feedback. We will also show that the choice of the star formation threshold has a strong effect on the slope of the $\dot{\Sigma}_\star$–$\Sigma_{\rm H_2}$ relation. As we will also discuss, these results can be explained using the analytic framework of Chapter 2.

This chapter is organized as follows. In Section 6.1, we demonstrate how the molecular KSR obtained in our simulations changes depending on the parameters of star formation and feedback. In Section 6.2, we show how the obtained results relate to the gas PDF in ISM patches and its scaling with gas surface density. In Section 6.3, we use our analytic model based on ISM gas cycling to explain our results and elucidate the origin of the linear slope of molecular KSR. In Section 6.4, we compare our model to previous works and discuss its implications for the KSR derived in observations and simulations of galaxies. In Section 6.5, we summarize our results and conclusions.

This chapter is based on the work published in Semenov et al. (2019).

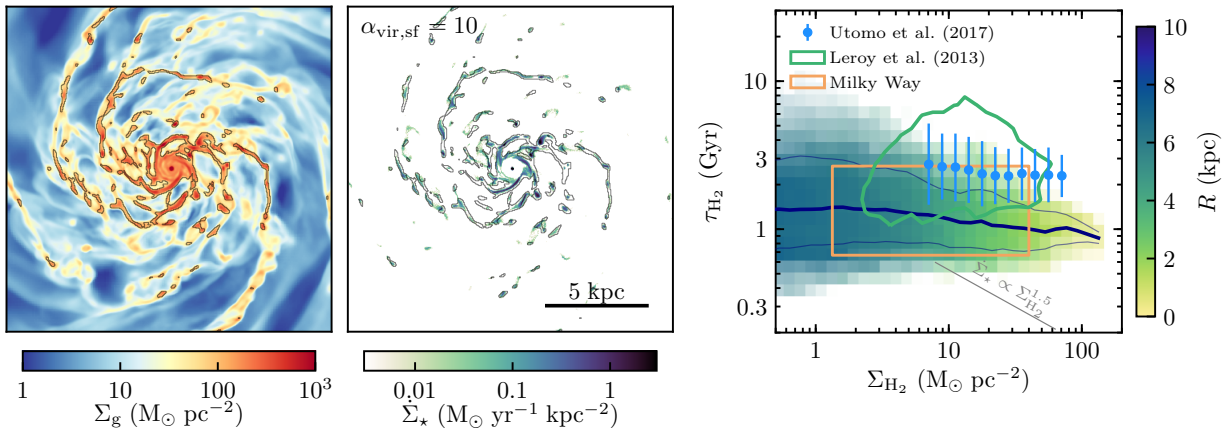

Figure 6.1: Results of our fiducial simulation with the star formation threshold in virial parameter, $\alpha_{\rm vir} < \alpha_{\rm vir,sf} = 10$. The depletion time of molecular gas is almost independent of $\Sigma_{\rm H_2}$ and thus the molecular KSR is almost linear in this simulation. The two face-on maps on the left show the surface densities of total gas, $\Sigma_{\rm g}$, and SFR, $\dot{\Sigma}_\star$. SFR is averaged over 10 Myr as explained in Section 3.4. The surface density of molecular gas, $\Sigma_{\rm H_2}$, is computed using the Krumholz et al. (2008) model (see Section 3.4), and the gray contours indicate regions where $\Sigma_{\rm H_2}/\Sigma_{\rm g} > 30\%$. The right panel shows the depletion time of molecular gas, $\tau_{\rm H_2} = \Sigma_{\rm H_2}/\dot{\Sigma}_\star$, averaged on 1 kpc scale as a function of $\Sigma_{\rm H_2}$. The distribution is averaged over 11 snapshots between 500 and 600 Myr and is colored according to the average galactocentric radius R. Dark blue lines show the running median (thick line) and 16$^{\rm th}$ and 84$^{\rm th}$ percentiles (thin lines). Blue points show the running median in the EDGE-CALIFA sample of galaxies from Utomo et al. (2017). The green contour shows 68% of points from Leroy et al. (2013); the median of this sample is very similar to Utomo et al. (2017), and therefore, it is not shown here. The orange rectangle shows $\tau_{\rm H_2} \sim 0.7$–2.7 Gyr estimated for the Milky Way using $\dot{M}_\star \sim 1$ M$_\odot$ yr^{-1} and $M_{\rm H_2} \sim 10^9$ M$_\odot$ (before correction for helium; Heyer & Dame, 2015) and adopting a factor of 2 uncertainty in $\tau_{\rm H_2}$ (Figure 7 in Kennicutt & Evans, 2012).

6.1 Molecular KSR in simulations

Figure 6.1 shows the results of our fiducial simulation with the star formation threshold in gas virial parameter, $\alpha_{\rm vir} < \alpha_{\rm vir,sf} = 10$, $\epsilon_{\rm ff} = 1\%$, and $\beta = 1.5$ in Equation (3.4). The left two panels show the surface densities of total gas, $\Sigma_{\rm g}$, and SFR, $\dot{\Sigma}_\star$. The surface density of molecular gas, $\Sigma_{\rm H_2}$, reflects the distribution of dense gas and, for reference, the gray contours indicate the regions where the molecular gas fraction is larger than 30%. The right panel shows the depletion time of molecular gas, $\tau_{\rm H_2} = \Sigma_{\rm H_2}/\dot{\Sigma}_\star$, as a function of $\Sigma_{\rm H_2}$ where both $\dot{\Sigma}_\star$ and $\Sigma_{\rm H_2}$ are averaged on 1 kpc scale using a 2D Gaussian filter with a width of 1 kpc.

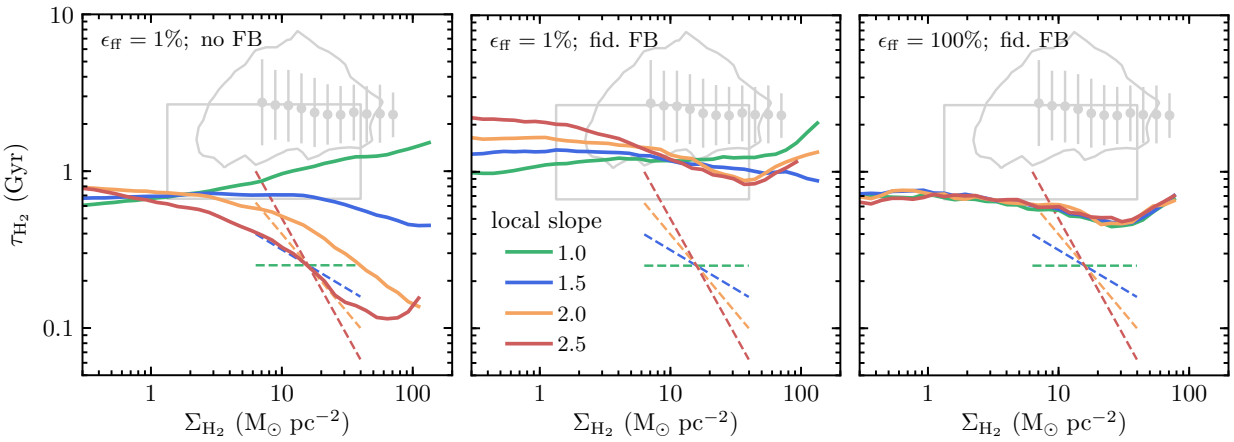

Figure 6.2: Dependence of the molecular KSR in simulations with $\alpha_{\rm vir,sf} = 10$ threshold on the slope of the local star formation relation: $\dot{\rho}_\star \propto \rho^\beta$, where β is varied from 1.0 to 2.5 (see Equation 3.4). The adopted slopes are indicated by dashed lines, which show the scaling of the local depletion time, $\rho/\dot{\rho}_\star \propto \rho^{1-\beta}$. Three panels show simulations with different $\epsilon_{\rm ff}$ values and feedback strengths per supernova, with the total feedback budget per local freefall time increasing from left to right. In simulations without feedback (left panel), the median $\tau_{\rm H_2}(\Sigma_{\rm H_2})$ on kiloparsec scales (thick lines) depends on the local slope. As the feedback budget increases, the sensitivity to the local slope becomes weaker in our fiducial simulation (middle panel) and completely disappears in simulations with 100 times larger local $\epsilon_{\rm ff}$ (right panel). Remarkably, in the latter regime of very efficient feedback, $\tau_{\rm H_2}$ becomes almost independent of $\Sigma_{\rm H_2}$ as observed in real galaxies (gray contours and error bars; see the legend in the right panel of Figure 6.1).

The figure shows that $\tau_{\rm H_2}$ in our fiducial simulation is almost independent of $\Sigma_{\rm H_2}$ and thus the molecular KSR is almost linear, $\dot{\Sigma}_\star \propto \Sigma_{\rm H_2}$, in agreement with the molecular KSR of observed galaxies at similar $\Sigma_{\rm H_2}$. This nearly linear slope is not imposed by the choice of our star formation prescription and its parameters. Instead, the near-linear slope emerges from a significantly steeper local star formation relation, $\dot{\rho}_\star = \epsilon_{\rm ff}\,\rho/t_{\rm ff} \propto \rho^{1.5}$. If the molecular KSR reflected this small-scale slope, it would have the slope shown by the thin gray line in the right panel, which is clearly much steeper than the slope we measure.

To stress this point, in the middle panel of Figure 6.2 we show that the $\dot{\Sigma}_\star$–$\Sigma_{\rm H_2}$ relation remains close to linear even when the local SFR is assumed to have a steeper dependence on gas density: $\dot{\rho}_\star \propto \rho^2$ and $\propto \rho^{2.5}$. Such weak sensitivity of the $\dot{\Sigma}_\star$–$\Sigma_{\rm H_2}$ slope to its local value provides a counter-example to the argument that the KSR on $\sim$kpc scales simply reflects the local star formation relation (Schaye & Dalla Vecchia, 2008; Gnedin et al., 2014) and demonstrates that the KSR slope can be nearly independent of the slope of the local relation.

The left and right panels of Figure 6.2 show that the emergence of the linear KSR slope and its independence of the local star formation relation depend on the efficiency of star formation and the corresponding efficacy of stellar feedback. Indeed, in simulations without feedback (left panel), the molecular KSR slope on kiloparsec scale becomes quite sensitive to the assumed local slope β. On the other hand, in simulations with $\epsilon_{\rm ff} = 100\%$ where feedback is very efficient (right panel), kiloparsec-scale molecular KSR becomes completely insensitive to the local star formation relation, and its slope stays close to linear. We have also checked that the relation remains linear when we increase feedback momentum input per supernova instead of increasing $\epsilon_{\rm ff}$ (Appendix C.1) and when we continuously vary $\epsilon_{\rm ff}$ with $\alpha_{\rm vir}$ instead of using a sharp threshold (Appendix C.2). We also find that the slope remains linear as long as the molecular KSR is averaged on $\gtrsim 500$ pc scales (see Appendix C.3).

Apart from feedback, the choice of star formation threshold also plays a crucial role in shaping the kiloparsec-scale molecular KSR. For example, Figure 6.3 shows that when we

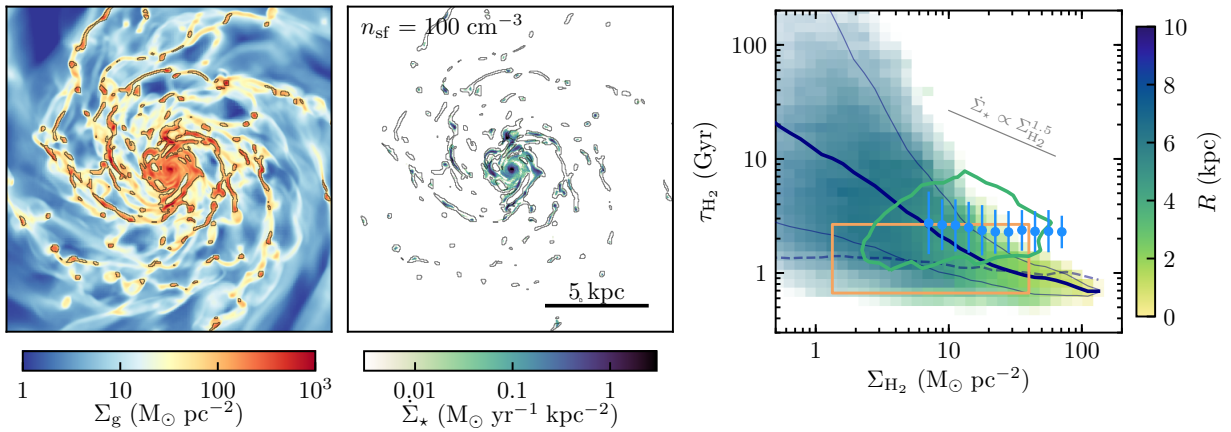

Figure 6.3: Same as Figure 6.1 but for a star formation threshold in gas density: $n > n_{\rm sf} = 100$ cm^{-3}. The dashed line in the right panel shows the median $\tau_{\rm H_2}$ from Figure 6.1. For a density threshold, the molecular KSR becomes significantly steeper than in the simulation with an $\alpha_{\rm vir}$-based threshold.

choose a threshold in density, $n > n_{\rm sf} = 100$ cm^{-3}, instead of the $\alpha_{\rm vir}$, the molecular KSR significantly steepens to $\dot{\Sigma}_\star \propto \Sigma_{\rm H_2}^{1.5}$ at $\Sigma_{\rm H_2} > 10$ M$_\odot$ pc^{-2} (galactocentric radii of $R < 6$ kpc) and to even steeper slope at $\Sigma_{\rm H_2} < 10$ M$_\odot$ pc^{-2} ($R > 6$ kpc). A similar steep molecular KSR was also found by Capelo et al. (2018), who also used the $n_{\rm sf} = 100$ cm^{-3} star formation threshold. In addition, we find that the slope steepens for larger values of $\epsilon_{\rm ff}$ and larger values of the $n_{\rm sf}$ threshold (see Appendix C.1). In other words, the emergence of the linear KSR and its insensitivity to local star formation parameters occur only when we use the $\alpha_{\rm vir}$-based threshold.

The qualitatively different behavior of the molecular KSR in simulations with $\alpha_{\rm vir}$- and $n_{\rm sf}$-based thresholds stems from different distributions of star-forming gas in simulations with different thresholds, which is evident from the $\dot{\Sigma}_\star$ maps in Figures 6.1 and 6.3. In the simulation with the constant $n_{\rm sf}$ threshold, the SFR is more centrally concentrated, and a significant fraction of molecular gas in the outskirts of the disk is not forming stars. This results in longer depletion times at large radii and steeper $\dot{\Sigma}_\star$–$\Sigma_{\rm H_2}$ relation.

The results presented above demonstrate that the slope of the molecular KSR has a nontrivial origin and is shaped by several factors. To understand the trends of the slope

with the choice of star formation threshold, $\epsilon_{\rm ff}$ value, and feedback strength, we will first examine our results from a different angle using the language of the PDF of gas properties (next Section). We will then discuss how our simulation results can be understood in the simple physical framework that we developed to explain the long gas depletion times of galaxies (Section 6.3).

6.2 Connecting the kiloparsec-scale KSR with gas PDF and star formation relation on small scales

Before we proceed to discuss the physical interpretation of the simulation results presented above, we will examine how kiloparsec-scale KSR is connected to the local SFR and PDF of gas properties. This connection not only clearly illustrates the interdependencies of different quantities via explicit equations but also elucidates the conditions required for the linearity of the molecular KSR. To this end, we will consider the depletion time of gas in star-forming regions, $\tau_\star = \Sigma_{\rm sf}/\dot{\Sigma}_\star$, and the mass fraction of molecular gas in these regions, $f_{\rm sf,H_2} = \Sigma_{\rm sf}/\Sigma_{\rm H_2}$, as it is the ratio of these quantities that defines the global depletion time of molecular gas:

$$\tau_{\rm H_2} = \frac{\Sigma_{\rm H_2}}{\dot{\Sigma}_\star} = \frac{\Sigma_{\rm H_2}}{\Sigma_{\rm sf}} \frac{\Sigma_{\rm sf}}{\dot{\Sigma}_\star} = \frac{\tau_\star}{f_{\rm sf,H_2}}. \tag{6.1}$$

The results presented in this section do not explain the simulation results presented above, but rather restate these results in a different useful way. Readers more interested in the physical interpretation of the results can proceed to Section 6.3. A detailed derivation of the equations used below is presented in the Appendix C.4.

6.2.1 Molecular Depletion Time and PDF of Gas Properties

To quantify the relation between molecular gas depletion time and gas PDF, we note that both $f_{\rm sf,H_2}$ and $\tau_\star$ in Equation (6.1) are the averages over the distribution of gas in the ISM patches. In particular, $f_{\rm sf,H_2}$ can be expressed in terms of the PDF of molecular gas, $P_{\rm H_2}$:

$$f_{\rm sf,H_2} = \iint_0^\infty \Theta_{\rm sf}(\rho,\mathbf{q}) P_{\rm H_2}(\rho,\mathbf{q}|\Sigma_{\rm H_2}) d\rho d\mathbf{q}, \tag{6.2}$$

where the star formation threshold, $\Theta_{\rm sf}(\rho,\mathbf{q})$, can depend on the density, ρ, and any other local properties of the region, $\mathbf{q}$, such as temperature, turbulent velocity, etc. For our choice of thresholds, $\Theta_{\rm sf}(\rho,\sigma) = \theta(\alpha_{\rm vir,sf} - \alpha_{\rm vir}(\rho,\sigma))$ and $\Theta_{\rm sf}(\rho) = \theta(\rho - \rho_{\rm sf})$, where θ is the Heaviside step function: $\theta(x) = 1$ for $x > 0$ and $\theta(x) = 0$ for $x < 0$.[1] $P_{\rm H_2}(\rho,\mathbf{q}|\Sigma_{\rm H_2})$ in the above equation is the mass-weighted PDF of the molecular gas averaged between patches with surface density $\Sigma_{\rm H_2}$; the PDF shape in general will depend on $\Sigma_{\rm H_2}$.

Similarly, $\tau_\star$ can be written as

$$\frac{1}{\tau_\star} = \int_0^\infty \frac{1}{t_\star} P_{\rm sf}(\rho|\Sigma_{\rm H_2}) d\rho \propto \int_0^\infty \rho^{\beta-1} P_{\rm sf}(\rho|\Sigma_{\rm H_2}) d\rho, \tag{6.3}$$

where $t_\star = \rho/\dot{\rho}_\star \propto \rho^{1-\beta}$ is the local depletion time,[2] and the mass-weighted density PDF of star-forming gas is defined as

$$P_{\rm sf}(\rho|\Sigma_{\rm H_2}) = \frac{\int \Theta_{\rm sf}(\rho,\mathbf{q}) P_{\rm H_2}(\rho,\mathbf{q}|\Sigma_{\rm H_2}) d\mathbf{q}}{\iint_0^\infty \Theta_{\rm sf}(\rho,\mathbf{q}) P_{\rm H_2}(\rho,\mathbf{q}|\Sigma_{\rm H_2}) d\rho d\mathbf{q}}. \tag{6.4}$$

First, note that the dependencies of $f_{\rm sf,H_2}$ and $\tau_\star$ on $\Sigma_{\rm H_2}$ in Equations (6.2) and (6.3) are rather nontrivial. To obtain a linear KSR, these dependencies must be similar and cancel out

1. In general, $\Theta_{\rm sf}$ can also parameterize smooth transitions to the star-forming state by continuously changing between 0 and 1.

2. The averaging of inverse $t_\star$ results from the averaging of local star formation rates $\dot{\rho}_\star = \rho/t_\star$: $\tau_\star^{-1} = \dot{\Sigma}_\star/\Sigma_{\rm sf} = \int t_\star^{-1} \rho dV / \int \rho dV = \langle t_\star^{-1} \rangle_{\rm sf}$, where the integrals are taken over star-forming regions in an ISM patch.

in Equation (6.1), which means that the gas PDF must scale with $\Sigma_{\rm H_2}$ in a very particular way. Second, the observed independence from the local slope β in simulations with efficient feedback implies that the trends of $f_{\rm sf,H_2}$ and $\tau_\star$ must remain similar when β is changed. This effect is also nontrivial because $\tau_\star$ depends on β explicitly (Equation 6.3), while $f_{\rm sf,H_2}$ depends on β only implicitly via the effect of β on the gas PDF. Finally, Equations (6.2–6.4) show that $f_{\rm sf,H_2}$ and $\tau_\star$ explicitly depend on the shape of the star formation threshold, $\Theta_{\rm sf}$. This means that, given a specific gas PDF, the above cancellation can occur for some thresholds but not for the others. In the next section, we will examine the trends of the gas PDF, $\tau_\star$, $f_{\rm sf,H_2}$, and $\tau_{\rm H_2}$ observed in our simulations.

6.2.2 Trends of the Gas PDF, $\tau_\star$, $f_{\rm sf,H_2}$, and $\tau_{\rm H_2}$ in Simulations

The dependence of the gas PDF, $\tau_\star$, $f_{\rm sf,H_2}$, and $\tau_{\rm H_2}$ on $\Sigma_{\rm H_2}$, the local star formation slope β, and the star formation threshold can be explored in simulations directly, as all of the relevant quantities can be measured. In particular, we will consider these trends in two simulations from our suite: the fiducial run in which the KSR is linear (Figure 6.1) and the run with the same parameters but with the density-based star formation threshold in which the molecular KSR is steep (Figure 6.3).

Figure 6.4 shows the distribution of gas in these simulations in the plane of gas density and total velocity dispersion, $\sigma_{\rm tot} = \sqrt{c_{\rm s}^2 + \sigma_{\rm t}^2}$, which includes both thermal and subgrid turbulent velocities. The distributions are averaged in 1 kpc-wide annuli at different galactocentric radii, R, and three horizontal panels show three representative radii. Given that the gas surface density exponentially decreases with increasing R, these distributions correspond to widely different $\Sigma_{\rm H_2}$ values.

As the top row in the figure shows, in our fiducial simulation, the gas PDF does change with changing $\Sigma_{\rm H_2}$, which results in trends of $\tau_\star$ and $f_{\rm sf,H_2}$ with $\Sigma_{\rm H_2}$. In particular, according to Equation (6.3), the trend of $\tau_\star$ is due to the scaling of the star-forming part of the PDF. To

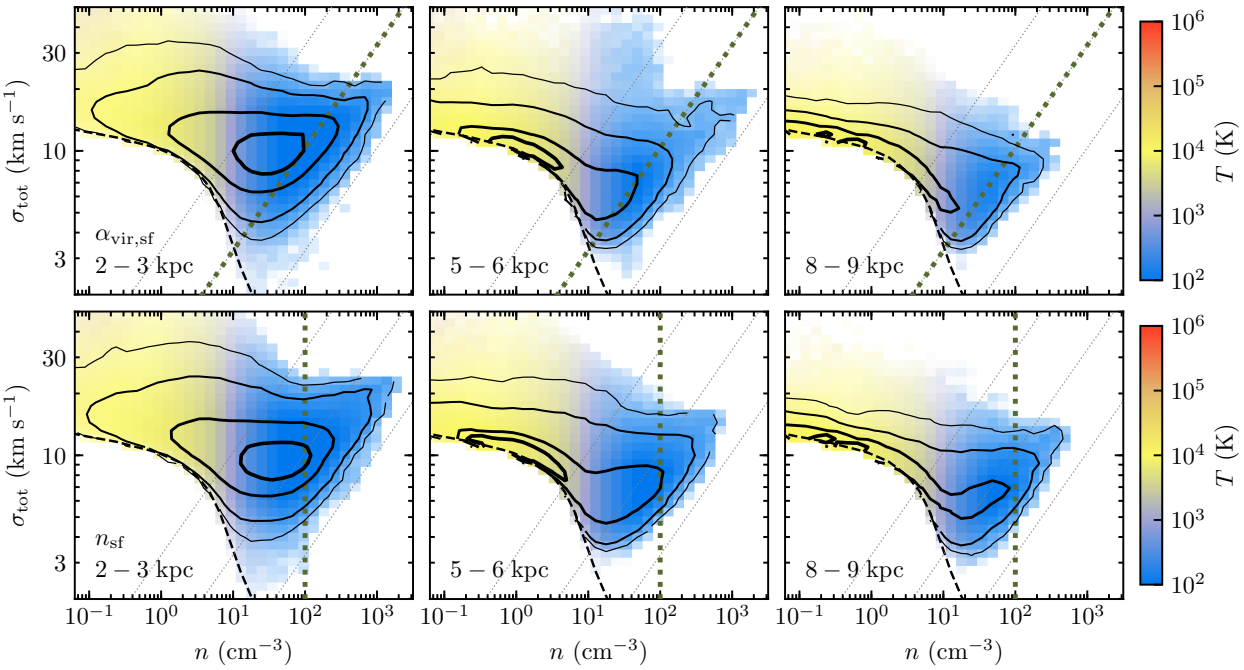

Figure 6.4: Dependence of gas distribution on galactocentric radius (and therefore on the average gas density) in the simulations with $\alpha_{\rm vir,sf} = 10$ (top row) and $n_{\rm sf} = 100$ cm^{-3} star formation threshold (bottom row). Each column of panels shows the distribution averaged between 500 and 700 Myr in 1 kpc wide annuli at different galactocentric radii: $R = 2$–3 kpc (left), 5–6 kpc (middle), and 8–9 kpc (right). Contours show 25%, 68%, 95%, and 99% of the PDF. The color of the distribution indicates the average temperature, and the blue region (cold gas) roughly indicates the distribution of molecular gas. The dashed line close to the lower envelope of the distribution shows the median temperature as a function of density. The thick dotted line shows the star formation threshold adopted in these simulations; star-forming gas resides to the right of the threshold. Thin dotted lines indicate constant values of the virial parameter: $\alpha_{\rm vir} = 100$, 10, and 1 from left to right.

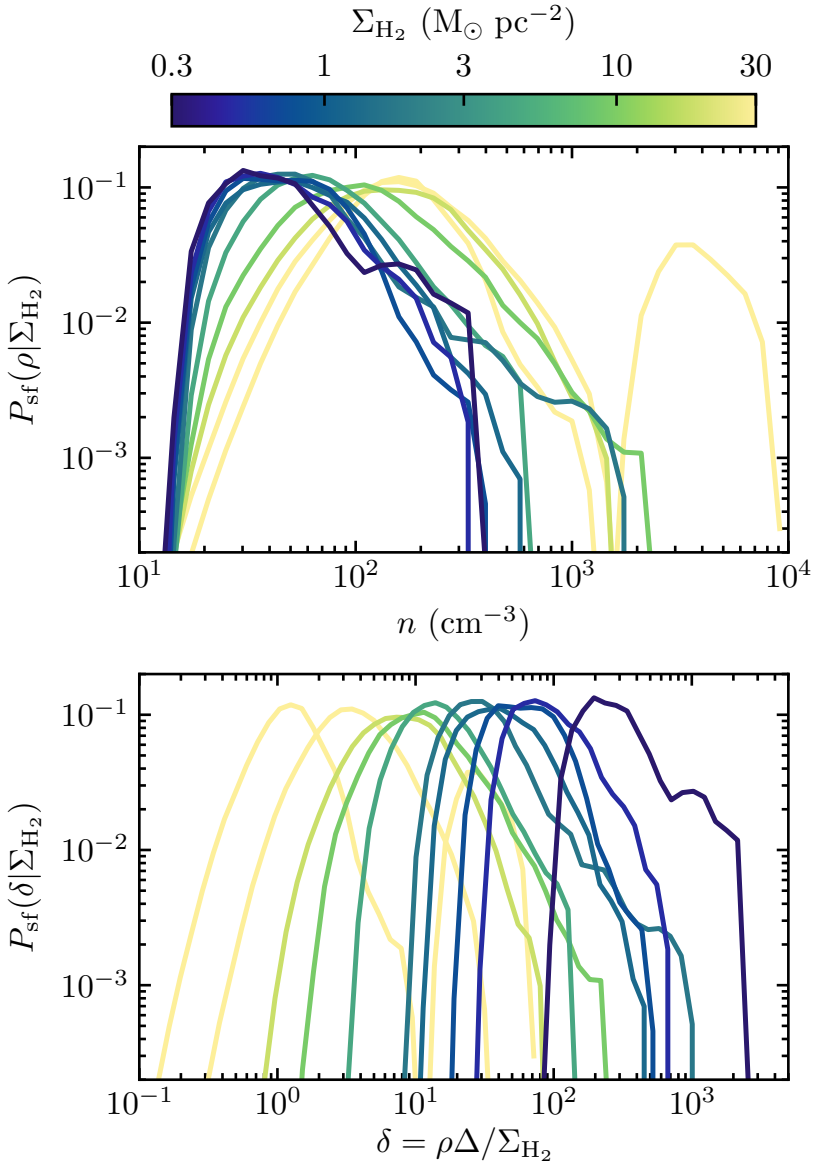

Figure 6.5: Density PDFs of star-forming gas (Equation 6.4) in concentric 1 kpc wide annuli in the simulation with the $\alpha_{\rm vir,sf}$ threshold. PDFs are averaged between 500 and 700 Myr and colored according to the average density of molecular gas in each annulus, $\Sigma_{\rm H_2}$. The top panel shows that PDFs are not fixed but scale with $\Sigma_{\rm H_2}$, while the bottom panel demonstrates that this scaling is weaker than self-similar. If the PDF scaled self-similarly, its shape would be fixed as a function of $\rho/\Sigma_{\rm H_2}$. To make this ratio dimensionless, we multiply it by our resolution $\Delta = 40$ pc. The PDF in the central region ($R < 1$ kpc, pale yellow) is bimodal, with a prominent bump at $n \sim (2-7) \times 10^3$ cm^{-3}, which corresponds to a central concentration of high-$\sigma_{\rm t}$ gas that does not form stars according to the $\alpha_{\rm vir} < 10$ criterion. When we use a density threshold (Figure 6.7), such a bump does not form because all gas at such densities would rapidly form stars.

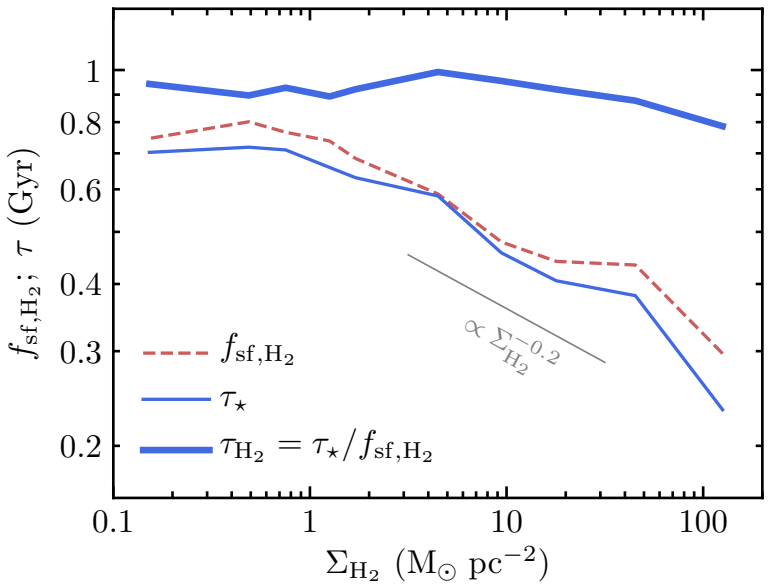

Figure 6.6: Dependence of molecular gas depletion time, $\tau_{\rm H_2}$ (solid line, left axis), star-forming gas depletion time, $\tau_\star$ (thin line, left axis), and the star-forming mass fraction of molecular gas, $f_{\rm sf,H_2}$ (dotted line, right axis) on the average surface density of molecular gas, $\Sigma_{\rm H_2}$, in radial annuli with widths of 1 kpc. The trends of $\tau_\star$ and $f_{\rm sf,H_2}$ with $\Sigma_{\rm H_2}$ cancel each other out in the expression for the molecular gas depletion time, $\tau = \tau_\star / f_{\rm sf,H_2}$, which results in a linear KSR for molecular gas.

explore the $\tau_\star$ trend in more detail, in Figure 6.5 we plot these parts of the PDF (integrated over $\sigma_{\rm tot}$) in concentric 1 kpc-wide annuli out to $R = 10$ kpc.

If star-forming gas PDF were independent of $\Sigma_{\rm H_2}$, $P_{\rm sf}(\rho|\Sigma_{\rm H_2}) = F(\rho)$, Equation (6.3) implies that $\tau_\star$ would also be independent of $\Sigma_{\rm H_2}$. This case corresponds to the "counting argument" often used as an explanation for the linearity of the molecular KSR (see Section 1.3). However, the top panel of Figure 6.5 shows that the PDF is not fixed but shifts to higher density with increasing $\Sigma_{\rm H_2}$. Therefore, $\tau_\star$ is not constant but decreases with $\Sigma_{\rm H_2}$.

On the other hand, if the PDF scaled self-similarly, $P_{\rm sf}(\rho|\Sigma_{\rm H_2}) = F(\rho/\Sigma_{\rm H_2})/\Sigma_{\rm H_2}$ where F is a function of a fixed shape and peak location, then $\tau_\star$ would inherit the slope from the local star formation relation: $\tau_\star \propto \Sigma_{\rm H_2}^{1-\beta} = \Sigma_{\rm H_2}^{-0.5}$ for $\beta = 1.5$, as is explicitly shown in Appendix C.4 (see also Gnedin et al., 2014). However, the bottom panel of Figure 6.5 shows that PDFs for different $\rho/\Sigma_{\rm H_2}$ do not coincide, with their peak changing significantly with $\Sigma_{\rm H_2}$. This strong deviation from self-similar scaling results in a scaling of $\tau_\star$ that is weaker than the self-similar expectation of $\tau_\star \propto \Sigma_{\rm H_2}^{-0.5}$.

The actual scaling of $\tau_\star$ with $\Sigma_{\rm H_2}$ produced in our fiducial simulation is shown with the thin line in Figure 6.6. According to the figure, $\tau_\star$ scales as $\tau_\star \propto \Sigma_{\rm H_2}^{-0.2}$. If the star-forming fraction $f_{\rm sf,H_2}$ were independent of $\Sigma_{\rm H_2}$, this scaling would be enough to make the KSR noticeably nonlinear: $\dot{\Sigma}_\star \propto \Sigma_{\rm H_2}^{1.2}$. However, as the dashed line in the figure shows, $f_{\rm sf,H_2}$ scales with $\Sigma_{\rm H_2}$ similarly to $\tau_\star$. Given that $\tau_{\rm H_2} = \tau_\star / f_{\rm sf,H_2}$ (Equation 6.1), these scalings cancel, resulting in $\tau_{\rm H_2}$ almost independent of $\Sigma_{\rm H_2}$ and a nearly linear molecular KSR (thick line in the figure).

We find that in the simulations with an $\alpha_{\rm vir}$-based threshold, such cancellation holds for all values of the slope of the local star formation relation β as long as feedback is as strong as in the fiducial simulation or stronger (see Section 6.1 and Appendix C.1). Such cancellation, however, does not happen in the simulations without feedback, in which the slope of the molecular KSR becomes sensitive to the local slope β, and in all of the simulations with the

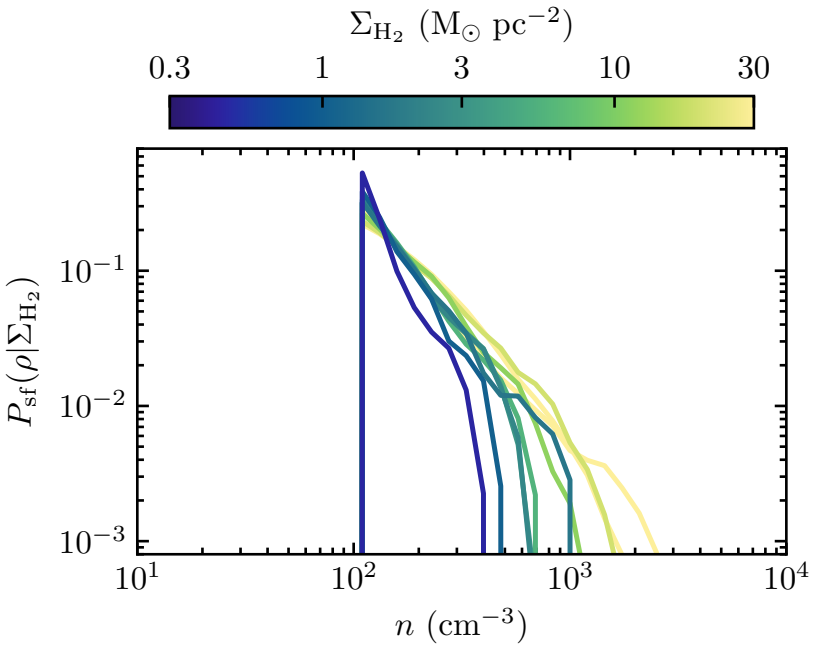

Figure 6.7: Same as the top panel in Figure 6.5 but for the simulation with the $n_{sf} = 100\,cm^{-3}$ star formation threshold. The dependence of PDF on Σ_{H_2} is much weaker compared to the simulation with the $\alpha_{vir,sf} = 10$ threshold.

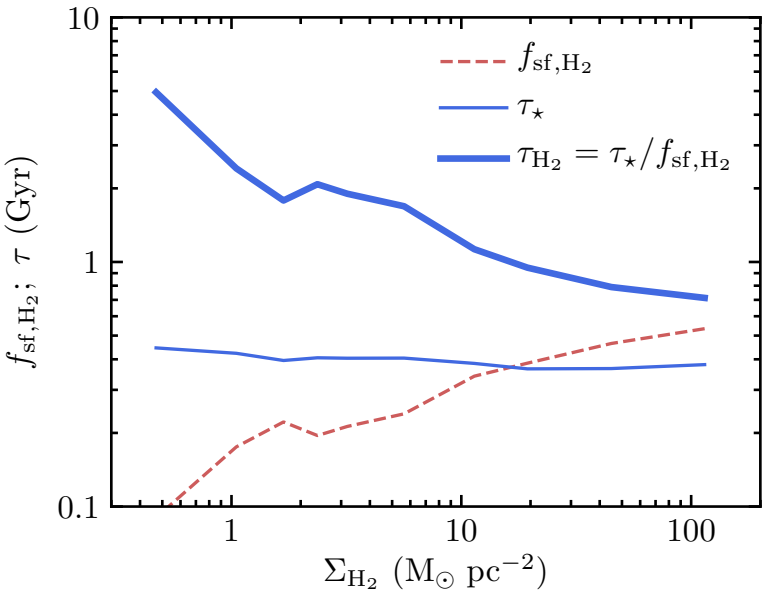

Figure 6.8: Same as Figure 6.8 but for the simulation with the $n_{sf} = 100\,cm^{-3}$ star formation threshold. In contrast to the simulation with $\alpha_{vir,sf} = 10$ threshold, the trends of $\tau_\star$ and f_{sf,H_2} with Σ_{H_2} do not cancel out, leading to a strong dependence of τ_{H_2} on Σ_{H_2} and a superlinear molecular KSR.

density-based star formation threshold. In the latter case, the density threshold defines only the high-density tail of distribution as star-forming gas (see the bottom row of Figure 6.4). Therefore, the PDF of star-forming gas and $\tau_\star$ become almost independent of $\Sigma_{\rm H_2}$, as shown in Figures 6.7 and 6.8. However, the star-forming fraction of molecular gas does increase at higher $\Sigma_{\rm H_2}$, and therefore $\tau_{\rm H_2} = \tau_\star / f_{\rm sf,H_2}$ decreases with increasing $\Sigma_{\rm H_2}$, resulting in a superlinear molecular KSR.

Results presented in this section clearly show that the linear slope of molecular KSR in the simulations with an $\alpha_{\rm vir}$-based star formation threshold and efficient feedback is rather nontrivial and results from a cancellation of trends of physical properties controlling $\tau_{\rm H_2}$ with both β and $\Sigma_{\rm H_2}$. The cancellation occurs only when feedback is efficient, and it depends on the choice of the star formation threshold.

The language of gas PDF is direct and clearly shows the relation between large-scale observables and small-scale properties of gas and star formation. However, we cannot use it to fully explain our simulation results because this requires knowledge of the exact functional form of the gas PDF, its dependence on $\Sigma_{\rm H_2}$, and its response to feedback. Therefore, in what follows, we will adopt an approximate approach that can qualitatively explain several of our key results.

6.3 The physics of the molecular KSR slope

In this section, we show that several key results of our simulations can be understood using the theoretical framework introduced in Chapter 2. The model is based on the conservation of mass and considers dynamic gas cycling between star-forming and non-star-forming states. In this model, the depletion time of total gas in an ISM patch is $\tau \sim N_{\rm c}(t_{\rm nsf} + t_{\rm sf})$, where $t_{\rm nsf}$ and $t_{\rm sf}$ are the average times in non-star-forming and star-forming stages in each cycle, and the number of cycles, $N_{\rm c} \sim \tau_\star / t_{\rm sf}$, is set by the condition that after many cycles, gas must spend on average $\tau_\star \equiv \Sigma_{\rm sf}/\dot{\Sigma}_\star$ in the star-forming state. The fraction of the initial gas

parcel mass that is converted into stars during each cycle is correspondingly $\epsilon \sim t_{\rm sf}/\tau_\star$.

6.3.1 Molecular KSR and Gas Evolution Timescales

In the dynamical framework outlined above, the star-forming mass fraction of molecular gas can be expressed as the relative time in star-forming and molecular stages on each cycle, $t_{\rm sf}$ and $t_{\rm H_2}$:

$$f_{\rm sf,H_2} \equiv \frac{\Sigma_{\rm sf}}{\Sigma_{\rm H_2}} \sim \frac{t_{\rm sf}}{t_{\rm H_2}}. \tag{6.5}$$

Here, $t_{\rm H_2}$ is the duration of the molecular stage during one evolution cycle—i.e., the time between the moment when gas becomes molecular and the moment when it becomes atomic again. The time $t_{\rm sf}$ is the total time during one cycle that gas spends in the star-forming state. Note that during $t_{\rm H_2}$ a given gas parcel may remain non-star-forming ($t_{\rm sf} = 0$) or become star-forming one or multiple times. In the latter case, $t_{\rm sf}$ is the sum of all star-forming stages that a gas parcel experienced.

Given these definitions, Equation (6.1) can be rewritten as

$$\tau_{\rm H_2} = \frac{\tau_\star}{f_{\rm sf,H_2}} \sim \frac{\tau_\star}{t_{\rm sf}}\, t_{\rm H_2} \sim \frac{t_{\rm H_2}}{\epsilon}. \tag{6.6}$$

Further derivation proceeds analogously to Chapter 2. To express $t_{\rm sf}$ via the timescales of the processes driving gas evolution, we note that the amount of star-forming gas in ISM patches, $\Sigma_{\rm sf}$, is regulated by the combined effect of gas consumption at the rate $\dot{\Sigma}_\star$ and dispersal of star-forming gas by feedback and dynamical processes (e.g., passages of spiral arms) at the rates of $F_{-,\rm fb}$ and $F_{-,\rm d}$, respectively. Analogously to Chapter 2, we parameterize these as

$$F_{-,\rm fb} = \xi \dot{\Sigma}_\star = \xi\, \frac{\Sigma_{\rm sf}}{\tau_\star}, \qquad F_{-,\rm d} = \frac{\Sigma_{\rm sf}}{\tau_{-,\rm d}}, \tag{6.7}$$

where ξ is the "mass-loading factor" of star-forming gas dispersal by feedback, while $\tau_{-,\rm d}$ is the characteristic timescale of the dynamical dispersal of star-forming regions. The total

rate of gas removal from star-forming regions is thus $\dot{\Sigma}_\star + F_{-,\mathrm{fb}} + F_{-,\mathrm{d}}$ and the characteristic time that gas spends in the star-forming state can thus be expressed as

$$t_{\mathrm{sf}} \sim \frac{\Sigma_{\mathrm{sf}}}{\dot{\Sigma}_\star + F_{-,\mathrm{fb}} + F_{-,\mathrm{d}}} = \tau_\star \left(1 + \xi + \frac{\tau_\star}{\tau_{-,\mathrm{d}}}\right)^{-1}. \tag{6.8}$$

To relate these quantities to the depletion time of molecular gas, consider the characteristic time that gas spends in molecular form, $t_{\mathrm{H_2}} = t_{\mathrm{H_2,nsf}} + t_{\mathrm{sf}}$, where $t_{\mathrm{H_2,nsf}}$ is the time that molecular gas spends outside of star-forming regions. Equations (6.6) and (6.8) then give

$$\tau_{\mathrm{H_2}} = (1 + \xi)\, t_{\mathrm{H_2,nsf}} + \left(1 + \frac{t_{\mathrm{H_2,nsf}}}{\tau_{-,\mathrm{d}}}\right) \tau_\star. \tag{6.9}$$

This expression is analogous to Equation (5.5) above and has similar behavior. In particular, only the second term explicitly depends on the slope of the local star formation relation β via the dependence of $\tau_\star$ on β (Equation 6.3). The first term can depend on β only implicitly. As we will detail below, the regimes in which one of these two terms dominates correspond to the regimes where molecular KSR is sensitive or insensitive to β (Figure 6.2), and thus these regimes are directly analogous to those discussed in Section 5.2. As we will also show, Equation (6.9) can help us understand why the molecular KSR is close to linear when an α_{vir}-based star formation threshold is used and why it steepens for a density-based threshold.

6.3.2 Dependence of Molecular KSR on the Local Slope β

When feedback is strong (ξ is large) and star formation is locally efficient, i.e. $\tau_\star$ is short (due to, e.g., large ϵ_{ff}), the first term in Equation (6.9) dominates. Given that only $\tau_\star$ in the second term explicitly depends on β (Equation 6.3), in this regime, $\tau_{\mathrm{H_2}}$ can be expected to only weakly depend on the local slope. Indeed, we showed that the sensitivity to β disappears completely for the $\epsilon_{\mathrm{ff}} = 100\%$ compared to a weak dependence in the $\epsilon_{\mathrm{ff}} = 1\%$

runs (Figure 6.2). This insensitivity indicates that in the context of our framework, the first term does not depend on β even indirectly. This can be understood as follows.

Equation (6.8) shows that in this regime ($\xi \gg \tau_\star/\tau_{-,\mathrm{d}}$), the characteristic time a gas parcel spends in a star-forming region in a single cycle is $t_{\mathrm{sf}} \sim \tau_\star/(1+\xi) \sim \tau_\star\epsilon$ and corresponds to the time it takes to form enough young stars to disperse a typical star-forming region. For the higher SFR of larger β values, and correspondingly smaller $\tau_\star$, the young star mass fraction ϵ required for dispersal will be reached faster, and t_{sf} will be shorter. Thus, both $\tau_\star$ and t_{sf} depend on β in a similar way, so that this dependence cancels in $\epsilon \sim t_{\mathrm{sf}}/\tau_\star$ rendering the integral stellar mass fraction required for dispersal roughly constant. Given that the lifetime of gas in the molecular state is not related to β, this cancellation is the main reason why $\tau_{\mathrm{H_2}} \propto t_{\mathrm{H_2}}\,\tau_\star/t_{\mathrm{sf}}$ is independent of β. The bottom panel of Figure 6.9 demonstrates that ϵ and $t_{\mathrm{H_2}}$ are indeed independent of β in the simulation with $\epsilon_{\mathrm{ff}} = 100\%$, even though $\tau_\star$ does depend on β, as shown in the top panel.

When feedback is weak (small ξ) or star formation is locally inefficient ($\tau_\star$ is long), the second term in Equation (6.9) dominates. This term is proportional to $\tau_\star$, which explicitly depends on the local slope β. As shown in Figure 6.10, this dependence of $\tau_\star$ on β also implies the dependence of the molecular KSR on β because $t_{\mathrm{H_2}}(\Sigma_{\mathrm{H_2}})$ does not depend on β, while in this regime $\epsilon(\Sigma_{\mathrm{H_2}})$ does. Their ratio $\tau_{\mathrm{H_2}} \sim t_{\mathrm{H_2}}/\epsilon$, therefore, is no longer close to constant, but depends on $\Sigma_{\mathrm{H_2}}$ in a way sensitive to β, as observed in our simulations without feedback (left panel of Figure 6.2). It is worth noting that although there is a value of β at which the large-scale slope becomes close to linear in these simulations, this is coincidental and holds only for $\beta \approx 1.5$. Physically, t_{sf} in this regime is controlled not by feedback but by dynamical processes that disperse star-forming and molecular regions, such as turbulent shear, differential rotation, expansion behind spiral arms, etc.

In the intermediate regime, in which the two terms in Equation (6.9) are comparable, we can expect an intermediate weak sensitivity of the KSR to β, as is indeed observed in

our simulations with fiducial feedback strength and $\epsilon_{\rm ff} = 1\%$ (middle panel of Figure 6.2). This behavior is explained by the contribution of two comparable terms to $\tau_{\rm H_2}$ which can be demonstrated explicitly.

According to Equation (6.9), the $\tau_{\rm H_2}$ in these simulations differ from the simulations with $\epsilon_{\rm ff} = 100\%$ and fiducial feedback only by the second term, which is 100 times smaller in the latter case. At the same time, $\tau_{\rm H_2}$ in the simulations with $\epsilon_{\rm ff} = 1\%$ and with or without feedback differ only by the first term. Therefore, Equation (6.9) predicts that the $\tau_{\rm H_2}$ in our fiducial simulations equals the $\tau_{\rm H_2}$ in simulations with $\epsilon_{\rm ff} = 1\%$ and no feedback plus the $\tau_{\rm H_2}$ in simulations with $\epsilon_{\rm ff} = 100\%$ and fiducial feedback. Figure 6.11 shows that this is indeed the case. For $\beta = 1.5$ and 2, the measured $\tau_{\rm H_2}$ and the sum agree extremely well, while for $\beta = 1$ and 2.5, they are within a factor of 1.5. A small difference in the latter case is due to the extra dependencies of $t_{\rm H_2,nsf}$, $\tau_{-,\rm d}$, and $\tau_\star$ on $\epsilon_{\rm ff}$, β, and feedback strength. For example, feedback disperses the high-density tail of the gas PDF, making $\tau_\star$ longer. This effect becomes stronger for larger β because steeper local star formation relation $\dot{\rho}_\star \propto \rho^\beta$ results in a more efficient dispersal of dense gas. The difference between the measured $\tau_{\rm H_2}$ and the sum therefore increases with increasing β.

6.3.3 Dependence on the Choice of Star Formation Threshold

Simulation results in Section 6.1 show that a near-linear KSR emerges only in simulations with efficient feedback *and* $\alpha_{\rm vir}$-based star formation threshold. In simulations with the same parameters but using a density-based threshold, the molecular KSR is significantly steeper (see Figure 6.3). This is not surprising, because the star formation threshold affects all terms in Equation (6.9), and thus the behavior of the molecular KSR can be different for different threshold choices. Figure 6.12 shows that $t_{\rm H_2}(\Sigma_{\rm H_2})$ is independent of the choice of threshold or feedback strength, but the $\epsilon(\Sigma_{\rm H_2})$ trend does steepen for the density-based star formation threshold and is thus responsible for the steepening of the molecular KSR in such

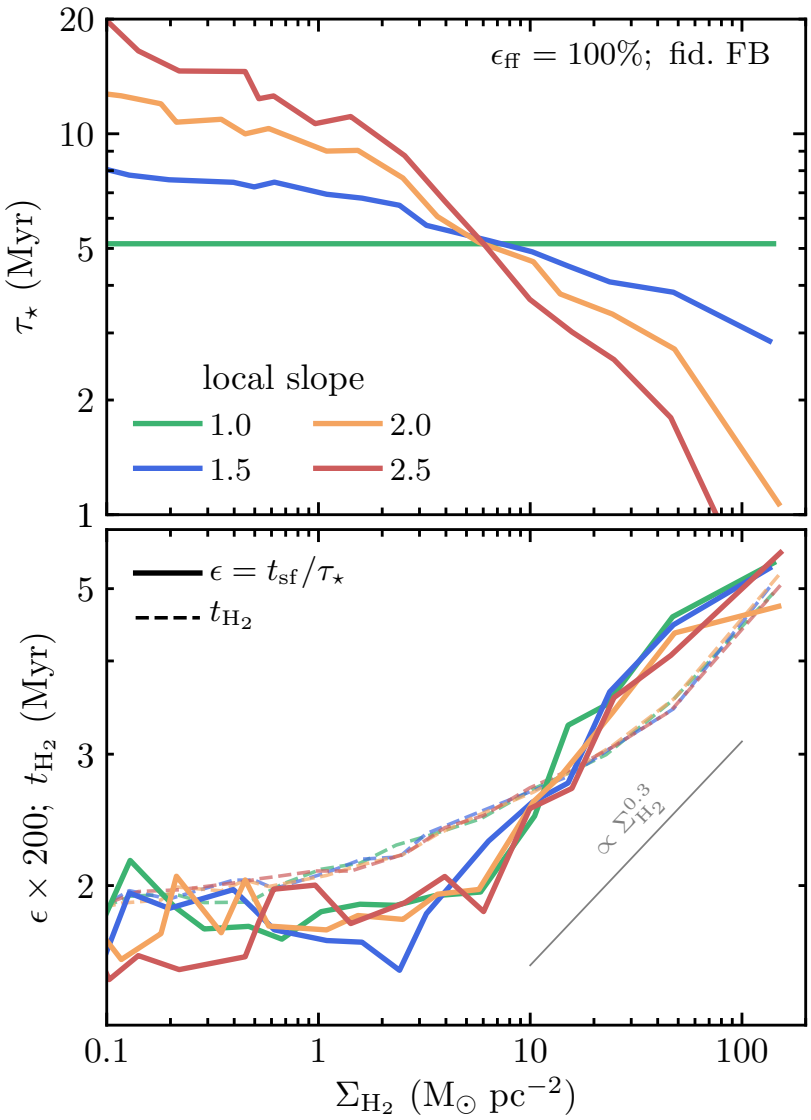

Figure 6.9: Trends of $\tau_\star$ (top panel), $\epsilon = t_{\rm sf}/\tau_\star$ and $t_{\rm H_2}$ (bottom panel) in our simulations with $\epsilon_{\rm ff} = 100\%$ and different slopes of the local star formation relation $\dot{\rho}_\star \propto \rho^\beta$, $\beta = 1$, 1.5, 2, and 2.5 (see Equation 3.4). We measure ϵ, $t_{\rm sf}$, and $t_{\rm H_2}$ for each molecular stage using gas-tracer particles as explained in Section 3.4 and show their values averaged in concentric annuli. The stages are accumulated between 450 and 800 Myr of disk evolution. The figure illustrates two types of cancellation that result in a near-linear KSR. First, the variation of the $\tau_\star$ trend with β cancels out by $t_{\rm sf}$ in $\epsilon = t_{\rm sf}/\tau_\star$. Second, the trends of ϵ and $t_{\rm H_2}$ with $\Sigma_{\rm H_2}$ nearly cancel in $\tau_{\rm H_2} \sim t_{\rm H_2}/\epsilon$, resulting in a nearly linear molecular KSR.

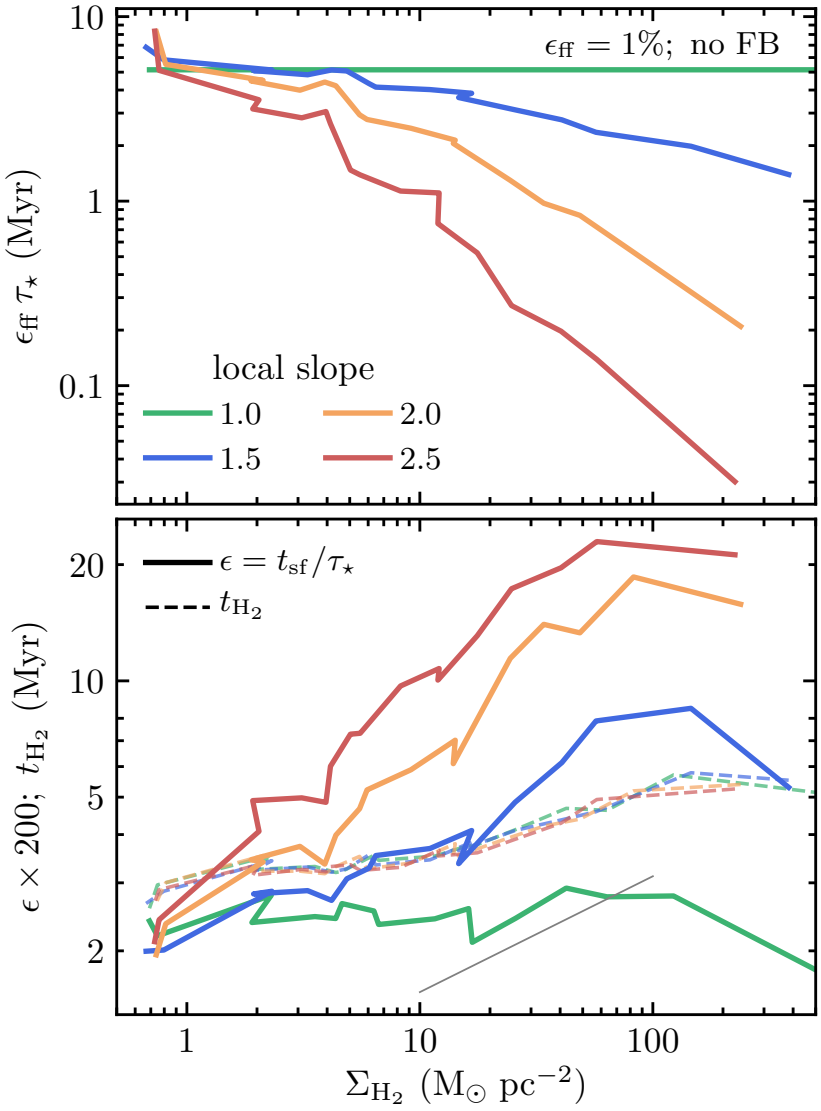

Figure 6.10: Same as Figure 6.9 but for simulations with $\epsilon_{\rm ff} = 1\%$ and no feedback. While the trends of $t_{\rm H_2}(\Sigma_{\rm H_2})$ remain almost the same as in Figure 6.9, there is no longer feedback-imposed cancellation of the trends in $\epsilon = t_{\rm sf}/\tau_\star$, and $\epsilon(\Sigma_{\rm H_2})$ becomes strongly dependent on β, which leads to the dependence of $\tau_{\rm H_2}$ and the KSR slope on β in simulations without feedback (left panel of Figure 6.2). To produce this plot, we accumulated molecular and star-forming stages of gas-tracers evolution over a shorter period of time (between 450 and 600 Myr) because for large β and no feedback, the total gas mass changes more rapidly due to the short global depletion times. The local depletion times in the top panel are normalized by $\epsilon_{\rm ff}$ to simplify the comparison with the trends in Figure 6.9. The thin gray line in the bottom panel repeats that from Figure 6.9.

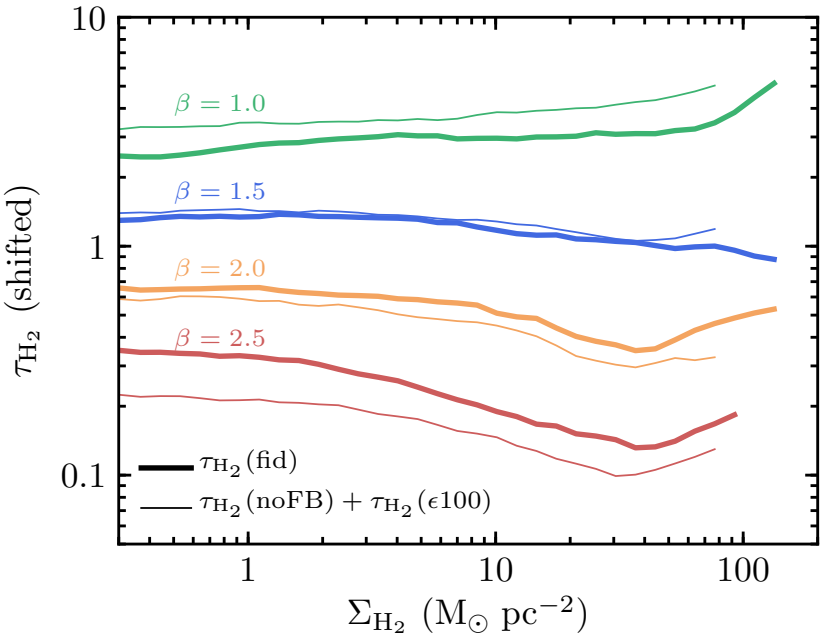

Figure 6.11: Comparison of our simulation results with the predictions of the analytical model. The thick lines show the τ_{H_2} in the simulations with $\epsilon_{ff} = 1\%$, fiducial feedback strength, and different slopes of the local star formation relation $\dot{\rho}_\star \propto \rho^\beta$, differentiated by color. These lines are equivalent to those shown in the middle panel of Figure 6.2 but shifted up and down by an arbitrary factor to avoid clutter. Our model predicts that the τ_{H_2} in these simulations must be close to the sum of the τ_{H_2} in our simulations without feedback (left panel of Figure 6.2) and the τ_{H_2} in our simulations with $\epsilon_{ff} = 100\%$ (right panel of Figure 6.2). These sums are shown with thin lines for corresponding values of β and they do indeed agree with the τ_{H_2} in our fiducial simulations.

simulation. This behavior can be understood using the gas distributions in simulations with different thresholds shown in Figure 6.4.

In all simulations, dense, supersonic gas reaches approximate equilibrium between turbulence production on the local dynamical time, $t_{dyn} \propto 1/\sqrt{G\rho}$, and turbulence decay on the local eddy-turnover time, $t_{dec} \sim \Delta/\sigma_t$, so that $t_{dyn} \sim t_{dec}$ and $\sigma_t \propto \rho^{0.5}$, and the gas PDF aligns along the lines of $\alpha_{vir} \propto \sigma_t^2/\rho \sim$ const, parallel to the $\alpha_{vir,sf} = 10$ threshold. This alignment persists at all Σ_{H_2}.

In simulations with the α_{vir}-based threshold, gas can become star-forming relatively quickly after becoming molecular because low-σ_t gas can be star-forming even at rather

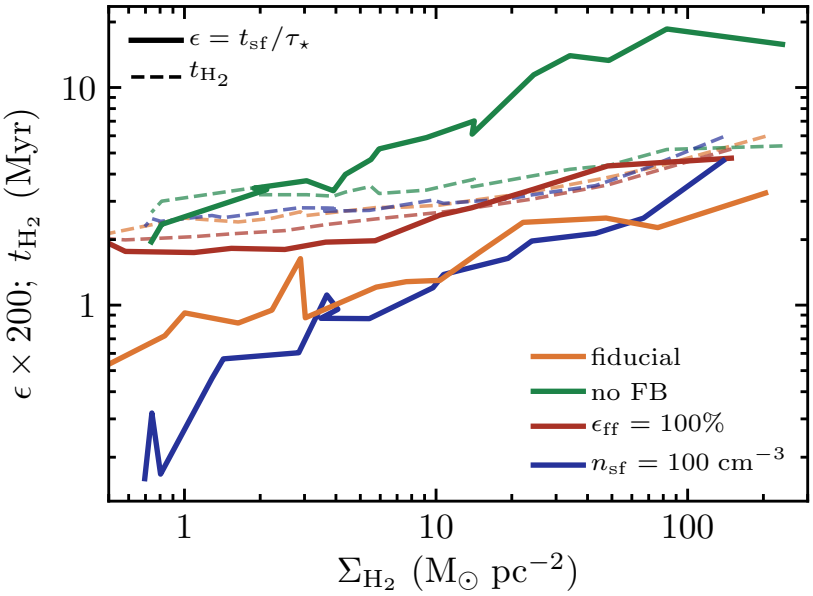

Figure 6.12: Effect of $\epsilon_{\rm ff}$, feedback strength, and star formation threshold on the $\epsilon(\Sigma_{\rm H_2})$ and $t_{\rm H_2}(\Sigma_{\rm H_2})$ trends. The fiducial case shown by the orange lines corresponds to $\epsilon_{\rm ff} = 1\%$, fiducial feedback, and $\alpha_{\rm vir,sf} = 10$ threshold. Other colors show simulations in which these parameters are changed as indicated in the legend. To illustrate the variation of trends with parameters, we compare simulations with the local slope $\beta = 2$ instead of the fiducial $\beta = 1.5$ because in these simulations trends vary more strongly due to a stronger dependence of $\tau_\star$ on $\Sigma_{\rm H_2}$ (see Figures 6.9 and 6.10). The trend of ϵ varies much stronger than that of $t_{\rm H_2}$, and therefore, it is the trend of ϵ that defines the dependence of $\tau_{\rm H_2} \sim t_{\rm H_2}/\epsilon$ on $\Sigma_{\rm H_2}$ and the slope of the molecular KSR.

small densities, while $\sigma_{\rm t}$ can become small simply by turbulence decay when it cannot be offset with compression or feedback. In contrast, in simulations with the density-based threshold, transition to the star-forming state is hindered because molecular gas must be compressed to relatively high densities to exceed the threshold.

This difference can be illustrated using the distributions of $\dot{\Sigma}_\star$ and molecular gas in the middle panels of Figures 6.1 and 6.3. In the simulation with the $\alpha_{\rm vir,sf} = 10$ threshold (Figure 6.1), almost every molecular region (gray contours) contains a star-forming subregion with young stars, and thus molecular gas is always either star-forming or is spatially close to a star-forming region. In contrast, in the simulation with the density-based threshold (Figure 6.3), a substantial number of molecular regions, especially in the disk outskirts, are not star-forming. As Figure 6.13 shows, they would be star-forming if we used the $\alpha_{\rm vir} < 10$ threshold instead of $n > 100$ cm^{-3}.

The incidence of star-forming regions is thus a steeper function of $\Sigma_{\rm H_2}$ in the simulation with the density-based threshold and so is $\epsilon(\Sigma_{\rm H_2})$ (Figure 6.12), which explains the steeper molecular KSR. For a density-based threshold, the average ϵ decreases at lower $\Sigma_{\rm H_2}$ because of the larger fraction of gas tracers that go through the molecular stage without reaching the star-forming state and thus have $\epsilon = 0$.

Although we have considered specific choices of thresholds here, our conclusions and their implications are more general. The basic scaling of $\tau_{\rm H_2}$ with timescales in Equation (6.6) holds for any choice of star formation threshold, while as we can see, $t_{\rm H_2}(\Sigma_{\rm H_2})$ is insensitive to the details of feedback and star formation prescriptions. Thus, any prescription that shapes $\epsilon(\Sigma_{\rm H_2})$ to be similar to $t_{\rm H_2}(\Sigma_{\rm H_2})$ will lead to a near-linear molecular KSR and vice versa. Possible reasons why the $\epsilon(\Sigma_{\rm H_2})$ and $t_{\rm H_2}(\Sigma_{\rm H_2})$ trends are similar will be discussed in the next section.

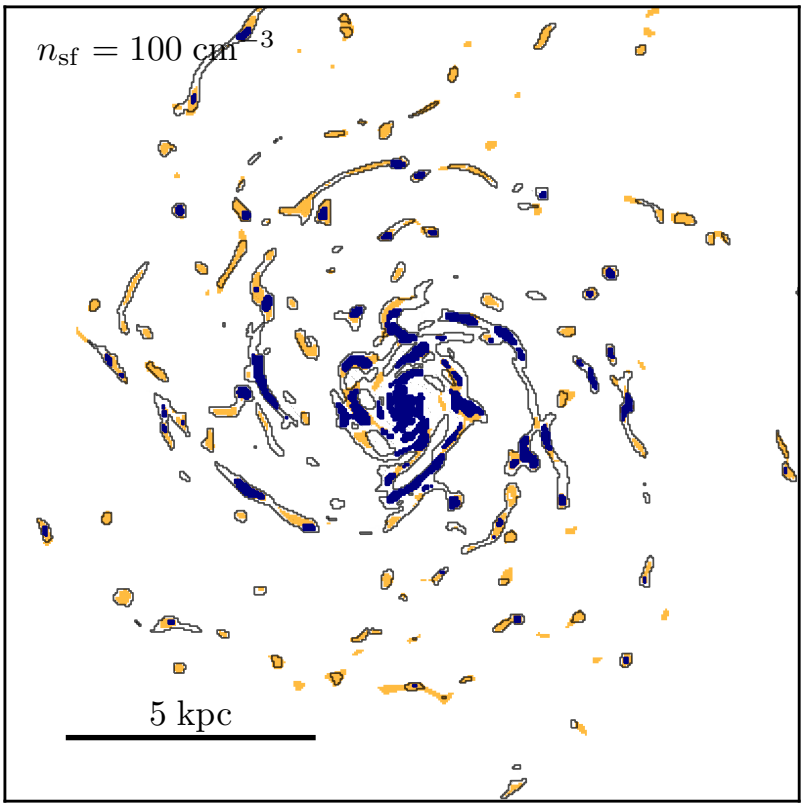

Figure 6.13: Distribution of molecular (gray contours) and star-forming gas (filled blue contours) in the simulation with the $n_{\rm sf} = 100$ cm^{-3} star formation threshold. The filled orange contours show regions with $\alpha_{\rm vir} < 10$. Non-star-forming molecular regions on the disk outskirts in this simulation would be star-forming if the star formation threshold were in the virial parameter, $\alpha_{\rm vir} < \alpha_{\rm vir,sf} = 10$. This is because it is much easier for gas to lose turbulence support and reach an $\alpha_{\rm vir}$ threshold than to be compressed to a threshold density.

6.3.4 The Origin of the Linear Molecular KSR

The results presented so far indicate that ϵ and $t_{\rm H_2}$ both depend on $\Sigma_{\rm H_2}$ and therefore, to produce a linear molecular KSR, these trends must cancel out in $\tau_{\rm H_2} \sim t_{\rm H_2}/\epsilon$. According to Equation (6.6), $\tau_\star/f_{\rm sf,H_2} \sim t_{\rm H_2}/\epsilon$ and thus this cancellation is simply another manifestation of the cancellation of the $\tau_\star(\Sigma_{\rm H_2})$ and $f_{\rm sf,H_2}(\Sigma_{\rm H_2})$ trends discussed in Section 6.2.

We can readily understand why the dependencies of ϵ and $t_{\rm H_2}$ on $\Sigma_{\rm H_2}$ should be of the same sign when feedback is efficient in dispersing star-forming regions. Indeed, ϵ is expected to increase with increasing $\Sigma_{\rm H_2}$, because at higher $\Sigma_{\rm H_2}$, the gravity of the disk and pressure of the ISM are larger, making it harder for feedback to disperse star-forming regions and thus requiring a larger ϵ for dispersal. At the same time, the time that the gas spends in the molecular state during one cycle, $t_{\rm H_2}$, can also increase because a larger fraction of gas is molecular at larger $\Sigma_{\rm H_2}$.

The quantitative explanation of why these trends are similar is less obvious, but can be understood as follows. Our analysis shows that in simulations with efficient feedback, gas tracers experience *local* chaotic fluctuations of their density and velocity dispersion, and they move randomly in the n–$\sigma_{\rm tot}$ plane. In simulations with an $\alpha_{\rm vir}$-based star formation threshold, most molecular gas is close to the threshold due to its alignment along the $\alpha_{\rm vir} =$ const direction (see Section 6.3.3), and therefore, it randomly transits into the star-forming state and back. If the probability of transition is close to uniform, the number of transitions during a molecular stage, $N_{\rm sf}$, will simply be proportional to the duration of this stage, $N_{\rm sf} \propto t_{\rm H_2}$. Although the duration of each star-forming stage is regulated by feedback as we discussed above, the total time the parcel spends in the star-forming state, $t_{\rm sf}$, will also be proportional to $N_{\rm sf}$ and the gas parcel thus converts the fraction $\epsilon \sim t_{\rm sf}/\tau_\star \propto t_{\rm H_2}$ into stars during one molecular phase. This leads to a constant molecular depletion time, $\tau_{\rm H_2} \sim t_{\rm H_2}/\epsilon \approx$ const, and a linear molecular KSR.

The above mechanism will also operate in a more general case of varying $\epsilon_{\rm ff}$ as long as $\epsilon_{\rm ff}$

is a strong function of $\alpha_{\rm vir}$. Such a strong dependence of $\epsilon_{\rm ff}$ on $\alpha_{\rm vir}$ is a generic prediction of theoretical models of star formation in a turbulent medium (see Padoan et al., 2014, for a review). In Appendix C.2 we show that the molecular KSR indeed remains linear when we vary $\epsilon_{\rm ff}$ as an exponential function of $\alpha_{\rm vir}$ instead of assuming a sharp threshold.

When feedback is inefficient, the evolution of molecular gas is not as chaotic, and the $\epsilon(\Sigma_{\rm H_2})$ trend becomes sensitive to feedback strength and $\epsilon_{\rm ff}$ value, as can be seen in Figure 6.12. Given that the $t_{\rm H_2}(\Sigma_{\rm H_2})$ trend is nearly independent of feedback strength and $\epsilon_{\rm ff}$, the depletion time $\tau_{\rm H_2}$ is no longer constant in such regimes.

Likewise, when a density threshold with a high value is used to define star-forming regions instead of $\alpha_{\rm vir}$, most of the molecular gas is far from the threshold and the transition to a star-forming state in this case is not due to random motions of gas parcels in the n–$\sigma_{\rm tot}$ plane, but is mainly due to secular evolution and gas compression to high densities. In this case, $t_{\rm sf}$ is no longer proportional to $t_{\rm H_2}$ and $\tau_{\rm H_2} \neq$ const. For lower values of a density threshold, a larger fraction of gas is near the threshold and transitions to a star-forming state again become dominated by random fluctuations, which makes the slope shallower and closer to linear (see Figure C.2 in the Appendix C.1). The slope in this case depends on the threshold value as the dynamical equilibrium between compression and turbulent pressure align gas along the $\alpha_{\rm vir} =$ const direction, not along $n =$ const.

The presented explanation for why ϵ and $t_{\rm H_2}$ exhibit similar trends with $\Sigma_{\rm H_2}$, and thus why $\tau_{\rm H_2} \approx$ const when feedback is strong, is admittedly qualitative. This question calls for further exploration both in high-resolution simulations of the ISM patches and observationally in studies of molecular and star-forming regions, as we discuss below in Section 6.4.2.

6.4 Discussion

6.4.1 Comparison to Previous Models

A commonly used explanation for the nearly linear molecular KSR is the so-called "counting argument" (e.g., Wu et al., 2005), in which one assumes that molecular regions have similar properties (e.g., density and thus depletion time $\tau_\star$) and have a fixed fraction of gas that is undergoing star formation (i.e., $f_{\mathrm{sf,H_2}}$). Then, $\tau_{\mathrm{H_2}} = \tau_\star / f_{\mathrm{sf,H_2}}$ (Equation 6.1) becomes independent of $\Sigma_{\mathrm{H_2}}$ because both $\tau_\star$ and $f_{\mathrm{sf,H_2}}$ are the same and independent of $\Sigma_{\mathrm{H_2}}$. However, as we showed in Section 6.2.2, our simulations indicate that both $\tau_\star$ and $f_{\mathrm{sf,H_2}}$ in molecular regions can vary with $\Sigma_{\mathrm{H_2}}$ and still produce a nearly linear molecular KSR. Furthermore, properties of molecular clouds do change with galactocentric radius and thus with surface density in observed galaxies (e.g., Heyer & Dame, 2015; Miville-Deschênes et al., 2017). The origin of the linear slope of the molecular KSR is therefore more nuanced.

Madore (2010) and later Elmegreen (2015, 2018) considered the origin of the KSR from the timescales of gas evolution in different states. Their approach is similar to the basis of our model, which allows a direct comparison. In particular, Madore (2010) expressed the depletion time of *total* gas as $\tau \equiv \Sigma_{\mathrm{g}} / \dot{\Sigma}_\star \sim (\tau_{\mathrm{c}} + \tau_{\mathrm{s}})/\epsilon$, where the duration of one gas cycle consists of the "collapse time" τ_{c}, on which average ISM gas evolves to the star-forming state, and "stagnation time" τ_{s}, on which star-forming gas is dispersed by feedback. The fraction of gas converted into stars in one cycle, ϵ, is assumed to be fixed. Then, assuming also that $\tau_{\mathrm{c}} \propto \Sigma_{\mathrm{g}}^{-0.5}$ and τ_{s} is constant, τ_{s} will dominate at sufficiently high Σ_{g} and the KSR will become linear because the depletion time will become independent of Σ_{g}: $\tau \sim \tau_{\mathrm{s}}/\epsilon$.

Elmegreen (2015, 2018) used principles similar to the Madore (2010) model but assuming that the *total* depletion time is proportional to the freefall time at the midplane density, t_{ff}, with constant efficiency, ϵ_{ff}, so that the depletion time of *molecular* gas[3] is $\tau_{\mathrm{H_2}} = f_{\mathrm{H_2}} t_{\mathrm{ff}} / \epsilon_{\mathrm{ff}}$.

3. In Elmegreen (2015), the molecular state is denoted by the subscripts "CO," indicating that in observations, this state corresponds to the gas visible in CO. For consistency with our notation, we have changed

Next, similarly to our Equation (6.5), the molecular fraction is expressed as the ratio of timescales in the corresponding states: $f_{\rm H_2} \sim t_{\rm ff,H_2}/(t_{\rm ff} + t_{\rm ff,H_2})$, where $t_{\rm ff,H_2}$ is the freefall time at the density of the molecular transition. The timescale $t_{\rm ff,H_2}$ is independent of $\Sigma_{\rm H_2}$ by construction because it is assumed to be set by the density of the atomic-to-molecular transition, which, in turn, is set by the local ISM properties rather than the large-scale surface density. For average ISM densities significantly lower than the molecular transition density, $t_{\rm ff} \gg t_{\rm ff,H_2}$ and therefore $\tau_{\rm H_2} \sim t_{\rm ff,H_2}/\epsilon_{\rm ff}$ becomes independent of $\Sigma_{\rm H_2}$ and the molecular KSR becomes linear. To compare with our model below, we note that in the Elmegreen (2015, 2018) model the duration of star formation cycle is assumed to be $t_{\rm ff} + t_{\rm ff,H_2}$ and thus the integral star formation efficiency per cycle is $\epsilon = \epsilon_{\rm ff}(t_{\rm ff} + t_{\rm ff,H_2})/t_{\rm ff} \sim \epsilon_{\rm ff}$.

Although the models of Madore (2010) and Elmegreen (2015, 2018) are rather insightful, their prediction of the linear slope for the molecular KSR follows from two strong assumptions that the characteristic time of molecular gas evolution ($\tau_{\rm s}$ in Madore 2010 or $t_{\rm ff,H_2}$ in Elmegreen 2015, 2018) and the integral efficiency of star formation ϵ are all independent of the kiloparsec-scale gas surface density. Neither of these assumptions holds in our simulations. As was shown in Figure 6.9, ϵ increases with $\Sigma_{\rm H_2}$ because at higher $\Sigma_{\rm H_2}$, feedback must overcome stronger forces to disperse a region and thus a larger fraction of molecular gas must be converted into stars. At the same time, the lifetime of molecular gas also increases. Nevertheless, in our simulations with the $\alpha_{\rm vir,sf}$ threshold and efficient feedback, the molecular KSR slope is still linear. As we showed, the slope is linear not because ϵ and the lifetime of molecular gas are independent of $\Sigma_{\rm H_2}$, but because they scale with $\Sigma_{\rm H_2}$ similarly, and their trends nearly cancel.

Finally, Gnedin et al. (2014) argued that the linear molecular KSR on a $\gtrsim 1$ kpc scale is indicative of a linear relation on small scales (i.e., $\beta = 1$ in our notation). As emphasized in that paper, this argument follows from the assumption that the gas PDF is self-similar *and*

subscripts "CO" to "H_2."

that star-forming gas can be defined using a threshold that is a simple function of gas density. In this case, the slope of the global relation is directly inherited from the small-scale relation in the regime when $f_{\mathrm{sf,H_2}} \to 1$ (see "special case 1" in Appendix C.4). As we explicitly showed in Section 6.2.2, the gas PDF in simulations with efficient feedback is not self-similar. This lack of self-similarity decouples the slope of the large-scale molecular KSR from the slope of the small-scale star formation recipe. Moreover, we showed that the definition of star-forming gas plays an important role in the resulting scaling, because the choice of the star-formation threshold explicitly enters the relevant equations (see Equations 6.1–6.4). Finally, our results clearly show that the variation of $f_{\mathrm{sf,H_2}}$ with $\Sigma_{\mathrm{H_2}}$ is important, as it compensates the scaling of $\tau_\star$ resulting from the particular scaling of the gas PDF with $\Sigma_{\mathrm{H_2}}$.

6.4.2 Implications for the Interpretations of the Observed Molecular KSR

The framework presented in Section 6.3 is rather general and can help us elucidate the physical processes shaping the slope of the star formation relations observed in different galactic environments, on different spatial scales, and for different gas tracers.

According to our model, a linear KSR for molecular gas is expected as long as the lifetime of gas in the molecular state, $t_{\mathrm{H_2}}$, and the fraction of gas mass converted into stars over this lifetime, ϵ, exhibit similar trends with $\Sigma_{\mathrm{H_2}}$ so that these trends cancel in $\tau_{\mathrm{H_2}} \sim t_{\mathrm{H_2}}/\epsilon$. The mechanism that makes the $t_{\mathrm{H_2}}$ and ϵ trends similar must be rather generic, because the KSR for molecular gas is observed to be linear in diverse environments: from the average ISM of normal star-forming galaxies across the Hubble sequence (Utomo et al., 2017; Colombo et al., 2018) to low-metallicity dwarf galaxies (Bolatto et al., 2011; Jameson et al., 2016) and low-density galactic disk outskirts (Schruba et al., 2011).

An example of such a generic mechanism would be the efficient regulation of molecular stages by feedback. As we discussed above, feedback in our simulations makes evolution of molecular gas chaotic and the mass fraction of young stars formed by a given gas parcel

during one molecular cycle becomes proportional to the duration of the cycle, $\epsilon \propto t_{\rm H_2}$, which renders the molecular depletion time constant, $\tau_{\rm H_2} \sim t_{\rm H_2}/\epsilon$.

The molecular KSR steepens in high-density environments typical in starburst galaxies (e.g., Genzel et al., 2010, 2015; Leroy et al., 2013). In the context of our model, the steepening corresponds to the regime in which feedback is less efficient in dispersing star-forming regions and dense molecular gas, the second term in Equation (6.9) becomes comparable to the first, and ϵ is no longer proportional to $t_{\rm H_2}$, which makes molecular KSR nonlinear. In addition, $t_{\rm H_2}$ becomes shorter, due to either stronger gravity at higher gas surface densities or shorter turbulent crossing time at higher gas velocity dispersions.

Our model can also be used to interpret the KSR observed on scales much smaller than a kiloparsec and for gas states much denser than normal molecular gas. To this end, Equation (6.6) should be rewritten as

$$\tau_S \sim \frac{\tau_\star}{t_{\rm sf}} t_S \sim \frac{t_S}{\epsilon}, \tag{6.10}$$

where τ_S is the depletion time of gas in a given state S, t_S is the average time that a gas parcel spends in this state in a single cycle, and $\epsilon \sim t_{\rm sf}/\tau_\star$ is the fraction of gas converted into stars in one cycle through the state S. To apply this equation on different scales, its terms must be defined appropriately for the chosen scale.

For example, this equation can explain why the KSR becomes superlinear on the scales of individual star-forming regions, $\lesssim 50$ pc (e.g., Evans et al., 2009, 2014; Heiderman et al., 2010; Gutermuth et al., 2011). Surveys of star-forming giant molecular clouds (GMCs) select only molecular gas from the star-forming stage, and therefore, the t_S in Equation (6.10) for such objects equals $t_{\rm sf}$. According to Equation (6.10), in this case depletion time is simply $\tau_{\rm GMC} \sim \tau_\star$ and there is no longer feedback-imposed cancellation of the dependency in the $\tau_\star/t_{\rm sf}$ ratio on the large-scale ISM properties. In this picture, the slope of the small-scale KSR for star-forming regions is thus expected to reflect any dependence that $\tau_\star$ has on the properties of these regions. Note also that mass fluxes of gas on the scales of GMCs are

likely out of equilibrium, which will lead to a large variation of $\tau_{\rm H_2}$ (see Sections 2.3 and 4.5) and thus a large scatter of the KSR, as is indeed observed on small scales (e.g., Lee et al., 2016; Vutisalchavakul et al., 2016; Leroy et al., 2017). Other sources of scatter include the intrinsic variation of gas properties in star-forming regions, incomplete sampling of different stages of gas evolution, and decoupled evolution of gas and star formation tracers (Feldmann et al., 2011; Kruijssen & Longmore, 2014).

Equation (6.10) can also be applied to interpret the linear relation between the amount of dense molecular gas traced by HCN and the total SFR observed on a wide range of scales (Gao & Solomon, 2004b,a; Wu et al., 2005). If we consider Equation (6.10) on a $\lesssim 1$ pc scale, typical for HCN gas, the star formation efficiency, ϵ, will correspond to a fraction of a dense core mass that is eventually incorporated in a star (e.g., $\epsilon \gtrsim 50\%$ in Federrath et al., 2014). The lifetime of such cores, $t_{\rm HCN}$, will be controlled by their local freefall time, on which the star is formed, and the rate at which the remaining dense gas is dispersed by feedback. With these definitions of ϵ and $t_{\rm HCN}$, the interpretation of the linear relation for HCN gas is similar to that for all molecular gas except that the separation between the scale on which HCN gas resides ($\lesssim 1$ pc) and the scale on which the relation is measured (up to the scale of entire galaxies) is much larger. Because of such large scale separation, both ϵ and $t_{\rm HCN}$ are expected to be independent of the large scale and thus $\tau_{\rm HCN} \sim t_{\rm HCN}/\epsilon$ will also be independent of the total HCN gas mass inside this scale, rendering the relation linear. Note, however, that the linear relation for dense molecular gas can also be in part an observational effect, due to the selection of gas from a narrow density range in the PDF tail (Krumholz & Thompson, 2007) or from the densest parts of isothermal spherical clouds (Parmentier, 2017).

6.4.3 Effect of Threshold on the Efficiency of Feedback in Galaxy Simulations

Our results show that the choice of star formation threshold in galaxy simulations has a significant impact on the resulting slope of the KSR. Contrary to previous arguments in the literature, we show that in our simulations the slope of the molecular KSR does not merely reflect the density dependence of the star formation recipe adopted at the resolution scale, but depends on the density PDF of the ISM gas, which is strongly affected by feedback. Physically, the threshold determines both the locations where current star formation proceeds *and* the timescale and efficacy with which feedback can render star-forming gas non-star-forming. The strong effect that the choice of threshold has on the results implies that this choice must be made with great care, as was indeed demonstrated in related contexts by Governato et al. (2010) and Hopkins et al. (2013a).

As was shown in Sections 6.3.2–6.3.4, the role of feedback in making the KSR linear is twofold. First, feedback must efficiently disperse star-forming gas, which results in self-regulation to constant star formation efficiency per cycle, ϵ, independent of the rate at which gas is converted into stars in the star-forming state. Second, feedback must be efficient in converting molecular gas into the atomic state and establishing a correlation between $t_{\rm H_2}$ and ϵ which leads to a near cancellation of their trends with $\Sigma_{\rm H_2}$ in $\tau_{\rm H_2} \sim t_{\rm H_2}/\epsilon$ and thus to a near-linear KSR.

Our results indicate that the efficacy of stellar feedback in both of these aspects is much higher when the star formation threshold is based on $\alpha_{\rm vir}$, compared to the threshold based on constant gas density. Indeed, it is generally faster to render gas non-star-forming by driving subgrid turbulence and thereby increasing $\alpha_{\rm vir}$ than to actually disperse a star-forming region and decrease its density. Similarly, the lifetime of gas in the molecular phase is also controlled by feedback to a much larger degree, because gas becomes star-forming shortly after it becomes molecular and therefore has less time to become denser and is more

difficult to be dispersed.

The above arguments and our simulation results thus favor a star formation threshold in virial parameter (see also Hopkins et al., 2013a) rather than the more popular threshold in gas density. Not only is such a threshold well motivated by models of star formation in turbulent ISM, it also naturally leads to a linear KSR for molecular gas when feedback is efficient. The use of this threshold in practice is somewhat complicated by the necessity to estimate turbulent velocity dispersion at the resolution scale and generally requires modeling of turbulent velocities on subgrid scales. On the other hand, our results indicate that simulations that use density-based or the $f_{\rm H_2}$ star formation threshold should be interpreted with caution, especially on the sub-galactic scale, where the gas distribution is strongly affected by the choice of threshold.

The optimal choice of the threshold and other parameters of star formation and feedback models will of course depend on the scale on which these models are applied. In particular, the mechanism of the linear KSR origin on kiloparsec scales requires high resolution so that the transitions of gas between atomic, molecular, and star-forming states on sub-kiloparsec scales are sufficiently resolved. The resolution of state-of-the-art large-volume cosmological simulations, $\lesssim 1$ kpc, is not yet sufficient to capture these transitions, and thus, the slope of the KSR on kiloparsec scales reflects that adopted in the star formation prescription.

6.5 Summary

Using a suite of isolated $L_\star$ galaxy simulations, we explored the origin of the slope of the relation between surface densities of molecular gas and SFR averaged on kiloparsec scales. We showed that when feedback is efficient and the star formation threshold is based on the virial parameter, this relation has a near-linear slope, regardless of the slope adopted in the resolution-scale relation between star formation rate and gas density. Thus, in this regime, the slope of the KSR on kiloparsec scales does not reflect the slope on small scales, contrary

to a number of previous arguments in the literature.

We showed that the linear slope of the molecular KSR and its insensitivity to the local slope result from the particular scaling of the gas PDF with the gas surface density. When feedback is efficient in shaping the PDF, the PDF scaling leads to a cancellation of trends exhibited by the average depletion times in star-forming gas and by star-forming mass fractions. When feedback is not efficient, the gas PDF is shaped by dynamical processes, such as ISM turbulence and passage of spiral arms, and the KSR becomes dependent on the local slope and thus is not necessarily linear.

We explained these results using an analytical model based on the conservation of interstellar gas mass as the gas cycles between atomic, molecular, and star-forming states (see Section 6.3)—the model we previously used to explain the physical origin of the gas depletion time and its dependence on star formation efficiency and feedback strength (Chapters 4–5). Our main findings can be summarized as follows:

1. In Section 6.3.2, we show that when feedback is efficient in dispersing star-forming gas, the typical duration of star-forming stages, $t_{\rm sf}$, is proportional to the local depletion time of star-forming gas, $\tau_\star$, so that the molecular depletion time, $\tau_{\rm H_2} \propto t_{\rm H_2}\,\tau_\star/t_{\rm sf}$, becomes independent of $\tau_\star$. This explains why the molecular KSR is insensitive to the local slope adopted in the subgrid prescription for star formation, because only $\tau_\star$ depends explicitly on the local slope (see Equation 6.3), while the time the gas spends in molecular form during each cycle, $t_{\rm H_2}$, does not.

2. When feedback is inefficient, $t_{\rm sf}$ is controlled by dynamical processes that disperse star-forming gas: turbulent shear, differential rotation of galactic disk, expansion behind spiral arms, etc. Star formation, and thus $\tau_\star$, reflects the gas PDF shaped by these dynamical processes, but does not affect this PDF via feedback. Thus, the trend of $t_{\rm sf}$ is no longer proportional to $\tau_\star$, and the molecular KSR becomes dependent on the local slope of the star formation prescription β.

3. Simulations in the regime intermediate between the regimes of efficient and inefficient feedback exhibit intermediate behavior. Thus, in our fiducial simulation with $\epsilon_{\rm ff} = 1\%$, the effects of feedback and dynamical processes are both important, and therefore, the molecular KSR is close to linear, but its slope weakly depends on the local slope (see Figure 6.2 and Section 6.3.2).

4. We show that a near-linear molecular KSR emerges only in simulations that use a star formation threshold in the virial parameter. The molecular KSR generally has a nonlinear slope in simulations with the same efficiency and feedback strength, but that use a density-based threshold, with the slope steepening with the increasing threshold value. We argue that this is because in the latter simulations, the time between the moment gas becomes molecular and the moment it becomes star-forming is much longer. As a result, at lower $\Sigma_{\rm H_2}$, a smaller fraction of molecular gas is able to reach the star-forming state, and the molecular KSR therefore becomes steep.

The theoretical framework we use to interpret our simulation results is rather general and can be used to interpret observations as well. For example, it can shed light on the origin of star formation relations observed for different gas tracers, on different spatial scales, and in different galactic environments, as we discuss in Section 6.4.2.

The framework is also useful for interpreting and designing galaxy formation simulations. In particular, our results indicate that attention should be paid not only to the modeling of feedback but also to the modeling of star formation and, in particular, the choice of criteria used to identify star-forming gas. Our simulation results favor a criterion based on the local virial parameter instead of the commonly used density-based criterion (Section 6.4.3).

CONCLUSION

We presented an intuitive physical model that explains the origin of gas depletion times in galaxies. Our framework is based on the equation of gas mass conservation and the idea of gas cycling between diffuse ISM and the dense star-forming state on characteristic timescales set by dynamical and feedback processes that drive gas evolution.

The short, $\sim$ 10–100 Myr, timescales of the physical processes driving the evolution of gas indicate that the ISM is vigorously "boiling" when considered on the Gyrs-long global depletion timescale. The global depletion time is long, because on each evolution cycle every gas parcel spends only a small fraction of time in the star-forming state and converts only a small fraction of mass into stars, thus requiring a large number of evolution cycles for gas depletion. This explains why global depletion times are much longer than the dynamical timescales in the ISM, that determine the duration of a single evolution cycle. Global depletion times are also longer than local depletion times in actively star-forming regions because gas spends significant fraction of each cycle in the non-star-forming state.

We illustrated our framework using the results of isolated $L_\star$ galaxy simulations. Our framework can explain the dependence of the global depletion time on the parameters of star formation and feedback assumed on the resolution scale in our simulations. In particular, we showed that gas depletion time scales inversely with the local star formation efficiency when this efficiency is assumed to be small, and becomes independent of efficiency when the efficiency is large.

The latter regime is usually described as "self-regulation" by feedback in the literature (e.g., Dobbs et al., 2011a; Hopkins et al., 2013a, 2017a), and our model explains the physical mechanism of this behavior. Global depletion time becomes independent of the local depletion time and efficiency in star-forming regions when stellar feedback limits the duration of star-forming stages and makes them negligible compared to the entire duration of the evolution cycle. As efficiency increases, local depletion time decreases, but so does the

duration of star-forming stages because the amount of young stars sufficient to destroy each star-forming region forms sooner. These two trends cancel out making the total number of evolution cycles required for gas depletion and global depletion time independent of local star formation efficiency.

The insensitivity of global depletion time to local star formation efficiency implies that its value cannot be used to constrain the efficiency in the self-regulated regime. However, as we showed, the mass fraction of star-forming gas in such a regime scales inversely with the local star formation efficiency and therefore it can be used to constrain the efficiency in this regime.

Our model also sheds light on the origin of the linear correlation between SFR and molecular gas surface densities observed on kiloparsec and larger scales in normal star-forming (non-starburst) galaxies. We showed that the slope of this relation has a similar behavior as the KSR normalization (i.e. global depletion time): when feedback is efficient, the molecular KSR slope becomes independent of the density dependence slope adopted locally. This behaviour is a counter-example to the argument that the KSR on large scales reflects the slope adopted in the star formation prescription (Schaye & Dalla Vecchia, 2008; Gnedin et al., 2014), and as we show, its physical origin is analogous to that of the self-regulation of the KSR normalization.

The presented model for the gas depletion timescale is a generic framework that can be applied not only to galaxies as a whole but also to individual ISM patches with sizes ranging from $\sim$ kiloparsec to a typical size of star-forming regions, ~ 10 parsec. It can also be used to predict and interpret trends of gas depletion time with the ISM properties, gas and stellar surface densities, metallicity, galaxy morphology, and redshift.

As a final comment, we note that in the context of galaxy evolution over cosmological timescales, the actual gas depletion time is often considered to be unimportant. For example, galaxies from the star-forming sequence are predicted to form stars at the rates regulated by

gas accretion and gas loss in winds, because gas depletion times in such galaxies are short compared to other relevant timescales (e.g., Bouché et al., 2010; Davé et al., 2012; Lilly et al., 2013). Note, however, that dwarf galaxies and galaxies from the green valley consume gas on extremely long timescales of $\gtrsim$ 5–10 Gyr, and, therefore, their depletion times do affect their evolution. Moreover, at $z \gtrsim$ 5–6, when the age of the universe is $\lesssim$ 1 Gyr, the Gyr-long gas depletion times become comparable to the cosmological evolution timescale and will therefore play an important role in controlling the SFR during the early stages of galaxies evolution (e.g., Dekel & Mandelker, 2014; Peng & Maiolino, 2014). The framework for modeling gas depletion time presented in this dissertation thus opens a way to refine theoretical models of galaxy formation in this regime, which is particularly important in the upcoming era of the James Webb Space Telescope.

APPENDIX A

SUBGRID TURBULENCE AND NONUNIVERSAL STAR FORMATION EFFICIENCY

In this chapter, we present the results of a galaxy simulation with explicitly modeled unresolved turbulence (Section 3.2) and star formation efficiency (SFE) per freefall time, $\epsilon_{\rm ff}$, that is not assumed constant but varied in each cell depending on the predicted level of unresolved turbulence. We use these results both to illustrate the unresolved turbulence model and to explain the motivation behind our fiducial choice of the star formation threshold in gas virial parameter adopted in the rest of the dissertation.

We use the same initial conditions of an isolated $L_\star$ galaxy as in all other simulations presented in this dissertation (see Section 3.1). The main differences of the simulation presented in this chapter are the adopted model for continuously varied $\epsilon_{\rm ff}$ and the assumed parameters of stellar feedback. These differences are detailed in Section A.1.

In Sections A.2 and A.3, we discuss the distribution of gas properties controlling local star formation efficiencies in our simulation: gas density, temperature, and subgrid turbulent velocity. In Section A.4, we show that the adopted star formation model predicts a wide variation of SFE with star formation happening only in cold dense gas without requiring any ad hoc density or temperature thresholds. In Sections A.5, we compare our results with observations of star formation on GMC scale in the Milky Way and nearby galaxies. In Section A.6, we discuss our findings and compare them with the results of previous studies.

This chapter is based on the work published in Semenov et al. (2016).

A.1 Turbulence-based star formation efficiency and stellar feedback

Observational evidence of turbulence in molecular clouds motivated development of analytic models that relate star formation to the properties of self-gravitating MHD turbulence in GMCs (Krumholz & McKee, 2005; Padoan & Nordlund, 2011; Federrath & Klessen, 2012; Hennebelle & Chabrier, 2013). Generally, these models predict variation of star formation efficiency with virial parameter $\alpha_{\rm vir}$ and both sonic and Alfvénic Mach numbers. However, such models usually rely on strong assumptions about turbulence in GMCs, such as the gas density PDF being static, and the critical density for collapse, that is assumed to be independent of local flow configuration. Recent direct MHD simulations of turbulent molecular clouds do confirm the strong variation of star formation efficiency with $\alpha_{\rm vir}$ but reveal a surprising insensitivity to other cloud properties (Padoan et al., 2012, 2017). Specifically, Padoan et al. (2012) find that the star formation efficiency per free-fall time of simulated GMCs can be parametrized by the following simple formula[1]:

$$\epsilon_{\rm ff} = \epsilon_{\rm w} \exp\left(-\sqrt{\frac{\alpha_{\rm vir}}{0.53}}\right), \tag{A.1}$$

where $\epsilon_{\rm w}$ is a normalization coefficient that takes into account mass loss during formation of stars from protostellar objects and virial parameter of a cubical region with a size Δ is computed as for a uniform sphere of radius $R = \Delta/2$: $\alpha_{\rm vir} \equiv 5\sigma_{\rm t}^2 R/(3GM) \propto \sigma_{\rm t}^2/(\rho\Delta^2)$ (Bertoldi & McKee, 1992). The range of $\alpha_{\rm vir}$ probed by Padoan et al. (2012) covers a wide range of SFE, $\epsilon_{\rm ff} \sim 0.5$–$50\%$, that matches the observed variation, and the above fit holds on the scales of GMCs, few to hundred pc. Therefore, this fit can be directly applied in galaxy formation simulations if the turbulent velocity $\sigma_{\rm t}$ on GMC scale is known.

1. Padoan et al. (2012) fit their $\epsilon_{\rm ff}$ as a function of the ratio of freefall, $t_{\rm ff} = \sqrt{3\pi/32G\rho}$, and box-crossing times, $t_{\rm cr} = \Delta/2\sigma$: $\epsilon_{\rm ff} = \epsilon_{\rm w} \exp(-1.6 t_{\rm ff}/t_{\rm cr})$, which is equivalent to Equation (A.1) because by definition $\alpha_{\rm vir} = 5\sigma^2\Delta/6GM \approx 1.35(t_{\rm ff}/t_{\rm cr})^2$.

The fit to the numerical results given by Equation (A.1) agrees within a factor of ~ 2 with the results obtained by other authors (Clark et al., 2005; Price & Bate, 2009; Wang et al., 2010; Krumholz et al., 2012b; Federrath, 2015), although such comparison requires care, as SFE is defined and measured differently in different studies.

Equation (A.1) indicates that SFE is exponentially sensitive to $\alpha_{\rm vir}$ and therefore, if GMCs have a range of $\alpha_{\rm vir}$ values, the formula implies a wide variation of $\epsilon_{\rm ff}$. This variation and the relative insensitivity to thermal and Alfvénic Mach numbers can be understood as follows. At a fixed sonic Mach number M, increasing $\alpha_{\rm vir} \propto M^2/\rho$ is equivalent to decreasing the average density of gas, ρ. As the critical density at which gas becomes self-gravitating in physical units is constant, the critical overdensity relative to the average density increases with decreasing ρ. As a result, the SFE decreases with decreasing fraction of gas mass at overdensities above critical (e.g., Padoan & Nordlund, 2011). The dependence of SFE on sonic and Alfvénic Mach numbers is more complex because their increase results in both widening the density PDF of MHD turbulence and increasing of the critical overdensity (Padoan & Nordlund, 2011). Padoan et al. (2012) results show that these effects roughly cancel each other and SFE becomes relatively insensitive to the actual values of these Mach numbers, at least at high M explored by these authors.

In the regime of low-M turbulence the contribution of thermal pressure to the support against gravity cannot be neglected. To extend the above formula to this regime, we redefine $\alpha_{\rm vir}$ to take into account thermal pressure support (Chandrasekhar, 1951):

$$\alpha_{\rm vir} \equiv \frac{5\sigma_{\rm tot}^2 R}{3GM} \approx 9.35 \frac{(\sigma_{\rm tot}/10\ {\rm km\ s^{-1}})^2}{(n/100\ {\rm cm^{-3}})(\Delta/40\ {\rm pc})^2}, \tag{A.2}$$

where $\sigma_{\rm tot} = \sqrt{\sigma_{\rm t}^2 + c_{\rm s}^2}$ includes both the sound speed, $c_{\rm s}$, and subgrid turbulent velocity dispersion, $\sigma_{\rm t}$.

In the simulation presented here, we estimate $\sigma_{\rm t} = \sqrt{2K/\rho}$ from the SGS turbulence energy K and compute SFE in each cell using Equations (A.1) and (A.2) with the cell size

for the value of Δ. We adopt $\epsilon_{\rm w} = 0.9$ consistent with the results of Federrath et al. (2014) who showed that the mass loss due to outflows does not exceed 10% on the scale where Padoan et al. (2012) form sink particles.

We stress that all parametrizations and parameter values in the star formation model adopted in this chapter are not tuned but taken from the results of simulations of star formation in GMCs.

Stellar feedback is modeled as described in Section 3.3 but with a choice of parameters different from their fiducial values. In contrast to our fiducial model, we do not boost the SN radial momentum predicted using the Martizzi et al. (2015) results. This regime corresponds to the "weak feedback" case explored in Chapter 5 ($b = 0.2$). In addition, we convert 30% of the radial momentum predicted by Martizzi et al. (2015) directly into subgrid turbulent energy via the term $S_{\rm SN}$ in Equation (3.1). The combined effect of both these changes is that the rate of momentum injection into the ISM by each young stellar particle is ~ 7 times smaller than in our fiducial simulation explored in Chapters 4–6. As a result, the ISM of the galaxy presented here is not as flocculent as in our fiducial run (Figure 4.1) with some of the gas being able to form long-lived high-density clumps.

A.2 Spatial distribution of gas density and temperature

The star formation efficiency in our simulation is predicted based on the self-consistently evolved local density, temperature, and subgrid turbulent velocity. Thus, in this and the next sections we discuss the distribution of these quantities in our simulated disk with a special emphasis on the turbulent velocities. We also compare to observations the star formation efficiencies and rates predicted by our turbulence-based star formation prescription.

As can be seen in panels a and b of Figure A.1, by $t \approx 600$ Myr most of the disk volume is filled by the diffuse ($n \sim 0.1$–2 cm^{-3}) warm ($T \sim 10^4$ K) gas, while denser gas resides in spiral structures. The spiral arms travel around the disk compressing diffuse gas for certain

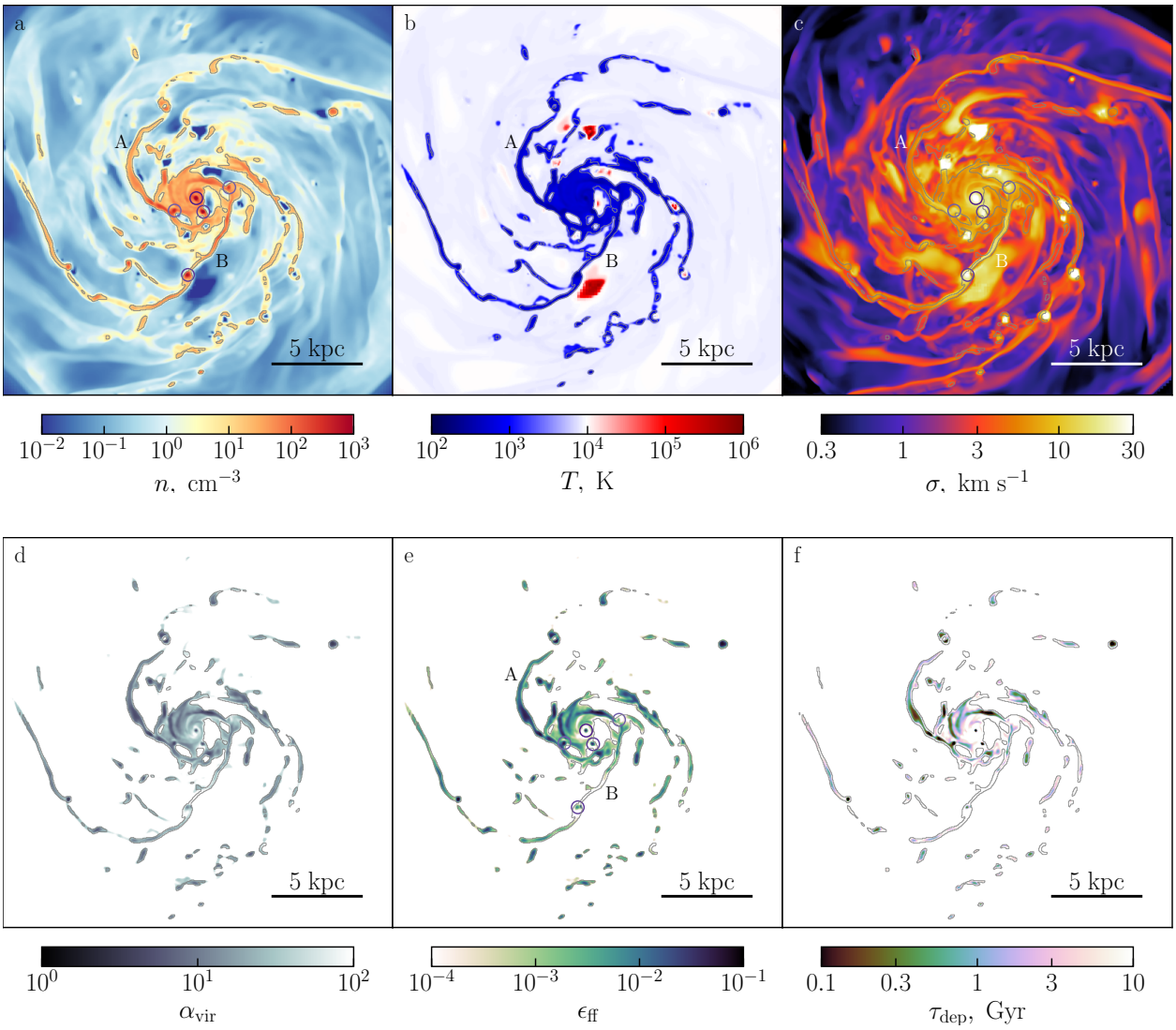

Figure A.1: Gaseous disk after 600 Myr of evolution. The top row shows from left to right slices of density (a), temperature (b), and subgrid rms turbulent velocity $\sigma_{\rm t} = \sqrt{2K/\rho}$ (c) in the disk plane. The temperature and rms velocities are derived from the thermal and subgrid turbulent energies respectively. The bottom row shows derived quantities related to the star formation prescription. Left panel (d) shows the virial parameter calculated using Equation (A.2). Only the gas mass was taken into account in estimation of $\alpha_{\rm vir}$. Equation (A.1) translates the derived $\alpha_{\rm vir}$ directly into SFE shown in the middle panel (e). Thin grey lines in all six panels indicate an iso-density contour that corresponds to $n = 10$ cm^{-3} and, therefore, encompasses cold dense gas. Thus, the predicted SFE exhibits strong spatial variation even in the cold gas. Right panel (f) shows the distribution of the local gas depletion time defined as $t_\star \equiv \rho/\dot{\rho}_\star$. Purple circles in panels a, c and e indicate dense gaseous clumps.

periods of time. Their motion relative to the diffuse gas is generally supersonic and these spiral waves are thus accompanied by shocks. As gas is being compressed, at $n \sim 5\,\mathrm{cm}^{-3}$ cooling by thermal excitation of C II and O I fine structure lines becomes efficient and gas rapidly cools down. This substantial cooling in spiral arms means that the pre-arm shocks are radiative and, therefore, they produce density jumps of orders of magnitude at the spiral arm interfaces.

The highest densities are reached in gaseous clumps. These clumps develop within the spiral arms due to local gravitational instabilities (e.g., Agertz et al., 2009b; Dekel et al., 2009; Bournaud et al., 2010). Several examples of such clumps are circled in Figure A.1a. In contrast to spiral arms, these high-density clumps are persistent physical objects rather than waves and so they may survive for a significant period of time. Examination of disk evolution shows that some of the clumps last up to a couple of disk revolutions, until they are disrupted by feedback or merged with the gas concentration in the disk center, as also found in a number of other studies (e.g., Genel et al., 2012). The long-lasting clumps may themselves drive the formation of the disk spiral structure (e.g., D'Onghia et al., 2013).

Hot rarefied bubbles of gas are another kind of prominent features seen in Figures A.1a and b. Some of these bubbles are inflated by exploding SNe in the regions with active star formation. Local injections of SNe energy and momentum affect the distribution of dense cold gas, as they disrupt gaseous clumps and tear spiral arms apart. Sometimes, as in the case of the large hot spot near the marker "B", the hot gas instead is being pushed into the disk plane from the hot halo ($T \approx T_{\rm vir} \sim 10^6$ K) in regions where the disk is thinned and its gas pressure is low.

A.3 Properties of the ISM turbulence

Given the importance of turbulence for our adopted star formation prescription, we begin with the discussion of the small-scale subgrid turbulence in the disk. Figure A.1c shows that

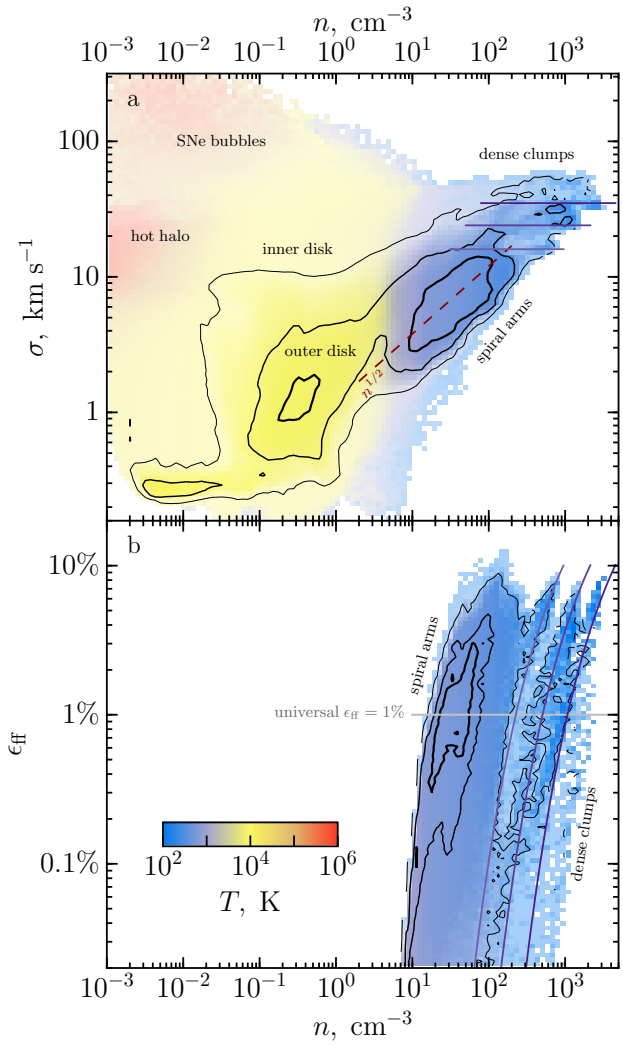

Figure A.2: The distribution of subgrid turbulent velocities σ_t (top panel) and the resulting star formation efficiencies per free-fall time ϵ_{ff} (bottom panel) at different densities. The distributions take into account all cells within cylindrical volume with $R < 20$ kpc (~ 6 initial scale radii) and $|z| < 1$ kpc (total height is ~ 6 initial scale heights) centered at the disk center. To increase statistics we average PDFs over 23 snapshots at 600 ± 10 Myr. Colors show the mass-weighted average temperature in bin and its intensity indicates the total mass in bin. Black contours enclose 25%, 68%, 95% (top) and 5%, 15%, 30% (bottom) of the current total gas mass. The turbulent velocities in cold spiral arms result from compression of diffuse gas and scale with density roughly as $\sigma_t \propto n^{1/2}$ (dashed red line given by Equation A.5). The linear structures at the upper right end of the $n - \sigma_t$ distribution correspond to dense gaseous clumps with $\sigma_t \approx$ const. Bottom panel shows the distribution of star formation efficiency computed using Equation (A.1). The adopted model naturally introduces an exponential cutoff at densities $n \sim 10\,\mathrm{cm}^{-3}$. If compared to universal ϵ_{ff} prescriptions turbulent model predicts broad variation by orders of magnitude, even though the average SFE is still $\sim 1\%$.

the subgrid model predicts the rms turbulent velocities, $\sigma_{\rm t}$, at the level of few to ten km s^{-1} on the scale of our smallest grid cells (40 pc). This result agrees with the observed velocity dispersion on GMC scales (Gammie et al., 1991; Bolatto et al., 2008; Sun et al., 2018), Milky Way dynamics (Kalberla & Dedes, 2008), and extragalactic HI data (Petric & Rupen, 2007; Tamburro et al., 2009), as well as with high resolution disk simulations (Agertz et al., 2009a). The turbulent velocities in our simulation increase towards the disk center where gravitational instabilities and frequent SNe maintain higher $\sigma_{\rm t}$ (Agertz et al., 2009a). High $\sigma_{\rm t}$ in bright spots that correspond to hot gas (10^5–10^6 K in Figure A.1b) are driven by expanding supernova bubbles. Dense cold spiral arms are typically more turbulent than the surrounding gas and therefore they are well traceable in the $\sigma_{\rm t}$ map, especially at $r > 5$ kpc. Enhanced turbulent velocities in the spiral arms result from the compression of inter-arm turbulence. Similarly, collapse of gas into dense gaseous clumps also results in high turbulent velocities (circled in Figures A.1a and c).

Quantitative conclusions about turbulence in different ISM phases can be drawn from the distribution of $\sigma_{\rm t}$ as a function of local gas density shown in Figure A.2a. In this plot several distinct phases are highlighted using color: the warm diffuse gas at $T \sim 10^4$ K (yellow), the cold dense gas in spiral arms and dense clumps (blue), and the hot tenuous gas at $T > 10^5$ K in the SNe bubbles and hot gaseous halo surrounding the disk (red). The contours enclosing different mass fractions show that most of the gas mass is in the warm and cold phases.

The warm gas phase corresponds to the diffuse gas between spiral arms and around the disk plane (white color in Figure A.1b). In this phase, turbulence is in an approximate equilibrium between production due to instabilities (e.g., Bournaud et al., 2010), sourcing by SNe and viscous dissipation into heat. Most of the gas mass in this phase resides on the disk outskirts ($r > 5$ kpc, labelled as the "outer disk") and the typical *subgrid* turbulent velocities are $\sim$ 1–2 km s^{-1} with a significant scatter of $\sim$ 0.5 dex. Note that the actual velocity dispersion of the disk would include resolved gas motions that are considerably

larger. As mentioned above, $\sigma_{\rm t}$ in the diffuse gas increases towards the disk center and may reach few tens to hundred km s^{-1}. Some of the warm gas with the largest velocity dispersions resides in expanding SNe bubbles, which drive turbulent velocities to the highest values found in our simulation, few hundred km s^{-1}.

The cold gas phase is, of course, the most interesting for star formation. The figure shows that such gas has typical subgrid turbulent velocities of $\sigma_{\rm t} \sim$ 3–10 km s^{-1}. This result agrees with the observed three-dimensional turbulent velocities in GMCs ($\sim$ 8 km s^{-1} on scales of 40 pc in Bolatto et al. 2008 and $\sim$ 2–20 km s^{-1} on 45–120 pc scales in Sun et al. 2018). We find that the actual value of $\sigma_{\rm t}$ correlates with the local compression rate, $-\nabla_i u_i$. This result indicates that the main source of turbulent energy in this regime is heating by compression of the diffuse gas (Robertson & Goldreich, 2012). Specifically, as a parcel of relaxed gas at $T \sim 10^4$ K enters a spiral arm both thermal and turbulent energies increase, as pressures associated with thermal and random motions do negative work during compression. However, at typical spiral arm densities the excess of thermal energy is quickly radiated away and the gas cools down. In contrast to thermal energy, turbulent energy dissipates on the local crossing time scale, $t_{\rm dec} \sim \Delta/\sigma_{\rm t}$ (e.g., Mac Low et al., 1998), which may be longer than the time spent by the gas parcel inside the spiral arm. The turbulent dissipation time scale and the time spent in the spiral arm can be estimated as

$$t_{\rm dec} \approx 4 \text{ Myr} \left(\frac{\Delta}{40 \text{ pc}}\right) \left(\frac{\sigma_{\rm t}}{10 \text{ km s}^{-1}}\right)^{-1}, \tag{A.3}$$

$$t_{\rm arm} \approx 3 \text{ Myr} \left(\frac{w_{\rm arm}}{300 \text{ pc}}\right) \left(\frac{v_{\rm arm}}{100 \text{ km s}^{-1}}\right)^{-1}, \tag{A.4}$$

where $w_{\rm arm}$ is a typical spiral arm width and $v_{\rm arm}$ is its typical velocity relative to the ambient gas. Here we neglect the fact that gas may enter into spiral arms at different angles and then travel along the spiral arm. We approximate the spiral arm passing time simply

as $w_{\rm arm}/v_{\rm arm}$ with typical values found in our simulation. Actual $t_{\rm arm}$ may vary around the estimation from Equation (A.4) depending on the local gas dynamics.

In the outer disk, where the pre-shocked gas has low turbulent velocities ($\sigma_{\rm t} \sim 1$ km s^{-1}), turbulence decays slowly ($t_{\rm dec} > t_{\rm arm}$) and $\sigma_{\rm t}$ increases in spiral arms. The bimodal distribution of mass in Figure A.2a indicates that the compression is fast and, therefore, the gas is either relaxed or resides in a spiral arm. In the inner disk where $\sigma_{\rm t}$ is high (~ 10 km s^{-1}) turbulence may decay during compression ($t_{\rm dec} \sim t_{\rm arm}$) and the increase of $\sigma_{\rm t}$ with density is shallower. Turbulence decays even more efficiently in the dense gaseous clumps where $\sigma_{\rm t}$ reaches few tens km s^{-1}. Their typical lifetime (> 100 Myr) is considerably longer than the turbulence decay time scale (few Myr from Equation A.3). As a result, $\sigma_{\rm t}$ reaches an equilibrium value, that weakly depends on density (purple lines in Figure A.2).

Star formation in our model proceeds in the cold dense gas. The pressure support in this gas is dominated by small-scale turbulent motions, as the sound speed in this phase is $c_{\rm s} \sim 1$ km s$^{-1}\sqrt{T/100\ {\rm K}}$ and the turbulent velocities ($\sigma_{\rm t} > 3$ km s^{-1}) are supersonic. Therefore, the gas in this regime forms stars with the efficiency that depends on $\sigma_{\rm t}$ (Equations A.1 and A.2). In our simulation, we find that the average $\sigma_{\rm t}$ in cold gas depends on density as (dashed red line in Figure A.2a)

$$\sigma_{\rm t} = 12\ {\rm km\ s^{-1}} \left(\frac{n}{100\ {\rm cm^{-3}}}\right)^{1/2}. \tag{A.5}$$

This scaling with density reflects the approximate balance between turbulence production on a local dynamical timescale and decay on a cell-crossing time. As gas gravity plays a major role in compressing the gas, we expect the former timescale to be $t_{\rm dyn} \propto (\rho G)^{-1/2}$, while the decay time is $t_{\rm dec} \sim \Delta/\sigma_{\rm t}$. In quasi-equilibrium, equating these two timescales results in the above scaling: $\sigma_{\rm t} \propto \rho^{1/2}$.

Note that this scaling implies that $\alpha_{\rm vir} \propto \sigma_{\rm t}^2/\rho \approx$ const, but it does not necessarily require that gas is in virial equilibrium with $\alpha_{\rm vir} \sim 1$. Instead, the value of $\alpha_{\rm vir}$ will depend

on the actual mix of processes that control local gas compression and dynamical production of turbulence. For instance, substituting Equation (A.5) into (A.2) shows that in the cold gas in our simulation $\alpha_{\rm vir} \sim 13$ on average.

Figure A.2a shows significant scatter around the average behavior expressed by Equation (A.5), ~ 0.3 dex. We find that this scatter is mostly due to the variation of local compression rate, $-\nabla_i u_i$. This offers hope that σ may be approximated in simulations without explicit subgrid turbulence modeling using dependencies of $\sigma_{\rm t}$ on density and $\nabla_i u_i$, that can be calibrated using simulations with such modeling. We will explore the relation of the local compression rate and the subgrid turbulent velocity in a future study.

In closing, we note that the above discussion shows that the key mechanism of turbulence production in star-forming regions of our disk is the compression of warm, transonic gas by spiral waves. This justifies the usage of the linear closure for the turbulent stress tensor τ_{ij}, as discussed in Section 3.2. In particular, production of subgrid turbulence from resolved motions is mostly important in diffuse gas with $T \sim 10^4$ K. This temperature corresponds to the sound speed of $c_{\rm s} \sim 10$ km s^{-1} and, therefore, the typical turbulent velocities in this gas (few km s^{-1}) are sub- or transonic, for which the linear closure for the stress tensor is more appropriate (Schmidt & Federrath, 2011).

A.4 Local star formation efficiency

In our simulation we derive the star formation efficiency $\epsilon_{\rm ff}$ in each cell using Equations (A.1) and (A.2). These equations parametrize local SFE via the virial parameter:

$$\alpha_{\rm vir} \propto \frac{\sigma_{\rm t}^2 + c_{\rm s}^2(T)}{\rho}, \tag{A.6}$$

where ρ, T and $\sigma_{\rm t}$ are the gas density, temperature, and subgrid turbulent velocity dispersion self-consistently evolved by the code. As can be seen in Figure A.1d the virial parameter of

modeled cells on scale of 40 pc is rather high and exhibits significant variation.

Given the exponential dependence of $\epsilon_{\rm ff}$ on the virial parameter, the $\alpha_{\rm vir}$ variation translates into an even wider spatial variation of $\epsilon_{\rm ff}$. This variation in the dense gas can be seen in panels e and f of Figure A.1 that show maps of $\epsilon_{\rm ff}$ and local gas depletion time relative to the gas denser than $n = 10$ cm^{-3}, shown by the thin gray contours.

The depletion time of molecular gas, and thus possibly $\epsilon_{\rm ff}$, is indeed observed to vary along the spiral arms of M51 (Meidt et al., 2013). As an extreme example of this spatial variation, compare the spiral arms denoted as A and B in the panel e of Figure A.1. Panels a and b of the figure show that the gas in these arms has similar density and temperature and, therefore, a common star formation model with a constant SFE above a fixed density threshold would predict the same efficiency and similar depletion time in both arms. However, in our simulation, the spiral arm A forms stars much more efficiently than the arm B due to lower turbulent velocity predicted by the subgrid model.

As discussed in Section A.3 the difference in $\sigma_{\rm t}$ originates from the variation in the local compression rates. The compression rate, in turn, may vary due to several reasons. First, gas may experience different compression in spiral arms depending on the large-scale dynamics and development of local disk instabilities. Second, turbulence may be suppressed (enhanced) in spiral arms due to local expansion (contraction) of gas along the arm. Third, spiral arms may be affected by hot gas from either SNe bubbles or the halo gas penetrating into the disk. In particular, as can be seen in Figure A.1b, the spiral arm B is adjacent to a bubble of hot gas in the downstream direction. The thermal pressure of this hot gas may contribute to compression.

In all three scenarios higher turbulent velocities result from stronger compression. More quantitative information about the SFE variation with density can be drawn from the phase diagram shown in Figure A.2b. The most noticeable features of this diagram are the sharp cutoff at $n \sim 10$ cm^{-3} and the orders of magnitude variation of $\epsilon_{\rm ff}$.

The exponential cutoff at $n \sim 10\,\mathrm{cm}^{-3}$ in our model arises naturally from the thermal support in warm diffuse gas. In particular, turbulent velocities in this phase are mostly subsonic and gas is supported against gravity mainly by its thermal pressure. This thermal support is codified in the definition of the virial parameter given by Equation (A.2), which results in the exponential suppression of $\epsilon_{\rm ff}$ in the diffuse gas, as the virial parameter becomes large: $\alpha_{\rm vir} \sim 10^3\,T_4/n_0$, where $T_4 = T/10^4$ K and $n_0 = n/1\,\mathrm{cm}^{-3}$.

In the cold phase, on the other hand, the turbulence is supersonic and its pressure provides the main support against gravity. The typical turbulent crossing time in this regime is of the order of the free-fall time: $\alpha_{\rm vir} \sim 10\ \sigma_{t1}^2/n_2$, where $\sigma_{t1} = \sigma_{\rm t}/10\,\mathrm{km\,s}^{-1}$ and $n_2 = n/100\,\mathrm{cm}^{-3}$. This value of $\alpha_{\rm vir}$ corresponds to $\epsilon_{\rm ff} \sim 1\%$, typical for observed star-forming regions. As a result, in the turbulent model only cold dense gas forms stars at a reasonably large efficiency. The transition from the negligible values of $\epsilon_{\rm ff}$ in the warm diffuse gas to $\epsilon_{\rm ff} \sim 1\%$ in the cold dense gas is sharp due to the abrupt drop in temperature. This sharp transition is responsible for the effective density threshold for efficient star formation at $n \sim 10\,\mathrm{cm}^{-3}$.

The most efficient star formation in our simulation occurs in the gas of density $n \sim$ 10–100 cm^{-3} in spiral arms and dense clumps. The average trend of $\sigma_{\rm t}$ with density ($\sigma_{\rm t} \propto n^{1/2}$ from Equation (A.5)) substituted into Equation (A.1) results in constant $\epsilon_{\rm ff} \sim 0.6\%$ independent of density, as $\alpha_{\rm vir} \propto \sigma_{\rm t}^2 n$. Therefore, the entire variation of $\epsilon_{\rm ff}$ around the average value originates from the scatter of modeled turbulent velocities around the average trend. As we mentioned before, this scatter is related to the variation of local compression rate.

Although the mass-weighted average $\epsilon_{\rm ff}$ in our disk is quite similar to the universal value $\epsilon_{\rm ff} \sim 1\%$ at $n > 10\,\mathrm{cm}^{-3}$ usually inferred from observations, the large spatial and temporal variation of the SFE predicted by our model may have important effects on galaxy evolution. For example, localization of efficient star formation in high-density regions may have a drastic

effect on the ability of galaxy to drive large-scale winds and affect the final morphology of the galaxy (e.g., Governato et al., 2010).

A.5 Comparison with observed GMCs

In order to check the viability of the star formation model used in this chapter, we compare its predictions to the SFRs in observed GMCs. Specifically, in Figure A.3 we compare the local gas surface density ($\Sigma_{\rm g} = \rho\Delta$) and the surface density of SFR ($\dot{\Sigma}_\star = \dot{\rho}_\star\Delta = \epsilon_{\rm ff}\rho\Delta/t_{\rm ff}$) in individual cells ($\Delta = 40$ pc) to the corresponding quantities measured in GMCs. For a fair comparison, we select the observed clouds with sizes in the range $\sim$ 5–100 pc, that straddle the cell size in our simulation.

The distribution of SFR in our disk has a sharp upper boundary with a wide tail towards lower rates. The observed local star-forming regions from Heiderman et al. (2010); Lada et al. (2010); Murray (2011) agree remarkably well with the upper envelope of our predicted distribution, whereas the extragalactic data agrees with the main mode of SF in our simulation. This may be because studies of the local GMCs focus on the regions with the most efficient star formation. On the other hand, blind surveys of star formation on GMC scales do reveal abundant gas with $\epsilon_{\rm ff} \ll 1\%$ both in the Milky Way (e.g., Lee et al., 2016; Vutisalchavakul et al., 2016) and in nearby star-forming galaxies (Utomo et al., 2018).

In contrast to the local surveys, GMCs in other galaxies are sampled more uniformly and do indicate prevalent dense gas with low star formation efficiency. For instance, the blue polygon in Figure A.3 summarizes the Rebolledo et al. (2015) results for three nearby spiral galaxies: NGC 6946, NGC 628 and M101. Their inferred SFRs do agree with the typical SFRs of the dense gas in our simulation. The observed SFR distribution in the Small Magellanic Cloud (SMC; pink polygon in Figure A.3; Bolatto et al., 2011) also reveals that most of its dense molecular gas forms stars rather inefficiently. However, the SMC is a dwarf galaxy with substantially different dynamics and significantly lower metallicity

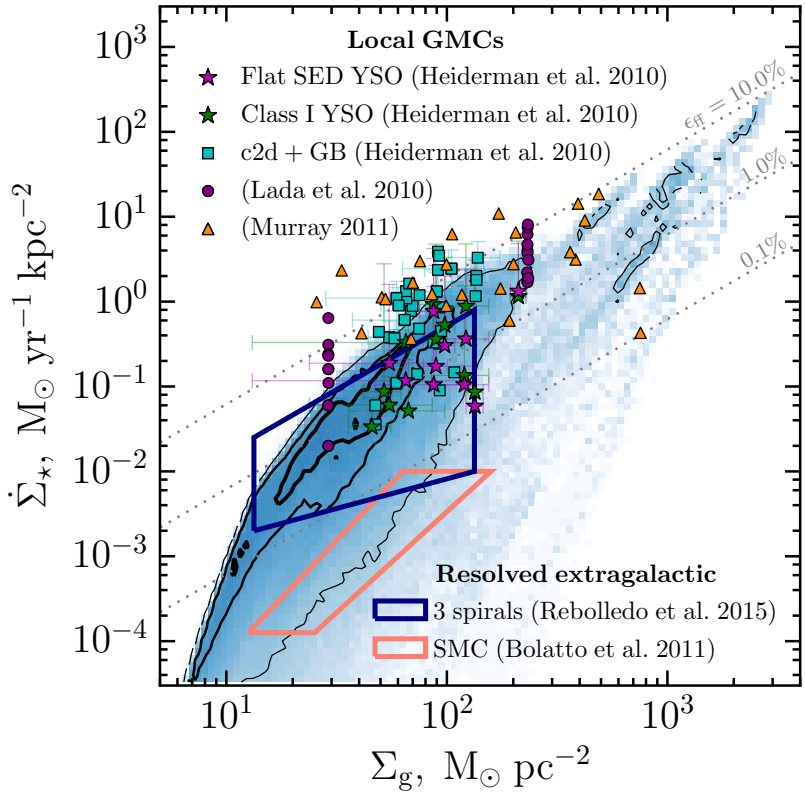

Figure A.3: Star formation rates obtained in our simulation are broadly consistent with observational data. Blue color indicates mass weighted distribution of cells in $\Sigma_{\rm g}$–$\dot{\Sigma}_\star$ plane. Black contours indicate 5%, 15% and 30% of the current total gaseous disk mass. Grey dotted lines correspond to constant values of $\epsilon_{\rm ff}$ in the simulated star-forming regions. The overplotted data points show different samples of GMCs in the Milky Way: Heiderman et al. (2010, stars and squares), Lada et al. (2010, circles) and Murray (2011, triangles). In this plot we show only GMCs with sizes in the range $\sim$ 5–100 pc that roughly correspond to our cell size, $\Delta = 40$ pc. Two polygons show resolved star formation rates in nearby galaxies. The blue one summarizes results of Rebolledo et al. (2015) for three nearby spirals: NGC 6946, NGC 628 and M101, while the pink one indicates star formation in the Small Magellanic Cloud (Bolatto et al., 2011). In the Rebolledo et al. (2015) sample we correct gas surface densities for helium assuming 25% mass fraction.

than the Milky Way, and therefore, its global SFR is considerably lower than that of our simulated galaxy. This discrepancy is yet another manifestation of the SFE variation and its dependence on galaxy properties.

A.6 Discussion

The results presented in this chapter show that our turbulence-based model for star formation predicts a wide variation of SFE from $\epsilon_{\rm ff} < 0.1\%$ to $\sim 10\%$. The predicted distribution of SFE at the resolution scale of our simulation, ~ 40 pc, agrees with the SFRs observed in star-forming regions on similar scales. As we show in Section C.2, such a model also predicts realistic molecular gas depletion times and a linear slope of molecular KSR in agreement with observations.[2] This agreement is non-trivial because on galactic scales our model predictions are determined by the small-scale spatial distribution of density and turbulent energy shaped by galactic evolution. Moreover, on the scales of individual star-forming regions (cells in simulations) the star formation rate is not tuned but is estimated from the local gas density and turbulent energy using predictions of GMC-scale simulations (see Section A.1). Once calibrated to reproduce the results of such simulations, parameters of both the subgrid turbulence model and the prescription for star formation remain fixed in our galactic disk simulations. Remarkably, the model predicts SFRs in agreement with observations without any additional tweaking of these parameters.

Although the agreement with the global SFR and gas depletion time can also be achieved in simulations that adopt universal $\epsilon_{\rm ff}$ recipes, such recipes require ad hoc assumptions about a value of $\epsilon_{\rm ff}$ and criteria for star formation. Also, as we show in Chapter 6, a commonly used recipe with a constant $\epsilon_{\rm ff}$ above a fixed density threshold leads to a molecular KSR

2. Note that the simulations presented in Section C.2 were run with stronger stellar feedback, $b = 1$ and 5, compared to $b = 0.2$ in the simulation presented in this chapter (see Section A.1). We checked that in the simulation with fiducial $b = 1$, the predicted distributions of $\sigma_{\rm t}$, $\epsilon_{\rm ff}$, and SFR on 40 pc scale remain in quantitative agreement with observations.

that is significantly steeper than the observed relation. In contrast, a simulation in which SFE varies in a way motivated by the model explored here, is able to reproduce the observed near-linear molecular KSR.

One important feature of the turbulence-based star formation model is the pronounced physical density threshold for star formation at $n_{\rm th} \sim 10\,{\rm cm}^{-3}$. Such density threshold is often set by hand in galaxy formation modeling. In our simulation, however, this threshold arises from the rapid drop in temperature as density increases beyond $n_{\rm th}$. Such threshold is quite similar to the effective thresholds in H_2-based models of star formation in which local SFE is modulated by the molecular gas mass fraction $f_{\rm H_2}$: $\dot{\rho}_\star = \epsilon_{\rm ff} f_{\rm H_2} \rho / t_{\rm ff}$ (Robertson & Kravtsov, 2008; Gnedin et al., 2009). In particular, the molecular fraction correlates with the cold gas abundance and, therefore, the threshold in our model corresponds to the density at which $f_{\rm H_2}$ rapidly increases. We thus also expect that $n_{\rm th}$ in our model should depend on gas metallicity similarly to the threshold in the $f_{\rm H_2}$-based models if gas thermodynamics is modeled properly to capture dependence of the net cooling function on gas metallicity.

Modeling of the star formation density threshold can be further improved if we take into account the effects of gas clumpiness on its net cooling rate: $\Lambda_{\rm cool} \propto C$, where $C \equiv \langle \rho^2 \rangle / \langle \rho \rangle^2 \geq 1$ is a clumping factor and brackets denote averaging over a certain spatial region. Galaxy formation simulations almost always assume $C = 1$ on the unresolved scales, but actual dense ISM can be quite clumpy in regions where turbulence is supersonic. Local clumping factor can be derived from the shape of the underlying subgrid density PDF, that can be estimated, for instance, with the aid of the subgrid turbulence model from the local parameters, such as effective Mach number. The clumping factor could then be accounted for in the calculation of the net cooling rate $\Lambda_{\rm cool}$. Overall, the star formation threshold should shift to lower values of density for $C > 1$.

The importance of turbulence for modeling star formation in galaxy formation simulations has been already recognized. Specifically, Hopkins et al. (2013a) developed a model for the

star formation threshold, in which star formation is allowed only in self-gravitating gas, $\alpha_{\rm vir} < 1$, but with a constant efficiency of $\epsilon_{\rm ff} = 100\%$. Even though their model also predicts significant localization of star formation, it substantially differs from the model presented in this chapter both technically and conceptually.

From the technical point of view, our subgrid turbulence model provides a more appropriate way to track local $\sigma_{\rm t}$ than an estimate based on the local velocity gradients on the resolution scale. Due to substantial effects of numerical viscosity on these scales such an estimate is not accurate.

More importantly, in our model we vary $\epsilon_{\rm ff}$ continuously with $\alpha_{\rm vir}$, as predicted by the Padoan et al. (2012) model, while the prescription of Hopkins et al. (2013a) adopts a fixed $\epsilon_{\rm ff} = 100\%$ for $\alpha_{\rm vir} < 1$ and $\epsilon_{\rm ff} = 0$ otherwise. For comparison, the Padoan et al. (2012) model predicts $\epsilon_{\rm ff} \approx 26\%$ for $\alpha_{\rm vir} \approx 1$ and $\epsilon_{\rm ff}$ reaches $> 99\%$ only at $\alpha_{\rm vir} \lesssim 0.1$. Moreover, in our model star formation can proceed in gravitationally unbound regions. In the turbulence-driven star formation, a given region may be globally unbound, but can contain local bound star-forming regions created by the turbulent cascade on small scales. For example, at $\alpha_{\rm vir} \approx 10$ the Padoan et al. (2012) model predicts $\epsilon_{\rm ff} \approx 1\%$, which is a healthy efficiency estimated for many GMCs (e.g., Krumholz et al., 2012a). Thus, the assumption of constant $\epsilon_{\rm ff}$ below a fixed $\alpha_{\rm vir}$ threshold is a simplification. As we show in Chapter 5, the predicted depletion times and mass-fractions and densities of star-forming gas do depend on the choice of $\epsilon_{\rm ff}$ and $\alpha_{\rm vir}$ threshold values.

Turbulent models of star formation with $\epsilon_{\rm ff}$ continuously varying with $\alpha_{\rm vir}$ were studied by other authors as well. In particular, Braun et al. (2014) examined a star formation prescription based on the model of Padoan & Nordlund (2011) coupled with a subgrid turbulence model in isolated disk simulations. Their subgrid model also included a prescription for multiphase ISM (Braun & Schmidt, 2012), and turbulent velocities were rescaled to the scale of cold self-gravitating clumps within this subgrid medium. Our disk models and star

formation implementations are sufficiently different, which complicates a direct comparison of our results. We only note that, although Braun et al. (2014) also found gas depletion time variation across the galaxy, in their case this variation was mostly due to the variation of $f_{\rm H_2}$, as the SF prescription based on the Padoan & Nordlund (2011) results predicted $\epsilon_{\rm ff} \sim 10\%$ in their star-forming regions with only a small scatter. The variation of the depletion time in our simulations is due to the wide variation of local $\epsilon_{\rm ff}$, which, in turn, is caused by the scatter in the virial parameter $\alpha_{\rm vir}$ that is dominated by the variation of turbulent velocities.

This origin of variation of SFE and local gas depletion times in our model is more in line with the models studied more recently by Braun & Schmidt (2015). These authors used a series of disk simulations similar to those in Braun et al. (2014), but examined several star formation prescriptions based on the local turbulent properties predicted by the subgrid model, including the model of Padoan et al. (2012, the "PHN" model), which we use in our work.

Although the overall level of turbulence predicted by the subgrid model in their disk is in qualitative agreement with our results, Braun & Schmidt (2015) found that the PHN model predicts values of SFE that are systematically too low: $\epsilon_{\rm ff} \lesssim 0.1\%$. According to Equation (A.1), such low $\epsilon_{\rm ff}$ should arise in regions with virial parameter: $\alpha_{\rm vir} \gtrsim 20$, which is significantly larger than the values estimated for the observed GMCs (e.g., Bolatto et al., 2008; Dobbs et al., 2011b). We believe that the origin of this discrepancy is in the subgrid model of multiphase gas distribution used by Braun & Schmidt (2015). In this model, the size of cold clouds is set by the condition of $\alpha_{\rm vir} = 1$, but at the same time, turbulent velocities are rescaled from the cell size to the cloud size assuming a turbulent cascade scaling which results in $\alpha_{\rm vir} \gtrsim 20$. This indicates that their model is not internally consistent.

Regardless of the difference in the actual values of $\epsilon_{\rm ff}$, the results of Braun & Schmidt (2015) are qualitatively consistent with our main finding that turbulence based star formation prescription predicts a wide variation of $\epsilon_{\rm ff}$.

Considering the results presented in this chapter, we conclude that the star formation prescription based on subgrid turbulence produces realistic star formation efficiencies and rates when applied in a galaxy-scale simulation. The lack of free parameters and the fact that this prescription relies on direct GMC-scale simulations put star formation modeling within this framework on a much firmer footing compared to standard recipes.

APPENDIX B

DEPLETION TIME MODEL DETAILS

B.1 Summary of model parameters

Our model equations,

$$\tau = (1+\xi)\tau_+ + \left(1 + \frac{\tau_+}{\tau_{-,\mathrm{d}}}\right)\frac{\tau_{\mathrm{ff}}}{\epsilon_{\mathrm{ff}}}, \tag{B.1}$$

$$f_{\mathrm{sf}} = \frac{1}{\epsilon_{\mathrm{ff}}}\frac{\tau_{\mathrm{ff}}}{\tau}, \tag{B.2}$$

are derived from the mass conservation equation between star-forming and non-star-forming states in the ISM, as explained in Chapter 2. The parameters used in our model and their meanings are summarized in Table B.1.

As we showed in Section 5.2.2, the model equations describe our simulation results even if we assume that all the model parameters, including τ_{ff}, are fixed. However, the accuracy of our model can be improved if the variation of τ_{ff} is incorporated.

To account for the variation of τ_{ff} with ξ and ϵ_{ff}, we note that star-forming gas is removed at a rate $\dot{M}_\star + F_{-,\mathrm{fb}} \propto (1+\xi)\epsilon_{\mathrm{ff}}$ and therefore τ_{ff} increases from $\tau_{\mathrm{ff}}^{\mathrm{dr}}$ to $\tau_{\mathrm{ff}}^{\mathrm{sr}}$ when $(1+\xi)\epsilon_{\mathrm{ff}}$ increases and the galaxy switches from the dynamics-regulation (thus the superscript "dr") to the self-regulation ("sr") regime. Note that the dependence of τ_{ff} on the combination $(1+\xi)\epsilon_{\mathrm{ff}}$ is itself a prediction of the model. This prediction is confirmed by the simulation results shown in Figure B.1, as τ_{ff} from all simulations with different ϵ_{ff} and ξ scale as a function of $(1+\xi)\epsilon_{\mathrm{ff}}$.

We then can interpolate τ_{ff} between $\tau_{\mathrm{ff}}^{\mathrm{dr}}$ and $\tau_{\mathrm{ff}}^{\mathrm{sr}}$ as a function of $\psi \equiv (1+\xi)\epsilon_{\mathrm{ff}}$ using a

Table B.1: Definitions of the quantities used in our model

Var.	Definition	Meaning	Model[a]
Modeled properties of the galaxy			
τ	$M_{\rm g}/\dot{M}_\star$	Global depletion time of total gas	Eq. (5.5)
$f_{\rm sf}$	$M_{\rm sf}/M_{\rm g}$	Star-forming gas mass fraction	Eq. (5.6)
$\tau_{\rm ff}$	$\langle 1/t_{\rm ff}\rangle_{\rm sf}^{-1}$	Mean freefall time in star-forming gas	Eq. (B.3–B.6)[b]
Model parameters			
$\tau_\star$	$M_{\rm sf}/\dot{M}_\star$	Depletion time of star-forming gas	$\tau_{\rm ff}/\epsilon_{\rm ff}$
τ_+	Eq. (2.4)	Dynamical timescale on which non-star-forming gas becomes star-forming	Eq. (B.8)
$\tau_{-,{\rm d}}$	Eq. (2.6)	Timescale on which star-forming gas is dynamically dispersed	Spline[c]
ξ	Eq. (2.8)	Average feedback mass-loading factor on the scale of star-forming regions	$60\ b^{0.75}$
$\tau_{\rm ff}^{\rm dr}$		$\tau_{\rm ff}$ in the dynamics-regulated regime	Spline[c]
$\tau_{\rm ff}^{\rm sr}$		$\tau_{\rm ff}$ in the self-regulated regime	Eq. (B.11)
Simulation parameters controlling local star formation and feedback			
$\epsilon_{\rm ff}$	Eq. (3.2)	Star formation efficiency per freefall time	
$\alpha_{\rm vir,sf}$	Sec. 3.3	Star formation threshold in virial parameter	
$n_{\rm sf}$	Sec. 3.3	Star formation threshold in gas density	
b	Sec. 3.3	Boost factor of momentum injected per SN	

[a] The last column indicates model predictions for τ, $f_{\rm sf}$, and $\tau_{\rm ff}$ and calibrated values for model parameters. Listed calibrations are obtained for the $\alpha_{\rm vir}$-based star formation threshold. Calibrations for the density-based threshold are provided at the end of Appendix B.1.

[b] The model predicts the position and the width of $\tau_{\rm ff}$ transition between $\tau_{\rm ff}^{\rm dr}$ and $\tau_{\rm ff}^{\rm sr}$.

[c] The values of $\tau_{-,{\rm d}}$ and $\tau_{\rm ff}^{\rm dr}$ as functions of $\alpha_{\rm vir}$ are obtained directly from the n–$\sigma_{\rm tot}$ distribution in our simulation with $\epsilon_{\rm ff} = 0.01\%$ and fiducial $b = 1$ and $\alpha_{\rm vir,sf} = 10$. We spline these values to obtain $\tau_{-,{\rm d}}(\alpha_{\rm vir,sf})$ and $\tau_{\rm ff}^{\rm dr}(\alpha_{\rm vir,sf})$ in simulations with different $\alpha_{\rm vir,sf}$ (see the end of Appendix B.1).

simple fitting formula shown with the solid line in Figure B.1:

$$\tau_{\rm ff} = \tau_{\rm ff}^{\rm dr} + f(\psi)\ (\tau_{\rm ff}^{\rm sr} - \tau_{\rm ff}^{\rm dr}), \tag{B.3}$$

$$f(\psi) = \frac{1}{\pi} \arctan\left(\frac{\log(\psi) - \log(\psi_{\rm cr})}{w}\right) + \frac{1}{2}, \tag{B.4}$$

in which the position, $\psi_{\rm cr}$, and the width, w, of transition can be predicted by our model. Specifically, from Equation (5.11), the transition happens at

$$\psi_{\rm cr} = \left(1 + \frac{\tau_+}{\tau_{-,\rm d}}\right) \frac{\overline{\tau_{\rm ff}}}{\tau_+}, \tag{B.5}$$

where, for simplicity, we assume average $\overline{\tau_{\rm ff}} = 4$ Myr, representative of our simulation results. The width of the transition can be estimated assuming that as $(1+\xi)\epsilon_{\rm ff}$ increases from very low values, the transition appears when $\dot{M}_\star + F_{-,\rm fb}$ becomes comparable to $F_{-,\rm d}$. This yields $(1+\xi)\epsilon_{\rm ff} \sim \tau_{\rm ff}^{\rm dr}/\tau_{-,\rm d}$ and thus the width is

$$w = \log(\psi_{\rm cr}) - \log(\tau_{\rm ff}^{\rm dr}/\tau_{-,\rm d}). \tag{B.6}$$

In the dynamics-regulation regime, i.e. at small $(1+\xi)\epsilon_{\rm ff}$, $\tau_{\rm ff}^{\rm dr}$ is determined by the high-density tail of the star-forming gas probability density function (PDF) and is independent of the star formation. In the self-regulation regime, i.e. at large $(1+\xi)\epsilon_{\rm ff}$, $\tau_{\rm ff}^{\rm sr}$ increases as the high-density tail is dispersed and the star-forming gas stays close to the star formation threshold. These trends of $\tau_{\rm ff}$ in the limiting regimes are apparent in the results of our simulation suite shown in Figure B.1.

Equations (B.3–B.6) augment the main equations of our model (B.1 and B.2) with the variation of $\tau_{\rm ff}$ with our model parameters: $\epsilon_{\rm ff}$, ξ, τ_+, $\tau_{-,\rm d}$, $\tau_{\rm ff}^{\rm sr}$, $\tau_{\rm ff}^{\rm dr}$. To calibrate the dependence of these parameters on our simulation parameters—i.e. local efficiency $\epsilon_{\rm ff}$, feedback

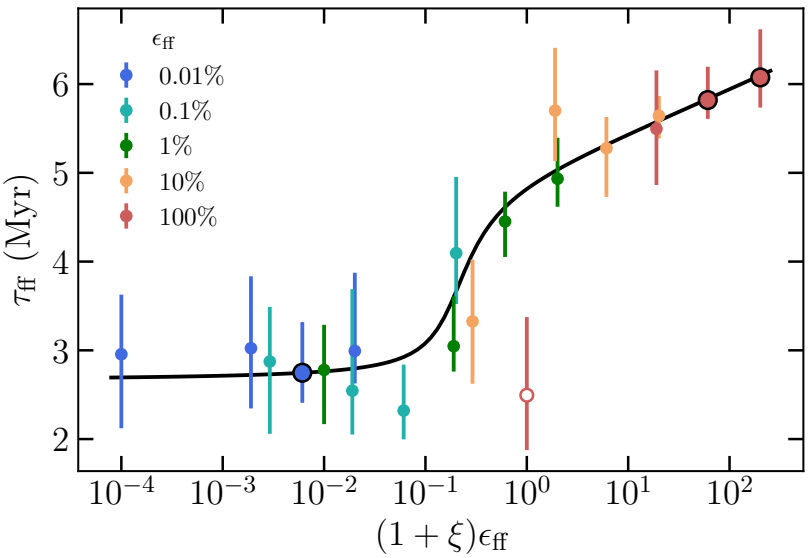

Figure B.1: Comparison of our model prediction for the variation of the freefall time in the star-forming gas, $\tau_{\rm ff}$, with the results of our simulations. To measure $\tau_{\rm ff}$ in the dynamics-regulation (small $(1+\xi)\epsilon_{\rm ff}$) and self-regulation (large $(1+\xi)\epsilon_{\rm ff}$) regimes and the parameters of the transition between these regimes, we use the the same runs that were used to calibrate $(1+\xi)\tau_+$ and $\tau_+/\tau_{-,\rm d}$ in Section 5.2.2 (indicated by circled points). The predictions of our model agree with the results of all simulations, except for the run with $b=0$ and $\epsilon_{\rm ff}=100\%$ (open circle), which does not remain in equilibrium owing to the rapid global gas consumption.

boost factor b, and star formation threshold $\alpha_{\rm vir,sf}$—we assume

$$\xi = \xi_0 b^{\beta}, \tag{B.7}$$

$$\tau_+ = (100\ {\rm Myr})\ (\alpha_{\rm vir,sf}/10)^{\gamma}, \tag{B.8}$$

$$\tau_{\rm ff}^{\rm sr} = (\tau_{\rm ff}^{\rm sr})_0\ (\psi/100)^a (\alpha_{\rm vir,sf}/10)^b. \tag{B.9}$$

Here we assume that at fiducial $\alpha_{\rm vir,sf} = 10$, $\tau_+ \sim 100$ Myr, as indicated by the results in Section 4.4. The value of τ_+ does depend on the star formation threshold because the threshold determines when the transition from the non-star-forming to the star-forming state happens in the evolution of each gas parcel. Equation (B.9) incorporates the dependence of $\tau_{\rm ff}^{\rm sr}$ on $\psi \equiv (1+\xi)\epsilon_{\rm ff}$ and star formation threshold discussed above.

Next, as detailed in Sections 5.2.2 and 5.2.2, we use three runs in the self-regulation regime with different feedback boost, b, and threshold, $\alpha_{\rm vir,sf}$, to estimate

$$(1+\xi)\tau_+ \sim (6\ {\rm Gyr})\ b^{0.75}\ (\alpha_{\rm vir,sf}/10)^{-0.5}, \tag{B.10}$$

$$\tau_{\rm ff}^{\rm sr} \sim (6\ {\rm Myr})\ (\psi/100)^{0.035}\ (\alpha_{\rm vir,sf}/10)^{0.4}, \tag{B.11}$$

which imply $\xi_0 = 60$, $\beta = 0.75$, $\gamma = -0.5$, $(\tau_{\rm ff}^{\rm sr})_0 = 6$ Myr, $a = 0.035$, and $b = 0.4$. Note, in particular, that $\xi \approx 60\ b^{0.75}$ which implies that our fiducial feedback ($b = 1$) is rather efficient and $\xi \gg 1$ in Equation (B.1).

Finally, the last two parameters, $\tau_{\rm ff}^{\rm dr}$ and $\tau_{-,\rm d}$, are measured as functions of $\alpha_{\rm vir,sf}$ directly from the n–$\sigma_{\rm tot}$ distribution in our run with $\epsilon_{\rm ff} = 0.01\%$ (bottom left panel of Figure 5.4). To this end, we note that because of the dynamics-regulation regime, this distribution would not change if $\alpha_{\rm vir,sf}$ was varied. We then measure $\tau_{\rm ff}^{\rm dr}(\alpha_{\rm vir,sf})$ as $\langle 1/t_{\rm ff}\rangle^{-1}$ in gas with $\alpha_{\rm vir} < \alpha_{\rm vir,sf}$ and $\tau_{-,\rm d}(\alpha_{\rm vir,sf})$ from $f_{\rm sf}(\alpha_{\rm vir,sf})$ using Equation (5.8): $\tau_{-,\rm d} = \tau_+/(1/f_{\rm sf} - 1)$. We spline $\tau_{\rm ff}^{\rm dr}(\alpha_{\rm vir,sf})$ and $f_{\rm sf}(\alpha_{\rm vir,sf})$ and show them with blue lines in the bottom two panels of the middle column in Figure 5.3. For example, at our fiducial threshold of $\alpha_{\rm vir,sf} = 10$,

$\tau_{\rm ff}^{\rm dr} \sim 2.5$ Myr and $f_{\rm sf} \sim 20\%$, which implies $\tau_{-,\rm d} \sim \tau_+/4 \sim 25$ Myr.

For the density-based star formation threshold we study only the dependence on $n_{\rm sf}$ but not on b. In other words, we replace Equations (B.7–B.9) with

$$\xi = \xi_0, \tag{B.12}$$

$$\tau_+ = (100 \text{ Myr}) \, (n_{\rm sf}/100 \text{ cm}^{-3})^{\gamma}, \tag{B.13}$$

$$\tau_{\rm ff}^{\rm sr} = (\tau_{\rm ff}^{\rm sr})_0 \, (n_{\rm sf}/100 \text{ cm}^{-3})^{-1/2}. \tag{B.14}$$

Note that the slope in the last equation is not a parameter because, in contrast to the $\alpha_{\rm vir}$-based threshold, the dependence of $\tau_{\rm ff}^{\rm sr}$ on the density threshold follows from definition, since in this regime all star-forming gas has density $\sim n_{\rm sf}$. For the same reason, $\tau_{\rm ff}^{\rm sr}$ does not depend on ψ for a density-based threshold.

The value $(\tau_{\rm ff}^{\rm sr})_0 = 5$ Myr is measured directly from the simulation with $\epsilon_{\rm ff} = 100\%$ and $n_{\rm sf} = 100$ cm^{-3}, and using another run with lower $n_{\rm sf}$ we get

$$(1+\xi)\tau_+ \sim (4.5 \text{ Gyr}) \, (n_{\rm sf}/100 \text{ cm}^{-3})^{0.5}, \tag{B.15}$$

and thus $\xi_0 = 45$ and $\gamma = 0.5$.

B.2 Model for molecular gas mass fraction

Similarly to star-forming gas above a given threshold, molecular gas distribution is also shaped by dynamical and feedback-driven gas flows. Therefore, similarly to Section 5.2.1, mass conservation can be considered for the molecular state of the ISM to derive the relation between the molecular mass fraction, $f_{\rm H_2} = M_{\rm H_2}/M_{\rm g}$, and the timescales of relevant processes supplying and removing molecular gas. In the equation for total molecular gas mass

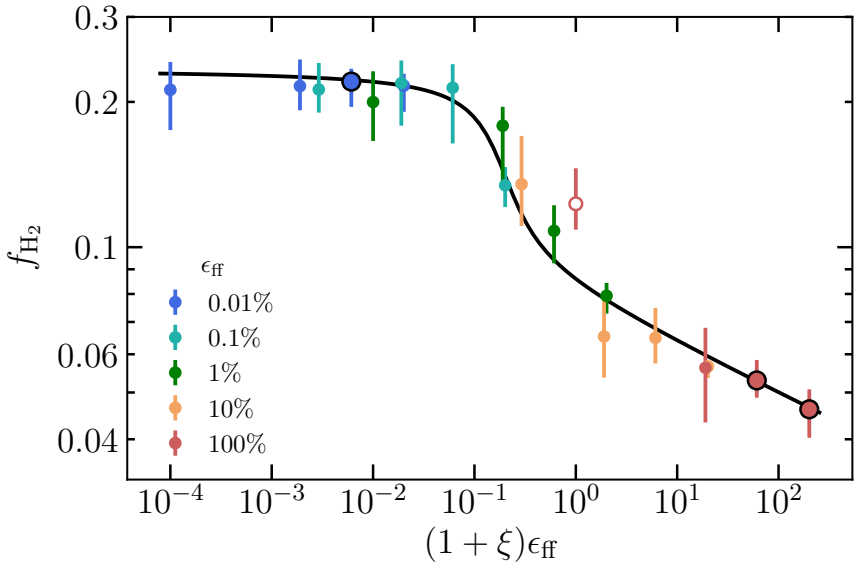

Figure B.2: Comparison of our model predictions for the variation of the global molecular mass fraction, $f_{\rm H_2} \equiv M_{\rm H_2}/M_{\rm g}$, with the results of the simulations. We average the total molecular mass in the simulations between 300 and 600 Myr, defining it as a sum of molecular masses in individual cells, which are computed using the Krumholz et al. (2009a) model (see Section 5.3 for details). To obtain model predictions, we interpolate $f_{\rm H_2}$ between its values at low and high $(1+\xi)\epsilon_{\rm ff}$ calibrated using the simulations in corresponding regimes (large circled points). The value of $(1+\xi)\epsilon_{\rm ff}$ at which this transition occurs and the width of the transition are predicted by the model (Equations B.5 and B.6). The open red circle indicates the run with $b = 0$ and $\epsilon_{\rm ff} = 100\%$, which does not remain in equilibrium owing to the rapid global gas consumption.

conservation,

$$\dot{M}_{\rm H_2} = F_+^{\rm H_2} - F_-^{\rm H_2} - \dot{M}_\star, \tag{B.16}$$

we parameterize relevant fluxes as

$$F_+^{\rm H_2} \equiv \frac{(1 - f_{\rm H_2})M_{\rm g}}{\tau_+^{\rm H_2}}, \tag{B.17}$$

$$F_-^{\rm H_2} \equiv \frac{f_{\rm H_2}M_{\rm g}}{\tau_-^{\rm H_2}}, \tag{B.18}$$

$$\dot{M}_\star \equiv \frac{f_{\rm sf}M_{\rm g}}{\tau_\star}. \tag{B.19}$$

That is, $F_+^{\rm H_2}$ and $F_-^{\rm H_2}$ are parameterized analogously to F_+ and F_- in Section 2.2 and the equation for $\dot{M}_\star$ repeats corresponding expression there.

Then, assuming steady state with $\dot{M}_{\rm H_2} \approx 0$, substitution of Equations (B.17)–(B.19) into Equation (B.16) yields

$$f_{\rm H_2} \approx \frac{1 - (\tau_+^{\rm H_2}/\tau_\star)f_{\rm sf}}{1 + (\tau_+^{\rm H_2}/\tau_-^{\rm H_2})}, \tag{B.20}$$

where $f_{\rm sf}$ can be computed using Equation (5.6).

At low $\epsilon_{\rm ff}$, $\tau_\star = \tau_{\rm ff}/\epsilon_{\rm ff} \to \infty$, and thus $f_{\rm H_2} \sim [1 + (\tau_+^{\rm H_2}/\tau_-^{\rm H_2})]^{-1}$, which is analogous to Equation (5.8), with $\tau_+^{\rm H_2}$ and $\tau_-^{\rm H_2}$ independent of star formation and feedback. At high $\epsilon_{\rm ff}$, all terms in Equation (B.20) are relevant and $\tau_-^{\rm H_2}$ depends on star formation and feedback parameters in a nontrivial way. This nontrivial dependence is more complex than a simple scaling with local depletion time $\tau_\star$—as was the case for the star-forming gas removal time $\tau_- \approx \tau_{-,\rm fb} = \tau_\star/\xi$—because $\tau_-^{\rm H_2}$ also depends on the dynamics of non-star-forming molecular gas and the details of its dissociation.

Thus, $\tau_-^{\rm H_2}$ cannot be easily related to the parameters of subgrid star formation and feedback, which does not allow to use Equation (B.20) for predicting how $f_{\rm H_2}$ depends on the parameters of star formation and feedback. However, this dependence can be calibrated using the same approach that we used to model variation of the freefall time in star-forming

gas, $\tau_{\rm ff}$ (Appendix B.1).

The approach is similar because the change of both $\tau_{\rm ff}$ and $f_{\rm H_2}$ reflects the response of the gas PDF to the changing feedback-induced flux parameterized by $(1+\xi)\epsilon_{\rm ff}$, and thus $f_{\rm H_2}$ variation with $(1+\xi)\epsilon_{\rm ff}$ is qualitatively similar to that of $\tau_{\rm ff}$. Indeed, as Figure B.2 shows, at $(1+\xi)\epsilon_{\rm ff} < 0.1$, the value of $f_{\rm H_2} \sim 20\%$ remains independent of ξ and $\epsilon_{\rm ff}$ because feedback is too weak to affect the gas PDF. Between $(1+\xi)\epsilon_{\rm ff} \sim 0.1$ and 1, the value of $f_{\rm H_2}$ decreases by a factor of 2 as feedback clears the high-density tail of the molecular gas distribution, and at $(1+\xi)\epsilon_{\rm ff} > 1$ the decrease of $f_{\rm H_2}$ slows down as the non-star-forming molecular gas accumulates above the star formation threshold. As the black curve shows, such variation of $f_{\rm H_2}$ with $(1+\xi)\epsilon_{\rm ff}$ can be approximated by the same fitting formula as the one used for $\tau_{\rm ff}$ (Equations B.3–B.6), with the limiting values of $f_{\rm H_2}$ at low and high $(1+\xi)\epsilon_{\rm ff}$ calibrated using the simulations: $f_{\rm H_2}^{\rm dr} = 23\%$ and $f_{\rm H_2}^{\rm sr} = 0.05\ [(1+\xi)\epsilon_{\rm ff}/60]^{-0.1}$.

The discussed effect of star formation and feedback on $f_{\rm H_2}$ also allows us to predict the variation of $f_{\rm H_2}$ with the star formation threshold. Namely, in the dynamics-regulation regime, we expect $f_{\rm H_2} \sim 23\%$ to be independent of the star formation threshold because the ISM gas distribution remains independent of star formation. In the self-regulation regime, $f_{\rm H_2}$ decreases when the threshold is shifted to higher $\alpha_{\rm vir,sf}$ or lower $n_{\rm sf}$, because the region in the n–$\sigma_{\rm tot}$ plane corresponding to the non-star-forming molecular gas shrinks.

APPENDIX C

MOLECULAR KSR — ADDITIONAL RESULTS

C.1 Dependence of molecular KSR slope on star formation and feedback parameters

Figure C.1 shows the dependencies of the molecular KSR slope on the efficiency of star formation per freefall time, $\epsilon_{\rm ff}$, and feedback strength in our simulations with $\alpha_{\rm vir,sf} = 10$ (blue lines) and $n_{\rm sf} = 100\,{\rm cm}^{-3}$ star formation thresholds (orange lines). In simulations with the $\alpha_{\rm vir,sf}$ threshold, the slope remains linear and only the normalization changes at different $\epsilon_{\rm ff}$ and feedback strength, as we showed in Figure 5.8. In simulations with the $n_{\rm sf}$ threshold, in contrast, the slope becomes steeper for larger values of $\epsilon_{\rm ff}$.

Figure C.2 shows the change of the molecular KSR slope in simulations with different values of the $\alpha_{\rm vir}$ and density threshold. For an $n_{\rm sf}$ threshold, the slope becomes shallower for lower $n_{\rm sf}$: for $n_{\rm sf} \gtrsim 30\,{\rm cm}^{-3}$, the slope is steeper than linear, but it becomes shallower than linear for smaller $n_{\rm sf}$ because non-molecular gas is identified as star-forming. For the $\alpha_{\rm vir,sf}$ thresholds, the sensitivity of the slope to the $\alpha_{\rm vir,sf}$ value is much weaker, although the slope still becomes somewhat shallower for very large values of $\alpha_{\rm vir}$.

C.2 Molecular KSR slope in simulations with explicitly modeled $\epsilon_{\rm ff}$

As was shown in Figure 6.1, our fiducial simulation with the $\alpha_{\rm vir,sf} = 10$ star formation threshold and constant $\epsilon_{\rm ff} = 1\%$ reproduces the observed near-linear slope of the molecular KSR. Figure C.3 shows that the molecular KSR remains linear when we vary $\epsilon_{\rm ff}$ using the

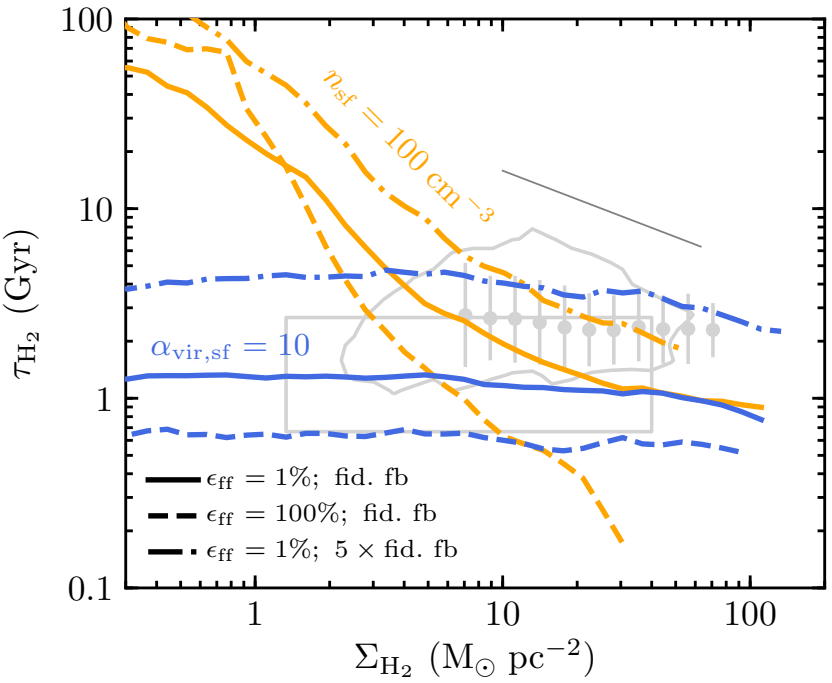

Figure C.1: Median depletion time of the molecular gas as a function of Σ_{H_2} in simulations with $\alpha_{vir,sf} = 10$ (blue lines) and $n_{sf} = 100$ cm^{-3} star formation thresholds (orange lines), and different values of local star formation efficiency ϵ_{ff} and feedback strength. Solid lines show τ_{H_2} for fiducial feedback strength and $\epsilon_{ff} = 1\%$ (i.e., the same as in Figures 6.1 and 6.3), dashed lines show τ_{H_2} for higher $\epsilon_{ff} = 100\%$, and dashed-dotted line show τ_{H_2} in simulations where the fiducial momentum input from supernovae is multiplied by a factor of 5 (see Section 3). Gray contours and points with error bars indicate the observed τ_{H_2} (see the legend in Figures 6.1), and the thin gray line shows the slope adopted in the star formation prescription: $\dot{\rho}_\star = \epsilon_{ff}\,\rho/t_{ff} \propto \rho^{1.5}$ and thus $\rho/\dot{\rho}_\star \propto \rho^{-0.5}$.

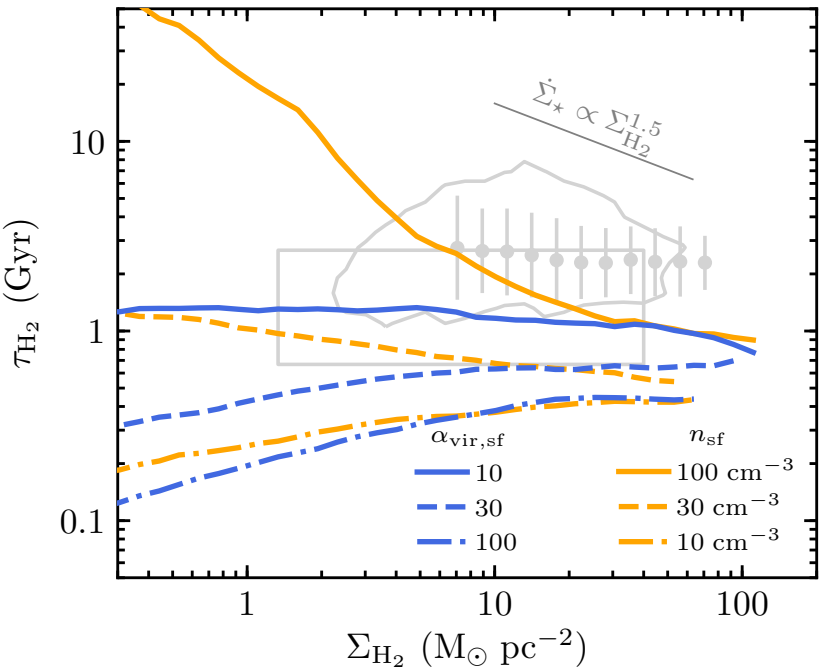

Figure C.2: Same as Figure C.1 but for different values of the star formation threshold: $\alpha_{\rm vir,sf} = 10$, 30, and 100 (blue lines), and $n_{\rm sf} = 100$, 30, and 10 cm^{-3} (orange lines).

fit to the simulation results of Padoan et al. (2012):

$$\epsilon_{\rm ff} = \exp(-\sqrt{\alpha_{\rm vir}/0.53}). \tag{C.1}$$

The figure also shows that the normalization of the KSR is affected by feedback strength in the same way as in the simulations with a sharp $\alpha_{\rm vir}$ threshold (see Appendix C.1).

The KSR in simulations with varied $\epsilon_{\rm ff}$ is similar to that in our fiducial simulation because our threshold choice, $\alpha_{\rm vir,sf} = 10$, approximates the exponential increase of $\epsilon_{\rm ff}$ for $\alpha_{\rm vir} \lesssim 10$ in Equation (C.1). A factor of ~ 2 difference in normalization can be explained by the somewhat higher $\epsilon_{\rm ff}$ values predicted by Equation (C.1), compared to our fiducial $\epsilon_{\rm ff} = 1\%$. Indeed, the $\alpha_{\rm vir}$ of the star-forming gas in our fiducial simulation ranges between 10 and ~ 2 (see Figure 6.4), and Equation (C.1) predicts $\epsilon_{\rm ff} \sim 1.3\%$–$14\%$ for such $\alpha_{\rm vir}$.

Interestingly, Lupi et al. (2018) used a star formation prescription with varying $\epsilon_{\rm ff}$ and

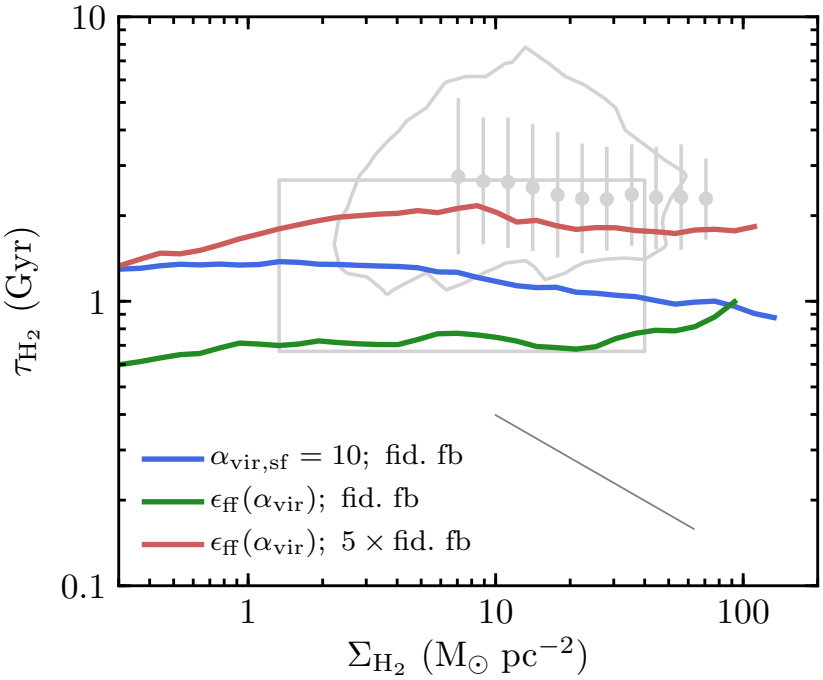

Figure C.3: Median depletion time of molecular gas as a function of Σ_{H_2} in simulations with ϵ_{ff} continuously varied according to Equation (C.1). Green and red lines show the results for our fiducial and 5 times stronger feedback, respectively. For reference, the blue line shows the results of our fiducial simulation with $\epsilon_{ff} = 1\%$ in gas defined by a sharp star formation threshold, $\alpha_{vir} < 10$. The thin gray line shows the slope of $\tau_{H_2} \propto \Sigma_{H_2}^{-0.5}$.

also found a shallow molecular KSR. Their KSR is somewhat steeper than linear, which can be due to a strong adopted dependence of ϵ_{ff} on density (see their Appendix A) and the resulting large effective local slope β. This result is consistent with our fiducial simulations with high β that also have a somewhat steeper than linear molecular KSR (see Figure 6.2). Lupi et al. (2018) also found that the molecular KSR slope depends on the assumptions about the unresolved clumping factor of the gas.

C.3 Dependence of molecular KSR slope on the averaging scale

In this work, we focused on the molecular KSR averaged on 1 kpc scales. The scale dependence of the KSR is an interesting related topic (e.g., Feldmann et al., 2011; Khoperskov & Vasiliev, 2017; Orr et al., 2018). Figure C.4 shows how the slope of the molecular KSR

in our fiducial simulation depends on the averaging scale. As expected, on scales close to the resolution scale of our simulation (40 pc), the KSR slope approaches the slope of the adopted star formation prescription, $\beta = 1.5$. However, as the averaging scale increases, the molecular KSR flattens and becomes near-linear at $\gtrsim 500$ pc scales. At any larger scale, the molecular KSR remains linear because when the slope is linear for a certain smoothing scale, it always remains linear on larger scales, as discussed for *special case 2* in Appendix C.4.

The transition scale of ~ 500 pc reflects the spatial coherence of star-forming and non-star-forming molecular gas in our simulations. Patches of < 500 pc size preferentially include only one of the states, while larger patches are sufficient to average between both states. This effect also leads to a scatter that increases on smaller scales (Kruijssen & Longmore, 2014). A similar coherence scale was also obtained for M33 by Schruba et al. (2011).

C.4 Derivation of the equations connecting molecular KSR with gas PDF and star formation on small scales

The depletion time of molecular gas in a single kiloparsec-scale patch can be expressed as a function of the local SFR density, $\dot{\rho}_\star$, and molecular gas mass in the patch, $M_{\rm H_2}$, as follows:

$$\frac{1}{\tau_{\rm H_2}} = \frac{\dot{\Sigma}_\star}{\Sigma_{\rm H_2}} = \frac{\dot{M}_\star}{M_{\rm H_2}} = \frac{1}{M_{\rm H_2}} \int \dot{\rho}_\star dV, \tag{C.2}$$

where integration is carried out over the patch volume. If we assume that $\dot{\rho}_\star$ is a power-law function of gas density, we can write $\dot{\rho}_\star$ as

$$\dot{\rho}_\star = A \rho^\beta \, \Theta_{\rm sf}(\rho, \mathbf{q}), \tag{C.3}$$

where $\Theta_{\rm sf}(\rho, \mathbf{q})$ is a function varying from 0 to 1 that defines star-forming gas as a function of gas density and a vector of other relevant properties $\mathbf{q}$. Furthermore, we can express the

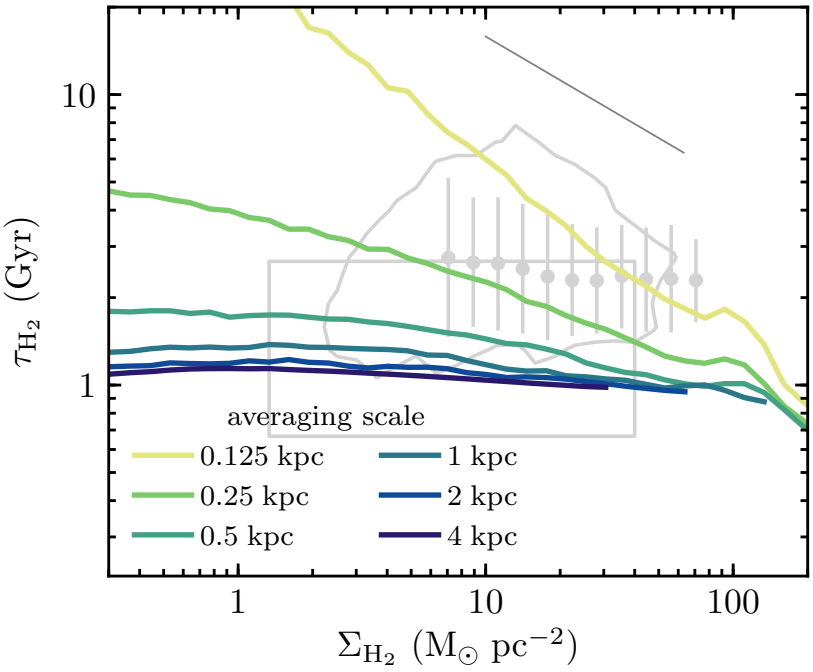

Figure C.4: The dependence of median $\tau_{H_2} = \Sigma_{H_2}/\dot{\Sigma}_\star$ on the width of the 2D Gaussian filter used to average the $\dot{\Sigma}_\star$ and Σ_{H_2} maps in our fiducial simulation with the $\alpha_{vir,sf} = 10$ star formation threshold and $\epsilon_{ff} = 1\%$. When the averaging scale is close to the resolution scale (40 pc), the molecular KSR slope approaches that adopted in the star formation prescription (shown by the gray line) and can become somewhat steeper due to the large scatter of τ_{H_2} on these small scales. At ~ 500 pc, the slope becomes near-linear (i.e. $\tau_{H_2} \approx$ const), and it stays linear at any larger scale.

volume element dV as

$$dV = \frac{\partial^2 V}{\partial \rho \partial \mathbf{q}} d\rho d\mathbf{q} = \frac{M_{\rm H_2}}{f_{\rm H_2}\rho} P_{\rm H_2}(\rho, \mathbf{q}) d\rho d\mathbf{q}, \tag{C.4}$$

where

$$P_{\rm H_2}(\rho, \mathbf{q}) = \frac{1}{M_{\rm H_2}} \frac{\partial^2 M_{\rm H_2}}{\partial \rho \partial \mathbf{q}} = \frac{f_{\rm H_2}\rho}{M_{\rm H_2}} \frac{\partial^2 V}{\partial \rho \partial \mathbf{q}} \tag{C.5}$$

is the mass-weighted distribution of molecular gas, and $f_{\rm H_2}$ is the local mass fraction of molecular gas, which can be a function of total gas density ρ, metallicity, radiation field, and other properties. In general, the variation of $f_{\rm H_2}$ in star-forming regions can be accounted for. However, most of the star-forming gas selected by our criteria has $f_{\rm H_2} \approx 1$, and therefore, we will adopt $f_{\rm H_2} = 1$ *in star-forming gas*. Under this assumption, Equations (C.2)–(C.4) can be combined to

$$\frac{1}{\tau_{\rm H_2}} = A \iint_0^\infty \rho^{\beta-1} \Theta_{\rm sf}(\rho, \mathbf{q}) P_{\rm H_2}(\rho, \mathbf{q}) d\rho d\mathbf{q}. \tag{C.6}$$

Equation (C.6) describes the relation between molecular gas depletion time and the PDF of molecular gas in a single ISM patch. The shape of $P_{\rm H_2}(\rho, \mathbf{q})$ in this equation can vary from patch to patch, leading to variation of $\tau_{\rm H_2}$. To obtain the molecular KSR, this equation must be averaged between patches with the same molecular surface density $\Sigma_{\rm H_2}$:

$$\left\langle \frac{1}{\tau_{\rm H_2}} \right\rangle = A \iint_0^\infty \rho^{\beta-1} \Theta_{\rm sf}(\rho, \mathbf{q}) \langle P_{\rm H_2} \rangle (\rho, \mathbf{q} | \Sigma_{\rm H_2}) d\rho d\mathbf{q}, \tag{C.7}$$

where the average shape of $\langle P_{\rm H_2} \rangle$ will depend on $\Sigma_{\rm H_2}$ and this dependence will define the dependence of the average $\tau_{\rm H_2}$ on $\Sigma_{\rm H_2}$, i.e. the slope of the molecular KSR.

Finally, omitting explicit averaging to simplify notation, Equation (C.7) can be rewritten as

$$\frac{1}{\tau_{\rm H_2}} = \frac{f_{\rm sf,H_2}}{\tau_\star}, \tag{C.8}$$

where, by definition,

$$f_{\mathrm{sf,H_2}} = \iint_0^\infty \Theta_{\mathrm{sf}}(\rho, \mathbf{q}) P_{\mathrm{H_2}}(\rho, \mathbf{q}|\Sigma_{\mathrm{H_2}}) d\rho d\mathbf{q} \tag{C.9}$$

is the star-forming mass fraction of molecular gas and

$$\frac{1}{\tau_\star} = A \int_0^\infty \rho^{\beta-1} P_{\mathrm{sf}}(\rho|\Sigma_{\mathrm{H_2}}) d\rho \tag{C.10}$$

is the inverse local depletion time $1/t_\star = \dot{\rho}_\star/\rho = A\rho^{\beta-1}$ averaged over the density PDF of star-forming gas:

$$P_{\mathrm{sf}}(\rho|\Sigma_{\mathrm{H_2}}) = \frac{\int \Theta_{\mathrm{sf}}(\rho, \mathbf{q}) P_{\mathrm{H_2}}(\rho, \mathbf{q}|\Sigma_{\mathrm{H_2}}) d\mathbf{q}}{\iint_0^\infty \Theta_{\mathrm{sf}}(\rho, \mathbf{q}) P_{\mathrm{H_2}}(\rho, \mathbf{q}|\Sigma_{\mathrm{H_2}}) d\rho d\mathbf{q}}. \tag{C.11}$$

Equations (C.8–C.11) show that the connection between the slope of the $\dot{\Sigma}_\star$–$\Sigma_{\mathrm{H_2}}$ relation on kiloparsec scales and its local value β is nontrivial and in general depends on the scaling of gas PDF with $\Sigma_{\mathrm{H_2}}$. However, in some special cases studied previously in the literature, these equations predict a direct relation between global and local slopes. In these special cases, $f_{\mathrm{sf,H_2}}$ is assumed to be independent of $\Sigma_{\mathrm{H_2}}$ as would be the case if, e.g., all molecular gas were star-forming, $f_{\mathrm{sf,H_2}} = 1$. The KSR slope is then determined only by the behavior of the integral in the definition of $\tau_\star$ (Equation C.10).

Special case 1. Star-forming gas PDF scales self-similarly with $\Sigma_{\mathrm{H_2}}$: $P_{\mathrm{sf}}(\rho|\Sigma_{\mathrm{H_2}}) = F(\rho/\Sigma_{\mathrm{H_2}})/\Sigma_{\mathrm{H_2}}$. In this case, $\tau_\star$ inherits the dependence on $\Sigma_{\mathrm{H_2}}$ from the local star formation relation, $1/t_\star \propto \rho^{\beta-1}$:

$$\frac{1}{\tau_\star} = A\Sigma_{\mathrm{H_2}}^{\beta-1} \int_0^\infty x^{\beta-1} F(x) dx \propto \Sigma_{\mathrm{H_2}}^{\beta-1}, \tag{C.12}$$

and therefore the KSR inherits the local slope β: $\dot{\Sigma}_\star \propto \Sigma_{\mathrm{H_2}}^{\beta}$ (cf. Gnedin et al., 2014).

Special case 2. Local relation is linear, $\beta = 1$. In this case,

$$\frac{1}{\tau_\star} = A \int_0^\infty P_{\rm sf}(\rho|\Sigma_{\rm H_2}) d\rho = A, \tag{C.13}$$

and the KSR is also linear: $\dot{\Sigma}_\star = A f_{\rm sf,H_2} \Sigma_{\rm H_2}$ (cf. Gnedin et al., 2014). Physically, when $\beta = 1$, the local depletion time $t_\star = \rho/\dot{\rho}_\star = \rho^{1-\beta}/A = A^{-1}$ is constant in all star-forming gas and thus its average $\tau_\star = t_\star = A^{-1}$ is independent of $\Sigma_{\rm H_2}$. This means, for example, that the linear molecular KSR observed on kiloparsec scales will remain linear when averaged on any larger scale (see Figure C.4).

Special case 3. The shape of the star-forming gas PDF is independent of $\Sigma_{\rm H_2}$: $P_{\rm sf}(\rho|\Sigma_{\rm H_2}) = F(\rho)$ and

$$\frac{1}{\tau_\star} = A \int_0^\infty \rho^{\beta-1} F(\rho) d\rho \tag{C.14}$$

becomes independent of $\Sigma_{\rm H_2}$, and therefore the KSR becomes linear regardless of the local slope β: $\dot{\Sigma}_\star \propto \Sigma_{\rm H_2}$. This is a more general case of the "counting argument," in which all star-forming regions are assumed to have the same density ρ_0 so that $P_{\rm sf}(\rho|\Sigma_{\rm H_2}) = \delta(\rho - \rho_0)$.

REFERENCES

Agertz, O., & Kravtsov, A. V. 2015, ApJ, 804, 18

—. 2016, ApJ, 824, 79

Agertz, O., Kravtsov, A. V., Leitner, S. N., & Gnedin, N. Y. 2013, ApJ, 770, 25

Agertz, O., Lake, G., Teyssier, R., et al. 2009a, MNRAS, 392, 294

Agertz, O., Romeo, A. B., & Grisdale, K. 2015, MNRAS, 449, 2156

Agertz, O., Teyssier, R., & Moore, B. 2009b, MNRAS, 397, L64

Benincasa, S. M., Wadsley, J., Couchman, H. M. P., & Keller, B. W. 2016, MNRAS, 462, 3053

Bertoldi, F., & McKee, C. F. 1992, ApJ, 395, 140

Bigiel, F., Leroy, A., Walter, F., et al. 2010, AJ, 140, 1194

—. 2008, AJ, 136, 2846

Bigiel, F., Leroy, A. K., Walter, F., et al. 2011, ApJLetters, 730, L13

Bissantz, N., Englmaier, P., & Gerhard, O. 2003, MNRAS, 340, 949

Bolatto, A. D., Leroy, A. K., Rosolowsky, E., Walter, F., & Blitz, L. 2008, ApJ, 686, 948

Bolatto, A. D., Leroy, A. K., Jameson, K., et al. 2011, ApJ, 741, 12

Bolatto, A. D., Wong, T., Utomo, D., et al. 2017, ApJ, 846, 159

Bouché, N., Cresci, G., Davies, R., et al. 2007, ApJ, 671, 303

Bouché, N., Dekel, A., Genzel, R., et al. 2010, ApJ, 718, 1001

Bournaud, F., Elmegreen, B. G., Teyssier, R., Block, D. L., & Puerari, I. 2010, MNRAS, 409, 1088

Braun, H., & Schmidt, W. 2012, MNRAS, 421, 1838

—. 2015, MNRAS, 454, 1545

Braun, H., Schmidt, W., Niemeyer, J. C., & Almgren, A. S. 2014, MNRAS, 442, 3407

Braun, R. 2012, ApJ, 749, 87

Capelo, P. R., Bovino, S., Lupi, A., Schleicher, D. R. G., & Grassi, T. 2018, MNRAS, 475, 3283

Cen, R., & Ostriker, J. P. 1992, ApJLetters, 399, L113

Chabrier, G. 2003, PASP, 115, 763

Chandrasekhar, S. 1951, Proceedings of the Royal Society of London Series A, 210, 26

Christensen, C., Quinn, T., Governato, F., et al. 2012, MNRAS, 425, 3058

Clark, P. C., Bonnell, I. A., Zinnecker, H., & Bate, M. R. 2005, MNRAS, 359, 809

Colella, P., & Glaz, H. M. 1985, Journal of Computational Physics, 59, 264

Colombo, D., Kalinova, V., Utomo, D., et al. 2018, MNRAS, 475, 1791

Daddi, E., Elbaz, D., Walter, F., et al. 2010, ApJLetters, 714, L118

Davé, R., Finlator, K., & Oppenheimer, B. D. 2012, MNRAS, 421, 98

Davis, B. L., Kennefick, D., Kennefick, J., et al. 2015, ApJLetters, 802, L13

de los Reyes, M. A. C., & Kennicutt, Robert C., J. 2019, ApJ, 872, 16

Dekel, A., & Mandelker, N. 2014, MNRAS, 444, 2071

Dekel, A., Sari, R., & Ceverino, D. 2009, ApJ, 703, 785

Diesing, R., & Caprioli, D. 2018, Physical Review Letters, 121, 091101

Dobbs, C. L., Burkert, A., & Pringle, J. E. 2011a, MNRAS, 417, 1318

—. 2011b, MNRAS, 413, 2935

Dobbs, C. L., Pringle, J. E., & Burkert, A. 2012, MNRAS, 425, 2157

Dobbs, C. L., Pringle, J. E., & Duarte-Cabral, A. 2015, MNRAS, 446, 3608

D'Onghia, E., Vogelsberger, M., & Hernquist, L. 2013, ApJ, 766, 34

Elmegreen, B. G. 2002, ApJ, 577, 206

—. 2015, ApJLetters, 814, L30

—. 2018, ApJ, 854, 16

Evans, II, N. J., Heiderman, A., & Vutisalchavakul, N. 2014, ApJ, 782, 114

Evans, II, N. J., Dunham, M. M., Jørgensen, J. K., et al. 2009, ApJS, 181, 321

Faucher-Giguère, C.-A., Quataert, E., & Hopkins, P. F. 2013, MNRAS, 433, 1970

Federrath, C. 2013, MNRAS, 436, 3167

Federrath, C. 2015, MNRAS, 450, 4035

Federrath, C., & Klessen, R. S. 2012, ApJ, 761, 156

Federrath, C., Schrön, M., Banerjee, R., & Klessen, R. S. 2014, ApJ, 790, 128

Feldmann, R., & Gnedin, N. Y. 2011, ApJLetters, 727, L12

Feldmann, R., Gnedin, N. Y., & Kravtsov, A. V. 2011, ApJ, 732, 115

Froebrich, D., & Rowles, J. 2010, MNRAS, 406, 1350

Gammie, C. F., & Ostriker, E. C. 1996, ApJ, 466, 814

Gammie, C. F., Ostriker, J. P., & Jog, C. J. 1991, ApJ, 378, 565

Gao, Y., & Solomon, P. M. 2004a, ApJS, 152, 63

—. 2004b, ApJ, 606, 271

Garnier, E., Adams, N., & Sagaut, P. 2009, Large Eddy Simulation for Compressible Flows (Springer Netherlands)

Gavagnin, E., Bleuler, A., Rosdahl, J., & Teyssier, R. 2017, ArXiv e-prints, arXiv:1701.07982

Genel, S., Naab, T., Genzel, R., et al. 2012, ApJ, 745, 11

Gentry, E. S., Krumholz, M. R., Dekel, A., & Madau, P. 2017, MNRAS, 465, 2471

Gentry, E. S., Krumholz, M. R., Madau, P., & Lupi, A. 2019, MNRAS, 483, 3647

Genzel, R., Tacconi, L. J., Gracia-Carpio, J., et al. 2010, MNRAS, 407, 2091

Genzel, R., Tacconi, L. J., Lutz, D., et al. 2015, ApJ, 800, 20

Gnedin, N. Y., & Hollon, N. 2012, ApJS, 202, 13

Gnedin, N. Y., & Kravtsov, A. V. 2011, ApJ, 728, 88

Gnedin, N. Y., Tasker, E. J., & Fujimoto, Y. 2014, ApJLetters, 787, L7

Gnedin, N. Y., Tassis, K., & Kravtsov, A. V. 2009, ApJ, 697, 55

Governato, F., Brook, C., Mayer, L., et al. 2010, Nature, 463, 203

Grand, R. J. J., Gómez, F. A., Marinacci, F., et al. 2017, MNRAS, 467, 179

Grisdale, K., Agertz, O., Romeo, A. B., Renaud, F., & Read, J. I. 2017, MNRAS, 466, 1093

Gutermuth, R. A., Pipher, J. L., Megeath, S. T., et al. 2011, ApJ, 739, 84

Hayward, C. C., & Hopkins, P. F. 2017, MNRAS, 465, 1682

Heiderman, A., Evans, II, N. J., Allen, L. E., Huard, T., & Heyer, M. 2010, ApJ, 723, 1019

Heiles, C., & Troland, T. H. 2003, ApJ, 586, 1067

Hennebelle, P., & Chabrier, G. 2013, ApJ, 770, 150

Hernquist, L. 1990, ApJ, 356, 359

Heyer, M., & Dame, T. M. 2015, ARA&A, 53, 583

Heyer, M., Gutermuth, R., Urquhart, J. S., et al. 2016, A&A, 588, A29

Hopkins, P. F., Kereš, D., Oñorbe, J., et al. 2014, MNRAS, 445, 581

Hopkins, P. F., Narayanan, D., & Murray, N. 2013a, MNRAS, 432, 2647

Hopkins, P. F., Narayanan, D., Murray, N., & Quataert, E. 2013b, MNRAS, 433, 69

Hopkins, P. F., Quataert, E., & Murray, N. 2011, MNRAS, 417, 950

—. 2012, MNRAS, 421, 3488

Hopkins, P. F., Wetzel, A., Keres, D., et al. 2017a, ArXiv e-prints, arXiv:1702.06148

—. 2017b, ArXiv e-prints, arXiv:1707.07010

Hunter, J. D. 2007, CSE, 9, 90

Jameson, K. E., Bolatto, A. D., Leroy, A. K., et al. 2016, ApJ, 825, 12

Jones, E., Oliphant, T., Peterson, P., et al. 2001-2016, http://www.scipy.org

Kalberla, P. M. W., & Dedes, L. 2008, A&A, 487, 951

Kalberla, P. M. W., & Kerp, J. 2009, ARA&A, 47, 27

Katz, N. 1992, ApJ, 391, 502

Kawamura, A., Mizuno, Y., Minamidani, T., et al. 2009, ApJS, 184, 1

Kennicutt, R. C., & Evans, N. J. 2012, ARA&A, 50, 531

Kennicutt, Jr., R. C. 1989, ApJ, 344, 685

—. 1998, ApJ, 498, 541

Khokhlov, A. 1998, Journal of Computational Physics, 143, 519

Khoperskov, S. A., & Vasiliev, E. O. 2017, MNRAS, 468, 920

Kim, C.-G., & Basu, S. 2013, ApJ, 778, 88

Kim, J.-h., Agertz, O., Teyssier, R., et al. 2016, ApJ, 833, 202

Kravtsov, A. V. 1999, PhD thesis, NEW MEXICO STATE UNIVERSITY

—. 2003, ApJLetters, 590, L1

Kravtsov, A. V., Klypin, A., & Hoffman, Y. 2002, ApJ, 571, 563

Kravtsov, A. V., Klypin, A. A., & Khokhlov, A. M. 1997, ApJS, 111, 73

Kritsuk, A. G., Nordlund, Å., Collins, D., et al. 2011, ApJ, 737, 13

Kruijssen, J. M. D., & Longmore, S. N. 2014, MNRAS, 439, 3239

Krumholz, M. R., & Burkhart, B. 2016, MNRAS, 458, 1671

Krumholz, M. R., Dekel, A., & McKee, C. F. 2012a, ApJ, 745, 69

Krumholz, M. R., Klein, R. I., & McKee, C. F. 2012b, ApJ, 754, 71

Krumholz, M. R., & McKee, C. F. 2005, ApJ, 630, 250

Krumholz, M. R., McKee, C. F., & Tumlinson, J. 2008, ApJ, 689, 865

—. 2009a, ApJ, 693, 216

—. 2009b, ApJ, 699, 850

Krumholz, M. R., & Tan, J. C. 2007, ApJ, 654, 304

Krumholz, M. R., & Thompson, T. A. 2007, ApJ, 669, 289

Kuhlen, M., Krumholz, M. R., Madau, P., Smith, B. D., & Wise, J. 2012, ApJ, 749, 36

Lada, C. J., Forbrich, J., Lombardi, M., & Alves, J. F. 2012, ApJ, 745, 190

Lada, C. J., Lombardi, M., & Alves, J. F. 2010, ApJ, 724, 687

Latif, M. A., Schleicher, D. R. G., Schmidt, W., & Niemeyer, J. C. 2013, MNRAS, 436, 2989

Lee, E. J., Miville-Deschênes, M.-A., & Murray, N. W. 2016, ApJ, 833, 229

Leitner, S. N., & Kravtsov, A. V. 2011, ApJ, 734, 48

Leroy, A. K., Walter, F., Brinks, E., et al. 2008, AJ, 136, 2782

Leroy, A. K., Walter, F., Sandstrom, K., et al. 2013, AJ, 146, 19

Leroy, A. K., Hughes, A., Schruba, A., et al. 2016, ApJ, 831, 16

Leroy, A. K., Schinnerer, E., Hughes, A., et al. 2017, ApJ, 846, 71

Lévêque, E., Toschi, F., Shao, L., & Bertoglio, J.-P. 2007, Journal of Fluid Mechanics, 570, 491

Li, H., Gnedin, O. Y., & Gnedin, N. Y. 2017a, ArXiv e-prints, arXiv:1712.01219

Li, H., Gnedin, O. Y., Gnedin, N. Y., et al. 2017b, ApJ, 834, 69

Li, Y., Mac Low, M.-M., & Klessen, R. S. 2005, ApJLetters, 620, L19

Licquia, T. C., & Newman, J. A. 2015, ApJ, 806, 96

Lilly, S. J., Carollo, C. M., Pipino, A., Renzini, A., & Peng, Y. 2013, ApJ, 772, 119

Lupi, A., Bovino, S., Capelo, P. R., Volonteri, M., & Silk, J. 2018, MNRAS, 474, 2884

Mac Low, M.-M., Klessen, R. S., Burkert, A., & Smith, M. D. 1998, Physical Review Letters, 80, 2754

Madore, B. F. 2010, ApJLetters, 716, L131

Madore, B. F., van den Bergh, S., & Rogstad, D. H. 1974, ApJ, 191, 317

Martizzi, D., Faucher-Giguère, C.-A., & Quataert, E. 2015, MNRAS, 450, 504

McKee, C. F., & Krumholz, M. R. 2010, ApJ, 709, 308

Meidt, S. E., Schinnerer, E., García-Burillo, S., et al. 2013, ApJ, 779, 45

Misiriotis, A., Xilouris, E. M., Papamastorakis, J., Boumis, P., & Goudis, C. D. 2006, A&A, 459, 113

Miville-Deschênes, M.-A., Murray, N., & Lee, E. J. 2017, ApJ, 834, 57

Murray, N. 2011, ApJ, 729, 133

Orr, M. E., Hayward, C. C., Hopkins, P. F., et al. 2018, MNRAS, 478, 3653

Ostriker, E. C., McKee, C. F., & Leroy, A. K. 2010, ApJ, 721, 975

Ostriker, E. C., & Shetty, R. 2011, ApJ, 731, 41

Padoan, P., Federrath, C., Chabrier, G., et al. 2014, Protostars and Planets VI, 77

Padoan, P., Haugbølle, T., & Nordlund, Å. 2012, ApJLetters, 759, L27

Padoan, P., Haugbølle, T., Nordlund, Å., & Frimann, S. 2017, ApJ, 840, 48

Padoan, P., & Nordlund, Å. 2011, ApJ, 730, 40

Parmentier, G. 2017, ApJ, 843, 7

Peng, Y.-j., & Maiolino, R. 2014, MNRAS, 443, 3643

Petric, A. O., & Rupen, M. P. 2007, AJ, 134, 1952

Pineda, J. L., Langer, W. D., Velusamy, T., & Goldsmith, P. F. 2013, A&A, 554, A103

Price, D. J., & Bate, M. R. 2009, MNRAS, 398, 33

Rahimi, A., & Kawata, D. 2012, MNRAS, 422, 2609

Rahmati, A., Pawlik, A. H., Raičevič, M., & Schaye, J. 2013, MNRAS, 430, 2427

Rebolledo, D., Wong, T., Xue, R., et al. 2015, ApJ, 808, 99

Renaud, F., Kraljic, K., & Bournaud, F. 2012, ApJLetters, 760, L16

Robertson, B., & Goldreich, P. 2012, ApJLetters, 750, L31

Robertson, B. E., & Kravtsov, A. V. 2008, ApJ, 680, 1083

Roman-Duval, J., Heyer, M., Brunt, C. M., et al. 2016, ApJ, 818, 144

Rudd, D. H., Zentner, A. R., & Kravtsov, A. V. 2008, ApJ, 672, 19

Safranek-Shrader, C., Krumholz, M. R., Kim, C.-G., et al. 2017, MNRAS, 465, 885

Sagaut, P. 2006, Large Eddy Simulation for Incompressible Flows (Springer-Verlag Berlin Heidelberg)

Saitoh, T. R., Daisaka, H., Kokubo, E., et al. 2008, PASJ, 60, 667

Salim, D. M., Federrath, C., & Kewley, L. J. 2015, ApJLetters, 806, L36

Sanduleak, N. 1969, AJ, 74, 47

Schaye, J., & Dalla Vecchia, C. 2008, MNRAS, 383, 1210

Schmidt, M. 1959, ApJ, 129, 243

Schmidt, W. 2014, Numerical Modelling of Astrophysical Turbulence (Springer International Publishing)

Schmidt, W., & Federrath, C. 2011, A&A, 528, A106

Schmidt, W., Almgren, A. S., Braun, H., et al. 2014, MNRAS, 440, 3051

Schruba, A., Leroy, A. K., Walter, F., Sandstrom, K., & Rosolowsky, E. 2010, ApJ, 722, 1699

Schruba, A., Leroy, A. K., Walter, F., et al. 2011, AJ, 142, 37

Schruba, A., Leroy, A. K., Kruijssen, J. M. D., et al. 2017, ApJ, 835, 278

Semenov, V. A., Kravtsov, A. V., & Gnedin, N. Y. 2016, ApJ, 826, 200

—. 2017, ApJ, 845, 133

—. 2018, ApJ, 861, 4

—. 2019, ApJ, 870, 79

Silk, J. 1997, ApJ, 481, 703

Silk, J., & Norman, C. 2009, ApJ, 700, 262

Simpson, C. M., Bryan, G. L., Hummels, C., & Ostriker, J. P. 2015, ApJ, 809, 69

Sofue, Y. 2017, MNRAS, 468, 4030

Springel, V., & Hernquist, L. 2003, MNRAS, 339, 289

Stecher, T. P., & Williams, D. A. 1967, ApJLetters, 149, L29

Stinson, G. S., Brook, C., Macciò, A. V., et al. 2013, MNRAS, 428, 129

Stone, J. M., Ostriker, E. C., & Gammie, C. F. 1998, ApJLetters, 508, L99

Sun, J., Leroy, A. K., Schruba, A., et al. 2018, ArXiv e-prints, arXiv:1805.00937

Tacconi, L. J., Genzel, R., Saintonge, A., et al. 2018, ApJ, 853, 179

Tamburro, D., Rix, H.-W., Leroy, A. K., et al. 2009, AJ, 137, 4424

Tan, J. C. 2000, ApJ, 536, 173

Toomre, A. 1964, ApJ, 139, 1217

Turk, M. J., Smith, B. D., Oishi, J. S., et al. 2011, ApJS, 192, 9

Utomo, D., Bolatto, A. D., Wong, T., et al. 2017, ApJ, 849, 26

Utomo, D., Sun, J., Leroy, A. K., et al. 2018, ApJLetters, 861, L18

van der Walt, S., Colbert, S. C., & Varoquaux, G. 2011, CSE, 13, 22

van Leer, B. 1979, Journal of Computational Physics, 32, 101

Vutisalchavakul, N., Evans, II, N. J., & Heyer, M. 2016, ApJ, 831, 73

Wang, P., Li, Z.-Y., Abel, T., & Nakamura, F. 2010, ApJ, 709, 27

Wolfire, M. G., McKee, C. F., Hollenbach, D., & Tielens, A. G. G. M. 2003, ApJ, 587, 278

Wong, T., & Blitz, L. 2002, ApJ, 569, 157

Wong, T., Xue, R., Bolatto, A. D., et al. 2013, ApJLetters, 777, L4

Wu, J., Evans, II, N. J., Gao, Y., et al. 2005, ApJLetters, 635, L173

Wyse, R. F. G., & Silk, J. 1989, ApJ, 339, 700

Yepes, G., Kates, R., Khokhlov, A., & Klypin, A. 1997, MNRAS, 284, 235

Zamora-Avilés, M., & Vázquez-Semadeni, E. 2014, ApJ, 793, 84

Zamora-Avilés, M., Vázquez-Semadeni, E., & Colín, P. 2012, ApJ, 751, 77

Zuckerman, B., & Evans, II, N. J. 1974, ApJLetters, 192, L149

Zuckerman, B., & Palmer, P. 1974, ARA&A, 12, 279